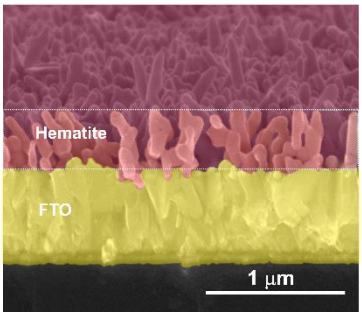

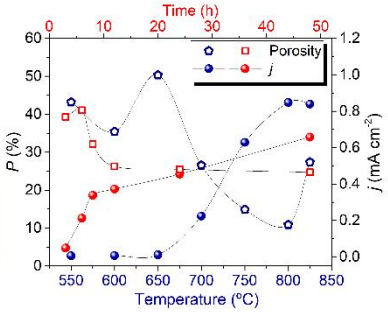

Environmentally friendly photoanodes for solar water splitting

Paula Virgínia Barros Quitério
Doutoramento em Física
Departamento de Física e Astronomia
2020

Orientador
Prof. João Pedro de Esteves de Araújo, FCUP

Coorientador
Dra. Célia Tavares de Sousa, FCUP

Coorientador
Prof. Adélio Mendes, FEUP

Paula Virgínia Barros Quitério

Environmentally friendly photoanodes for solar water splitting

Supervisor: Prof. João Pedro de Esteves de Araújo, FCUP

Co-Supervisor: Dr. Célia Tavares de Sousa, FCUP

Prof. Adélio Mendes, FEUP

*Thesis submitted to the Faculty of Sciences of the U*niversity of Porto in partial fulfilment of the requirements for the degree *of Doctor in Physics*

Department of Physics and Astronomy

Faculty of Sciences of the University of Porto

2020

Institutions involved in this thesis:

Funding:

This PhD work was supported by the Fundação para a Ciência e a Tecnologia (Portuguese Agency for Research) fellowship SFRH/BD/110698/2015, and STSM grant Marie Sklodowska-Curie Grant Agreement No. 734801, within the Magnamed Project.

FCT
Fundação para a Ciência e a Tecnologia
MINISTÉRIO DA CIÊNCIA, TECNOLOGIA E ENSINO SUPERIOR

To my mother and my father,

To my sisters and nephews,

To Zé.

À minha mãe e ao meu pai,

Às minhas irmãs e meus sobrinhos,

Ao Zé.

Acknowledgements

I would like to express my deepest gratitude to everyone who supported me during this thesis, to all of those without whom it wouldn´t have been possible. For all the guidance, help, support, friendship, I am truly thankful. I really hope I am not forgetting anyone.

I would like to sincerely thank my supervisor, Professor João Pedro Araújo for everything, for the opportunity of being part of such a wonderful and prestigious research group, for welcoming me so well (since 2012), as a family, for all the consideration, trust, friendship, help and support during all these years, and for making this work possible.

To my co-supervisor Professor Adélio Mendes, who so kindly welcomed me in his group, for his dedication and support, and for allowing me the opportunity to work in the area of photoelectrochemical cells and to learn about it, I am deeply grateful.

To my co-supervisor Professor Célia Sousa, a fantastic person and supervisor, with a unique and exceptional sense of humour, truly kind and friendly, I must thank her for all the support, dedication and opportunities through all these years and especially during this thesis, for making this work possible. For the enormous friendship, teaching, professional advices, and trust deposited in my work, my gratitude goes beyond words.

I would like to thank Arlete Apolinário for being such a good and genuine friend. I must thank her for all the constant support and dedication and for her endless patience during those times (many times) I showed up by her office door with interminable doubts. For all your help, guidance, concern and support my gratitude goes beyond words, and therefore, I also dedicate this work to her.

To David Navas for friendship, good mood and all the support. A special thanks for all the uninterrupted hours at synchrotron and most importantly, for the opportunity to be there!!

I would like to express thanks to Professors Klebert Pirota and Fanny Beron for their hospitality and availability in receiving our team at Unicamp. It was a great experience and an excellent opportunity to learn within this collaboration specialized in alumina and magnetic materials. Also, a big thanks for all help, support, friendship and kindness from Rahul, Alex and Marcus. To Vivian and Suellen for being such great hostesses in Brazil, for all friendship, help and support, and for the great moments sharing a “pastel da feira”, “coxinha” or “bolo de leite ninho”. A special thanks to Suellen for being up all night (and several nights) at synchrotron with me!! To Professor Gustavo, Junior, Daniela and

Santiago from LNLS, also to Marlene and Natalia from LNLS laboratory, who welcomed us so well, for all the technical support and help with XAFS that so much improved the work developed in this thesis, I am deeply grateful. A special thanks to Lucas Rodrigues, who so kindly helped with the XAFS data.

I also want to thank the members of the jury, Professor Olga Caballero, Professor Aurelio Hierro, Professor Bernardo Almeida and Professor José Luís dos Santos for their availability and for taking the time to read this thesis.

I also have to appreciate the CEMUP´s team, especially to Rui Rocha, for his dedication during the SEM sessions, friendship, good mood and above all, professionalism. Also, to Professor Carlos Sá, Daniela Silva and Ana Queirós, for their kindness and support. A special acknowledgment for the opportunity to participate in the SEM sessions with the students at each Summer school.

I would like to thank to Professor Bernardo Almeida for receiving us so well at Minho University, allowing me the opportunity to learn and use the PLD system, and also for his sympathy and kindness. Also, a special thanks to Vivian for her support with PLD.

Also, to Professor Pedro Tavares from UTAD that so kindly teach and helped me with the XRD refinements.

I must express my gratitude to the LEPABE-FEUP team, especially to Paula Dias, João Azevedo for all the support, availability, kindness, and all the help with measurements and technical support with equipment's at LEPABE. Also, to Tânia Lopes, Luísa Andrade, Mafalda Pereira and Filipe Moisés, I am very thankful for the help, support with the measurements and for their sympathy.

To Sérgio Magalhães, I would like to thank his great dedication to this work, support, help, friendship and kindness to explain such a difficult technique, RBS, that highly improved this work. And to Professor Eduardo Alves for the opportunity of collaboration, his kind words and support.

To Engenheiro Francisco for his dedication, patience, friendship and for all the important knowledge that always transmitted each time (lots) that I had to bother him. To Isabel Alves for her enormous dedication, friendship, patience, promptitude, and efficiency in solving each problem, even when it was not her matter. To Dra. Armanda for her kindness, dedication, promptitude and professionalism. To Fernando for his patience and hard work that put on each autoclave and small pieces I had to ask him to optimize this work. To Florbela, Dona Armanda, Dona Cristina, Dona Filomena, Pedro, Hernani, Dra. Maria, Ângela, Sr. José, Sr. Rui and all security staff, Dona Sandra and cleaning staff, and all the FCUP collaborators who so kindly helped and supported me through all these years.

To all IFIMUP Professors: João Ventura, Armandina Lopes, André Pereira, Agostinho Moreira, Abílio Almeida, Hélder Crespo for their kindness, collaboration, help, friendship and team-spirit. Also, to Professor Moreira and Professor Bessa for their sympathy and kindness.

I am also thankful to former members Maria Susano, Mónica Cerquido, Mariana Proença, Aurélio Hierro, Maria Paz, Pedro Sampaio, Ana Gomes, Vanji, Bolaji, Mourad, Majid, Inês Figueiredo, Nathalie, Joel Puga, Bernardo, Marcelo, Sílvio, Teresa Carvalho, Diogo Costa, Sara Piano, Iuliia, Alvita, Pedro Resende, Ricardo Teixeira and Tiago Leal for their help, support, friendship and kindness.

To all my dear IFIMUP colleagues for their friendship, help support, collaboration, and good moments: Pedrito Rodrigues, Cátia Rodrigues, Suellen Moraes, Ana Pires, Ana Silva, Catarina Dias, Rui Vilarinho, Vivian, João Horta, Gonçalo, Bogdan, Sofia Teixeira, Ricardo Magalhães, Ana Tresguerres, Sofia Caspani, Ludgero, Simão, João Fradet, João Cabaço, Pedro Machado, José Pedro, Mariana Gomes, Manjunath, Rita Veloso, Francisca, Ana Rita, Margarida, Joana, Rui Costa, Mariana Rocha, Leandro Martins, Miguel Canhota, Neenu, Maryam, Jamal, Henrique, and the nanosolar team Afonso, Francisco and Nuno.

To my good friends from other research groups Catarina Cosme, Claúdio Gomes, Vasco, Jisha, Niaz, Robert, André, Balaji, Abbas, Duarte Viveiros, Joana Paiva, Rita Ribeiro and Nuno Pereira, thanks for your true friendship, dedication and support. A special thanks to Catarina Cosme for being such a good friend, always so kind, for being there for me, for the comforting words, even so far away.

To the pilates class, especially to Catarina (for “dragged” me to classes), Isabel, Cristina, Ana, Constança, a big thanks for the friendship and good moments, to “Mestre” Leandro and to “Mestre” Rafael for their friendship and dedication.

To the Mulherendo association, in particular to Susana Fonseca for the excellent work, help and support. To Dr. Hélder Ferreira for all the medical help, without which it would have been very difficult to carry out this PhD, and for the words of encouragement in each consultation “Paulita, how is the PhD going?”. Thank you very much for your dedication to the SNS.

À minha irmã Tina, por seres um pilar na minha vida, por seres uma verdadeira fonte de inspiração, pela amizade e sorrisos, por me dares força e me ajudares a levantar cada vez que me vou abaixo. Apesar de estares longe, nunca me fazes sentir só. À minha irmã Irene, pelo carinho, enorme amizade, dedicação e todo o apoio durante todos estes anos, um grande beijinho. Aos meus cunhados, Jorge e Zé Couto pelo apoio e amizade; um obrigado especial ao Zé Couto e à Dona Ana por toda a ajuda, hospitalidade e apoio que me deram ao longo de todos estes anos de doutoramento.

Aos meus queridos sobrinhos, Joaninha e Jorgito, pela vossa amizade, carinho, por serem tão bons miúdos, e ao meu querido sobrinho e afilhado Gustavo, obrigada por seres tão fixe, seres meu amigo, seres genuíno e poder contar contigo. Sou uma tia muito orgulhosa!! Um agradecimento especial aos meus pequeninos patudos Bolinha, Chico e Quico, obrigado por aparecerem na minha vida, por me encherem de sorrisos e pelos vossos carinhos genuínos. Ao Zé, especialmente por me aturares há tanto tempo (lol), pela tua dedicação, por nunca me deixares ir abaixo, pelo carinho, amizade, e todo o teu apoio, a minha gratidão vai para além das palavras. Aos meus queridos pais, Mariana e Nicolau por serem os grandes pilares da minha vida, pelos sacrifícios, amor incondicional, carinho, compreensão, amizade, por estarem sempre ao meu lado, por poder contar sempre convosco nos bons e maus momentos. Um infinito obrigado.

Resumo

O hidrogénio (H_2) tem-se tornado uma solução energética de extrema relevância, devido à necessidade de encontrar uma alternativa para as necessidades energéticas globais e resolver os problemas ambientais associados ao uso dos combustíveis fósseis, representando um combustível limpo e de baixo custo. As células fotoeletroquímicas (PEC) para produzir H_2 diretamente a partir de recursos sustentáveis e limpos, como luz solar e a água, usando semiconductores fotoativos, têm-se tornado uma das formas alternativas mais esperançosas de converter energia solar em energia química. Os avanços rápidos na nanotecnologia permitiram a produção e o desenvolvimento de nanoestruturas que podem atender a esse tipo de demanda.

Um dos maiores desafios é encontrar um semicondutor adequado, que cumpra todos os requisitos para formar um dispositivo fotoeletroquímico sustentável, que reúna eficiência, baixo custo, estabilidade, não-toxicidade e que seja escalável. Entre várias possibilidades existentes, materiais como o óxido de ferro hematite (α-Fe_2O_3), trióxido de tungsténio (WO_3) e dióxido de titânio (TiO_2) têm atraído cada vez mais atenção por reunirem excelentes propriedades.

O uso da configuração 1D com uma elevada organização, como é o caso dos nanotubos (NTs) ou nanofios (NWs), permite uma separação de cargas eficiente e o transporte de eletrões no fotoelétrodo. Para obter essas nanoestruturas, a escolha do método de síntese é também um factor determinante na viabilidade dos dispositivos PEC.

O método hidrotérmico e a anodização electroquímica têm mostrado ser formas simples e de baixo custo para obter nanoestruturas com diferentes morfologias. Neste trabalho de doutoramento, nanoestruturas tais como NTs e NWs de α-Fe_2O_3, e nanoplacas de WO_3 foram produzidas por método hidrotérmico, e NTs de α-Fe_2O_3 e de TiO_2 foram produzidos por anodização. As propriedades morfológicas, estruturais, óticas e fotoeletroquímicas das nanoestruturas produzidas foram sistematicamente caracterizadas.

A hematite é um material não tóxico, com alta estabilidade química e pequeno hiato energético (2.2 eV), que absorve luz até 600 nm. No entanto, a hematite apresenta várias limitações de desempenho nas células PEC, como a baixa condutividade eletrónica e dos vazios, que levam a perdas de eficiência significativas devido à elevada recombinação de pares lacunas-eletrões. Os NWs de hematite, devido a uma maior

área superficial fotoativa e caminhos mais diretos para o transporte de cargas no fotoânodo, têm sido amplamente explorados na literatura, principalmente numa perspetiva de caracterização fotoeletroquímica. Aqui, explorámos a compreensão físico-química dos NWs de hematite produzidos por método hidrotérmico, seguido pela aplicação de diferentes condições de recozimento, uma etapa considerada crítica para obter a fase de hematite e aperfeiçoar a sua condutividade e cristalinidade. O tempo de recozimento, geralmente um parâmetro desvalorizado, é de particular interesse, pois permite o uso de temperaturas mais baixas (como 600 ºC) com substratos de óxido de estanho dopado com flúor (FTO) consideravelmente mais baratos, com interesse à escala industrial dos dispositivos PEC. As melhores conversões energia solar para corrente, j ~0.9 mA·cm^{-2} [a 1.45 V vs. RHE (elétrodo de hidrogénio reversível)], foram obtidas para os NTs de hematite recozidos a 550 ºC (2 h) com um recozimento curto adicional a 800 ºC. No entanto, foi obtida uma foto-performance de ~0.7 mA·cm^{-2} para os NTs de hematite recozidos a 600 ºC com tempo prolongado (48 h), valor 35 vezes superior ao obtido com 3 h de recozimento. Nestas condições de maior temperatura e maior tempo de recozimento, os fotoânodos de hematite apresentaram propriedades melhoradas que beneficiam a foto-eficiência, tais como maior cristalinidade e ordenação de ligações atómicas, e uma maior difusão de Sn do substrato FTO, que leva ao aumento da condutividade.

A dopagem intencional da hematite, usando o elemento Ti, é um dos caminhos mais promissores para o melhoramento da eficiência PEC. Neste trabalho, os NWs de hematite dopados com Ti foram fabricados por método hidrotérmico. Investigou-se não apenas o efeito do Ti, mas também a influência da temperatura de recozimento, comparando com os NWs de hematite sem dopante. Neste trabalho, os maiores valores de j ~1.27 mA·cm^{-2} (a 1.45 V_{RHE}) foram obtidos com a dopagem de Ti e o recozimento adicional a 800 ºC, um aumento significativo em comparação com os valores mais baixos de j obtidos com os fotoânodos sem dopante nas mesmas condições de recozimento. Além disso, estes fotoânodos mostraram-se estáveis durante 2 h de medições de fotocorrente contínuas (a 1.23 V_{RHE}). Uma estratégia diferente para melhorar a condutividade da hematite foi através da incorporação de Sn. Numa colaboração entre o IFIMUP e o IST-CTN (Lisboa), foi possível usar a técnica de implantação iónica (não amplamente disponível) e estudar diferentes fluências e o seu efeito nas propriedades dos NWs de hematite. A fluência revelou afetar significativamente as características morfológicas e estruturais dos NWs de hematite, mas é um caminho promissor para a melhoria da eficiência PEC.

O método hidrotérmico também pôde ser usado para produzir NTs de hematite com sucesso. No entanto, estas nanoestruturas não nucleiam diretamente no FTO, como

acontece com os NWs, formando-se apenas em solução. Em vez disso, cresceram no FTO novas estruturas com morfologias de agulha e esféricas, revelando propriedades interessantes. Comparativamente aos NWs de hematite obtidos a 550 ºC (*j* = 0.01 $mA \cdot cm^{-2}$), as nanoagulhas/esferas produziram *j* ~0.1 $mA \cdot cm^{-2}$ nas mesmas condições. Adicionalmente, os NTs formados em solução foram usados para revestir o FTO, testando o uso de polímeros. No entanto, a baixa adesão ao substrato leva ao desprendimento e aos baixos valores de *j*. Mesmo assim, estas nanoestruturas constituem um trabalho promissor a ser posteriormente desenvolvido.

Outra maneira simples e de baixo custo para o fabrico de NTs de hematite é por anodização eletroquímica, através da qual a forma das nanoestruturas pode ser controlada com precisão. Aqui, explorámos a fabricação de NTs de hematite por anodização rápida de folhas de Fe. Foi estimado o efeito do potencial de anodização nas características morfológicas, como comprimento, espessura da parede, diâmetro dos poros, distância entre poros e porosidade dos NTs. Foi estabelecida uma relação entre as curvas de carga de anodização, o comprimento dos NTs e a porosidade. O regime ideal de anodização para um crescimento mais rápido e organizado de NTs foi encontrado para potenciais de anodização de 20 até 60 V (em que NTs longos com ~4,6 µm podem crescer em apenas 5 minutos), com interesse prático para aplicações PEC. Um valor de fotocorrente de ~0.5 $mA \cdot cm^{-2}$ (1.23 V_{RHE}) foi obtido para os fotoânodos anodizados a 20 V, apresentando um melhor regime de porosidade.

Com uma maior mobilidade de eletrões e comprimentos de difusão de portadores de carga mais longos comparativamente à hematite, o WO_3 também é considerado um material promissor para a separação PEC de água. Aqui, os fotoânodos de WO_3 foram preparados usando várias camadas de nanoplacas obtidas por etapas sequenciais de processos hidrotérmicos e de recozimento. O número de camadas foi testado até atingir uma limitação no desempenho da fotocorrente *j*. Foi alcançada uma melhoria de *j* de 0.56 para 0.96 $mA \cdot cm^{-2}$ (a 1.45 V_{RHE}), respectivamente de 1 para 5 camadas.

Os NTs de TiO_2 possuem propriedades físico-químicas únicas, tornando-os um material versátil para várias aplicações, permitindo um amplo uso em ambos dispositivos PEC e células solares sensibilizadas com corante (DSC). No IFIMUP, existe um forte conhecimento estabelecido nos últimos anos na nanofabricação de matrizes de alumina nanoporosa e NTs de TiO_2. No entanto, ainda existem algumas questões em aberto, em particular a reutilização de eletrólitos entre anodizações, com interesse para as aplicações industriais. Estudou-se o efeito da re-utilização de eletrólitos em anodizações com diferentes potenciais na morfologia dos NTs (diâmetro e taxa de crescimento), correlacionada com as curvas de anodização. A presença de morfologia estriada (ribs),

aqui obtida com a re-utilização sucessiva do eletrólito, foi reportada pelo seu interesse prático nas aplicações DCS e PEC.

Finalmente, incluímos um capítulo com o trabalho em curso, onde foram desenvolvidos fotoânodos promissores: filmes finos de ferro depositados diretamente no FTO através das técnicas de feixe de eletrões e deposição por feixe de iões. Estes filmes, com espessuras médias na ordem dos 500 nm, são depois utilizados para a formação de NTs de óxido de ferro por anodização. Num outro trabalho, a deposição de filmes finos de Fe (~122 nm) por deposição a laser pulsado também originou valores de *j* promissores na ordem dos 0.34 $mA \cdot cm^{-2}$ (a 1.45 V_{RHE}). Pretendemos dar continuidade a este trabalho no futuro, através da otimização das condições de deposição e utilização de dopantes, como Sn ou Ti.

Palavras-chave: Colheita de energia solar, Células fotoeletroquímicas, Semicondutor, Hematite, Trióxido de tungsténio, Dióxido de titânio, Nanofios, Nanotubos, Nanoplacas, Hidrotérmico, Anodização eletroquímica.

Abstract

Hydrogen (H_2) energy has become of upmost importance due to the imperative requirements of solving the global energy demand and environmental problems related with the use of fossil fuels, representing a clean and low-cost fuel. Photoelectrochemical (PEC) cells for directly producing H_2 from sustainable and clean resources such as sunlight and water, using photoactive semiconductors are becoming one of the most hopeful alternative ways for converting solar energy into chemical energy. The quick advances in nanotechnology allowed the production and development of nanostructures that can address this kind of demand.

One of the major challenges is to find a suitable semiconductor that fulfills all the requirements for a sustainable PEC device, one that encounters efficiency, low-cost, stability, nontoxicity and scalability. Among several possibilities, materials such as iron oxide hematite (α-Fe_2O_3), tungsten trioxide (WO_3) and titanium dioxide (TiO_2) have been attracted increasing attention for gathering outstanding properties.

The use of highly ordered 1D configuration, such as nanotubes (NTs) or nanowires (NWs), allows an efficient charge separation and electron transport inside the photoelectrode. In order to obtain these nanostructures, the choice of the synthesis method is also key factor for the viability of PEC devices.

Hydrothermal method and electrochemical anodization have shown to be simple and low-cost ways to obtain nanostructures with different morphologies. In this PhD work, nanostructures such as α-Fe_2O_3 NWs and NTs, and WO_3 nanoplates were produced by hydrothermal method, while NTs of α-Fe_2O_3 and TiO_2 were produced by anodization. The morphological, structural, optical and photoelectrochemical properties of the produced nanostructures were systematically characterized.

Hematite is a non-toxic material, with high chemical stability and small band gap (2.2 eV), which absorbs light up to 600 nm. However, hematite presents several limitations to PEC´s photoperformance, such as poor conductivity and small hole diffusion length, which lead to significant efficiency losses due to the high electron-hole recombination. Hematite NWs, due to enhanced photoactive surface area, have been widely explored in literature, mainly in a perspective of PEC characterization. Here, we explored the physical-chemical insights of hematite NWs produced by hydrothermal method, followed by different annealing conditions, a critical step to obtain the hematite phase and enhance its conductivity and crystallinity. Annealing time, usually an overlooked

parameter, is of particular interest, since it allows the use of lower temperature (600 ºC) with considerably cheaper fluorine-doped tin oxide (FTO) substrates, important to the scale-up of PEC devices. The best solar-to-current conversions, j ~0.9 mA·cm^{-2} [at 1.45 V *vs*. RHE (reversible hydrogen electrode)], were attained for hematite NWs annealed at 550 ºC (2 h) with additional short annealing at high 800 ºC. Nevertheless, a photoperformance ~0.7 mA·cm^{-2} was also attained for hematite NWs annealed at 600 ºC with prolonged time (48 h), 35 times higher than sample annealed for 3 h. Under conditions of higher temperature and longer annealing time, the hematite photoanodes showed improved properties that benefit the photoperformance, such as higher crystallinity, enhanced bond ordering, and higher Sn diffusion from FTO substrate, which leads to increased conductivity.

The intentional doping of hematite, using Ti element, is one of the most promising routes towards the PEC´s efficiency enhancement. In this work, hematite NWs doped with Ti were fabricated by hydrothermal method. It was investigated not only the effect of Ti-doping but also the influence of annealing temperature, comparing with hematite NWs without dopant. Highest j value of ~1.27 mA·cm^{-2} (at 1.45 V_{RHE}) was obtained with Ti doping and additional annealing at 800 ºC, a significant increase comparatively with lower j values for photoanodes without dopant with the same annealing conditions. Also, these photoanodes revealed to be stable under 2 h of continuous j measurements (at 1.23 V_{RHE}). A different strategy to improve the hematite´s conductivity was achieved by incorporation of Sn element. Within a collaboration between IFIMUP and IST-CTN (Lisbon), it was possible to use ion implantation technique (not widely available), and study different fluences and its effect on the properties of hematite NWs. It revealed to significantly affect the morphological and structural features of hematite NWs, but to be a promising way towards the PEC efficiency improvement.

Hydrothermal method was also used to successfully produce hematite NTs. However, these nanostructures did not nucleate upon FTO, as happen with NWs, but were formed in the precursor solution. Instead, new structures with needle and spherical morphologies were grown on the FTO surface, revealing interesting properties. Comparatively with hematite NWs obtained at 550 ºC (j = 0.01 mA·cm^{-2}), the nanoneedles/spheres yielded j ~0.1 mA·cm^{-2} in the same conditions. Additionally, the NTs formed in solution were coated on FTO, by testing the use of polymers. However, poor adhesion to substrate lead to detachment and low j values. Nevertheless, these nanostructures constitute a promising work to be further developed.

Hematite nanotubes (NTs) were also fabricated by using another simple and low-cost approach, the electrochemical anodization, in which the shape of NTs can be effectively controlled. Here, a fast anodization of Fe foils was performed. The effect of the

anodization potential in the morphological features, such as length, wall thickness, pore diameter, interpore distance and porosity of the NTs was estimated. A relation between the anodization charge curves, NTs length and porosity was established. The optimum anodization regime for a faster and organized growth of NTs was found for bias voltage from 20 V up to 60 V (in which long nanotubes with ~4.6 µm can grow in just 5 minutes), with practical interest for PEC applications. A *j* ~0.5 mA·cm^{-2} (1.23 V_{RHE}) was achieved for the 20 V photoanodes that presented an improved porosity regime.

With higher electron mobility and longer charge carrier diffusion lengths comparatively with hematite, WO_3 is also considered a promising material for PEC water splitting. Here, WO_3 photoanodes were designed using several layers of nanoplates obtained by sequential steps of hydrothermal and annealing processes. The number of layers were tested up to a limitation of *j* performance was achieved. A *j* improvement, from 0.56 to 0.96 mA·cm^{-2} (at 1.45 V_{RHE}) respectively for 1 to 5 layers, was achieved.

TiO_2 NTs have unique physical-chemical properties, making them a versatile material to several applications, allowing a broad use in both dye-sensitized solar cels (DSC) and PEC devices. At IFIMUP, there is a strong know-how established in the recent years in the nanofabrication of alumina nanopores and titania NTs, specifically by Ti anodization. However, there are still some open issues, namely the electrolyte re-utilization between anodizations with interest for industrial applications. It was studied the effect of electrolyte re-use at different bias voltages on the NTs morphology (diameter and growth rate), correlated with the anodization curves. The presence of ribs morphology, here obtained with successive electrolyte re-use, was reported for its practical interest in DCS and PEC´s applications.

Finally, we include ongoing work, with other promising photoanodes developed by using thin films of iron deposited directly on the FTO using electron beam and ion beam deposition techniques. These films (with thicknesses ~500 nm) are then used to form iron oxide NTs by anodization. In another study, the deposition of thin Fe films (~122 nm) by pulsed laser deposition gave rise to promising *j* values in the order of 0.34 mA·cm^{-2} (at 1.45 V_{RHE}). Promising photoanodes will be expected, by optimizing the deposition and annealing conditions and the incorporation of dopants, such as Sn or Ti.

Keywords: Solar energy harvesting, Photoelectrochemical cells, Semiconductor, Hematite, Tungsten trioxide, Titanium dioxide, Nanowires, Nanotubes, Nanoplates, Hydrothermal, Electrochemical anodization.

Table of Contents

List of Figures

List of Tables

List of Abbreviations and Symbols

BB, Bragg-Brentano

BSE, backscattered electrons

BZ, Brillouin zone

c, Speed of light

CB, Conduction band

CE, Counter electrode

D, Diameter

d_{hkl}, plane spacing

D_{int}, Interpore distance

D_{out}, Outer diameter

DSC, Dye-sensitized solar cells

D_p, Pore diameter

D_{XRD}, Crystallite size

e^-, electron

E, Electric field

EDS, Energy dispersive X-ray spectroscopy

E_g, Band gap

EG, ethylene glycol

EXAFS, Extended X-Ray Absorption Fine Structure

F, Faraday constant

FF, Fill-factor

FTO, Fluorine-doped tin oxide

FWHM, Full width at half maximum

h, Planck constant

h^+, hole

HCPA, Hexagonal close-packed arrays

I_0, X-ray intensity incident on a sample

I, X-ray intensity transmitted through the sample

IBD, Ion beam deposition

IPCE, Incident photon-to-current conversion efficiency

ISTC, Intrinsic solar to chemical conversion

IV, Infrared

j, Photocurrent density

j_{anod}, Current density

J_{Photo}, Photocurrent density

j_{min}, Current density minimum

j_{max}, Current density maximum

L, Length/Thickness

MEA, Membrane Electrode Assembly

NPs, Nanoparticles

NTs, Nanotubes

NWs, Nanowires

OER, Oxygen Evolution Reaction

PAA, Porous anodic alumina

PB, Parallel beam

PEC, Photoelectrochemical

PEM, Proton Exchange Membrane

PLD, Pulsed Laser Deposition

P_{light}, intrinsic photovoltaic power

P, Porosity

PV, Photovoltaic

PVD, Physical vapor deposition

Q, Charge

RE, Reference electrode

RBS, Rutherford Backscattering Spectrometry

RHE, Reversible hydrogen electrode

RT, Room temperature

SCE, Standard calomel electrode

SE, Secondary electrons

SEM, Scanning Electron Microscopy

SRIM, Stopping and Range of Ions in Matter

T_C, Curie temperature

T_M, Morin transition

UV, Ultra-violet

U_{dark}, Potential necessary to reach the same current in dark

V, Voltage

V_{anod}, Anodization voltage

VB, Valence band

V_{cell}, Volume of the unit cell

V_{onset}, Onset potential

V_{Photo}, Photopotential

V_{RHE}, Voltage *vs.* RHE (reversible hydrogen electrode)

w, Full width at half-maximum (FWHM) of Bragg peaks

W, Wall thickness

WE, Working electrode

XAFS, X-ray absorption fine structure

XANES, X-ray absorption near the edge structure

XPS, X-ray photoelectron spectroscopy

XRD, X-ray diffraction

ΔE^o, Standard electric potential

ΔG^o, Standard Gibbs free energy

θ, Diffraction angle

η_{el}, Electrolysis efficiency

σ^2, Debye–Waller factor

λ, Wavelength of irradiation

ε, Microstrain

δ_b, Oxide barrier layer

υ, Frequency

μ, Absorption coefficient

$\chi(k)$, Oscillations as a function of the photo-electron wave number

η, Viscosity

ω_{vib}, Vibrational frequencies of the molecules

ω_R, Frequency of photon emitted by a sample

k, Scherrer constant

Thesis Outline

The main focus of this thesis is the development of nanostructured semiconductor materials to be used as photoelectrodes in solar energy harvesting applications, in particular for photoelectrochemical (PEC) hydrogen generation from water splitting.

Three semiconductor materials, hematite, α-Fe_2O_3, titanium dioxide, TiO_2, and tungsten trioxide, WO_3, were chosen for gathering important properties, such as low-cost, availability, scalability, chemical stability, and mostly to constitute environmentally friendly resources. The developed nanostructures were mostly produced by simple and low-cost methods such as hydrothermal and electrochemical anodization.

This PhD work was developed under the collaboration between the research group of Multifunctional Magnetic Materials and Nanostructures from the Institute of Physics for Advanced Materials, Nanotechnology and Photonics (IFIMUP), at the Faculty of Sciences of the University of Porto (FCUP), led by Prof. João Pedro Araújo, and the research Laboratory for Process, Environment, Biotechnology and Energy Engineering (LEPABE) at the Faculty of Engineering of the University of Porto (FEUP), in the research group of Prof. Adélio Mendes.

In a first stage, an intense and systematic optimization of the synthesis process was carried out, since several nanostructures were synthesized for the first time at IFIMUP. In this respect, nanostructures such as hematite nanowires (NWs) and nanotubes (NTs), and WO_3 nanoplates were successfully obtained by using the hydrothermal method. Then, the photocurrent of the developed nanostructures was evaluated at LEPABE in order to understand in depth the impact of the physical properties in the photoelectrodes performance. This work also helped to pave the way for future development and optimization of this kind nanostructures.

This thesis is structured in nine chapters, comprising an Introduction, the Experimental techniques, five Chapters describing the developed nanostructures and the main results and discussion, a Chapter reporting ongoing research work, and a final Chapter with Conclusions and Future Perspectives.

A brief summary is given:

Chapter 1 - Introduces the principles of the photoelectrochemical (PEC) cells, the hydrogen as a fuel for the future, its advantages and applications. The materials used as photoanodes in PEC cells are presented, in particular hematite, tungsten trioxide and

titanium dioxide, respective properties, their main advantages as semiconductors and the main synthesis methods.

Chapter 2 - In this chapter, it is presented a description of the experimental methods and characterization techniques used. The first section comprises the description of reagents and the synthesis methods such as anodization, hydrothermal and thin film deposition. In the second section are described the characterization techniques, in particular the morphological, structural, optical and photoelectrochemical techniques used for the characterization of the produced photoanodes.

Chapter 3 - In this chapter, it is described the development of hematite nanowires (NWs) by hydrothermal method, followed by optimization of the annealing conditions to obtain the hematite pure phase. The relation between physical-chemical properties such as morphological features, crystallinity improvement and Sn diffusion from the substrate are presented and discussed. A model for porosity based on the morphological and light absorption properties of the hematite NWs is also unveiled.

Chapter 4 – As in the previous chapter, the same kind of photoanodes by hydrothermal method were developed, with addition of titanium (Ti) doping. The NWs features were explored. In another approach, the use of ion implantation (technique not widely available) was used to introduce tin (Sn) ions into hematite. Significant changes were observed with the introduction of both elements, Ti and Sn; the improvement on the NWs photoperformance was achieved.

Chapter 5 – The formation of hematite nanotubes (NTs) by two distinct methods is here presented: hydrothermal and anodization. By hydrothermal, surprisingly different nanostructures nucleated on the fluorine-doped tin oxide (FTO) substrates. By anodization, the relation of anodization curves with the morphological features and porosity of self-organized NTs is presented. From 20 V up to 60 V, an optimum porosity and self-organized regime is achieved, above this potential we enter in the regime of hard anodization occurs, affecting the NTs tops by dissolution.

Chapter 6 – Here, a different material was synthesized, tungsten trioxide WO_3, originating nanoplates by hydrothermal method. The effect of different hydrothermal conditions, especially the temperature, time, and layer-by-layer thickness increase were studied. Ideal conditions were obtained with hydrothermal 90 ºC and 12 h in terms of

photoresponse and then applied in the layer-by-layer hydrothermal growth approach. Photocurrents improvements over 70 % where achieved with the studied conditions.

Chapter 7 – In this chapter, titanium dioxide TiO_2 NTs were produced by electrochemical anodization. The effect of electrolyte re-utilization in the morphological features of the NTs was evaluated. A detailed study of the bias voltage effect on the anodic NTs for fresh and re-used electrolytes was performed. Also, the possibility of obtaining NT arrays with ribs morphology, with interest in solar energy harvesting application, just by re-using the electrolyte was unveiled.

Chapter 8 – This chapter includes the ongoing work, involving promising photoanodes based on Fe thin films, using techniques such as electron beam evaporation, ion beam deposition and pulsed laser deposition. In the later, a promising photocurrent performance of 0.34 $mA.cm^{-2}$ at 1.45 V_{RHE} was obtained.

Chapter 9 – In this last chapter, the main conclusions and future work are summarized.

Chapter 1

Introduction

Chapter 1

Introduction

1.1. Solar Energy Harvesting

One of the forefront challenges that mankind is facing today is the supply of sustainable and environmentally friendly energy sources that will meet the growing needs of an expanding population [1]. Despite all efforts to find alternative sustainable energy sources, we are still very dependent on fossil fuels to attend our daily energy demands. However, the drastic increase in the last decades of all the social, political, economic and environmental problems associated with the use of oil has led to a global concern that urgent changes are needed to overcome this situation. Fossil fuel´s depletion is also a stated reality, since its over-extraction takes place extremely fast to attend the increasing consumption necessities, while it takes millions of years to the natural reserve's replenishment. Predictions point out to its decline for the next decades/centuries: oil ~35-40 years, gas ~40-70 years, and coal can last up to 100-200 years [2,3], although the expected time strongly depends on the extraction technology.

The solar energy is the main opponent to this global consuming tendency, as an inexhaustible natural resource [4]. The sun supplies energy to planet Earth in the order of $3x10^{24}$ J/year, which is approximately 10·000 times more than the global population currently consumes [5,6], and far above from other renewable energies, such as wind, hydroelectric or biomass. However, it is estimated that only 1% of the total consumed energies worldwide come directly from the sun [7]. Among the main forms to obtain energy (fuel or electricity) from solar radiation (Figure 1.1), the photovoltaic (PV) solar cells still remain as the most used solution. A PV solar device is based on a semiconductor that, when illuminated with solar radiation, creates electric current that can be readily used (Figure 1.1, right). However, without an efficient storage solution, the electricity produced by PV is not dispatchable, relying on the intermittent and geographically dependent nature of the solar energy (efficient PV devices require a secondary device such as a battery or supercapacitor to store the produced electrical energy) [7,8]. Besides, the actual PV technology costs are still not competitive enough

to overthrow the fossil fuels empire. Nevertheless, PV costs have shown a considerable fall of 73% in the period of 2010-2017, from USD 0.32-0.10/kWh, while fossil fuels costs were estimated in USD 0.05-0.17/kWh [9]. As a better alternative to the actual PV cells, stands out the hydrogen production using photoelectrochemical (PEC) cells for water splitting. Similar to photosynthesis (Figure 1.1, left), the solar energy is harvested and stored in the form of chemical bonds to provide fuel [10]. Essentially, PEC cells differ from the typical PV solid state junction devices by replacing the phase in contact with the semiconductor by an electrolyte (liquid, gel or organic solid; Figure 1.1, at the center), allowing the direct conversion of photon energy into chemical energy in the form of hydrogen molecule, using water as raw material [10].

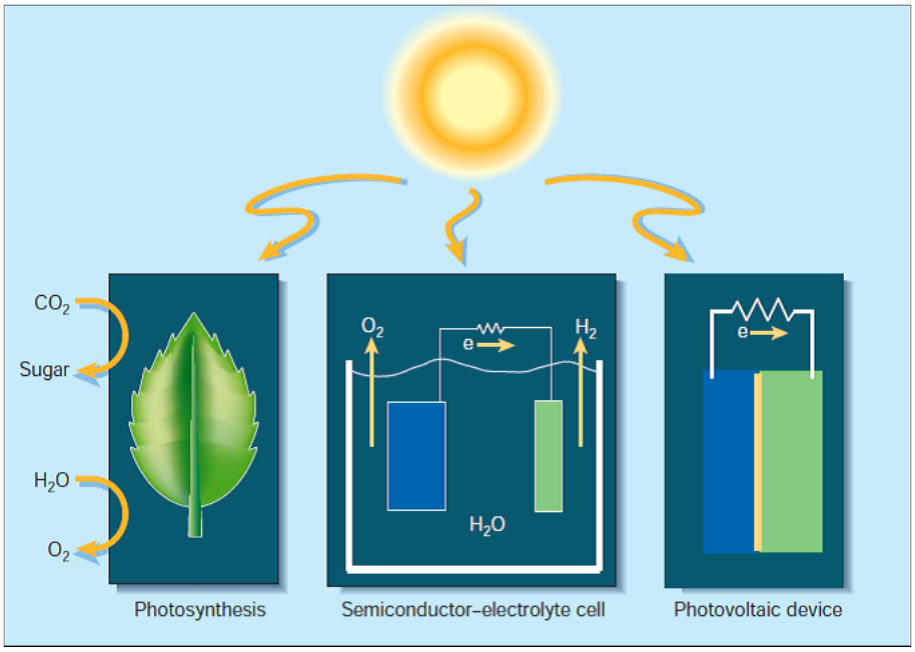

Figure 1.1. Three routes for conversion of sunlight into fuel or electricity: photosynthesis (left), photoelectrochemical cells (center) and photovoltaics (right). The semiconductor material is represented in blue color and the metallic electrode in green color. (Reprinted with permission of [10]. Copyright © 2001).

1.2. Hydrogen fuel production and applications

Hydrogen is for many considered the fuel for the future. As automobile industry lacks from a quick/effective response to the actual problem of the poor autonomy of electric vehicles, hydrogen as a sustainable alternative solution is gaining rising strength.

Hydrogen is considered a clean, carbon free (water is the only waste product upon utilization), efficiently converted in electricity, renewable, low-cost, storable,

transportable and readily dispatchable fuel that can be used in combustion engines in vehicles, propulsion of spacecraft, and has the potential to be commercialized for passenger electric vehicles and aircraft [6].

In the case of fuel cells based on proton exchange membrane (PEM), the hydrogen (acts as a chemical energy source) is used with oxygen (oxidizing agent) to generate electricity through several redox reactions, releasing water as waste product [as schematized in Figure 1.2(a)]. It comprises a membrane electrode assembly (MEA) in which hydrogen gas (H_2) is oxidized on the anode catalyst, while oxygen gas (O_2) is reduced on the cathode, all compressed by bi-polar plates that introduce gaseous reactants and coolants to the MEA and harvest the electric current. The MEA electrodes are attached to a solid polymer PEM that conducts the protons. Produced gases and water are diffused through porous layers between the flow fields and catalyst surfaces, while exchanging electrons between them [11].

Differently from the electric-vehicle rechargeable lithium-ion batteries, fuel cells can provide electricity in a continuous way, as long as hydrogen fuel and oxygen are available. The electrical energy that is generated is used to move the vehicle, and a travel autonomy is now estimated in ~450 Km [that is the example of the new vehicle from Toyota, the model Mirai, Figure 1.2(b), already available on the market [12]]. It seems very competitive comparing with an autonomy between 220-500 Km presented in general for electrical cars using Li^+ batteries (considering more economical automotive brands to top-range cars like Tesla [13]), which gives an autonomy ratio between fuel cells/Li^+ batteries of ~1.25.

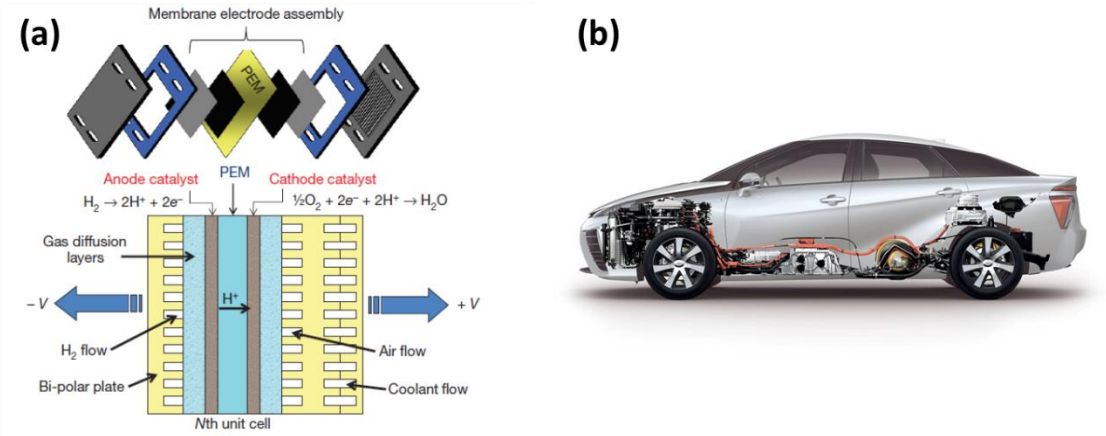

Figure 1.2. (a) Scheme of a fuel cell, where hydrogen and oxygen are used to generate electric current to supply the automobile engine (Reprinted with permission of [11]. Copyright © 2012). (b) The new fuel cell vehicle from Toyota, the Mirai model [12].

Currently, hydrogen is mostly produced from fossil fuels such as natural gas or coal (about 96%), which contributes to the global warming through CO_2 release [4,6]. However, there has been an increasing investment interest in solar harvesting solutions. Looking in a closer perspective, Portugal is one of the European countries with higher solar irradiation (Figure 1.3). In fact, very recently (final 2019) the Portuguese government publicly announced the future construction of an industrial unit to produce hydrogen, powered by PV energy source. It is a consortium between Portugal and the Netherlands, with funds from private capital and European Community financing, to be built in the industrial complex in Sines (Portugal), with a prediction to provide around 160.000 tons of hydrogen fuel per year in a sustainable way [14].

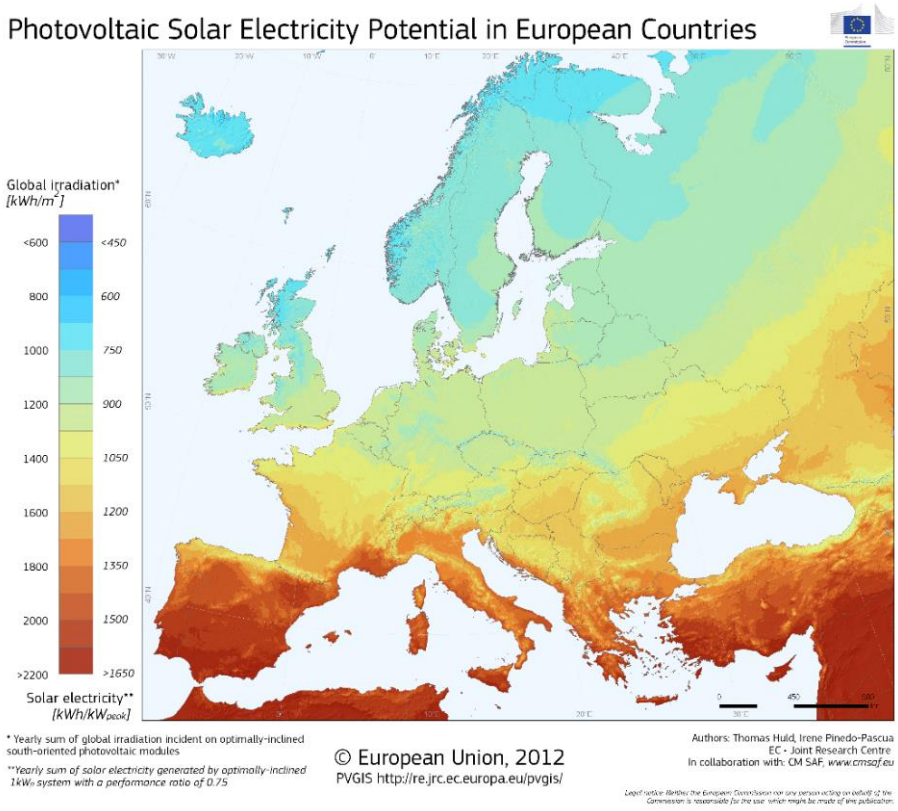

Figure 1.3. Map of solar irradiation in European countries (extracted from [15]).

1.3. Photoelectrochemical (PEC) cells for water splitting: basic working principles

There are several techniques that can be used for water splitting, such as water electrolysis, biophotolysis, thermochemical, and photoelectrochemical (PEC) water

splitting, being the later considered one of the most promising and efficient ways to produce hydrogen from water [6,16].

The photoelectrochemical process consists essentially in the decomposition of water into hydrogen (H_2) and oxygen (O_2) by passing electric current (generated by light harvesting), in the presence of an electrolyte solution. The electric current is generated by a photoactive semiconductor material, that can be either an n-type or p-type semiconductor.

A single-photon PEC cell for water-splitting (scheme in Figure 1.4) comprises two electrodes: the working electrode (in this example is an n-type semiconductor, also called photoanode) and the counter electrode (usually a metal resistant to corrosion, e.g. Pt), both immersed in the electrolyte solution (acidic or basic, containing the appropriate redox couples) [5,16].

When the semiconductor photoanode absorbs photons with sufficient energy to inject electrons from the valence band (VB) to the conduction band (CB), electron-hole (e^--h^+) pairs are generated:

$$2h\upsilon + \text{semiconductor} \rightarrow 2e^- + 2h^+ \quad (1.1)$$

where $h\upsilon$ is the photon energy (h = Planck constant; υ = frequency). The e^--h^+ pairs have a spatial separation from each other due to the presence of the electric field inside the semiconductor [16]. The excited electrons percolate through the semiconductor layer and are transferred through the external circuit to the counter-electrode, reducing water to form hydrogen at its surface (in basic media):

$$\text{Cathode:} \quad 4H_2O + 4e^- \rightarrow 2H_2 + 4OH^- \qquad E^\circ_{H_2O/H_2} = -0.828\ \text{V} \quad (1.2)$$

while holes oxidize water to form oxygen gas at the semiconductor surface:

$$\text{Anode:} \quad 4OH^- + 4h^+ \rightarrow 2H_2O + O_2 \qquad E^\circ_{O_2/OH^-} = 0.401\ \text{V} \quad (1.3)$$

The overall reaction for the photoelectrochemical water splitting is:

$$H_2O + h\upsilon \rightarrow H_2 + \tfrac{1}{2}\, O_2 \quad (1.4)$$

with ΔG = 237 kJ/mol [5,6,16,17].

Equations (1.2) and (1.3) are written regarding a basic media. For an acidic one, the equations are obtained by subtracting or adding the dissociation reaction of water into protons and hydroxyl ions:

Cathode: $2H^+ + 2e^- \rightarrow H_2$ $E^{\circ}_{H^+/H_2} = 0.0$ V (1.5)

Anode: $H_2O + 2h^+ \rightarrow 2H^+ + ½\ O_2$ $E^{\circ}_{H_2O/H_2} = 1.23$ V (1.6)

Under standard conditions, the water electrolysis is not spontaneous, and a minimum potential of 1.23 V at 25 ºC is needed, according with the relation $\Delta G^o = -nF \cdot \Delta E^o$, where ΔG^o is the standard Gibbs free energy change (ΔG=237 kJ/mol) i.e., the necessary energy supplied from an external power source to electrolyze water, F is the Faraday constant and ΔE^o is the standard electric potential of the reaction [16,17].

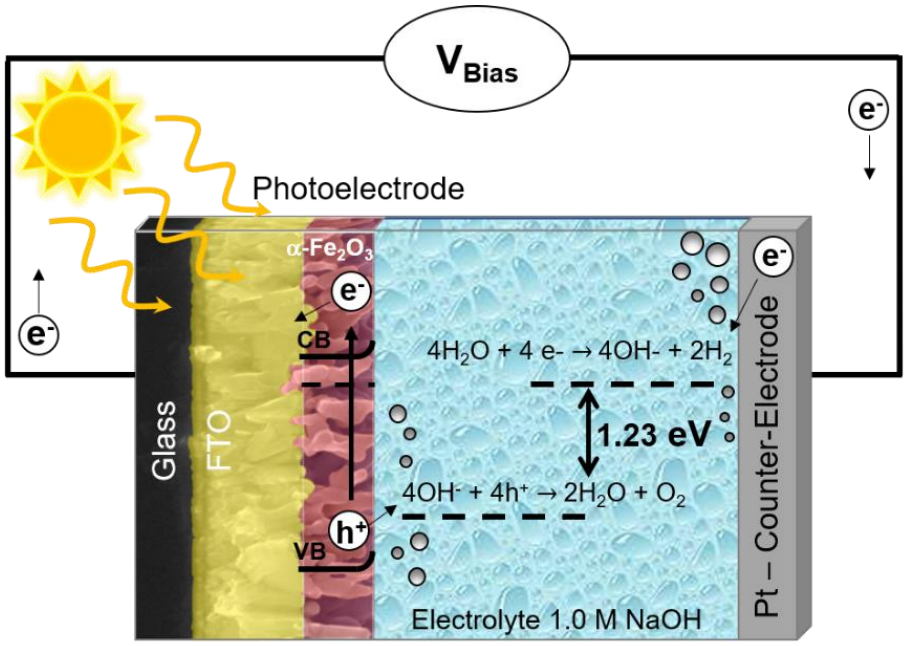

Figure 1.4. Schematic illustration of a photoelectrochemical cell, with a n-type semiconductor (hematite). The main water splitting reactions are represented.

The PEC cell configuration, in which a semiconductor can generate electron-hole pairs, has the advantage that oxygen and hydrogen can be produced in distinct places within the cell and, therefore, easily separated; under solar irradiation, the photoexcited electrons reduce water producing H_2 at the metal electrode, whereas the holes oxidize water at the semiconductor surface to form O_2 [10].

1.4. Semiconductor materials for PEC cells

In 1972, Fujishima and Honda reported for the first time the process of photo-assisted water splitting into H_2 and O_2 using TiO_2 semiconductor material as photoanode, providing the possibility for the conversion of solar energy into chemical energy in a cheap and renewable way [18]. Later, in 2001, Gratzël described a tandem device based on nanocrystalline WO_3 biased by dye-sensitized nanocrystalline TiO_2 for water splitting. For this device, an overall solar light to chemical conversion efficiency of 4.5 % was reported [5,19]. Since then, several approaches have been investigated for increasing the PEC cells efficiency. Besides TiO_2 and WO_3 photoanodes, α-Fe_2O_3 [20,21], Cu_2O [22-25], SnO_2 [6,16,17], $SrTiO_3$ [6] or $BiVO_4$ [26] have been thoroughly investigated, however the efficiencies, so far, demonstrated to be very low [8,21]. Besides, a minimum solar-to-hydrogen conversion efficiency of 10 % is required for PECs to be commercially viable [7,27,28]. On the other hand, materials such as GaAs and $GaInP_2$ had shown to be more promising concerning solar-to-hydrogen efficiencies (12.4 %), but presented poor stability on water (lifetime of only a few hours) and are expensive materials [16,29].

The key component in PEC devices is the semiconductor material, that must fulfill the following requirements:

- Strong absorption of visible light,
- High chemical stability (in dark and under illumination),
- Efficient charge separation and transport,
- Low kinetic overpotentials for reduction/oxidation reactions,
- Suitable band edge potentials for the reduction/oxidation of water,
- Be a low-cost and harmless material [16,17,21].

Finding a single material that encompasses all these requirements is a very difficult task. The choice of the materials depends considerably on the band gap (E_g, energy at which the materials absorb light), which width is a measure of the chemical bond strength [5,10]. Figure 1.5 presents several semiconductor material and the respective band gaps [5]. As already seen in Eq. 1.4, for water splitting a semiconductor must have at least a band gap of 1.23 eV (the minimum thermodynamic potential to dissociate H_2O molecule into H_2 and O_2) [21]. However, due to occurrence of thermodynamic energy losses including electron-hole recombination, resistivity of electrodes connections, and over-potentials at the electrode-electrolyte interface, the voltage needed to split water ascends to ~2 eV [30,31]. Although several semiconductors have the band edge positions to cover both water oxidation and reduction, the band gap turns out to be too large, limiting the

sunlight harvesting [10]. Thus, in most cases, the application of extra bias is still necessary [17,30].

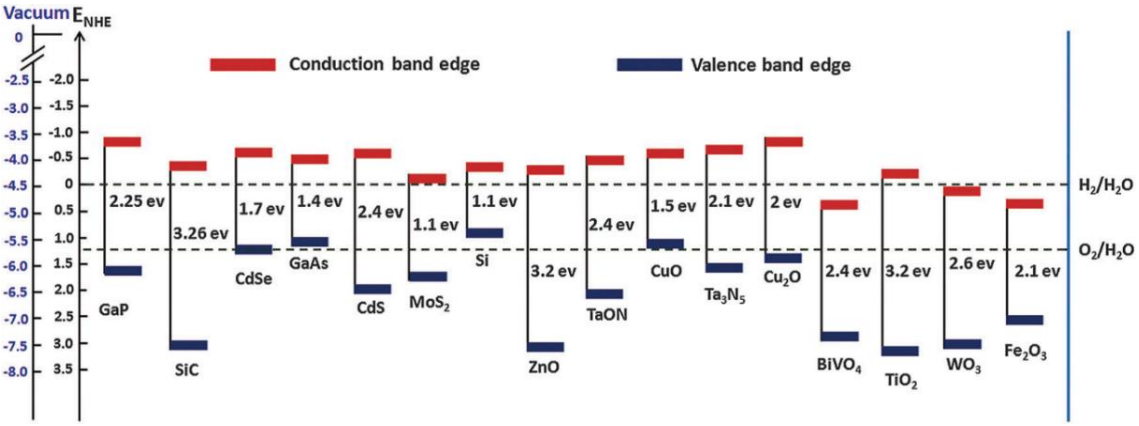

Figure 1.5. Band edge positions of several semiconductors in contact with aqueous electrolyte at pH = 0. Superior and inferior dashed lines indicate respectively the water reduction and oxidation. (Reproduced from Ref. [8], with permission from The Royal Society of Chemistry).

1.4.1. Sustainable materials by bottom-up approaches

As already referred, the perfect semiconductor for PEC applications is hard to find, one that absorbs sufficient sunlight, with an efficient charge transport, that covers both oxidation/reduction of water, or that is conductive enough without loss of stability. Usually, materials that are stable in water do not absorb enough sunlight, on the other hand, materials with higher sunlight absorption cannot withstand water-splitting in an auto-effective way [10]. The energy conversion efficiency is usually considered one of the most important requirements concerning the PEC cell performance. However, in practical terms, it is useless to have a good photoconversion efficiency if afterward a PEC device only stands for a few hours under the harsh chemical environment of outdoor conditions of utilization. Another underestimated parameter is the scalability of photoanodes (or photocathodes) for usage on an industrial scale; usually studied at a low scale (few cm) [32,33]. When upscaling of PEC devices, the presence of inhomogeneities or defects in a large area may diminish the efficiencies obtained initially using small areas, and few studies have taken into account this essential factor [34,35]. And most of all, it is crucial to use nontoxic, i.e., environmentally friendly, and low-cost materials, since the main principle of PEC hydrogen production is precisely to reduce the pollution associated with the CO_2 releasing energies. Therefore, there are five key indicators for the semiconductor material - efficiency, scalability, stability, low-cost,

nontoxicity - whose combination can lead to the development of competitive and sustainable PEC cell devices (Figure 1.6) [36].

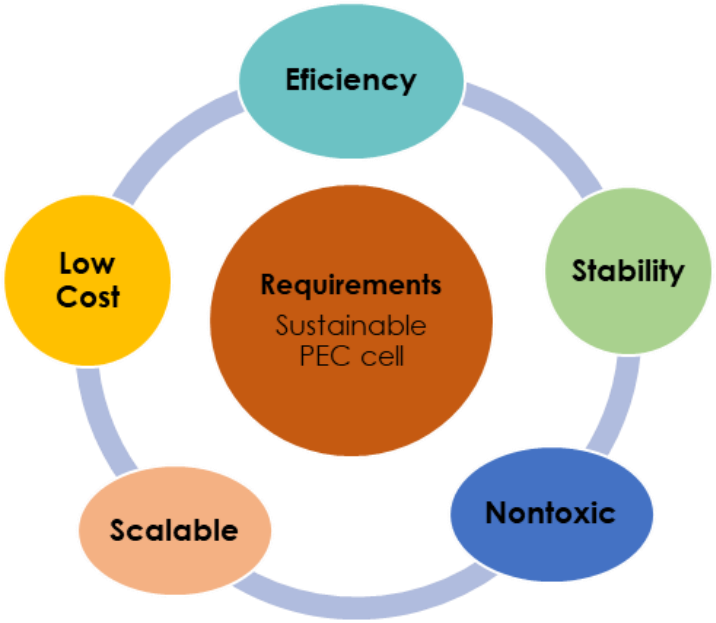

Figure 1.6. Main pillars of PEC cells sustainability.

From the various materials available, there are few that gather most of the mentioned requirements and, therefore, should be considered for PEC´s applications. Hematite (Fe_2O_3), titanium dioxide (TiO_2) and tungsten trioxide (WO_3) stand out for their important and advantageous properties, and have been considered for many as semiconductor materials with high potentiality for application in PEC cells, being widely studied [5,21,37-40].

This work targets the development of nanostructured photoanodes based on these three semiconductor materials: α-Fe_2O_3, WO_3 and TiO_2. However, particular attention is given to hematite, due to its outstanding properties, and to have one of the highest theoretical photoconversion efficiency of 12.9 % [41]. The fabrication method employed to produce the nanostructures also determines the sustainability of the PEC devices, and in this context, the use of self-assembly bottom-up methods, that do not require expensive resources, is also seen as a practical asset. The scheme of Figure 1.7 resumes the strategies that were chosen in the development of this thesis, using bottom-up methodologies such as hydrothermal and electrochemical anodization, to develop several nanostructures (nanowires, nanotubes or nanoplates) of α-Fe_2O_3, WO_3 and TiO_2.

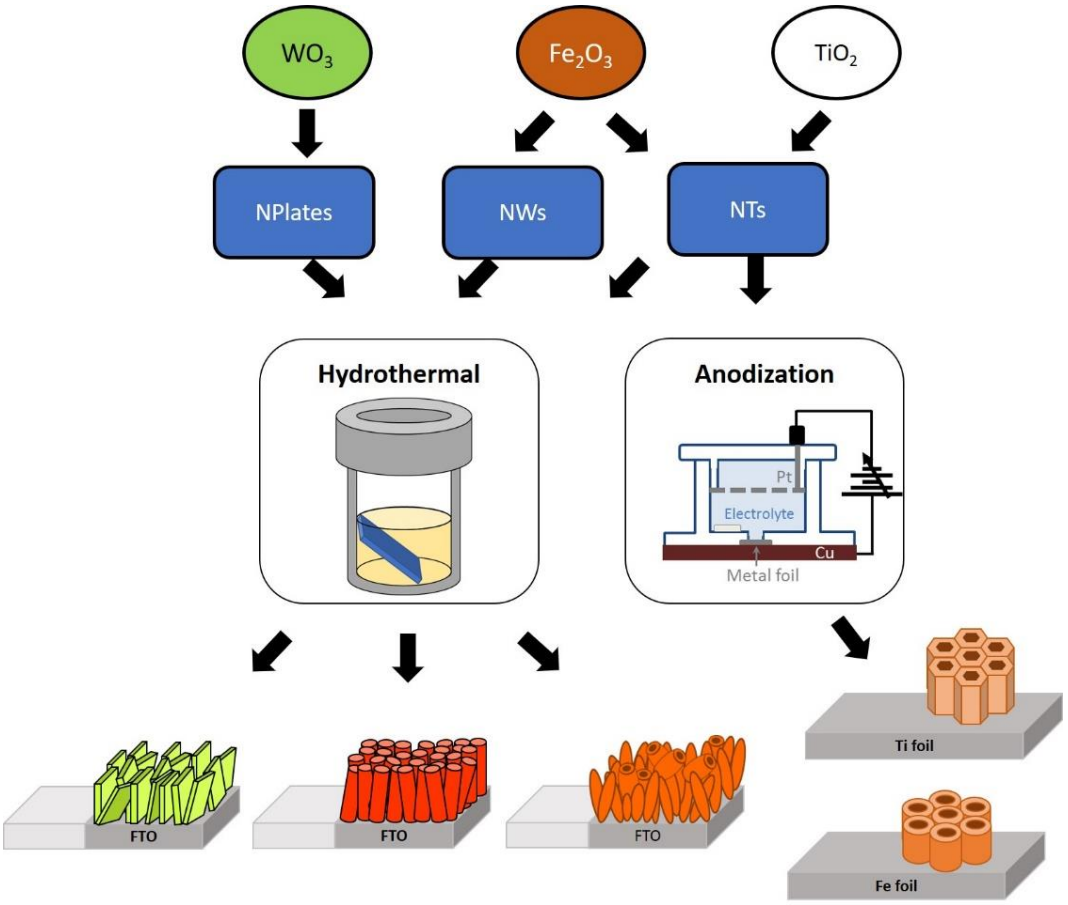

Figure 1.7. Schematic illustration of WO_3, α-Fe_2O_3 and TiO_2 nanostructured photoanodes fabricated by hydrothermal and anodization methods.

1.4.1.1. Hematite

Iron, one of the most available metals on earth, oxidizes easily into ferrous (2+) and ferric (3+) states in air atmosphere. Among the several iron oxide forms, hematite (α-Fe_2O_3) is a material that has been extensively studied due to its semiconductor properties and chemical stability. The name hematite (from Greek haima = blood) comes from its characteristic red-brown color. These chromatic properties are also indicative of its ability to absorb solar irradiation [39,42].

The use of hematite (α-Fe_2O_3) photoanodes for PEC water splitting have been gathering considerable attention due to their abundance, low cost, nontoxicity, excellent long-term stability against photocorrosion and a suitable band gap (1.9-2.2 eV) [8,16,21,39,41,43,44]. However, the performance of hematite is mainly limited by its low absorption coefficient, poor conductivity ($\sim 10^{-14}$ $\Omega^{-1}\cdot cm^{-1}$) and low carriers mobility ($\sim 10^{-2}$ $cm^2\cdot V^{-1}\cdot s^{-1}$) [45,46]. In particular, the short hole diffusion length of hematite (2-4 nm), comparing with the light penetration depth of around 120 nm (at 550 nm) [47,48], favours

the high electron-hole recombination rates and significant efficiency losses [8,39,49]. Then, hematite is usually referred by its ultrafast recombination of generated charge carriers which has been assigned to the high density of trapping states caused by internal and superficial defects [33,50]. Also, its conduction band edge energy position does not accomplish water reduction and the application of an external bias is required [16,51].

Therefore, the solar spectrum photoconversion efficiencies reported to date for hematite are still far from the theoretical value of 12.9% for this material [16,41]. However, α-Fe_2O_3 is one of the materials with highest potential for photoconversion of solar energy into hydrogen, being appointed as an excellent material for application in solar energy harvesting and with the potential to reach the maximum efficiency predicted of 16.8% for an ideal material with a band gap of 2.03 eV [8,21,39,41].

To overcome hematite limitations, several strategies have been developed to lead hematite photoanodes towards high photoconversion efficiencies and improve its optical and electronic properties, to name a few: nanostructuring, doping, use of plasmonic nanoparticles, catalysts, or carbon materials.

Nanostructuring is one of the most important methods for improving the photon harvesting for water splitting. Nanostructured materials provide a large interfacial area in contact with the electrolyte, favorable for the charge carriers transfer kinetics, i.e. charge separation and transportation [8,16,39]. This aspect will be further explored in this Chapter.

Due to low charge carrier mobilities and poor conductivity intrinsic of hematite, the use of dopants is crucial for practical applications such as PEC devices [16,39]. Doping has proved to be critical for narrowing the band gap to achieve visible absorption. It can be performed by introducing impurities into the semiconductor crystal lattice, while changing its band gap or create new energy levels for visible light absorption [52]. Dopants, such as Si [53-55], Sn [56], Ti [57-59], Pt [60], Ge [58], Mn [58,61], Ni [62], Zn [60] or Zr [60], have been used in hematite photoelectrodes. Si^{4+}, Ti^{4+} or Sn^{4+} are examples of electron donor-type dopants in hematite (where Fe^{3+} sites are substituted by dopant ions and reduced to Fe^{2+}) [49,56]. The extra valence electron conferred by the donor atom is slightly bound to the nucleus and can be excited to the conduction band, where it then contributes to the conductivity [16]. In particular, Sn was even mentioned by its advantages over other dopants, since it presents a similar ionic radius to the one of Fe, and also a similar Pauling electronegativity [63].

Annealing is an important step in the conversion of crystalline phase of the semiconductor materials. At the right temperature, it will not only improve the crystallinity, but also will reduce the gap of the grain boundaries, promoting the connectivity between grains, further leading to the charge recombination sites elimination [33,52,64-67].

The use of plasmonic metal nanoparticles (Au or Ag) can highly improve PEC performance, since the ability to trap and scatter photons should improve photon absorption and utilization in PEC devices. Besides, it can change the distribution of electromagnetic energy. Certain metallic nanoparticles display a collective oscillation of conduction electrons at frequencies corresponding to solar radiation [68]. Plasmonic metal nanoparticles can change the location where the charge carriers are generated, by acting as an antenna that localizes the optical energy and transfers it to the semiconductor within approximately 10 nm of the metal [68,69]. This near-field absorption enhancement used to confine light absorption to the proximity of metal nanoparticles (to a reduced volume of semiconductor) can lead to optimized PEC designs, eventually decreasing material costs [16]. In addition, the presence of Au plasmonic particles prolonged the charge carrier lifetime in hematite, due to an intense local plasmonic field at the metal/hematite interface [70].

The addition of an active surface electrocatalyst on hematite photoanodes has also been proposed to improve PEC device performance. Co-catalysts can be divided in water oxidation catalyst and water reduction catalyst, which acts as activation sites for the evolution of O_2 (photoanode) or H_2 (photocathode), respectively. Inorganic catalysts such as IrO_2 Co-Pi, IrO_2, RuO_2 or Pt compounds are generally used as oxidation catalysts. Since for a metal oxide photoanode the overpotential for water oxidation can easily exceed 0.6 V, co-catalysts are often used for the reduction of the electrochemical activation overpotential, enhancing the reaction kinetics, and also may contribute for the chemical and photochemical stability. Good catalysts were also referred to enhance the plateau photocurrent [16,71,72].

There is also an increasing interest in the combination of carbon-based materials, such as the carbon nanotubes or graphene, responsible for diminishing the recombination processes in materials such as TiO_2 or hematite [73].

1.4.1.1.1. Hematite physical properties

Crystalline structure. Hematite (α-Fe_2O_3) is a highly thermodynamically stable material and the most abundant form of crystalline iron oxide. It crystallizes in rhombohedral structure, with the same crystal structure than corundum (α-Al_2O_3); with trigonal-hexagonal scalenohedral symmetry in the space group R-3c, lattice parameters a = 5.0356 Å, c = 13.7489 Å, and six formula units per unit cell, where the oxygen atoms are arranged in hexagonal closed packed-array along the [001] direction [8,39,42]. The Fe^{3+} ions occupy two-thirds of the sites, arranged regularly with two filled sites being

followed by one vacant site in the (001) plane (forming six fold rings) [42]. The arrangement of cations produces pairs of FeO_6 octahedra that share edges with three neighboring octahedra in the same plane and one in an adjacent plane in the [001] direction (Figure 1.8). This octahedral face sharing, occurring at the c-axis, causes repulsion between Fe atoms along the direction normal to the [001], causing the cations to shift closer to the unshared faces. The O-O distances along the shared face of an octahedron are shorter than the distance along the unshared edge, causing a trigonal distortion from ideal packing. The O and Fe arrangement around a shared face influences the magnetic properties of the oxide [8,39,42]. The crystal orientation of the nanostructures is also a determinant factor in the photocurrent; structures with more than one orientation were referred to yield less photocurrents, while a preferential orientation in [110] direction was related with strong anisotropic conductivity [49,51,65,74,75].

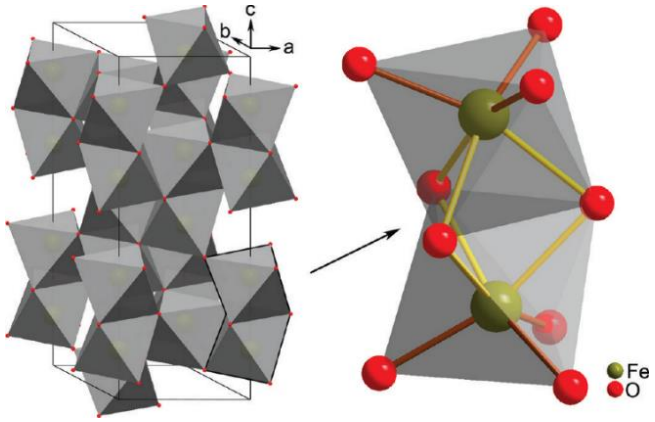

Figure 1.8. Schematic illustration of the unit cell of hematite with octahedral face-sharing (left). The magnification (right) represents one face-sharing dimer (Fe_2O_9), with longer (yellow) and shorter (brown) Fe-O bonds resulting from the repulsion between the Fe^{3+} cations (Reprinted with permission from [65]. Copyright © 2010 American Chemical Society).

Magnetic properties. The magnetic properties of hematite depend essentially on the temperature, crystallinity and particle size [42]. Bulk hematite is weakly ferromagnetic at room temperature, while above 956 K (Curie temperature, T_C) it is paramagnetic. At temperatures below 260 K (the Morin temperature, T_M), it undergoes a phase transition to an antiferromagnetic state. Below the T_M, the two magnetic sub-lattices are oriented along the c-axis and are exactly antiparallel [Figure 1.9(a)]. Above the Morin transition (e.g. room temperature, RT), it exhibits weak ferromagnetism [Figure 1.9(b)], due to a small misalignment of the spins within the rhombohedral (111) basal plane, created by a slight spin canting of the two magnetic sublattices [39,42]. The Morin transition, from a weakly ferromagnetic to an antiferromagnetic phase, is sharp due to the large change in spontaneous magnetization across the transition [76,77].

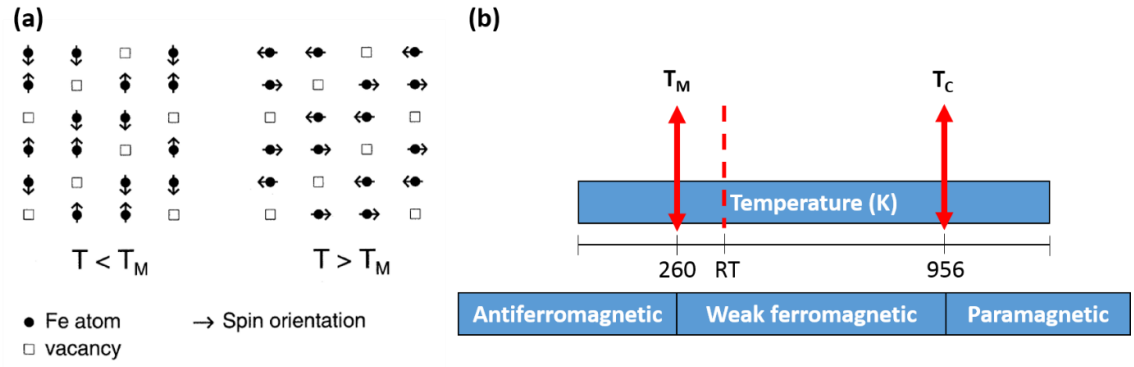

Figure 1.9. (a) Spin order in hematite below and above the Morin temperature (T_M) (Reprinted with permission of [42]. Copyright © 2003 Wiley-VCH Verlag GmbH & Co. KGaA); (b) Magnetic temperature transitions in bulk hematite.

Optoelectronic properties. Hematite begins to absorb photons in the near-infrared spectral region, extending into ultraviolet (UV) region. This is due to *d-d* (forbidden) transition states between energy levels for the electron configuration d^5 of Fe^{3+} ion, that are split by an intrinsic crystal field and weakens the absorption [8,39,78]. With radiation below the band gap, sustained photocurrent is not observed, but at the band gap energy (E_g = 1.9-2.2 eV, corresponding to λ = 650 to 560 nm), the absorption coefficient of pure hematite highly increases. The strong absorption of yellow to ultraviolet radiation in the visible spectrum and transmission of orange to infrared photons gives hematite its characteristic red-brown color [39].

Hematite is considered an n-type semiconductor, where the electron excitation is achieved by irradiation with visible light of the appropriate wavelength [42]. At room temperature, hematite has a very low carrier mobility (10^{-2} $cm^2 \cdot V^{-1} \cdot s^{-1}$) [46], and a small conductivity of 10^{-14} $\Omega^{-1} \cdot cm^{-1}$ [45], attributed to the Fe^{3+}/Fe^{2+} valence alternation on spatially localized 3*d* orbitals [39,42]. This is the main cause of the low photoresponses usually reported for bare hematite [~0.1 $mA \cdot cm^{-2}$, at 1.23 V *vs*. RHE (reversible hydrogen electrode)] [33,79,80]. Additionally, the diffusion length of holes (2-4 nm) is significantly lower than many other (III-V) oxides [19,47]. The flat band potential was reported to be -0.5 V *vs.* SCE (standard calomel electrode) in 1M KOH (a pH dependent value), a low value to reduce water, thus an external bias is required to complete the water-splitting reaction [16,81]. The semiconductor properties are strongly dependent on the morphology of the hematite structures, and factors like doping or surface treatments can promote the electrons mobility and highly improve the conductivity [42].

Photocurrent density-voltage curves. To evaluate the efficiency of a photoelectrode in a PEC cell, the photocurrent density-voltage (*j-V*) curves are usually

monitored, in the dark and under simulated sunlight. The two most important factors to observe in the photocurrent curve are the plateau current (defined as the highest value of photocurrent after subtraction of the dark current) and the onset potential (determined by analysis of the curve derivative) [32,82]. Figure 1.10 shows the *j-V* curve for an ideal hematite photoanode, where the plateau current reaches the theoretical maximum of 12.6 mA·cm^{-2} and a 0.4 V onset potential necessary to start the water splitting reaction [39]. This efficiency is very hard to achieve, due to the several limitations in hematite structures (pure phase, grain boundaries, reflection and recombination losses). With low mobility and shorter diffusion length, holes will accumulate on the surface of Fe_2O_3 electrode, leading to more positive flat band potentials [83,84].

To enhance the photocurrent to the maximum photoconversion efficiency of 12.9% predicted for hematite (and towards the theoretical 16.8% for an ideal material with band gap of 2.03 eV) [41], the improvement of the hematite nanostructures and catalysis must be accomplished, towards the direction of the arrows represented in Figure 1.10 [82,85].

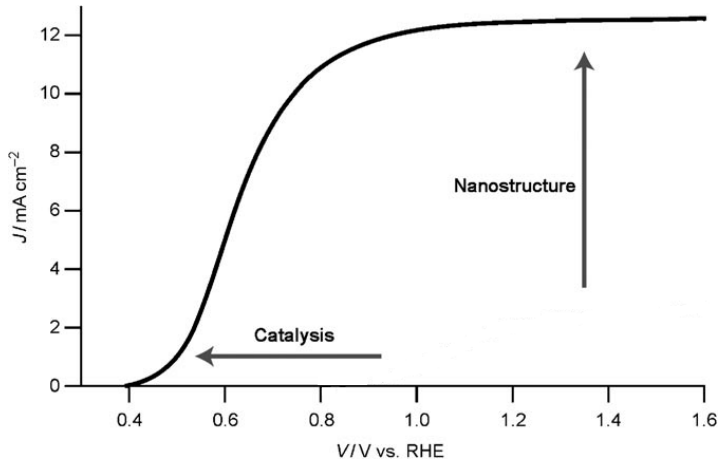

Figure 1.10. *j-V* curve of an ideal hematite photoanode [under AM 1.5G 100 mW.cm^{-2} simulated sunlight (Adapted from [82]. Copyright © 2010 WILEY-VCH Verlag GmbH & Co. KGaA, Weinheim).

An important factor usually considered to evaluate the limiting factors of the photoelectrode performance is the incident photon-to-current conversion efficiency (IPCE) [86]. IPCE is the efficiency of conversion of incident photons on the PEC cell into electrons that can be measured by the outer circuit between the working and counter electrodes, as a function of wavelength of the incident radiation, and is given by:

$$IPCE(\lambda) = \frac{hc}{e}\left(\frac{J_{photo}(\lambda)}{\lambda P_{light}(\lambda)}\right) \quad (1.7)$$

where h is the Planck's constant, c the speed of light, J_{photo} the photocurrent density measured under monochromatic illumination at a particular wavelength λ (in nm) and P_{light} the power of light [16,41].

IPCE can be calculated for any radiation spectrum. An IPCE of 100% corresponds to the generation of one photoelectron for each incident photon. However, the obtained IPCE percentages are usually much lower, due to losses associated with the reflection of incident photons, incomplete absorption by the semiconductor, and recombination of charge carriers within the semiconductor [16,41].

1.4.1.1.2. Hematite nanostructures

The major limiting factors in hematite are the poor charge carrier mobility and short hole diffusion lengths that lead to e^--h^+ recombination, as discussed in the previous sections. Hematite nanostructures have been widely investigated to improve these limitations, since they confer a large interfacial area between the photoelectrode and the electrolyte, which increases the electron transport, the charge separation efficiency and the solar irradiation absorption, enhancing the PEC activity [8,16,39].

New generation of photoanodes (Figure 1.11) arose by using bottom-up or top-down approaches, and nanostructures such as nanoparticles (NPs), nanorods, nanowires (NWs), nanotubes (NTs), cauliflowers or nanocones, among several others, have been developed using different synthesis techniques, such as chemical vapor deposition, spray pyrolysis, hydrothermal, electrochemical anodization, electrodeposition or nanoimprint [8,33,39,43,87-96].

In the case of planar films, comparative studies between thick and thin films showed that thicker films presented more limitations. In thick films the photogenerated carriers that are created far from the electrolyte-semiconductor interface are often lost due to recombination processes, enhanced by the defects due to stress interaction between the film and the substrate [8]. Thin films are better to extend the hole transport distance, but the surface area and photon absorption are not sufficient to increase significantly the photocurrent [8]. Nevertheless, thin films in the order of 19 nm yield photocurrents of *ca.* 0.94 $mA \cdot cm^{-2}$ at 1.45 V_{RHE}, while keeping a morphology quite similar to the fluorine-doped tin oxide (FTO) coated glass substrates surface [43].

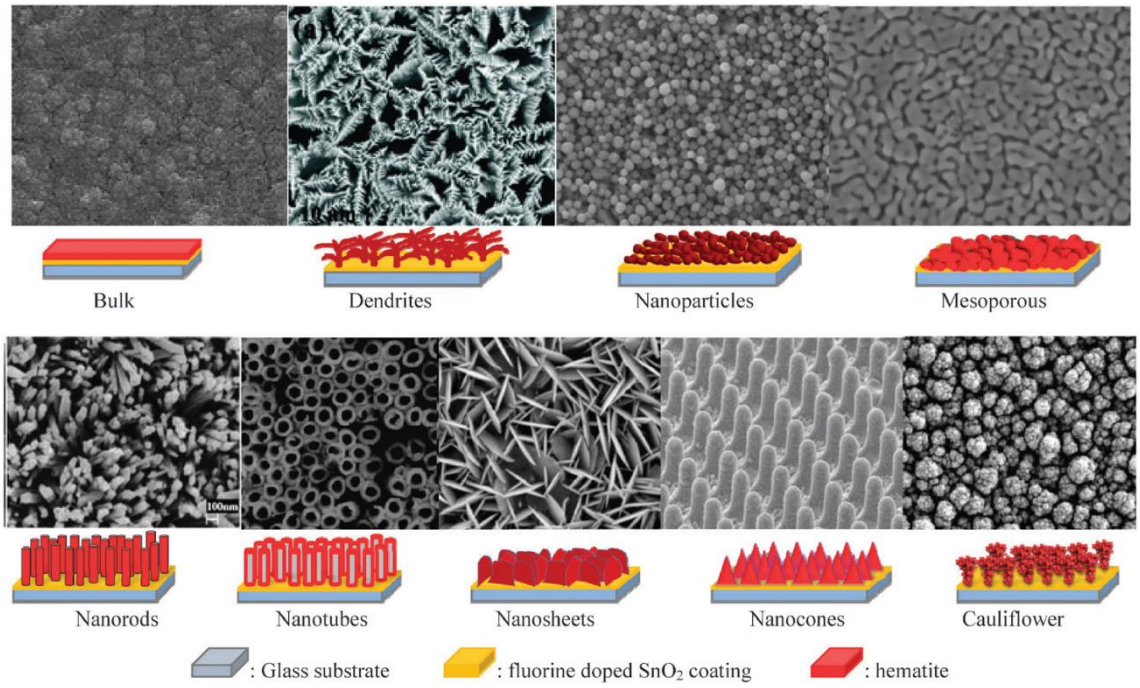

Figure 1.11. SEM images and respective schemes of different hematite nanostructures grown on the FTO coated glass substrate showing the different morphologies used for PEC water splitting (Reproduced from Ref. [8] with permission from The Royal Society of Chemistry).

Then, complex nanostructures like dendrites were reported to minimize the diffusion distance of the generated holes to reach the Fe_2O_3/electrolyte interface, while allowing an efficient light absorption [97]. On the other hand, the fact that these structures are denser is related to the higher recombination and poor charge transportation across grain boundaries between adjacent particles, justifying the low efficiencies ~ 43 $\mu A \cdot cm^{-2}$ at +0.6 V *vs.* Ag/AgCl [8,98].

Warren *et al.* reported NPs aggregates with a structure composed mainly by a single principal crystallographic orientation, yielding high photocurrents of 4.0 ± 0.1 $mA \cdot cm^{-2}$ (at 1.53 V_{RHE}) [99]. However, the presence of grain boundaries in these nanostructures may decrease the photocurrent values, because they act as recombination centers (have high concentration of interface states) and can generate a potential barrier that blocks the majority charge carrier transport between contiguous crystals [8,99]. Besides, the NPs provide indirect pathways for electron transport, susceptible of higher e^--h^+ recombination [89].

In hematite, there is a mismatch between the conduction band edge position and the hydrogen evolution potential (the conduction band of hematite is lower than the water reduction potential, as shown in Figure 1.5), so hematite cannot accomplish both water photo-oxidation and photoreduction. An external bias, generally a PV device or a photocathode in tandem, must be applied in order to completely split water [85,100]. The

use of surface treatments with appropriate electrocatalysts or doping proved to be efficient strategies to enhance the conductivity and charge separation efficiency of hematite (through changes in carrier concentration or mobility), shifting the conduction band position without application of external bias [50,101]. The modification of hematite surface with a catalyst promotes the interfacial charge transfer, reducing the recombination (Figure 1.10) [82]. Within this scope, Tilley *et al.* [82] reported in 2010 for the first time the use of IrO_2 catalyst in hematite in combination with a porous cauliflower-type morphology, providing an improved surface area. They achieved not only a water splitting photocurrent of over 3 $mA \cdot cm^{-2}$ (at applied potential of 1.23 V_{RHE} under AM 1.5G 100 $mW \cdot cm^{-2}$ simulated sunlight), but also a reduction of the overpotential onset to 0.8 V. The balance between nanostructuring and modification of hematite surface with a catalysts, that promotes the interfacial charge transfer, naturally leads to improved photocurrents (Figure 1.10) [82].

In semiconductor photoanodes the path travelled by holes to reach the surface, avoiding electron-hole recombination, is a crucial factor of photoresponse. Structures such as NPs, thin films, cauliflowers, dendrites or mesoporous hematite films often suffer recombination and poor electron percolation across grain boundaries [8,102]. In this regard, one-dimensional (1D) nanostructures such as nanowires (NWs) and nanotubes (NTs), with high-aspect-ratios and large surface areas, have been suggested as potential candidates for PEC cells, as they provide a more direct pathways for charge transportation up to the charge collector and reduce the recombination losses at grain boundaries, as shown in schemes of Figure 1.12 [8,33,39,52,64,89,102-106]. Figure 1.12(a) shows that NWs arrays with small diameters (5‑10 nm) provide efficient holes transport to the electrolyte, while benefiting from large surface areas (lengths of 400‑500 nm) to accomplish the light absorption. Figure 1.12(b) illustrates the movement dynamics of the charge carriers (e^--h^+ generated by the photon energy) inside the NTs structure. The electrons flow directly through the nanotube toward the back contact, while the holes move toward the surface to react with water. Due to the ultrathin walls of the NTs, the holes can reach the surface faster than in other nanostructures, representing a key factor for the NTs photoresponse [89].

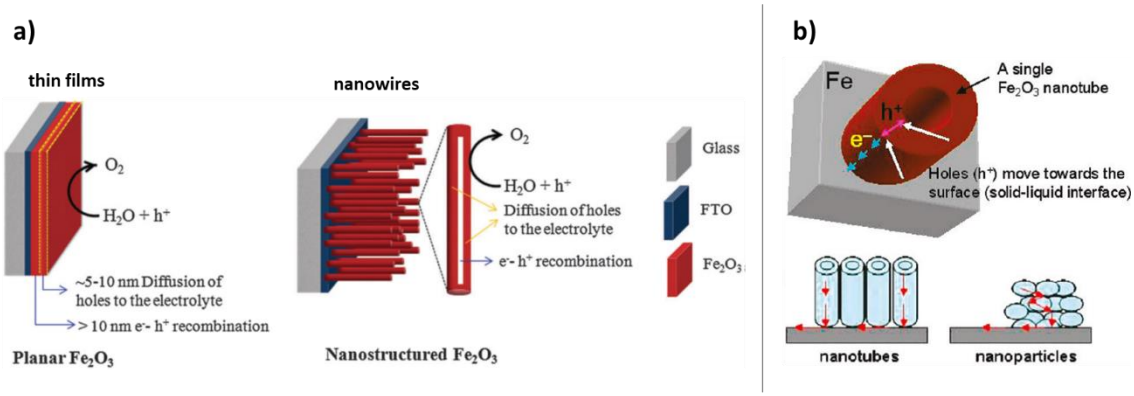

Figure 1.12. (a) Schematic diagram of planar-type photoanodes (thin films) compared with nanostructured hematite (nanowires) (Reproduced from Ref. [8] with permission from The Royal Society of Chemistry). (b) Scheme of electron and hole moves through Fe_2O_3 nanotube arrays used for H_2 generation; comparing with nanoparticles (NPs), nanotubes (NTs) provide direct pathways for electron transport that minimize the charge trapping and e^--h^+ recombination (Reprinted with permission from [89]. Copyright © 2009 American Chemical Society).

1.4.1.1.2.1. Hematite nanowires

Hydrothermal. Several methods can be used to produce hematite NWs, for example by template assisted method, where nanoporous anodic aluminum (PAA) templates are first obtained using a two-step anodization, where pore diameter and length can be tailored [107,108], and then arrays of NWs can grow inside the PAA pores, further allowing to vary their length. Other methods, for example by dip-coating of iron oxide NPs synthetized by sol-gel in the alumina pores [109], or by pulsed electrodeposition of Fe [110], have also been reported.

However, the hydrothermal growth of NWs has been described as the most effective method to increase hematite photocurrent [8,33,39,64,105,111]. The term hydrothermal, often associated with geological sciences, was first introduced by geologist Sir Roderick Murchison (1792–1871) about the process for the formation of earth rocks and minerals by action of water at high temperature and pressure. The growth of crystals (quartz crystals) using this methodology was first reported by the german geologist Karl von Schafhäutl, in 1845 [38,112].

Hematite NWs can be easily prepared by hydrothermal method based on the work described by Vayssieres *et al.* [91]; since then, several works have been developed regarding this topic [8,33,39,64,105,111]. These NW structures could grow in vertical orientation on FTO substrate from an aqueous chemical bath solution, due to the thermodynamically equilibrium that leads to a stable nucleation of the iron ions under the

right conditions of temperature and pressure [Figure 1.13(a)]. The use of low pH chemical solution with a high ionic strength promoted the formation of the metastable iron oxyhydroxide phase (*β*-FeOOH, also called akaganeite), by lowering the interfacial tension between the solution and the crystals being formed [91,112]. Each nanowire consisted of a sufficiently high-aspect-ratio nanostructure of about 4-5 nm diameter with 1D quantum confinement, with effects on the band gap blue-shift and reduction of the electron-hole recombination, which makes direct water reduction possible without the need of additional bias [91,105].

Additionally, the use of dopants can highly increase the donor density and improve the electrical conductivity of hematite NWs, playing an important role in PEC performance [33,57,113,114]. With this respect, a state-of-the-art photocurrent of ~6 $mA \cdot cm^{-2}$ was achieved using hydrothermal NW structures doped with titanium (Ti), shortening the 12.9% photoconversion efficiency goal for hematite [41,115]. Dopants also allow the deviation of onset potential toward lower values. A lower potential onset was reported by Ling *et al.*, using Sn-doped hematite NWs and nanocorals as photoanodes in PEC cells. These nanostructures were obtained by hydrothermal process using a FTO substrate, followed by high temperature sintering in air in order to diffuse the Sn into the nanostructure. A two-step annealing (550 °C for 2 h followed by 20 minutes at 800 °C) allowed an effective Sn incorporation leading to a pronounced photocurrent of 1.24 $mA \cdot cm^{-2}$ at 1.23 V *vs.* RHE and shifting the onset of photocurrent to lower potentials (0.6-0.7 V *vs.* RHE) [33]. A similar approach has led to a potential onset of 0.45 V; in this case, the application of a re-growth treatment inducing surface modifications allowed to reduce surface disorders, resulting in a turn-on potential approximated from the one of ideal hematite [Figure 1.13(b)] [116]. On the other hand, Kim *et al.* reported a hematite photoanode showing a worm-like feature, in which the combination of annealing temperature and doping/surface catalyst lead to a photocurrent performance of 4.32 $mA \cdot cm^{-2}$ (at 1.23 V_{RHE} under simulated 1-sun irradiation, 100 $mW \cdot cm^{-2}$), which corresponds to *ca.* 34% of the maximum theoretical limit expected for hematite (with a band gap of 2.1 V). A Pt-doping was used to improve the electrical conductivity of hematite while a co-catalyst (e.g. cobalt phosphate, Co-Pi) was used as a surface modifier to help the oxygen evolution reaction at reduced over-potential [Figure 1.13(c)]. Also here, a two-step annealing at 550 °C and 800 °C was used [111]. Annealing proved to be always a determinant parameter to obtain and improve the NWs photoanodes performance, that is going to be addressed in the following chapters.

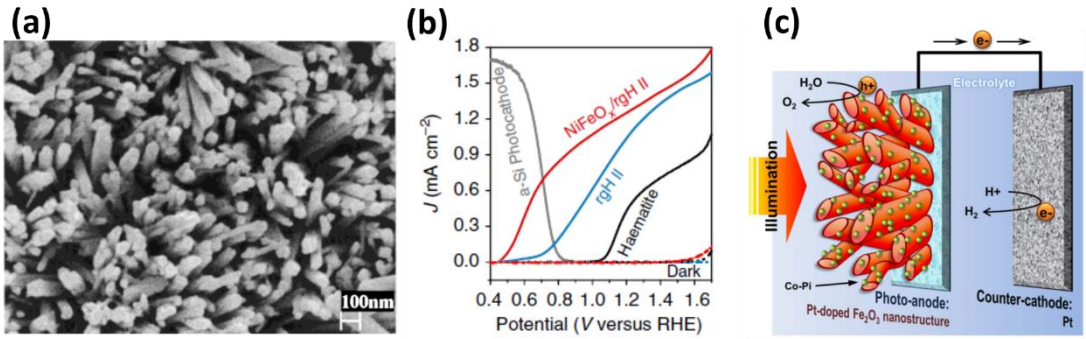

Figure 1.13. (a) SEM image of self-assembled hematite nanowires (NWs) grown on fluorine-doped tin oxide (FTO) glass substrate (Adapted with permission from [91]. Copyright © 2001 American Chemical Society). (b) Current density-potential of hematite photoelectrodes with surface modification by photochemical deposited NiFeOx, evidencing a low onset potential [Adapted with permission from [116]. Copyright © 2015, The Author(s)]. (c) Schematic diagram of a photoelectrochemical cell; the photoanode consists in a Pt-doped crystalline hematite thin film with worm-like nanostructure, modified with Co-Pi as an oxygen evolution co-catalyst on its surface [Adapted with permission from [111]. Copyright © 2013, The Author(s)].

1.4.1.1.2.2. Hematite nanotubes

Electrochemical anodization. Among 1D nanoarchitectures, NT arrays can provide higher surface areas than NWs or nanorods, due to the additional surface enclosed inside the hollow structure. NTs are of great interest not only for their high surface-to-volume ratios but also for their size dependent properties [1,52,117,118]. As in other cases, such as titanium and carbon, where the NT structures shown improved properties [117], also for hematite, this is the most promising configuration [8,65].

There are several approaches to fabricate NTs, namely by electrodeposition, sol-gel, electrospinning, atomic layer deposition (ALD) and anodization [89,109,119-124]. The use of ALD method to form Fe_2O_3 NTs, from dinuclear iron(III) *tert*-butoxide complex [$Fe_2(OtBu)_6$] was reported, originating smooth NTs with high aspect-ratios. Several types of NTs, e.g. $La_{2/3}Ca_{1/3}MnO_3$ nanotube arrays or silica NTs revested by magnetite (Fe_3O_4) nanoparticles, were produced using a alumina template assisted sol–gel method [109,121]. Also, vertically aligned 10 μm long iron oxide NTs were successfully obtained through electrodeposition of Fe inside PAA templates [119], with a photocurrent density ~2.2 mA·cm^{-2} (at 0.43 V *vs.* Ag/AgCl), however too many steps are needed to obtain these kind of structures [119]. Recently, a very promising double-walled iron oxide nanotubular structure was reported, obtained by pulsed electrodeposition of Fe inside PAA followed by thermal oxidation, however the photoconversion properties of these structures were not assessed yet [96]. Although the described methods resulted in highly

ordered NTs with high aspect-ratio, some disadvantages such as high cost or time consuming can be appointed.

A more easy and inexpensive way of producing self-organized Fe_2O_3 NTs with high orientation is by electrochemical anodization, in which precise shape of the nanostructures can be effectively controlled, depending on the experimental conditions used. The use of anodization technique gained greater interest in 1953, with the work of Keller *et al.* on the fabrication of alumina hexagonal close-packed arrays (HCPA) [125]. Since then, it has been deeply studied and applied in several other valve metals such as titanium [1,126-128], hafnium [129,130] or tungsten [131]. Basically, this process consists in the formation of self-organized porous/tubular anodic oxides on the top of the metal (the anode) by passing an electric current in the presence of an electrolyte solution. In the anodization process, there are three basic mechanisms responsible for the NTs formation:

(a) field-assisted oxidation of the metal (occurring at the bottom of the NTs),
(b) field-assisted dissolution of the formed oxide (also at the bottom of the NTs),
(c) chemical dissolution, occurring mainly at the NTs top.

In particular for iron anodization in fluoride-based electrolytes, the chemical equations that describe the oxidation and dissolution reactions are respectively [132]:

$$2Fe + 3H_2O \rightarrow Fe_2O_3 + 6H^+ + 6e^- \quad (1.8)$$

and

$$Fe_2O_3 + 12F^- + 6H^+ \rightarrow 2[FeF_6]^{3-} + 3H_2O \quad (1.9)$$

A typical iron anodization curve is plotted in Figure 1.14, showing the four main stages of the NTs formation. First the current density (j_{anod}) sharply decreases due to the oxide layer formation (that increases the resistance), until a minimum current value is reached (stage I). Afterwards, the current density starts to increase (stage II) due to the beginning of pore nucleation, i.e., formation of pits on the oxide surface assisted by field-enhanced dissolution and the presence of fluoride ions (F^-). Then, the pores reorganize and compete among themselves during the self-organization process (Stage III). Finally, the current density almost stabilizes (stage IV) during the continuous NTs growth in vertical orientation [89,132]. However, in the case of anodization with additional heating of the electrolyte, a current density increase can be observed in this last stage [90].

The anodization conditions are determinant in the morphological properties of the resulting NTs. In particular, anodization parameters such as the electrolyte type (e.g.

concentration and pH), anodization temperature, time and applied potential will influence the NTs' geometrical features such as pore diameter (D_p), interpore distance (D_{int}), wall thickness (W) or NTs length (L). Usually stated for anodic oxides, the values of D_p, D_{int}, W and L show a linear dependence on the anodization voltage (V) [1,90,126].

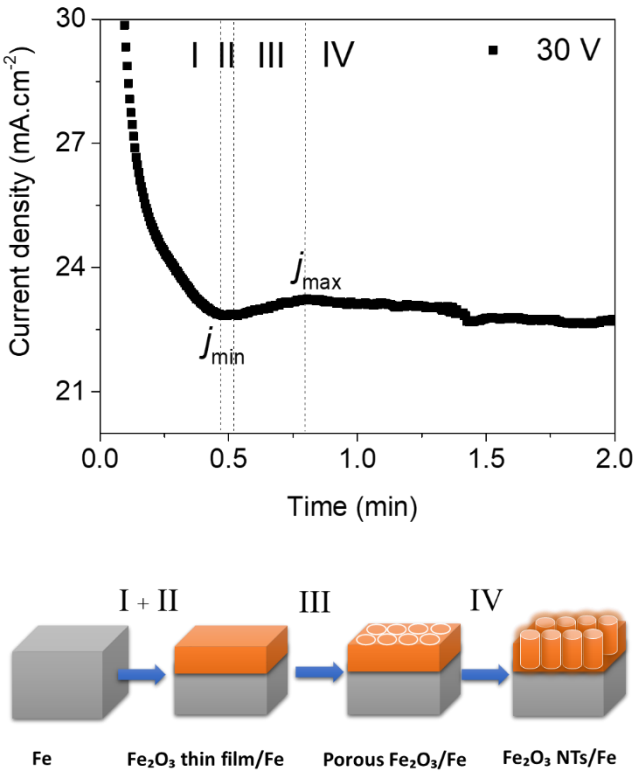

Figure 1.14. Typical anodization curve for iron (plot of current density *vs.* time; anodization conditions: 30 V in an ethylene glycol solution containing 0.5 wt% NH_4F and 3 vol% H_2O); scheme of the four stages of oxide NTs growth corresponding to the anodization curve transients (Adapted with permission from [89]. Copyright © 2009 American Chemical Society).

Electrochemical anodization results in nanostructures that are amorphous in nature. After anodization, annealing is a very important step to obtain the hematite crystalline structure that otherwise could not be used as a photoanode for water splitting [132]. A minimum temperature of 390 ºC was reported to obtain crystalline hematite [91].

The fabrication of self-assembled Fe_2O_3 nanoporous structures by electrochemical anodization was first introduced by Grimes´s research group in 2006 [133], taking advantage of the background and knowledge on the synthesis of self-organized anodic TiO_2 NTs using organic fluoride based electrolytes [118]. Using different anodization conditions of temperature, electrical potential and electrolyte concentration, they obtained highly ordered hematite nanoporous films with pores ranging from 50 to 250 nm in diameter and 300–600 nm in length. In particular, a glycerol electrolyte solution with 1% HF, 0.5 -1% NH_4F and 0.2% HNO_3, at different temperatures (4 and 10 °C) and

applied potentials (40, 60 and 90 V), was used [133]. Appling lower potentials (25-40 V) and temperatures (0-5 °C), no pores were formed, while higher anodization temperatures (15 and 20 °C) originated a particulate morphology, showing that the electrolyte temperature and concentration of NH_4F have an important role in the morphology of the structures. The crystalline hematite phase (band gap determined to be 2.2 eV) was obtained after thermal annealing of the nanoporous films at 400 ºC for 30 min, exhibiting a net photocurrent density of 0.51 $mA \cdot cm^{-2}$ (at 0.6 V *vs.* Ag/AgCl in an electrolyte containing 1 M NaOH + 0.5 M H_2O_2, under simulated AM 1.5 sunlight) [133]. One year after, the same group highly enhanced the photocurrent to 2 $mA \cdot cm^{-2}$ (at 0.65 V under AM 1.5) using Ti-Fe-O NTs, obtained by anodization of Ti-Fe metal films in ethylene glycol + NH_4F electrolyte and annealed at 500 °C [134].

In 2009, several groups reported the production of nanopores/NTs by anodization using ethylene glycol (EG) electrolytes containing NH_4F and deionized water. Albu *et al.* described the formation of vertically oriented self-organized nanoporous iron oxide using 0.1 M NH_4F + 1 M H_2O in EG for 1 h at 20 °C, at variable voltage (40–80 V). The temperature effect on NTs properties was also tested. Temperatures higher than 60 °C lead to a change from nanoporous to tubular structure, with the material between pores very brittle by dissolution. Application of increasing anodization voltage (10-100 V) showed an increase of the oxide layer thickness, as well as the D_{int} and D_p, which is the same tendency as observed for TiO_2 NTs [135].

At the same time, Mohapatra *et al.* reported a simple sonoelectrochemical anodization method for fast grow of smooth and ultrathin (5-7 nm thick) Fe_2O_3 NT arrays (3.7 μm long, 50-60 nm in diameter) using 0.5 wt% NH_4F + 3% H_2O in EG at 50 V, at room temperature [89]. It was the first time that NTs (with well-defined separated walls), and not nanopores were obtained. Depending on the anodization time, either thin films, nanopores or NTs were obtained, respectively. Comparing 1D NTs with nanoparticles (NPs), the NTs showed better photocurrent density performances probably due to the ultrathin walls, in which holes can reach the surface faster, reducing the losses by e^--h^+ recombination [89]. The authors found that the charge transport properties of the NTs are 40–50 times higher than those of the NPs. After annealing the NT arrays at 500 °C, a photocurrent density of 1.41 $mA \cdot cm^{-2}$ at 0.5 V *vs.* Ag/AgCl was obtained (under AM 1.5 illumination in 1 M KOH solution) [89].

The transition between porous and nanotubular structure has been described as dependent of the anodization parameters used [89,132,135]. As in the case of TiO_2, the presence of the fluoride rich layer was also reported for Fe_2O_3. The Fe-F-layer was referred to be dependent of water content, and it is determinant for the transition from nanopores to NTs [136].

In turn, Rangaraju *et al.* reported the synthesis of Fe_2O_3 NTs by single-step electrochemical anodization in EGWF electrolyte (EG solution containing 0.1 M NH_4F and 3 vol% water) at 50 V for 15 min, resulting in NTs with 1.5 μm thickness, D_p of 54–100 nm and *W* of 12–22 nm (Figure 1.15). After conversion to hematite phase by annealing at 550 °C in acetylene environment, photocurrent densities less than 0.2 $mA \cdot cm^{-2}$ (at 0.2 $V_{Ag/AgCl}$ in 1 M KOH with AM 1.5 light illumination) where measured. In the same work, a two-step anodization procedure with first anodization at 20 V in a mixed solution of 90 vol% EGWF + 10 vol% of 0.2 M aqueous phosphate followed by a second anodization at 50 V in EGWF solution resulted in a two-layered structure: dendrite morphology on the top of NT arrays. For these structures, higher photocurrent densities of 0.74 $mA \cdot cm^{-2}$ at 0.2 V *vs.* Ag/AgCl and 1.8 $mA \cdot cm^{-2}$ at 0.5 V *vs.* Ag/AgCl were obtained [83].

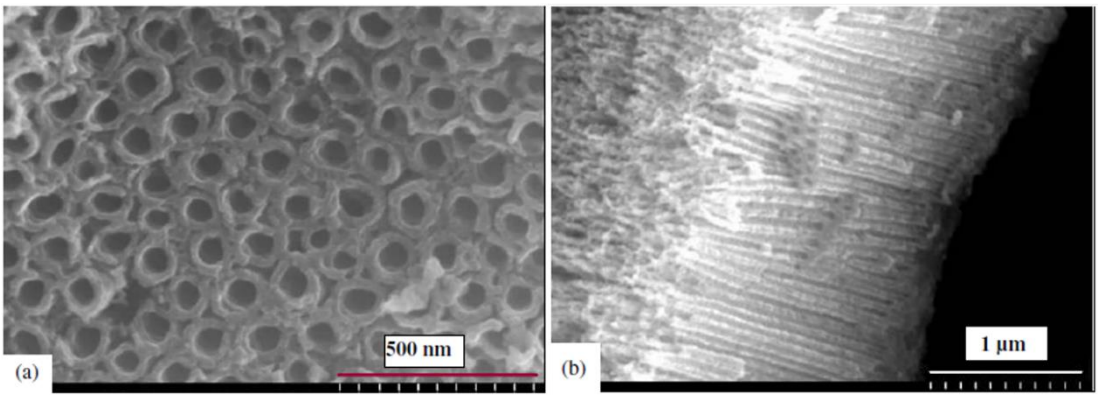

Figure 1.15. SEM images of Fe_2O_3 NTs arrays prepared by anodization of iron in EGWF solution, at 50 V for 15 min. (a) Top view of the NTs and (b) cross-sectional view of the NTs with about 1.5 μm thickness (Republished with permission of © 2009 IOP Publishing, from [83]; permission conveyed through Copyright Clearance Center,Inc).

Lastly, Grimes *et al.* also reported the synthesis of Fe_2O_3 NTs structures with an improved morphology, by anodization over a potential range of 30-60 V, using an EG electrolyte containing 0.2-0.5 wt% NH_4F and 2-4% H_2O, at temperatures varying from 22-75 °C (Figure 1.16) [90]. The nanotube formation was found to be strongly dependent on the electrolyte bath temperature and F^- content. Although lower temperatures were being used (22 °C), the electrolyte self-heating for longer anodization times of 20 min originated templates of 4.5 μm thickness with a mixture of NTs growing on a nanoporous base. The formation of NTs arrays only occurs at higher temperatures (45-75 °C), with D_p ranging between 30-80 nm and a minimum *W* of ~10 nm. Highly ordered iron oxide NTs were obtained with *L* ranging from 2.6 to 4 μm in just 180 s. The NTs *L* and D_p increased with temperature, being an important parameter to influence the anodization.

Furthermore, thermal annealing conditions were tested, at 400 °C using different atmospheres: air, N_2, Ar and H_2. While the hydrogen-annealed sample presented magnetite contribution, the sample annealed in air atmosphere presented predominantly the hematite phase.

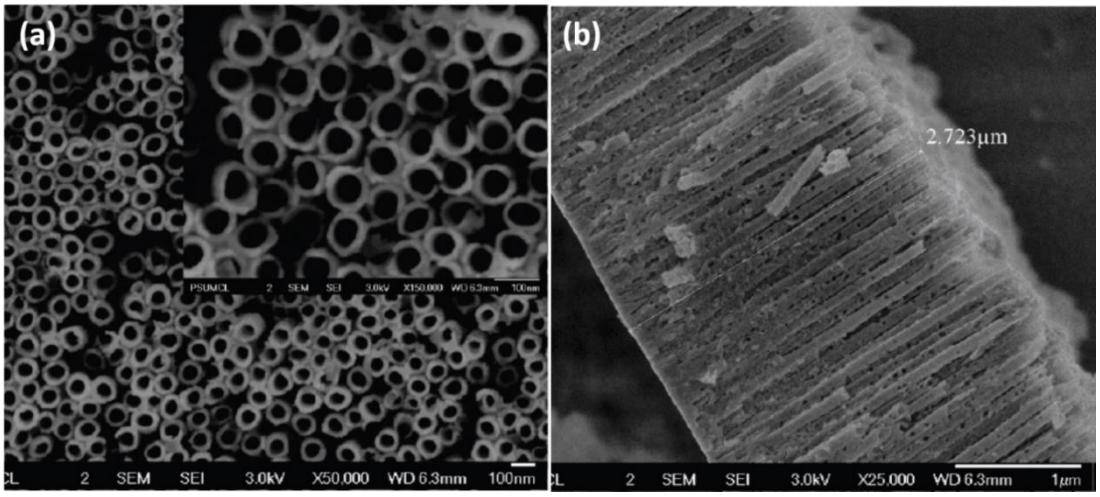

Figure 1.16. SEM images of Fe_2O_3 NTs arrays prepared by anodization of iron in EG solution + 0.5 wt % NH_4F + 3.0% H_2O, at 50 V for 180 s at 45 ºC. (a) Top view of the NTs morphology and (b) cross-sectional view of the NTs with about 2.7 μm thickness (Reprinted with permission from [90]. Copyright © 2009 American Chemical Society).

Later, a different approach was adopted, considering the effect of pre-treatment of the substrate before anodization. Three different iron substrates were evaluated: (i) bare iron foils; pre-treated iron substrates by cathodic polarization (for 4 hours in 0.1 M NH_4F aqueous solution) at two different potentials: (ii) −0.8 V and (iii) −1.0 V. For the three cases, the potential values are more negative than the reversible potential of water oxidation, which indicates a photocatalytic effect. All samples show a maximum IPCE value between 350 and 375 nm, being the samples pre-treated at −1.0 V that shows the highest IPCE value: 45% at 375 nm [137].

Another important factor is the maximum conversion of the amorphous iron oxide into the hematite phase, since the electronic band mismatch between hematite and other structures such as magnetite increases the hole trapping-sites across grain boundaries. The presence of magnetite phase further increases the e^--h^+ recombination [89]. Recently, a by-layered hematite structure (consisting in a nanosphere layer on top of NTs) was synthetized for water splitting [132]. It was performed a detailed study of the annealing conditions considering sequentially several factors: temperature (300-500 °C), heating rate (2, 5 and 15 °C·min^{-1}, and directly placed in the furnace) and annealing environment (air and Ar). Comparing annealing temperatures, the sample annealed at

500 °C resulted in more pronounced hematite peaks (results confirmed by Raman spectroscopy). Even though hematite was the predominant phase, magnetite was always present in all samples. The 500 °C temperature also resulted in a better photocurrent performance for higher potentials: 0.078 $mA \cdot cm^{-2}$ at 1.54 V_{RHE}, probably due to a slow recombination process. Comparing the heating rates, it was shown a best performance for the faster heating rate (15 $°C \cdot min^{-1}$). A faster heating rate induces a quicker crystallization of the structure, with the incorporation of oxygen vacancies (lattice structural defects) that act as donor states, decreasing the e^--h^+ recombination and enhancing the electrical conductivity [83,132]. For the sample directly placed in furnace (without heating rate), a non-uniform structure was obtained, due to abrupt variation in temperature. Comparing the annealing atmosphere, the Ar resulted in enhanced photocurrent densities. The authors described these results due to the fact that the annealing in non-oxidizing atmospheres (argon) promotes the formation of magnetite in the nanostructure, and oxygen vacancies which improve the electrical conductivity of the nanostructure. Contrarily to the previous stated by Mohapatra *et al.* [89], here the presence of magnetite benefits the photocatalytic properties of the nanostructure and so the water splitting performance. To compare these works, Table 1.1 summarizes the main results obtained in literature.

Although all these studies considered the thermal annealing a key factor to achieve the best crystalline structure, there was no agreement relative to the optimal conditions. Indeed, further investigations were suggested to determine the anodic iron oxide NTs optimal annealing conditions to improve the PECs efficiency [90]. Despite NTs are the most promising morphology, the photocurrent values obtained for NTs by Fe anodization are still very low. In fact, more work is needed in this field to optimize the homogeneity of this nanostructures and annealing conditions to convert them into pure hematite phase.

The magnetic properties of hematite nanostructures are strongly dependent on their size and crystalline properties. Until now, few works referred the magnetic properties of hematite NTs [122]. Different from the bulk hematite (with TM at 260 K), a reduced Morin transition was reported for hematite NTs obtained by electrospinning process, in the order of 125-127 K. A recent study on the magnetic properties of hematite NTs produced by electrodeposition on AAO templates revealed even lower transitions, at 32 K and 106 K , ascribed to the small tubular-structure dimensions of the hematite NTs within a small amount of particles [138]. Similar to NTs, other structures such as NWs or nanorods also presented lower TM values, at 123-125 K and at 120 K respectively [139-141]. More detailed studies must be performed in order to determine the magnetic properties of NTs obtained by electrochemical anodization and its impact in the photoresponse.

Table 1.1. Comparison between the experimental conditions, correspondent morphological features and PEC results, reported in literature for Fe electrochemical anodization (performed using ethylene glycol solution containing NH_4F and H_2O).

Electrolyte (EG solution)		Potential (V)	Time (units)	Temp. (ºC)	Results				Morphology	Annealing	PEC Performance (*j*/IPCE)	Ref.
NH_4F	H_2O				*L* (μm)	D_p (nm)	D_{int} (nm)	*W* (nm)				
0.1 M	1 M	10 -80	1 h	20	1-13	~30 -110	~35 -150	-	Nanopores	500 ºC (in air): α-Fe_2O_3 and Fe_3O_4	-	[135]
		100			~5	~ 110	~ 150	-				
		40	1 h		7.5	80	130	-				
			3 h		11.5	-	-	-				
		40	1 h	>60	-	-	-	-	Change from porous to tubular structure			
0.5 wt %	3 vol%	50	2 min	RT	-	-	-	-	Thin films	-	-	[89]
			6 min	RT	-	-	-	-	Nanoporous	-	-	
			13 min	RT	~3.7	50-60	-	5-7	Nanotubes	500 ºC (O_2 + H_2, 10 % in Ar) for 3 h: α-Fe_2O_3 and Fe_3O_4	0.81 mA.cm^{-2} at 0.5 $V_{Ag/AgCl}$	
										500 ºC (H_2) for 6 h: pure α-Fe_2O_3	1.41 mA.cm^{-2} at 0.5 $V_{Ag/AgCl}$ (efficiency =0.84%, AM 1.5)	
		30	25 min	RT	-	-	-	-	No nanotubes	-	-	
0.1 M	3 vol%	50	15 min	-	1.5	54-100	-	12-22	Nanotubes	500 ºC (H_2 + Ar) for 1 h: α-Fe_2O_3 (predominant) + γ-Fe_2O_3 (minor peaks)	<0.10 mA.cm^{-2} at 0.2 $V_{Ag/AgCl}$	[83]
										500 ºC (C_2H_2 + H_2 + Ar) for 10 min: γ-Fe_2O_3 (predominant) + α-Fe_2O_3 (minor peaks)	<0.20 mA.cm^{-2} at 0.2 $V_{Ag/AgCl}$	
1st step anodization					Nanodendrite: Wide = 50 nm; Long = 150 nm				Dendrite + Nanoporous	550 ºC (C_2H_2+ H_2+Ar) for 10 min:	0.74 mA.cm^{-2} at 0.2 $V_{Ag/AgCl}$; 1.8 mA.cm^{-2} at 0.5 $V_{Ag/AgCl}$ (AM 1.5)	
90 vol% EGWF + 10% STPF		20	10 min	-								
2nd step anodization												

0.1 M	3 vol%	50	15 min	-					γ-Fe_2O_3 (predominant) + α-Fe_2O_3 (minor peaks)		
0.3 wt %	3 vol%	50	180 s	60	>3	55	-	~10	Nanotubes	400 ºC (air) for 1800 s: hematite	-	[90]
										400 ºC (Ar) for 1800 s α-Fe_2O_3 peaks with predominant (104) and (110) + Fe_3O_4 (smaller peaks)	IPCE drops (<3.5%) for λ>400 nm	
										400 ºC (N_2) for 1800 s: α-Fe_2O_3 peaks with predominant (104) and (110) + Fe_3O_4 (smaller peaks)	-	
										400 ºC (5% H_2) for 1800 s: iron diffraction peak along with Fe_3O_4	-	
			180 s	35-55	~2-3.45	~45-56	-	-	Nanoporous to nanotubes	-	-	
			30 s	75	1.67		-	-	Nanotubes	-	-	
			60 s	75	2.75		-	-		-	-	
0.2 wt %	2 vol%	50	180 s	75	~4	~42	-	~20		-	-	
0.5 wt %	3 vol%	50	180 s	45	~2.6	~60	-	~8		-	-	
0.35 wt %	3 vol%	50	1200 s	22	~4.5	-	-	-	Electrolyte self-heats; nanotubes formed in nanoporous base	-	-	
0.5 wt %	3 vol%	50	180 s	50	-	-	-	-	Nanoporous$^{HN(w/o)}$	-	IPCE ≈ 33% at λ=375 nm	[137]

					1			30	Nanotubes HN(-0.8V)	-	IPCE ≈ 37% at λ=375 nm	
					-	-	-	20	Nanotubes HN(-1.0V)	500 ºC for 3 h: predominantly α-Fe_2O_3	IPCE ≈ 45% at λ=375 nm	
0.1 M	3 vol%	50	15 min	-	1.15	D_{outer}: 70-85	-	~30	Nanotubes (sponge-like structure on top of the nanotubes)	300 ºC (air; 15 ºC/min) α-Fe_2O_3 + Fe_3O_4	<0.078 mA.cm^{-2} at 1.54 V	[132]
									Nanotubes (sponge-like structure on top of the nanotubes)	400 ºC (air; 15 ºC/min) α-Fe_2O_3 + Fe_3O_4	<0.078 mA.cm^{-2} at 1.54 V	
									Bi-layer structure (nanospheres on top of nanotubes	500 ºC (air; 15 ºC/min) predominant α-Fe_2O_3 + Fe_3O_4 (smaller peaks)	~0.078 mA.cm^{-2} at 1.54 V ~0.0204 mA.cm^{-2} at 0.4 V	
									Spalling off of the oxide layer	500 ºC (air; put directly in the furnace)	No photocatalytic activity	
									Bi-layer structure (nanospheres on top of nanotubes	500 ºC (Ar; 2 and 5 ºC/min)	0.032-0.048 mA/cm2 at 1.54V	
										500 ºC (Ar; 15 ºC/min) Predominant α-Fe_2O_3 with increasing Fe_3O_4	~0.143 mA.cm^{-2} at 1.54 V ~0.0256 mA.cm^{-2} at 0.2 V	

EGWF: 0.1 M NH_4F + 3 vol% H_2O in ethylene glycol

STPF: 0.2 M Sodium tripolyphosphate ($Na_5P_3O_{10}$) + 0.05M NH_4F

HN(w/o): bare iron foils, without pre-treatment

HN(-0.8 V): iron substrates electrochemically pre-treated for 4 hours in an 0.1 M NH_4F aqueous solution at -0.8 V

HN(-1.0 V): iron substrates electrochemically pre-treated for 4 hours in an 0.1 M NH_4F aqueous solution at -1.0 V

Hydrothermal. The hydrothermal method is considered a cheap, easy and an effective way to control the size and shape of nanostructures, through variation of the experimental conditions (reagent, concentration, temperature, pressure and reaction time).

Hematite NTs can be also obtained by hydrothermal method, where the shape of the nanotubes depend on the temperature, time and chemical agent precursors (such as phosphate or sulfate ions) added to the hydrothermal solution [142-144]. The presence of phosphate ions was referred by Jiu *et al.* [143] as a crucial parameter that induces the formation of the tubular structure, resulting from the selective adsorption of phosphate ions at the surface of hematite particles and their ability to coordinate with ferric ions. The mechanism of NTs formation consists in the "dissolution" of the spindle-like precursors from the outer tips down to the interior, until the formation of hollow tubes; the hydrothermal time dictated the stage of the process, varying from spindle, rod-like nanocrystals, semi-nanotubes and complete nanotubes [Figure 1.17(a)-(e)]. The use of acidic solution helps to promote the dissolution, and a re-crystallization process on the surface also accompanies the dissolution [143].

On the other hand, the use of both phosphate and sulfate ions induces the formation of two kinds of precursors, a large amount of spindles and a few ellipsoids [Figure 1.17 (f)-(h)]. While spindles growing along [001] crystallographic direction were formed in the presence of phosphate ions, ellipsoid nanoparticles were obtained with the addiction of sulfate ions. This fact leads to a "multi-site dissolution" process, due to randomly distributed high-energy sites on the top of the ellipsoids. After 48 h, nanostructures with a tube-in-tube morphology were formed, as can be seen in Figure 1.17 (h). The produced nanostructures showed to have already the hematite structural phase [Figure 1.17 (i)] [144].

This kind of nanostructures have been explored only due to its magnetic properties [142,144] and lithium-storage applications [145], and few data are available about the photoelectrochemical properties of this kind of nanostructures [146].

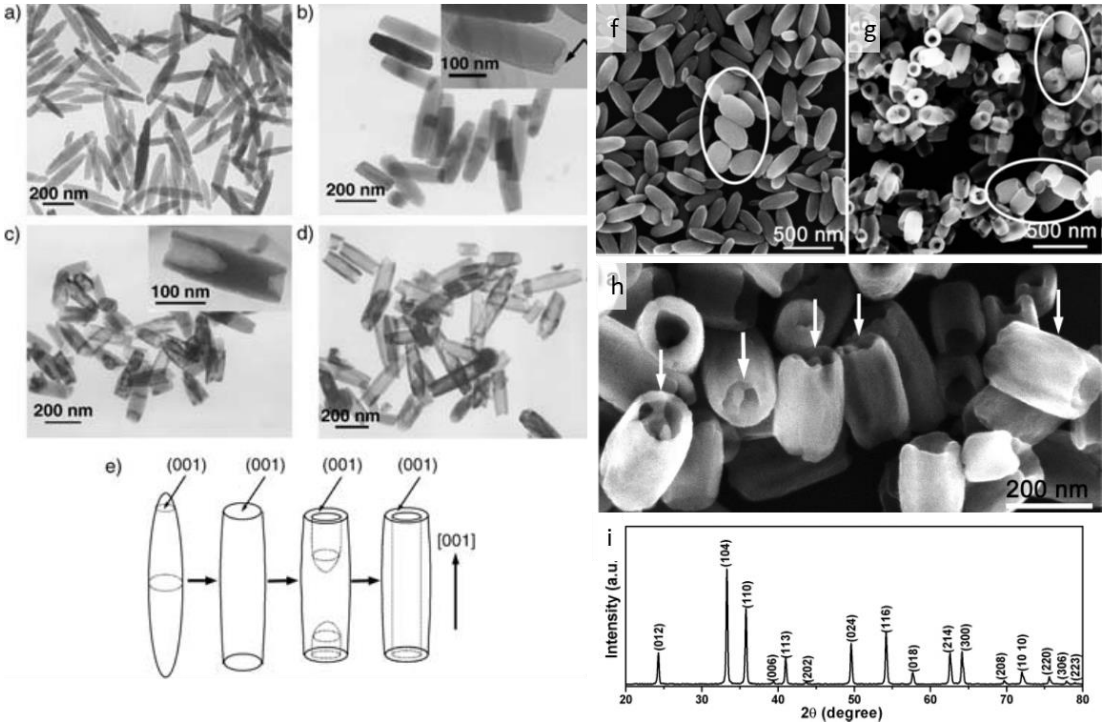

Figure 1.17. TEM images of Fe_2O_3 NTs obtained at 220 °C along the reaction time: (a) 2 h, (b) 8 h, (c) 12 h, and (d) 48 h; (e) schematic illustration of the tube-formation mechanism (from [143]). SEM images of the hematite Fe_2O_3 NTs with sulfate precursor prepared with reaction times of (f) 1 h, (g) 24 h and (h) 48 h; (i) XRD spectra of as-prepared hematite tube-in-tube nanostructures (Reprinted with permission from [144]. Copyright © 2007 American Chemical Society).

1.4.1.2. Tungsten trioxide

Tungsten trioxide (WO_3) has also been subject of intensive research for many technological applications. It started by attracting great interest as an electrochromic (EC) material in the mid-1960s, turning out to be part of the first commercially available EC ‘‘smart window’’, a great advance into energetic sustainability [147,148]. Also, it has been used in several other areas, such as gas sensing, photocatalysis, superconductivity, optical recording or image storage [37,147,148].

As a semiconductor material, it has also been highly explored for water splitting applications, since it was first revealed for this purpose by Hodes *et al.* in 1976 [149]. In this earlier stage, two different approaches were used to obtain WO_3 photoelectrodes: by using heated tungsten metal or by using ammonium tungstate sprayed on a conductive glass substrate, where photocurrents of ~0.2 $mA \cdot cm^{-2}$ and ~0.05 $mA \cdot cm^{-2}$ were obtained, respectively [149].

Like hematite, it is a low-cost material, widely available, presents a high stability against photocorrosion, and can be easily synthesized by viable methods such as

electrochemical anodization or hydrothermal, as already mentioned above for hematite [37,148,150].

Comparingly with hematite, WO_3 presents several advantages, such as a higher carrier lifetime (1-9 ns), higher electron mobility (6.5-16 $cm^2 \cdot V^{-1} \cdot s^{-1}$), higher carrier concentration (5 $x10^{19}$ cm^{-3}), long hole (~150 nm) and electron (~500 nm) diffusion lengths, favorable energy band edge for oxygen evolution, high stability in acidic aqueous solutions and presents isotropic electronic properties [8,37,148,151-153]. However, it has a larger band gap 2.6–2.8 eV and, consequently, only absorb 12% of the solar spectrum (near-UV, but also visible blue). Taking into account kinetic losses, only a maximum solar-to-hydrogen conversion efficiency of 4.8% (under standard AM 1.5 solar illumination) is expected [16,41].

Its valence band has energy enough for water oxidation, however, as conduction band is too low to accomplish water reduction, an external bias can be provided: for example, if incorporated in a tandem cell with a dye-sensitized TiO_2 cell, as described by Grätzel in 2001; this device demonstrated a water splitting efficiency of 4.5% (Figure 1.18) [39,154].

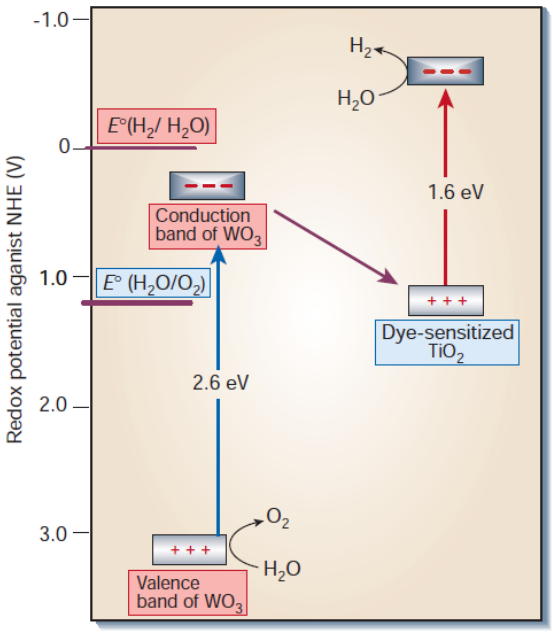

Figure 1.18. Scheme of a tandem cell for solar water splitting, with two photocatalytic systems (WO_3 and dye-sensitized TiO_2 cell) (Reprinted by permission from: Nature [154], Copyright © 2001, Nature Publishing Group).

1.4.1.2.1. Tungsten trioxide physical properties

Structural properties. The crystal structure of WO_3 is dependent on temperature and pressure, determined by the distortion and tilting angles of the corner-sharing of WO_6 octahedra, with reference to the "ideal cubic structure". For bulk WO_3, the phase transformation occurs in the following sequence: monoclinic II (ε-WO_3 for < -43 ° C), triclinic (δ-WO_3 from -43 °C to 17 °C), monoclinic I (γ-WO_3 from 17 °C to 330 °C), orthorhombic (β-WO_3, 330 ° C to 740 °C) and tetragonal (α-WO_3 for > 740 °C) (Figure 1.19) [40,148,155]. Monoclinic I (γ-WO_3) has been reported the most stable phase for bulk at room temperature [37,40,148]. For nanostructured WO_3, the phase transition annealing temperatures are generally lower than for the bulk, since the morphology affects the crystal phases [40]. The reduction of the size of WO_3 crystallites enhances the surface energy of the system, which decreases the annealing temperatures [148].

Crystalline WO_3 is in general formed by corner and edge sharing of WO_6 octahedra, exhibiting an ABO_3 perovskite-like structure. However, ideal cubic perovskite WO_3 is not normally observed in practice, due to distortions corresponding to antiferroelectric displacements of W atoms and mutual rotations of the oxygen octahedra [148,151,156].

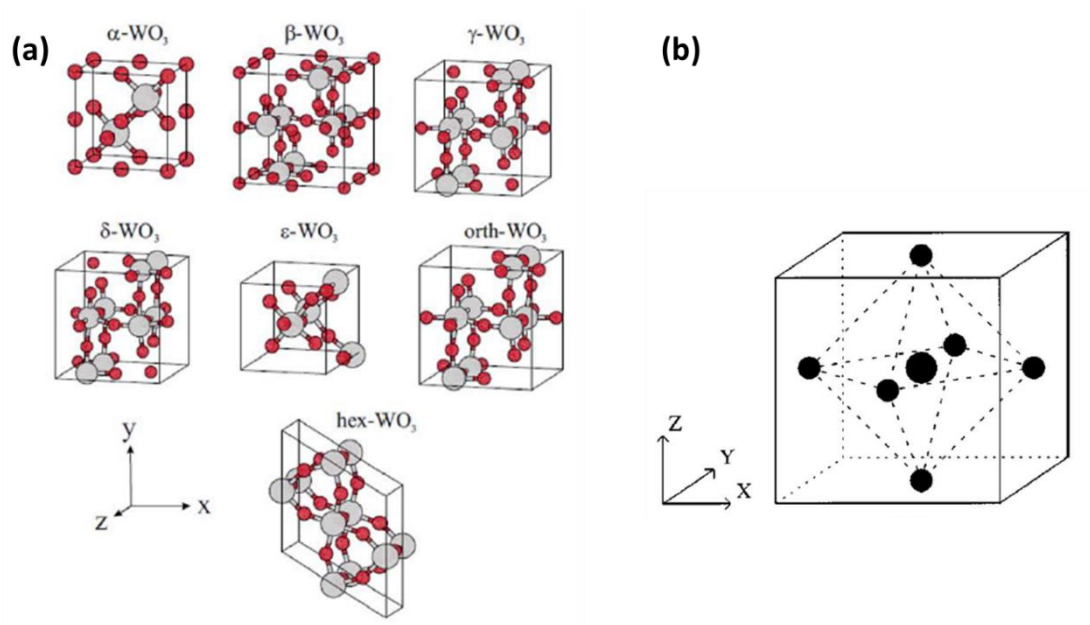

Figure 1.19. (a) Unit cells for the WO_3 different phases. (b) WO_3 cubic perovskite crystal structure (Reproduced from [151] with permission from The Royal Society of Chemistry).

Optoelectronic properties. WO_3 is a n-type semiconductor with an indirect bandgap, only absorbs approximately 12% of the solar spectrum and in the visible spectrum up to 500 nm. Although WO_3 has a higher minority carrier diffusion length (~150 nm) than

hematite, due to the indirect bandgap transition, the pathways that visible light has to travel inside the photoanodes are significantly higher, which limits the photoanodes photoresponse [17,150]. The WO_3 band gap, E_g = 2.5–2.8 eV, corresponds to the difference between the energy levels of the valence band (VB), formed by filled O 2p orbitals, and the conduction band (CB), formed by empty W 5d orbitals. The changes of crystal phase of WO_3 determined by the degree of distortion from the "ideal" cubic phase could lead to the increase in E_g, as the occupied levels of the W 5d states also increase [148,156].

1.4.1.2.2. Tungsten trioxide nanostructures

Amorphous and crystalline WO_3 thin films have been used as efficient photoanodes for water splitting, however, the formation of crystalline structures helps to reduce the surface imperfections associated to higher carrier recombination and charge trapping sites [17,157]. A photocurrent density of 2.7 $mA \cdot cm^{-2}$ at 1.0 V_{RHE} was reported for highly stable nanocrystalline WO_3 thin film, with a long-term stability tested over 144 h of photoelectrolysis (under simulated 1-sun AM 1.5 light) [150].

The use of nanostructuring has brought enormous advantages to enhance the PEC performance of WO_3. The changes in the morphology favour the band gap reduction [40,148,158,159] and in that sense, diverse nanostructures, such as NPs [160], nanoporous films [131] , NWs or nanoplates [37,161,162], have been widely explored. For that, several physical, chemical and electrochemical techniques have been used: spray pyrolysis, hydrothermal, solvothermal, electrochemical anodization, sol-gel, sputtering deposition or chemical vapor deposition [37,162-166].

For example, a considerable photocurrent of 2.7 $mA \cdot cm^{-2}$ (at 1.6 V *vs.* SCE, under 100 $mW \cdot cm^{-2}$ illumination) was obtained by sputtering deposition [166]. Although is an expensive technique, the photoanodes presented good crystallinity, and few lattice defects.

In turn, low-cost techniques such as electrochemical anodization of W foils have been also explored. Whereas in Fe or Ti anodization, a frequent nanotubular morphology is obtained, in W case, different morphologies such as nanoporous, flower-like, crispy or spongy structures are often reported, depending on foil pre-treatments, anodization electrolytes (*N*-methylformamide/H_2O/NH_4F, H_2SO_4/NaF, Na_2SO_4/NaF, etc.), potentials, and annealing temperatures used [131,158,167-169]. High photocurrents of 3.8 $mA \cdot cm^{-2}$ (at 1 V *vs.* SCE), with collection efficiencies of 60–70% (estimated from IPCE) were obtained [167]. However, the WO_3 nanostructures by anodization grow on the surface of

W metallic foils. The fact that W foil is not a transparent substrate (unlike FTO) and could be oxidized during PEC measurements, could be unfavourable for light absorption [37].

One of the best photocurrents, 3.5 mA·cm^{-2} (at 1.23 V_{RHE} under 100 mW·cm^{-2}), was reported for photoanodes prepared from commercial powders using doctor-blade technique (Figure. 1.20, at left) [170]. Interestingly, different electrolytes used in photocurrent density-voltage measurements originated different photocurrent densities, meaning a photooxidation of the electrolyte instead of water (Figure. 1.20, at right) [37,170]. Electrolytes containing $CH_3SO_3^-$ originated improved photocurrents [37,170,171], as well as with incorporated polyoxometalates catalysts, as reported by Sarnowska *et al.*, with a photocurrent of 4.5 mA·cm^{-2} (at 1–1.1 V_{RHE}, under simulated AM 1.5G irradiation) [172].

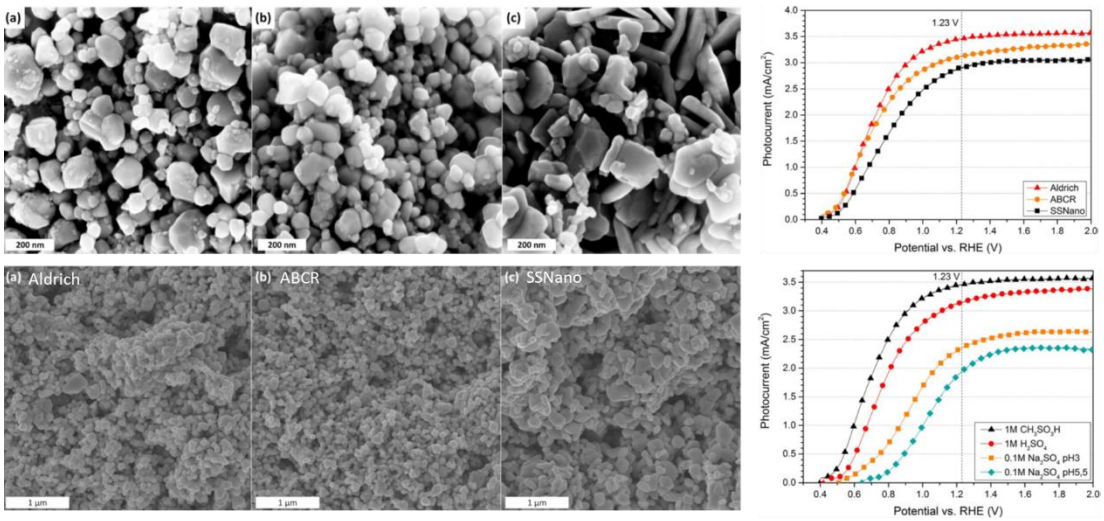

Figure 1.20. SEM images of several WO_3 commercial powders, and respective photoanodes prepared by doctor-blading and after annealing (left). Photocurrents as high as 3.5 mA·cm^{-2} were obtained, further improved using CH_3SO_3H electrolyte (right). (Adapted with permission from [170]. © 2016 WILEY-VCH Verlag GmbH & Co. KGaA, Weinheim).

The use of dopants (Co, Cu, Fe, Ni, V, Sn, etc.) is also an effective strategy to lower the band gap and to lead to the increase of PEC efficiency [173,174]. As an example, the use of Co dopant increased the photocurrent of undoped WO_3 nanoplates from 0.25 to 0.64 mA·cm^{-2}.

Another approach with high potential to explore is the formation of heterojunctions, i.e., interface layers with another semiconductor material that will help in the absorption of light, improve the charge separation efficiency and transport or reduce the band gap, comparatively with the single semiconductor. Recently, the use of heterojunction WO_3 photoanodes with Fe_2O_3 NWs or Ti-doped Fe_2O_3 presented, respectively, photocurrents

of 1.6 $mA \cdot cm^{-2}$ (at 1.8 V_{RHE}) and 2.15 $mA \cdot cm^{2}$ (at 1.23 V_{RHE}) [175,176]. To construct an effective heterojunction is necessary to use appropriate materials with matched properties (such as band position). Taking as example the WO_3/α-Fe_2O_3 heterojunction [175], the band bending at the interface between the two semiconductors causes a potential gradient and a directional flow of electrons. When the heterojunction absorbs visible light, the excited electrons in α-Fe_2O_3 will be transferred to the CB of WO_3 and in turn to FTO substrate; on the other hand, holes from the VB of WO_3 will be transferred to the VB of α-Fe_2O_3 and then to the electrolyte interface to oxidize water. The insertion of the Fe_2O_3 heterojunction allowed an enhanced charge separation and fast transport of generated charge carries within the photoelectrode, thus avoiding the electron-hole recombination, ultimately leading to photocurrents 5 and 7 times higher than those of single WO_3 and α-Fe_2O_3, respectively [175].

The annealing conditions seems to be a determinant parameter to obtain highly ordered, crystalline nanostructures and with less surface defects. In addition, the change of amorphous WO_3 to monoclinic upon annealing (500 °C) was stated to decrease the band gap energy and thus improve the photocurrent conversion efficiencies [37,158,159]. The effect of parameters such as temperature, time or annealing atmosphere on photoanodes photoresponse have been widely explored [37,158].

Significant changes occurred on WO_3 films morphologies by varying the annealing temperatures: from 250 to 500 °C changed from flower-like to rod structures [168]. Also, NPs changed from long needle, small plate to large-like, varying the temperature from 400 to 600 °C [177]. Furthermore, the increase of particles diameter (30–500 nm) and crystallite size (37–129 nm) with annealing temperature (500–800 °C) lead to the enhancement of the photocurrent [37,178].

Optimal annealing temperatures are dependent on the WO_3 preparation method, since different methods originate different particle size, crystalline structure and morphology. Liu *et al.* reported the increase of annealing temperature (up to 450 °C) improved the photoactivity, as crystalline degree increased, and surface defects decreased; afterwards, additional annealing temperature had a negative impact in the photoactivity of the WO_3 films [179]. On the other hand, in the thin films reported by Ng *et al.*, despite 600 °C presented a higher crystalline structure, 400 °C displayed the highest PEC water splitting performance. They concluded that higher annealing temperature affects particle size and those changes could decrease the effective surface area for charge collecting within the photoanode [168].

Additionally, the annealing atmosphere has shown to influence the WO_3 photoelectrodes efficiencies. It is the case of nanoporous WO_3 annealed in NH_3/N_2-

atmosphere, in which the N atoms were incorporated into crystal lattice of photoelectrodes acting like a N-dopant, and ultimately improving the photocurrent density [179]. Likewise, the annealing in air atmosphere showed to improve the photocurrent, by removing the water content and increasing the oxygen deficiency, while the O_2 atmosphere had a contrary effect, since promotes higher degree of oxygen. In the case of H_2 atmosphere, an excess of oxygen deficiency causes the increase the defective sites and consequently higher e^--h^+ recombination [37,180].

Recently, parameters such as annealing ramp showed to influence the photoresponse of WO_3 nanoplatelets films, as reported by Apolinário *et al.*, since a ramp of 60 °C·h^{-1} highly improves the photocurrent when compared with a 500 °C·h^{-1} ramp [37].

1.4.1.2.2.1. Hydrothermal synthesis

Hydrothermal synthesis of WO_3 is a very versatile method, since different morphologies can be formed using this simple and cost-effective way. The morphology of the nanostructures depends mainly on the initial precursor, type of the chemicals used, and control of the experimental parameters (for example temperature and time of the hydrothermal process) [181]. Nanostructures such as nanoparticles, nanocrystals, nanowires, nanoplates, wedge-like, and sheet-like were reported (Figure 1.21), with photocurrents densities varying from 0.5 mA·cm^{-2} (at 1.45 V *vs.* Ag/AgCl) to 2.7 mA·cm^{-2} (at 1.4 V_{RHE}), under 100 mW·cm^{-2} [148].

In some works, it was referred nanostructures that were first produced by hydrothermal process, filtered, then annealed, dispersed using organic solvents and polymers as binding agents and then spread into FTO substrates by doctor blading, followed by new annealing to eliminate organic compounds and convert to crystalline phase [181]. This kind of process only allows an aleatory dispersion of the nanostructures; besides, it involves several steps and is time consuming. Limited photocurrent was attained using this methodology: 0.77 mA·cm^{-2} (at 1.8 V *vs.* Ag/AgCl, AM 1.5G illumination, 100 mW·cm^{-2}). Other methods, consisting in the deposition of seed layers upon FTO using a W precursor solution were developed followed by annealing before the hydrothermal method, leading to a photocurrent of 1.43 mA·cm^{-2} under AM 1.5G illumination [161].

Yang *et al.* reported the vertical growth of nanoplates directly on FTO substrate, without the use of seed layers or the doctor-blade deposition [162]. With a simple recipe [with sodium tungsten dehydrate $Na_2WO_4.2H_2O$ and ammonium oxalate $(NH_4)_2C_2O_4$

acidic solution], it allowed a direct nucleation upon the substrate, as well as good coverage of FTO [Figure 1.22(a)], which highly improved the photocurrent to 4.13 $mA \cdot cm^{-2}$ (at 1.6 V *vs.* Ag/AgCl). However, comparingly with hematite, the stability of WO_3 presented a photocurrent decrease of 28.4% after 40 min [43,162].

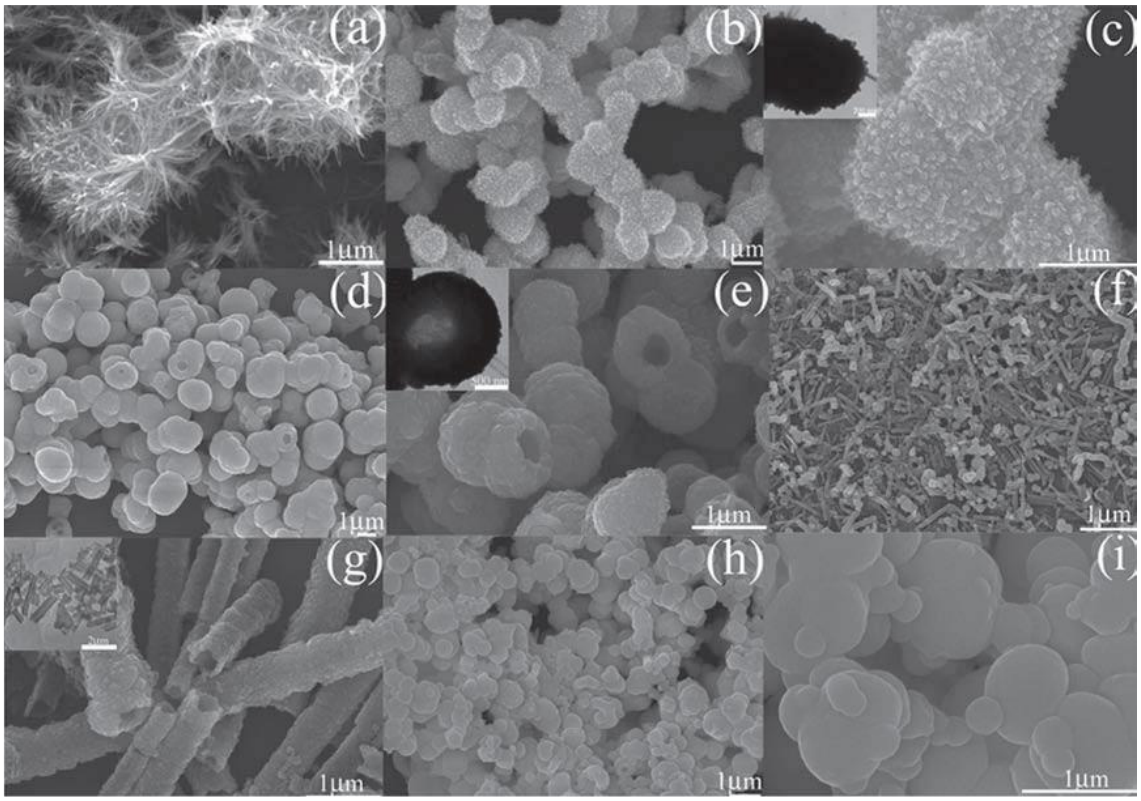

Figure 1.21. SEM and TEM images of different nanostructured morphologies of WO_3 prepared by hydrothermal method (Reproduced with permission from [148]. Copyright © 2011 WILEY-VCH Verlag GmbH & Co. KGaA, Weinheim).

Afterward, other hydrothermal formulation also allowed the nucleation upon FTO, resulting in thinner nanoplate-like structures [Figure 1.22(b)], however an expensive W precursor ammonium paratungstate $[(NH4)_{10}(H_2W_{12}O_{42})4H_2O]$ was used [182], resulting in a photocurrent of 2.26 $mA \cdot cm^{-2}$ (at 1.23 V_{RHE}) and an incident photon-to-current conversion efficiency (IPCE) of 35% at 400 nm.

The nanostructured films thickness was also reported to influence positively the PEC efficiencies, ascribed to the fact that thicker WO_3 films increase the light absorption (reduced band gap) and active area, while decreasing the percolation path to the FTO surface [37,158]. In this regard, the use of variable film thickness, allied to a more viable hydrothermal procedure [162], was the strategy adopted for WO_3 photoanodes synthesis, that we are going to discuss further in this thesis.

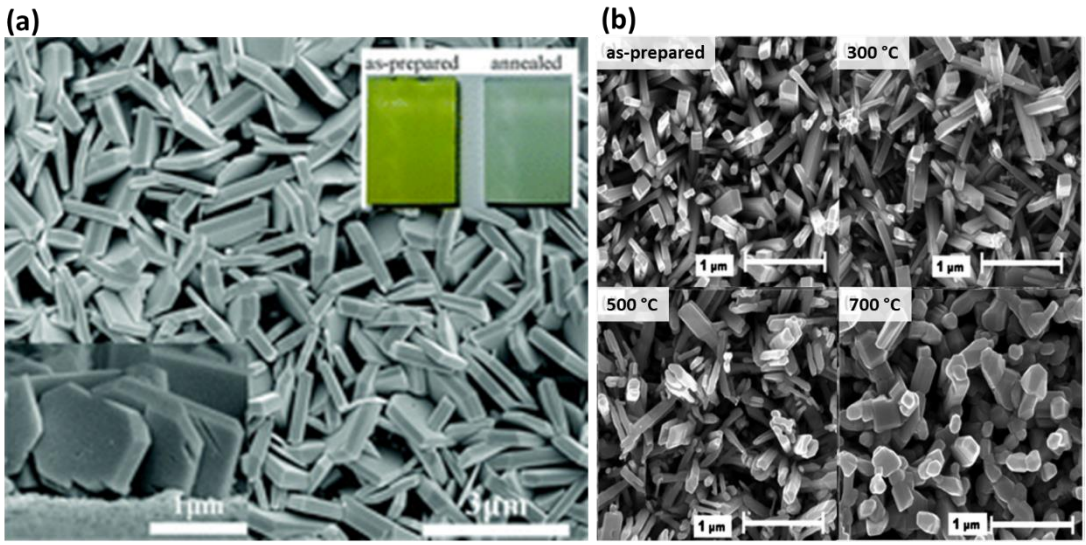

Figure 1.22. Different nanostructures obtained by hydrothermal method: (a) WO_3 nanoplate-like array film grown directly on FTO substrate (Reproduced from Ref. [162] with permission from The Royal Society of Chemistry); (b) WO_3 nanorods, as-prepared and annealed with different temperatures (Adapted from Ref. [182] with permission from The Royal Society of Chemistry).

1.4.1.3. Titanium dioxide

In the last decades, titanium dioxide (TiO_2) has been widely explored in diverse applications such as photocatalysis, solar cells, electronic devices, gas sensors, supercapacitators, paint industry, bio-applications (bone implants, for example) or wastewater treatment [21,52,183-190]. In particular, since Fujishima and Honda reported in 1972 the photo-assisted water splitting using a TiO_2 photoanode [18] that this semiconductor material turned out to be extensively investigated for PEC applications, due to its outstanding photoelectronic properties (such as the easily-modified electronic structure, high charge carriers mobility, or excellent surface chemical properties, especially in the anatase phase) [188,191,192].

TiO_2 shows an excellent chemical stability and charge transport properties, it is a low-cost material, widely available and nontoxic. However, due to its large band gap (E_g = 3.2 eV), only absorbs a small fraction (~4%) of sunlight (in the near-ultraviolet region) and so presents low conversion efficiencies [5,21,39,41]. TiO_2 optoelectronic properties allows an effective direct transfer of light into highly reactive chemical species [188]. In particular, TiO_2 has been considered a preferential semiconductor for application in dye-sensitized solar cells (DSCs). These devices were first introduced by Grätzel *et al.*, using mesoporous TiO_2 photoanodes coated with a dye sensitizer [193]. Since then, TiO_2 received increasing attention for DSCs due to its advantageous and attractive features,

such as small cost, few corrosion problems, high performance indoor and under low light conditions, and a variety of designs and colors [1,52].

Comparatively with PEC cells, DSCs are considered regenerative-type cells: they are semiconductor photovoltaic devices that convert directly solar radiation into electric current, without occurrence of any chemical change [193,194]. In Figure 1.23(a) is represented an illustrative scheme of a DSC with TiO_2 semiconductor; like a PEC cell, it is composed by a working electrode (photoanode) and a counter electrode (commonly a Pt counter electrode), both in contact with an electrolyte solution. However, in DSCs the dye molecules are responsible for the light absorption and charge generation. In the particular case of n-type TiO_2 semiconductor, when the dye absorbs photons with enough energy from sunlight it is promoted to an excited state; the generated electrons are injected into the TiO_2 CB and then transferred through the external circuit. The electrolyte used in DSCs is normally an iodide/triiodide redox pair (I^- /I_3^-) that plays an important role on the dye regeneration (by electron donation from I_3^-), while the formed I^- is regenerated to I_3^- by the electrons injected from the counter-electrode [52,193,194]. The dyes are usually organic molecules, being the ruthenium based materials such as N719, N3, CYC-B11 and C106 the most used [195], giving efficiencies over 11% [52]. They are usually monolayers, covalently bonded to the surface of the oxide semiconductor, helping to enhance the light absorption [194]. DSC devices can be colored according to the dye used, and the possibility to use different colors make these devices truly appellative [Figure 1.23(b)].

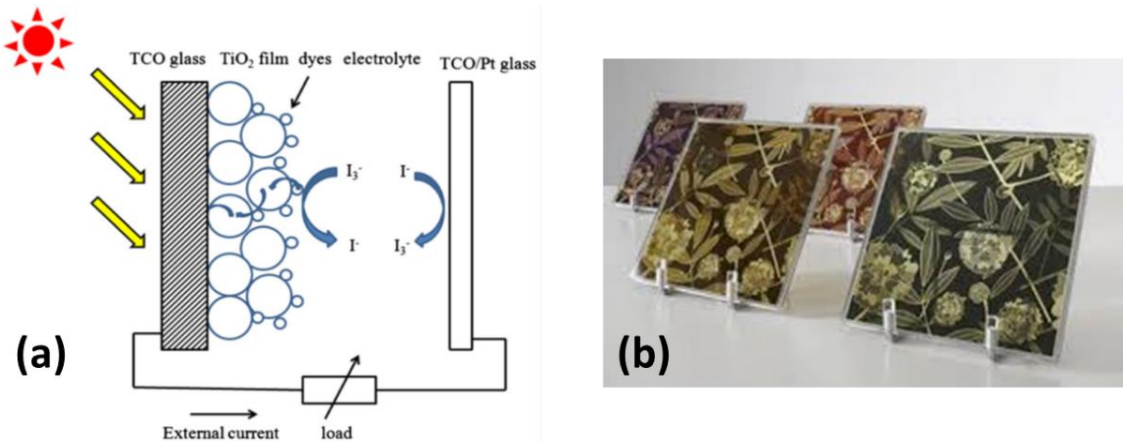

Figure 1.23. (a) Scheme of a typical dye-sensitized solar cell (DSC) device with a TiO_2 photoanode (Reprinted from [194], Copyright © 2012, with permission from Elsevier). (b) Sony prototypes of DSCs, showing appealing variety of colors and designs [196].

1.4.1.3.1. Titanium dioxide physical properties

Crystalline structure. The ionic and electronic properties of TiO_2, that determine its use on specific applications, are mainly depend on the crystal structures in which TiO_2 is converted [188]. TiO_2 crystallizes into three main structures: tetragonal anatase, tetragonal rutile and orthorhombic brookite (Figure 1.24) [188,197]. All consist of TiO_6 octahedra (with each Ti^{4+} at the center, that coordinates with six O^{2-} ions), however differ in the distortion of the octahedron units and in the way of sharing edges and corner [191,198].

Anatase is considered the most stable phase at nanoscale (considering crystallite sizes < 10–30 nm) and the most widely investigated for PEC applications [199]. However, for bulk TiO_2, rutile is considered the most thermodynamic stable phase and has the lowest free energy compared with the other crystalline forms. Rutile is also the typical structure of the native oxide layers formed in oxygen containing environments [188]. Though rutile form is more stable, the anatase phase appears to be more beneficial for electron conduction and more chemically active for DSC and PEC cells [52,188]

The crystalline form of TiO_2 mainly depends on the annealing temperature [52,188]. In general, the TiO_2 nanostructures (for example the as-anodized TiO_2 NTs) are amorphous in structure, being converted in crystalline phase after annealing. For NTs, anatase formation is observed at temperatures > 280 °C, while rutile is formed > 500 °C. Thus, the photocatalytic properties highly increase at temperatures above 300 °C [188].

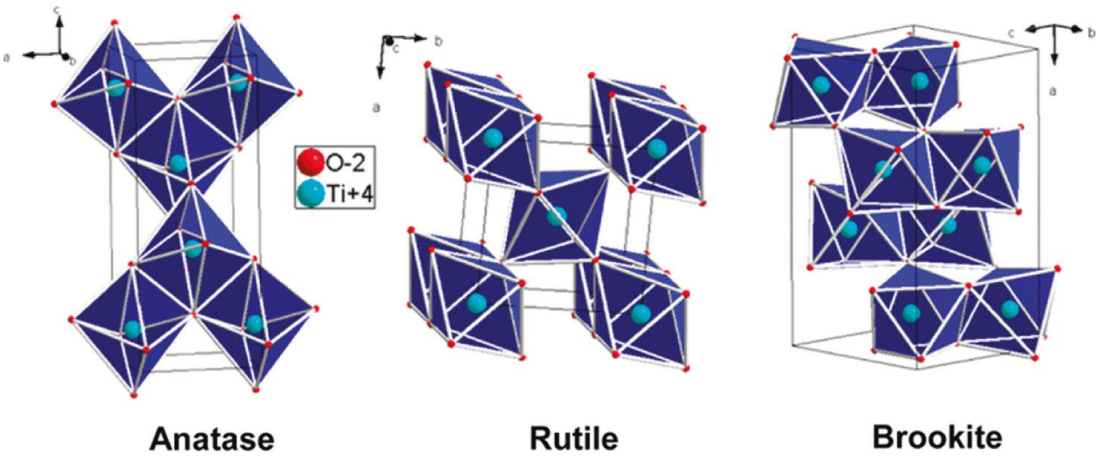

Figure 1.24. (a) Representations of the structural phases of TiO_2: anatase, rutile, and brookite (Reprinted with permission from [197]. Copyright © 2010 American Chemical Society).

Optoelectronic properties. TiO_2 is an n-type semiconductor, its VB is formed by the filled O2p bands and the CB is formed by vacant Tid_{xy} bands. The full O2p states (in particular, non-bonding p_π states) define the VB, while the lowest empty energy levels

Tid_{xy} are representative of the CB edge. This is the general distribution of states for both anatase and rutile. The maximum of the VB and minimum of the CB in the reciprocal space are located in the Γ point of the Brillouin zone (BZ). In rutile the transition of Γ3→ Γ1 constitutes the lowest energy transition (band gap), while in anatase this transition is dipole forbidden. The band gap energy for an indirect electron transition in bulk is 3.0 eV for rutile and 3.2 eV for anatase. It was also mentioned that the Fermi level in anatase is about 0.1 eV higher than that of rutile [200]. Moreover, it has been reported anatase thin films with wider optical absorption gap and higher charge carriers mobility than rutile films [200].

Therefore, only ultraviolet irradiation in solar spectrum can be absorbed by TiO_2 [188,191]. The conductivity of undoped anatase and rutile is more or less similar (in the range of 10^{-4}–10^{-7} $\Omega^{-1}\cdot cm^{-1}$) [188]. Hole diffusion length of TiO_2 was evaluated to be 10-20 nm, while the electron diffusion is in the order of 10 μm, significantly higher than Fe_2O_3 or WO_3 semiconductors [8].

1.4.1.3.2. Titanium dioxide nanotubes

Titanium, like other valve metals such as iron, spontaneously form a protective thin oxide layer at its surface, particularly in oxygen environments, which prevents from corrosion [201,202]. This native oxide layer is often in the nanometer range (for Ti is 1.3-5.4 nm) [201], however, by application of specific experimental conditions, thicker oxide layers can be obtained. This remarkable property of valve metals makes them suitable to be used in several applications with technological impact. One example is the use of TiO_2 nanotubes (NTs) in applications such as DSCs and PEC cells for hydrogen production by water splitting [5,21,52,198,203]. NTs configuration has been also referred for other applications, such as gas sensing or tailored wettability surface applications [193,204]. As already referred for hematite in section 1.4.1.1.2.2, 1D architectures such as NTs allow an efficient and fast charge transportation, reducing the probability of electron-hole recombination.

One of the most common methods to obtain TiO_2 tubular nanostructures is by electrochemical anodization of Ti foils and/or thin films. Understanding the microscopic mechanisms behind the formation and growth of anodic TiO_2 is fundamental to control anodization conditions and to obtain highly-ordered and optimized 1D structures [1,127].

The fabrication of self-assembled TiO_2 NTs was introduced by Zwilling *et al.* in 1999 [205]. Increasing attention has been since paid in the investigation of the corresponding fabrication process and growth mechanisms. However, this first generation of NTs was

produced in aqueous hydrofluoric acid-based electrolytes which has a high TiO_2 chemical dissolution rate. The NTs growth was therefore limited to lengths of up to 500 nm [206,207]. Subsequently, in the second generation, the NTs length was increased (up to 4.4 µm) by controlling the anodization electrolyte pH and thus reducing the chemical dissolution effect of TiO_2 during anodization [208,209].

To suppress local concentration fluctuations and pH bursts during anodization, viscous organic electrolytes were introduced in the third generation of NTs, leading to smoother NTs with several micrometers or even millimetres in length [118,203,210,211]. It is the case of the works reported by Grimes' research group, in which NTs up to 220 µm with very thin walls [Figure 1.25(a)] showed a remarkable water photoconversion efficiency of 16.25% [~23 $mA \cdot cm^2$ at 0.5 V *vs.* Ag/AgCl; Figure 1.25(b)] [118,191,203].

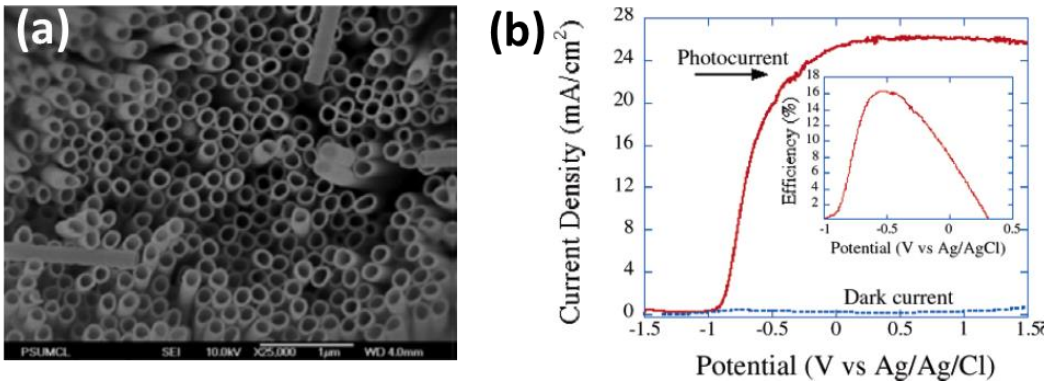

Figure 1.25. (a) SEM image of TiO_2 nanotubes grown at 40 V in DMSO containing 2% HF and (b) Photocurrent density of 45 µm long nanotubes and corresponding photoconversion, with the maximum value of 16.25% (Adapted with permission from [118]. Copyright © 2006 American Chemical Society).

The mechanism of NTs growth by anodization is quite similar to the one already explained for hematite NTs formation, consisting in three simultaneous processes: (1) electrochemical oxidation of Ti metal to form the oxide TiO_2, (2) field-assisted dissolution of formed TiO_2, and (3) chemical dissolution of TiO_2 due to etching, mainly on NTs tops.

At IFIMUP research group, there is a strong know-how in the preparation and characterization of advanced materials and nanostructures, particularly alumina and titania nanoporous templates and nanotubes [1,126-128,212-214]. Titanium dioxide properties have been thoroughly studied, in particular 1D nanotubular structures.

Characteristics such as foil pre-treatment and roughness have shown to highly influence the NTs morphology, especially the organization. This parameter is crucial for solar harvesting applications. Pre-treatments such as chemical etching, mechanical polishing and electropolishing lead to a decrease of Ti surface roughness, enhanced the

resulting TiO_2 NTs length and significantly improved the template organization quality [through large areas with hexagonal-close packed arrays (HCPA) of NTs], due to the optimized surface topography. Larger domains of highly ordered NTs, with 6.6 and 4.3 μm^2 were obtained respectively for electropolishing and mechanical polishing Ti pre-treatments [213,214].

NTs morphology, geometrical features [pore diameter D_p, oxide barrier layer thickness δ_b, wall thickness W, interpore distance D_{int} or outer diameter D_{outer}, as represented in Figure 1.26(a) and (b)] or porosity, have been widely explored parameters [1,127,128]. In particular, anodization for long time at a constant voltage showed a cyclic porosity tendency [1]. It was shown to be influenced by the electrolyte acidification over prolonged anodization time, causing cyclic local variations of pH, leading to several re-balances of the oxidation–dissolution rates at the bottom of NTs, ultimately affecting the NTs growth rate and porosity. This unbalance between oxidation–dissolution reactions typical of Ti anodization is attributed to the electrolyte dynamics, i.e. to the slow ionic diffusion (H^+ moving to NTs' tops and F^- to NTs' bottoms) caused by the high viscosity of the electrolyte. NTs self-ordered regimes, with optimum porosity values ~5.3%, were obtained for NTs with 17-21.5 h anodization. The cyclical porosity self-ordered regime is repeated at the 35–40 h and 60–72 h intervals [1].

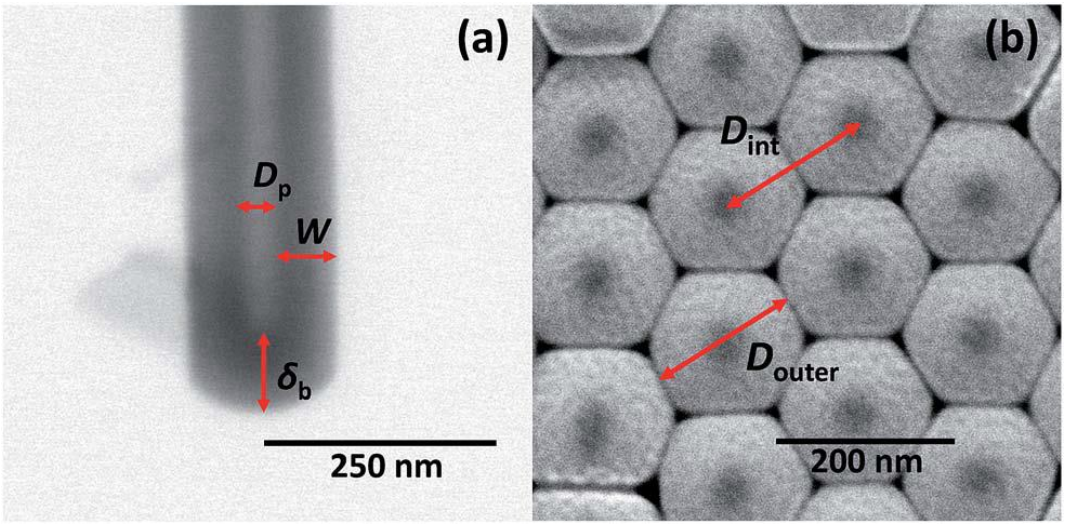

Figure 1.26. (a) STEM and (b) SEM images of TiO_2 NTs, illustrating the geometrical parameters: pore diameter (D_p), oxide barrier layer (δ_b), interpore distance (D_{int}), outer diameter (D_{outer}) ([1] - Reproduced by permission of The Royal Society of Chemistry).

In other work, an oxide barrier layer growth model, with different anodization voltage and time, was conceived, where anodization time showed to be a crucial parameter to take into account [126].

However, some issues were still open, namely regarding the electrolyte re-utilization, since it is important in practical terms to assess its viability after consecutive uses and influence on the morphological aspects of resulting NTs.

In this thesis work, we explored the re-utilization of the electrolyte usage in the anodization of TiO_2, that can have a practical interest for industrial applications.

Chapter 2

Experimental Techniques

Chapter 2

Experimental Techniques

In this chapter, a brief description of the synthesis methods used to produce the studied semiconductor materials is presented, followed by an overview of the experimental techniques used to characterize the resulting materials. First, we introduce to hydrothermal, anodization and thin films deposition techniques used to produce Fe_2O_3, WO_3 and TiO_2 photoanodes. In a second part, the techniques used for their morphological, structural, optical and photoelectrochemical characterization are generally reviewed.

2.1. Materials, Reagents and Samples Preparation

2.1.1. Material and Reagents

All the commercial materials and chemical reagents used during the experimental work are described as follows. Their purity, chemical formula and the supplier company are referred.

Reagents

Substrate Cleaning:

C_2H_6O, Ethanol (JMGS, 99% Vol.);

Detergent (Derquim, 5-10%);

KOH, Potassium Hydroxide Pellets (Panreac, 85%);

CH_3COCH_3, Acetone (Labsolve, 99.7% Vol.);

H_2O_2, Hydrogen peroxide solution (Sigma Aldrich, > 30%).

Hydrothermal method:

$FeCl_3.6H_2O$, Iron (III) chloride hexahydrate (Acros Organics, 99+%);

$NaNO_3$, Sodium Nitrate BioXtra (Sigma Aldrich, ≥99%);

HCl, Hydrochloric acid (Fisher Scientific, 37%);

$Ti[OCH(CH_3)_2]_4$, Ti isopropoxide (Aldrich);

$Na_2WO_4.2H_2O$, Sodium tungstate dihydrate (Acros Organics, 99+%);

$(NH_4)_2C_2O_4$, Ammonium oxalate (Chem-Lab);

K_2HPO_4, Di-potassium Hydrogen Phosphate (Merck, ≥99.0%);

$(NH_4)_2SO_4$, Ammonium Sulfate (Sigma Aldrich, ≥99.0%);

Na_2SO_4, Sodium sulfate anhydrous (Acros organics);

H_2SO_4, Sulfuric acid (Sigma Aldrich, 95-97%);

$(C_2H_2F_2)n$, Poly(vinylidene fluoride) (Alfa Aesar).

Electrolyte for PEC measurements:

Na_2SO_4, Sodium sulfate anhydrous (Acros organics);

NaOH, Sodium Hydroxide [Chem-Lab, 1 M (1 mol/L)].

Electrolyte anodization (Ti, Fe):

NH_4F, Ammonium Fluoride (Alfa Aesar, 98% min);

$C_2H_6O_2$, Ethylene glycol (Acros Organic, 99.81%);

Metallic Foils:

High purity Titanium foil (99.99+%), 0.127 mm thick from Alfa Aesar;

High purity Iron foil (99.99%), 0.25 mm thick from Alfa Aesar.

Substrates

- FTO - Fluorine-doped tin oxide coated glass substrates (Solaronix, Switzerland, 7 $\Omega \cdot square^{-1}$, 2.2 mm thick);
- FTO - Fluorine-doped tin oxide coated glass substrates (Solaronix, Switzerland, 10 $\Omega \cdot square^{-1}$, 1.0 mm thick).

2.1.2. Samples preparation

FTO substrates were cleaned, based on a sequential cleaning method reported by Francisco *et al.* [215]. First the FTO pieces, 1.2 x 2.5 cm^2 were rubbed with soapy water. Then, they were sequentially placed in ultrasonic bath with:

(a) Soapy water, for 10 min;
(b) Ethanol 95%, for 10 min;
(c) Soapy water, for 10 min;
(d) Ethanol 95%, for 10 min;
(e) Solution of 2M KOH in ethanol 70%, for 20 min;

(f) Deionized water, for 10 min.

At the end, the substrates were dried with a nitrogen stream. To allow the electrical contact in the photoelectrochemical measurements, a small area of the FTO (~1.2 x 0.75 cm^2) surface was covered with Kapton® tape.

The metal foils for anodization were cut into pieces with the desired sample dimensions: Ti with 1 x 1 cm^2, and Fe with 1.5 x 1.5 cm^2 and 1.2 x 2.5 cm^2 (for photocurrent-voltage measurements). Prior to the anodization, different cleaning methods were applied to each metal:

(a) Ti were ultrasonically cleaned with ethanol and deionized water for 10 minutes (each step);

(b) Fe pieces were ultrasonically cleaned with acetone for 10 min.

After anodization, Ti anodized samples were sequentially rinsed with ethanol, deionized water and dried with a nitrogen stream, while Fe anodized samples were rinsed with ethanol, and after few minutes with H_2O_2 to remove a residual layer covering the top of the NTs.

2.2. Synthesis methods

In this section, it is presented a detailed description of the experimental procedures used during this PhD work.

All the experiments were performed under safety conditions. Previously to experimental procedures, the safety data sheets of chemical reagents were consulted, in order to know all the risks associated with its use and to be aware of individual safety equipment to use, such as googles, lab coat, gloves or masks. A mask FFP3 (maximum protection) was used to weight all the powder reagents, and gas mask respirator with double filter A1B1E1K1P3 for the case of liquids/solvents. All chemical procedures with associated risks were manipulated inside a hotte bench.

2.2.1. Hydrothermal method

The hydrothermal method allows the fabrication of several nanostructures, either in solution or nucleated on the surface of a substrate such as FTO. The reaction process involves the soluble precursor metal salts in an aqueous and/or organic solution in an autoclave under conditions of high temperature and pressure. The growth of single crystals involves the sum of macro- and microprocesses occurring between the interface boundary of the solution and the crystal. Parameters such as the chemical composition,

concentration of the solution, temperature, pressure and hydro-dynamic conditions are determinant to the regime and rate of dissolution of the chemical species in solution, mass transport and formation of crystal phases [112]. The metallic precursor in solution is placed in the lower part of the autoclave. Upon heating, a temperature gradient is created inside the autoclave. The metal solute dissolves in the hotter zone and the saturated aqueous solution is transported by convection to the upper cooler zone where it is deposited on seed crystal. Supersaturation is achieved by reducing the temperature in the crystal growth zone, which allows the crystallization to occur [216]. The crystal nucleation starts on the substrate surface, with or without seeds, and subsequent oriented growth leads to the crystal's alignment on the substrate. In general, crystals tend to grow on its seed layer through an spontaneous Ostwald ripening process, thermodynamically more favourable and energetically more stable [38].

Generally, an acidic solution is used (low pH, in the order of 1.5) to avoid the precipitation of species in solution (Fe, W or other) during the process, allowing their availability for the nucleation. In particular case of the iron oxyhydroxide phase (*β*-FeOOH), the use of low pH chemical solution with a high ionic strength promoted its formation by lowering the interfacial tension between the solution and the crystals being formed [91,112].

In the hydrothermal process, it is required a reaction recipient, the so-called stainless-steel autoclave. It is composed by an inner recipient, usually an inert material such as Teflon is used, and an outer resistant structure made of stainless-steel material, to allow the conditions of high pressure inside the autoclave. Due to safety issues using this equipment, and due to the conditions of pressure and temperature, no more than ¾ of capacity can be filled.

Figure 2.1. Teflon stainless-steel autoclave for hydrothermal synthesis.

2.2.2. Electrochemical Anodization

The electrochemical anodization process allows the growth of self-organized nanoporous or nanotubular structures of iron or titanium oxides.

A home-made setup was used to obtain the Fe_2O_3 and TiO_2 NTs. The anodization cell consists in a Teflon container where the Fe (or Ti) metallic foils (the anode) are placed, in contact with a copper plate. The anodization area has a circular shape with a diameter of 0.5 cm^2 for Ti and 1 cm^2 for Fe. Then the cell is filled with an electrolyte solution: an ethylene glycol solution containing NH_4F and H_2O, with variable concentrations depending on whether Ti or Fe is being anodized.

An inert Pt mesh (counter electrode) is inserted at the top of the cell, working as the cathode. A typical electrochemical cell used in anodization is shown in Figure 2.2. During the anodization, the temperature of the electrolyte solution was maintained constant and stirred at 75 rpm. Anodization were conducted at room temperature in the case of Ti, and at 45 ºC in the case of Fe.

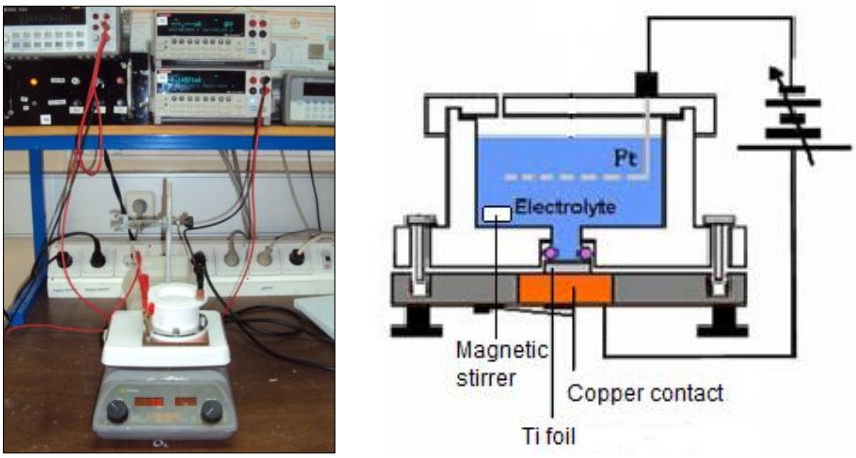

Figure 2.2. Anodization set-up implemented at IFIMUP-IN (left) and schematic figure (right).

During anodization, a constant potential was applied and the time evolution of the current density [$j(t)$ curves] was recorded and monitored using a DC power supply Keithley 2004 Sourcemeter, remotely controlled by a home-developed LabView application [69].

2.2.3. Thin films deposition

In order to produce thin films directly on the FTO transparent substrate, with interest for PEC´s applications, in this work several Physical Vapor Deposition (PVD) techniques were used. PVD techniques uses physical means like evaporation or ion bombardment to deposit atomistically thin films on the surface of a substrate, by driving the source atoms (solid or liquid) into gaseous phase, under high vacuum environment [217,218].

2.2.3.1. Electron-beam evaporation

The electron-beam (*e*-beam) evaporation is a PVD method that consists on the evaporation of an anode target material (in this case Fe) which is bombarded with an electron beam (originated by a charged tungsten filament) in a high vacuum chamber, by thermionic emission [217]. High vacuum allows the evaporated particles to travel directly to the deposition substrate without colliding with the background gas (with a long mean free path), and thus with high deposition rates and low contamination. The high vacuum is provided by the combination of rotative and diffusion pumps. By applying a potential difference and by the existence of a magnetic field, the beam will be accelerated and directed to the target containing the Fe to evaporate. The pressure inside the chamber must be below the point where the mean free path is longer than the distance between the evaporation source and the substrate. The electron beam causes atoms from the target to transform into the gaseous phase. The atoms will then cross the vacuum chamber towards the substrate. These Fe atoms then precipitate into solid form, coating the substrates in the vacuum chamber with a Fe thin layer [217].

The Fe thin films were deposited using an e-beam evaporation system (Edwards Auto 306) at CEMUP Clean Room unit (MNTEC, University of Porto), Figure 2.3, deposited on previous cleaned FTO substrates (2.5 x 1 cm^2). The vacuum chamber reaches a base pressure of ~ 10^{-6} mbar and a working pressure of ~1 – 9.0 x 10^{-5} mbar. The Fe films were deposited under a deposition rate of ~8 $nm \cdot min^{-1}$. After the deposition the as-prepared Fe thin films thickness were calibrated in a profilometer, in the range of ~500-700 nm.

Figure 2.3. Electron-beam evaporation system used for Fe thin films deposition.

2.2.3.2. Ion beam Deposition

Ion beam deposition (IBD) is a physical process for thin film deposition, where highly homogeneous thin films can be produced, maintaining its stoichiometry.

Generally, an IBD system consist in an ion gun source, that generates ions with energies of a few keV, and an evaporation source. A tungsten filament (cathode) is used to produce an accelerated ion beam (in the presence of Ar inert gas) towards a target material. The removed ions from the target are then deposited on the substrate surface.

A commercial IBD system Commonwealth Scientific Corporation unit (at CEMUP-MNTEC cleanroom unit) was used for Fe thin film deposition, Figure 2.4. IBD system includes two ion beam guns (3-cm diameter Kaufman DC ion sources, one destined for film deposition and other for assisted deposition or ion-milling), a substrate holder and a target assembly. Typically, several different targets are placed on a rotating target holder; the target of the desired material to be deposited is then aligned with the ion beam. The substrate holder can rotate up to 30 rpm to enhance the deposition uniformity. The vacuum chamber is sustained by turbo molecular pumps, backed up by rotary mechanical pumps. The chamber is further pumped with a cryogenic pump (3.8×10^{-8} Torr base pressure) which is backed by an oil free mechanical pump [69,219].

For Ar ionization, the W filament is heated releasing thermionic electrons. The cathode current, typically 5.0-7.0 A, is set and measured at the terminals of the W filament. The magnets placed around the anode confine the electron paths thus enhancing ionization rate. After the plasma is formed, it is extracted only when a voltage is applied to Mo grids, placed at the exit of the ion sources. The two Mo grids are used

in a focused configuration (with the focal point at the target). The inner grid prevents the erosion of the outer (acceleration) grid, where the voltage for beam extraction is applied. Both ion sources are also equipped with neutralizer filaments for deposition/milling [69].

IBD deposition was performed using the following conditions: a base pressure of 1.6x 10^{-7} Torr, a work pressure of 1.4 x 10^{-4} Torr, with a 5.65 sccm Ar flow. The conditions of the current and voltage, namely of the cathode, discharge, beam and accelerator are displayed in Table 2.1. With these conditions a deposition rate of 0.54 Å.s^{-1} for Fe was obtained. Thin films in the range of ~150 nanometers were deposited on clean FTO substrates.

Table 2.1. Conditions used during ion beam deposition.

Conditions	Cathode	Discharge	Beam	Accelerator
Current (mA)	6.9	2	6	0.8
Voltage (V)	5.5	38.2	994	148.5

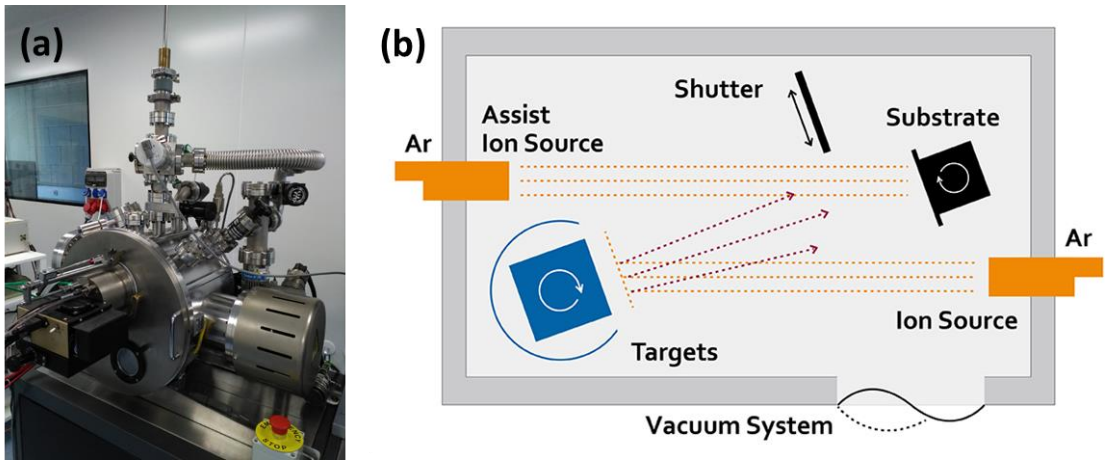

Figure 2.4. (a) Ion beam deposition (IBD) system at clean-room CEMUP and (b) respective schematic representation (Extracted from [220]).

2.2.3.3. Pulsed Laser Deposition

Pulse laser deposition (PLD) technique comprises a high-power laser pulse, in vacuum atmosphere, with energy typically of 10^8 W·cm^{-2}, that causes ablation from a target due to photonic interaction [218]. The laser, situated outside the vacuum deposition chamber, is focused onto the target surface by means of external lenses [217]. Each laser pulse vaporizes or ablates a small amount of the metallic target, forming a plasma plume which rapidly expands away from the target, reaching a typical

propagation velocity of 10^4 $m \cdot s^{-1}$. The highly direction plume material recondenses on the substrate placed on the opposite position, forming the thin film (Figure 2.5). High-quality samples with excellent precision are obtained by this deposition method. The introduction of gases such as O_2 or N_2 into the vacuum chamber can also help to maintain film stoichiometry or to promote surface reaction [217,218,221].

Within a collaboration with the Physics Center of the University of Minho, a Nd:Yag PLD system was used. Iron pieces Alfa Aesar, irregularly shaped, 12 mm (0.5 in) down, 99.97+% (metal basis), were used as the target material. The conditions for PLD deposition are described in Table 2.2.

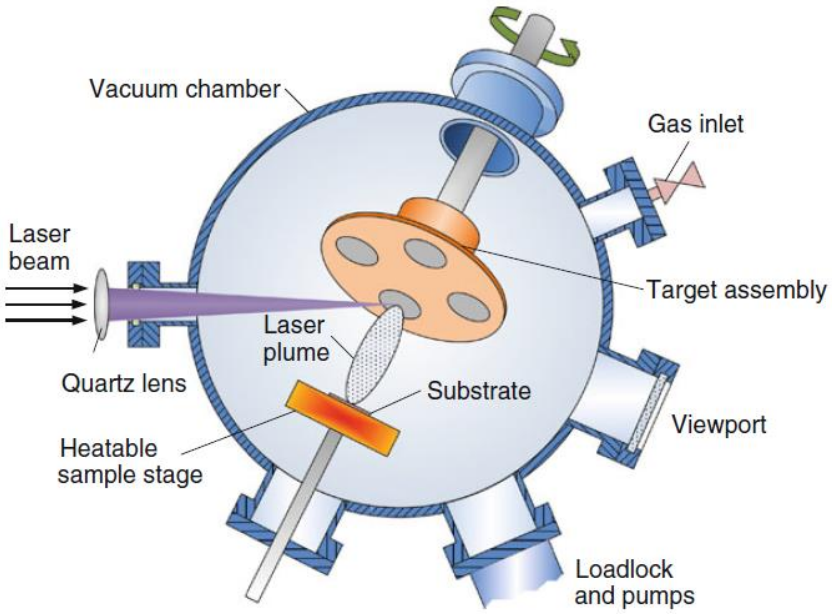

Figure 2.5. Schematic representation of pulsed laser deposition system (Reprinted by permission from: Springer Nature [218], Copyright © 2015 Springer-Verlag Berlin Heidelberg).

Table 2.2. Conditions used during pulsed laser deposition (PLD) of Fe on FTO substrates.

Target	Pressure (Torr)	Frequency (Hz)	Atmosphere	Distance sample-target (cm)	Laser energy (mJ)	Deposition time (h)
Iron	10^{-8}	10	No	2.5	250	1 + 1
Iron	10^{-8}	10	No	1	400	1

2.3. Characterization Techniques

2.3.1. Morphological Characterization

2.3.1.1. Scanning Electron Microscopy

Scanning electron microscopy (SEM) is one of the most versatile and powerful techniques for the investigation of nanostructures morphology, also gives information about its chemical composition [222]. SEM allows the observation and characterization on nanometer (nm) to micrometer (µm) length scale, a resolution ranging from few millimeters to 5 nm, and presents a magnification in the range of 10 – 500.000x [223]. The history of the Scanning Electron Microscopy (SEM) brings us back to 1942 and to Dr. Zworykin, who recognized that the emission of secondary electrons could provide a topographic contrast by biasing the collector positively relative to the specimen in observation [223,224].

The basic principle of the electronic microscopy is the production of an electron beam with controlled kinetic energy, under high vacuum, using electrostatic and magnetic lenses for the electron beam setting and focusing [223]. It includes several modes, such as Scanning Electron Microscopy (SEM), Scanning Transmission Electron Microscopy (STEM), Transmission Electron Microscopy (TEM) or Energy Dispersive X-ray Spectroscopy (EDS), depending on the characteristics of the lighting system (the incident electron beam generation and guidance control), the detecting mode of radiation emitted from the sample and the construction of the image.

The basic components of a SEM equipment consist in an electron column and control console, as represented in Figure 2.6(a). The electron column consists in an electron gun that emits the beam of accelerated electrons, with energies in the range 0.1-40 keV, usually with pressure around 10^{-4} Pa (~ 10^{-6} Torr) [223]. Since the electron beam can be controlled by magnetic field, it is focused to a small diameter through a series of magnetic focusing lenses, in order to demagnify it and reduce aberrations. These lenses have defining apertures which limits the divergence of the electron beam and determine the path of the electrons through the column tube. In the lower part of the column there is the sample chamber, with two type of detectors: secondary and backscattered. The electron beam is raster scanned across the surface of the sample and the detectors create an image by mapping the detected signals with the beam position [222,223,225].

In SEM, a high-energy electron beam is focused into a fine probe that interacts with a small sample area, creating various signals that can be detected, depending on their energies and the range of depth that they are scattered from the sample. The type of signals generated, the so-called interaction volume, includes secondary electrons (SE),

backscattered electrons (BSE), characteristic x-rays (EDX), and other photons of various energies, Figure 2.6(b).

The SE are low-energy electrons (less than 50 eV) resultant from inelastic collisions of the primary electron-beam with the atoms of the sample surface (few nanometers from the surface), as represented in Figure 2.6 (b). The emission of SE, which depends on the angle at which the probe beam hits the surface, causes a topography contrast effect. Therefore, these type of electrons can be used to observe the topography of the sample, producing high resolution 2D imaging [225,226].

In turn, BSE are high-energy electrons, resulting from the elastic collision of the primary-beam with the sample atoms, at a deeper level, Figure 2.6(b). The number of BSE will produce a contrast based on atomic number (Z-contrast) and density, since that elements with high atomic number emit electrons more strongly than elements with low atomic number, originating a brighter image. This contrast is then related with the differences in the local chemical composition of the samples [223,225].

Besides electrons emission, the inelastic interaction of the electron beam with the sample just below the surface may generate X-ray photons, Figure 2.6(b). The decay of an excited inner shell electron that was ejected from the atoms beneath the sample due to collision with primary beam, produces photon emission with energies between 0.1 and 20 keV that are characteristic of the sample elements and can be detected by an energy dispersive X-ray detector. The use of characteristic X-ray peaks to provide chemical information is widely used with the SEM technique [222,223,225].

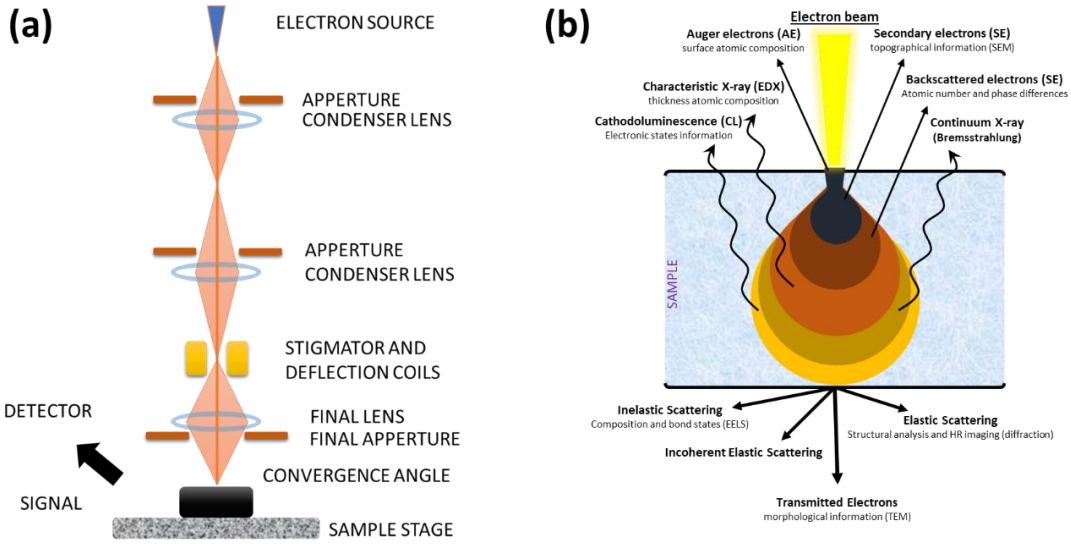

Figure 2.6. (a) Scheme of the scanning electron microscope (SEM) components (Adapted from [225], Copyright © 1992 Butterworth-Heinemann, with permission from Elsevier) and (b) cross-section of the different kinds of signals generated by the electron-beam interaction with the sample (Adapted from [227]).

In this work, the morphological characterization of all nanostructures (surface and cross-section views) was performed using a Phillips-FEI/Quanta 400 FEG high resolution scanning electron microscope (SEM), at the Materials Center from University of Porto (CEMUP), Figure 2.7.

In general, the samples did not require any special preparation for SEM, they were simply placed in carbon tape (in contact with the FTO conductive part, in order to avoid charging effects) and fixed to a sample holder for top-view. For cross-sectional view, a small portion of the FTO with the nanostructures deposited is broken with pliers.

SEM images of top and cross-section views were taken from random areas of the samples. Using *ImageJ* program [228] we measured the geometrical features of the produced nanostructures, such as nanowires or nanotubes diameter (*D*) and thickness (*L*), walls thickness (*W*), or nanoplates width and height, taken respectively from the SEM top and cross-section images. For each sample, about 20 measurements were taken per SEM image, and at least two images with higher magnification were obtained per sample.

Figure 2.7. Scanning Electron Microscope, model Quanta 400FEG ESEM/EDAX Genesis X4M, at the CEMUP center from University of Porto (Extracted from [229]).

2.3.1.1.1. Energy Dispersive X-Ray Spectroscopy

Energy Dispersive X-ray Spectroscopy (EDS or EDX) is a technique usually attached to conventional SEM system. It is used to obtain a chemical analysis, i.e., elemental composition of the sample. The electron beam interacts with the sample atoms through the ionization of an inner shell electron, leaving a hole. The resultant vacancy is filled by an outer electron, which releases its energy with the emission of Auger electrons or X-

rays. As released energy is characteristic of each atomic transition, it is possible to identify the elemental composition of the material [223,230].

Therefore, EDS can be used to provide qualitative and/or semi-quantitative information about the elements present at different points of the samples, and it is also possible to map the concentration of an element as a function of the position. However due to the relatively low lateral resolution that comes from the fact that X-rays are generated deep within a comparatively large volume interaction, the quantitative analysis in nanostructured materials is limited [223,231].

2.3.2. Structural Characterization

2.3.2.1. X-Ray Diffraction

The X-ray diffraction (XRD) allows the identification and structural characterization of crystalline materials. Each crystalline solid produces a characteristic diffraction pattern which can be used for phase identification. From this technique, other important information such as crystallite size and microstrain can be also determined [232].

When X-rays beam interact with the electrons from the atoms of a sample results in scattering of the radiation. The wavelength of the X-ray radiation has values in the order of the lattice parameters of crystalline materials. Thus, if distance between the atoms has the same magnitude as the wavelength of the X-rays, interference of the scattered waves in these materials will occur and form a diffraction pattern with constructive or destructive interferences. When the scattered waves interfere in constructive way, the X-rays are scattered at characteristic angles based on the spaces between the atomic planes. Generally, the crystals have several sets of planes passing through their atoms, each of them with a specific interplanar distance *d* that originate a characteristic angle of diffracted X-rays, defining their crystalline structure. This leads to Bragg's law [233]:

$$n\lambda = 2d_{hkl}sin\theta \tag{2.1}$$

that gives the relation between wavelength (λ), plane spacing (d_{hkl}) and θ the diffraction angle formed by the propagating vectors of the incident and scattered waves (represented in Figure 2.8.)

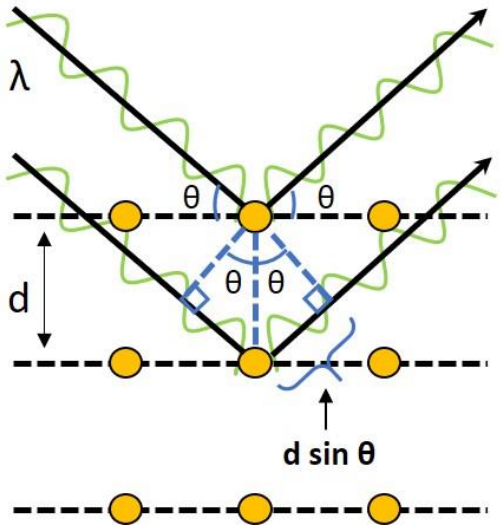

Figure 2.8. Schematic representation of the Bragg's relation (Adapted from [234]).

XRD technique was used to evaluate the crystallinity of the produced samples. The crystallographic analysis was performed using a SmartLab Rigaku® diffractometer, with a copper Cu Kα radiation λ = 1.540593 Å, and anode x-ray tube operated at 45 kV and 200 mA, Figure 2.9.

Two configurations, Bragg–Brentano $\theta/2\theta$ (for powder samples) and parallel-beam 2θ with grazing incidence omega angle (for semiconductor materials deposited on FTO substrate) were used.

Here, a Le Bail refinement analysis was considered to provide the necessary information from the XRD diffractograms and characterize the crystallographic phases of the photoanodes.

From peak broadening analysis, crystallite size (D_{XRD}) and microstrain (ε) were estimated, using the Williamson-Hall method [235]:

$$w\cos\theta = \frac{k\lambda}{D_{XRD}} + 4\varepsilon\sin\theta \qquad (2.2)$$

with w the full width at half-maximum (FWHM) of Bragg peaks, θ the diffraction angle, k the Scherrer constant (0.94) and λ the incident X-ray wavelength (1.540593 Å). From the $w{\cdot}\cos(\theta)$ *vs.* $4{\cdot}\sin(\theta)$ plots, D_{XRD} and ε were estimated from the intercept and slope, respectively.

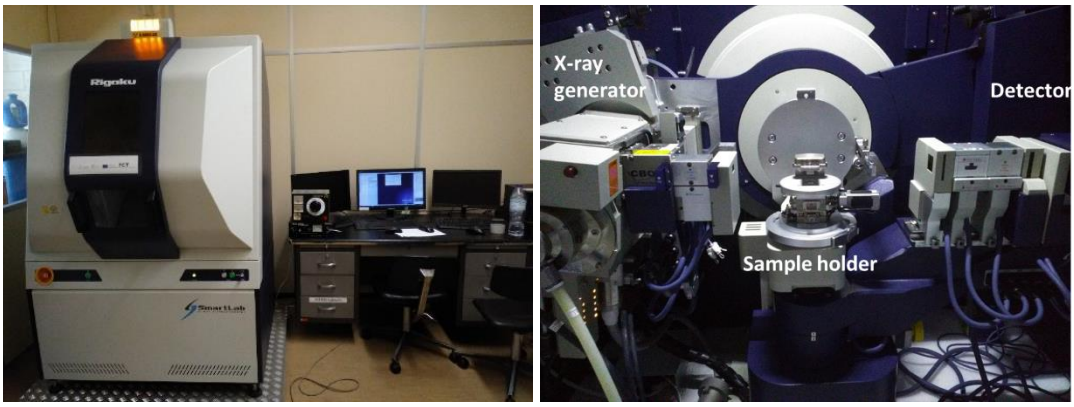

Figure 2.9. Rigaku® SmartLab XRD (at IFIMUP). On the right, the main components on the inside of the equipment (X-ray tube, a sample holder and an X-ray detector).

X-ray diffraction (XRD) analysis, in particular grazing angle X-ray diffraction (GAXRD) [106,134,137], was performed testing different omega (ω) angles, in order to remove the SnO_2 signal from the FTO substrate, usually the most intense one in literature [33,56,57,64,114,115], Figure 2.10.

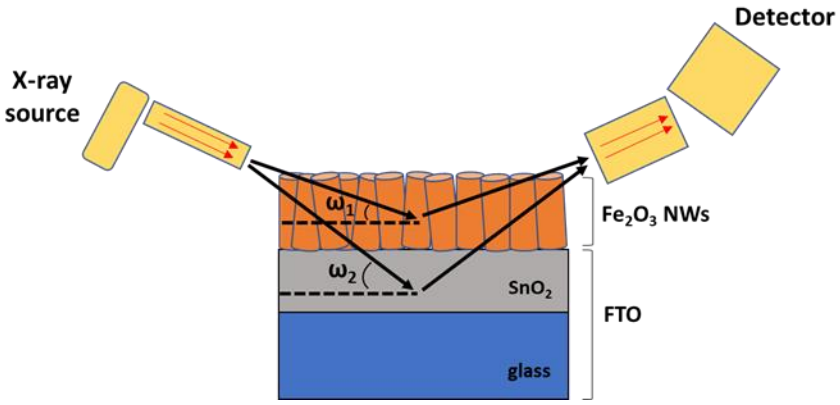

Figure 2.10. Schematic representation of the Grazing Angle X-Ray Diffraction (GAXRD) measurements of hematite NWs samples.

Here, it was performed an intensive work and a deep study in order to achieve the best measurement conditions and isolate the peaks of our samples from FTO signal. Taking the example of hematite nanowires (described in Chapter 3) with small thickness (~250-300 nm), in Figure 2.11 we can see that as the ω angle decreases, the peak signal from the FTO substrate also decreases, which means that we are getting more signal from the hematite nanostructure [peak (110) is in this case is the preferential orientation, the most intense peak for hematite nanowires] and less from the FTO peak (200) (the most intense for FTO). To notice that these data pre-acquisition was performed with a fast scan-speed, just in order to find the right angle (however the complete

measurements for all the samples were performed with a long acquisition time, at 0.008 deg·s^{-1}).

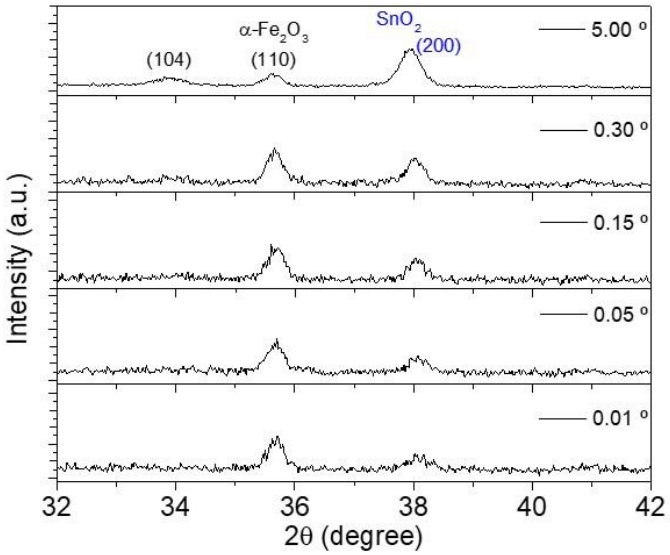

Figure 2.11. XRD diffractograms of α-Fe_2O_3 samples annealed at 800 ºC with different ω angle.

2.3.2.2. Rutherford Backscattering Spectrometry

Rutherford backscattering spectrometry (RBS) is a very sensitive structural analysis technique that can be used to determine the composition and the distribution in depth of chemical elements [236-239]. In addition, knowing the density of the material and how the material prevents the path of the ion beam, the film thickness is obtained [240].

RBS consists on the bombardment of a sample with a high energy ion beam (1-3 MeV) positively charged ($^4He^+$), the ions backscattered in the near surface region of the sample are collected and counted, and their energy measured, usually with solid state Si surface barrier detectors [236,240]. The principle is based on the Rutherford scattering and in Geiger and Marsden experiments [236]. The backscattering principle is illustrated in Figure 2.12.

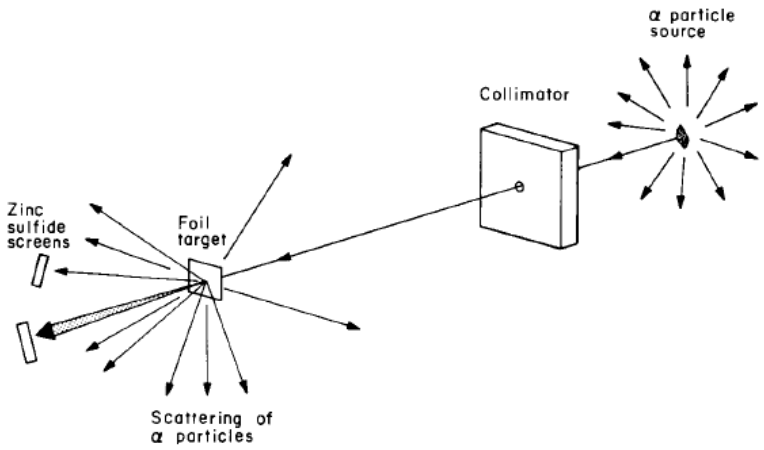

Figure 2.12. Conceptual layout of a scattering experiment: a beam of alpha particles ($^4He^+$) impinges perpendicularly on a target, if sample target is thin, the beam is transmitted through the thin target with only very little loss and only slightly altered direction of particles. But if the sample is thick, only the particles scattered backward by angles of more than 90° from the incident direction can be detected (Reprinted from [236], Copyright © 1978 ACADEMIC PRESS, INC., with permission from Elsevier).

The RBS measurements of hematite nanowires, and respective simulations were performed by Dr. Sérgio Magalhães, within a collaboration between IFIMUP and CTN-IST, Lisbon.

RBS system consists in a Van de Graaff accelerator, that generates a beam of 2 MeV $^4He^+$. This beam is directed to the respective RBS line, achieved by adjusting the intensity of the magnetic field, through a deflecting magnet, which selects the energy and mass of the ion beam. The beam is stabilized through the current measurements with slits. Before entering the chamber, the beam is collimated. Low pressure (2×10^{-6} mbar) is maintained in the beam line during the measurements, in order to minimize the spread of the beam due to collision with air molecules [240,241].

In this work, RBS analysis was performed to determine the in-depth profile distribution of the atomic elements in hematite nanowires, using a Van de Graaff accelerator with 2.0 MeV $^4He^+$ (α) particles. The backscattered particles were collected at +165 °, -140 ° and -165 ° using silicon p-i-n diode detectors, and random spectra were taken by tilting samples at three different angles (θ = 5, 20, 30 °) for more accurate data analysis. Simulations and fitting were performed using the NDF code [237,242], parameters such as roughness and volume fraction (voids) were considered.

2.3.2.3. X-ray Absorption Fine Structure (XAFS)

X-ray Absorption Fine Spectroscopy (XAFS) is a powerful technique for the study of the atomic-level structure, electronic and magnetic properties of matter, and has innumerous applications, such as in atomic and molecular physics, chemistry, biology, environmental or geosciences.

XAFS refers to of how x-rays are absorbed by an atom, at energies near and above the core-level binding energies of that atom [243,244].

In XAFS process, an x-ray photon (with energies ranging from 500 eV - 500 keV, and wavelengths from ~ 25 - 0.25 Å) is absorbed by an electron in a strongly bound quantum core level (such as the 1s or 2p level) of an atom, in Figure 2.13(a). If the incident energy is higher than the binding energy, the electron may be removed from its quantum level. In this case, the x-ray energy is absorbed and the energy in excess is given to a photo-electron that is ejected from the atom.

According to Beer's Law, the absorption coefficient, μ, gives the probability that X-rays will be absorbed:

$$I = I_0 e^{-\mu t} \tag{2.3}$$

where I_0 is the x-ray intensity incident on a sample, t is the sample thickness, and I is the intensity transmitted through the sample, Figure 2.13(b).

When incident X-ray energy is equal to that of the binding energy, there is a sharp rise in absorption: an absorption edge corresponding to the promotion of this core level to the continuum. Thus, XAFS spectra gives the relation between the intensity of μ as a function of energy, near and at energies just above the binding energy of a known core level of a known atomic species [243-245]. A typical XAFS spectrum (of FeO) is shown in Figure 2.13(c).

In the near edge region (from just below the edge to 50 eV above the threshold) it is often referred to as X-ray Absorption Near Edge Structure (XANES) which probes densities of states and local symmetry, to be distinguished from Extended X-ray Absorption Fine Structure (EXAFS) in the extended region (50 eV up to as much as 1000 eV above the threshold) which contains information about the interatomic distance and the local dynamics of the system.

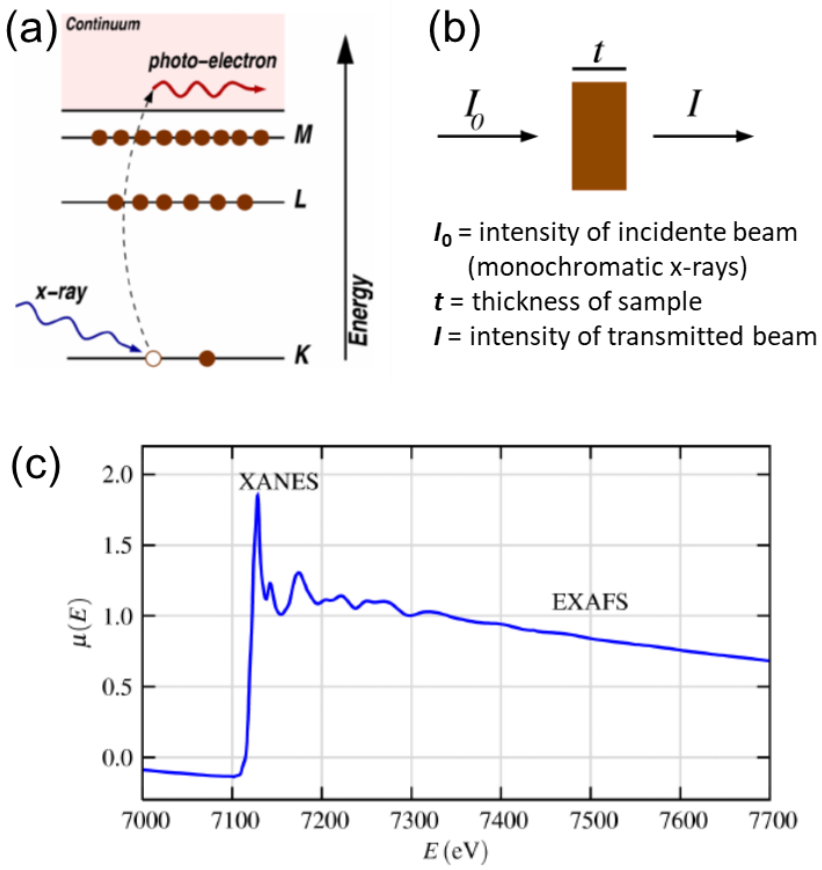

Figure 2.13. Schemes representing (a) the photoelectric effect, in which a core level electron is promoted out of the atom, after X-ray absorption and (b) X-ray Absorption measurements; (c) Typical spectrum of XAFS $\mu(E)$ for FeO, with the XANES and EXAFS regions identified. (Adapted from [244]).

During the PhD, and in the frame of Magnamed Project (Marie Sklodowska-Curie Grant Agreement No. 734801), two proposals to the Brazilian Synchrotron Light Laboratory (LNLS) were accepted to perform XANES/ EXAFS in iron oxide nanowires. LNLS is a 2nd-generation synchrotron light source, built in 80-90s [Figure 2.14(a)].

XANES/EXAFS experiments were performed at LNLS XAFS2 beamline, Figure 2.14(b). This beamline operates with a 1.37 GeV source, a maximum current of 250 mA, a critical energy of 2.08 keV and delivers photons from 3.5 up to 17 keV [246].

Figure 2.14. (a) General overview of synchrotron beam-lines at LNLS and (b) particular overview of XAFS2 beamline.

2.3.2.3.1. X-ray Absorption Near the Edge Structure (XANES)

XANES is strongly sensitive to oxidation state and coordination chemistry (for example octahedral or tetrahedral coordination) of the absorbing atom.

In this work, we had the opportunity to measure the iron oxide nanowires grown by hydrothermal method followed by different annealing conditions. The samples were analyzed with the FTO substrate, in fluorescence mode, with an incident angle of 75 ° (to avoid self-absorption effect), in the Fe K edge. In fluorescence mode, as there was no transmitted beam, the absorption spectrum of the metallic reference was obtained through the beam spread by aluminum foil placed at 45 ° in the outlet of the vacuum tube, after the ionization chamber I_0. The setup, with three ionization chambers, a multi-element solid state Ge fluorescence detector and a 5 K cryostat, is represented in Figure 2.15. By this way, the absorption spectrum is given by: $\ln(I_0/I)$. With this set-up configuration, it was allowed to study our samples also in the extended X-ray absorption fine structure (EXAFS).

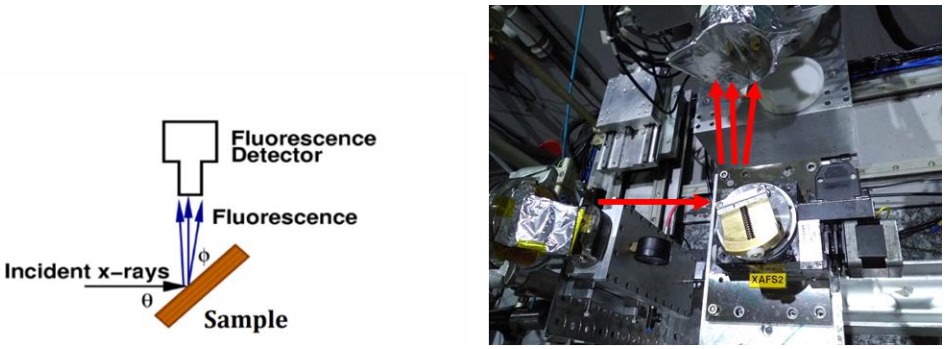

Figure 2.15. (a) Scheme and (b) picture of XAFS measurements set-up.

Five iron oxide references, hematite (αFe_2O_3), maghemite (γ-Fe_2O_3), magnetite (Fe_3O_4) and two phases of iron(III) oxyhydroxide, FeOOH and γ-FeOOH, some supplied by the LNLS User Support Chemistry Lab and others from our lab, were prepared and used to help us determine the composition of the iron oxide phases present in the different groups of samples. Differently from the samples (could not be removed from FTO), the references (powders) could be analyzed using the transmission mode.

Then, the resulting data were analyzed with ATHENA: XAS Data Processing software [243,247]. For each scan, each channel was carefully analyzed, and channels with much noise were not considered.

2.3.2.3.2. Extended X-ray Absorption Fine Structure (EXAFS)

Extended X-ray Absorption Fine Structure (EXAFS) yields information about the interatomic distances, near neighbor species and coordination numbers, and lattice dynamics [243-245].

As described by Matthew Newville in “Fundamental of XAFS” [243,244], for the EXAFS it is of interest the oscillations well above the absorption edge, and the EXAFS fine-structure function $\Delta(E)$ can be defined as:

$$\chi(E) = \frac{\mu(E) - \mu_0(E)}{\Delta\mu_0(E)} \qquad (2.4)$$

where $\mu(E)$ is the measured absorption coefficient, $\mu_0(E)$ is a smooth background function representing the absorption of an isolated atom, and μ_0 is the measured jump in the absorption $\mu(E)$ at the threshold energy E_0 (Figure 2.16) [243,244].

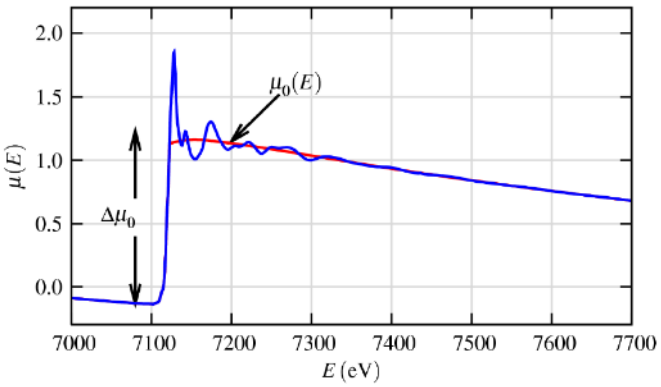

Figure 2.16. $\mu_0(E)$ - smooth background function of $\mu(E)$, and the edge-step $\Delta\mu_0(E_0)$ (Extracted from [244]).

However, EXAFS is best understood in terms of the wave behaviour of the photo-electron created during the absorption process. Thus, it is common to convert the X-ray energy into the photo-electron wave number, *k*, with dimensions of 1/distance, and defined as:

$$k = \sqrt{\frac{2m(E-E_0)}{h^2}} \tag{2.5}$$

where E_0 is the absorption edge energy and *m* is the electron mass. The primary quantity for EXAFS is $\chi(k)$, the oscillations as a function of the photo-electron wave number, and $\chi(k)$ is well-known as "the EXAFS". As an example, given by the author, the EXAFS extracted from the Fe K-edge for FeO is shown in Figure 2.17(a). As can be seen, the EXAFS is oscillatory with a quickly decay with *k*. In order to accentuate the oscillations, $\chi(k)$ is often multiplied by a power of *k* typically k^2 or k^3 [Figure 2.17(b)].

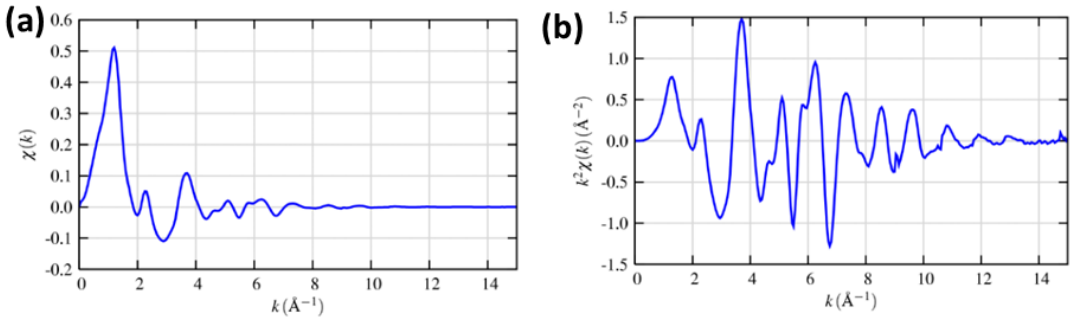

Figure 2.17. (a) Isolated EXAFS $\chi(k)$ for FeO and (b) the *k*-weighted XAFS $k^2\,\chi(k)$. (Extracted from [244]).

In program Athena there is the option of *k*-weighting for use when plotting in *k*-space or when making a forward Fourier transform. It is a common practice in EXAFS to multiply $\chi(k)$ by different *k*-weights. This means that the $\chi(k)$ array is multiplied point-by-point by *k*-array. For example, for k^1 weighted data, $\chi(k)$ at *k*=5 is multiplied by 5 and $\chi(k)$ at k=10 is multiplied by 10. Likewise, for k^2 weighted data, $\chi(k)$ at *k*=5 is multiplied by 25 and $\chi(k)$ at *k*=10 is multiplied by 100. This has an amplifying effect on the spectrum at the high-*k* end. This *k*-weighting is a way to make the high-*k* oscillations more visible in a plot, since normally the oscillations reduce very fast after the edge (as can be observed in the right part of a typical spectrum, in Figure 2.16). *k*-weighting is also used to emphasize the contributions of certain elements, that can have small scattering amplitudes either at low-*k* or at high-*k* [244,248].

2.3.2.4. Raman scattering

Raman spectroscopic technique is used to analyze the inelastic light scattering interactions of the incident photons of monochromatic laser beam with the molecules of a sample. The frequency shift from the incident radiation and the scattered radiation – Raman shift - corresponds to the vibrational frequencies of the molecules (ω_{vib}). The vibrational frequencies originate from oscillations between the constituent atoms of the molecules. Since the vibrations depend on the particular molecular structure, the vibrational spectrum constitutes a characteristic pattern of a molecule [249].

In Raman scattering, a molecule absorbs a photon with frequency ω and emits a photon at a different frequency ω_R, which is counterbalanced with respect to ω by a vibrational frequency ω_{vib} of the molecule: $\omega_R = \omega \pm \omega_{vib}$.

When the change in energy of the scattered photon is less than the incident photon, the scattering is called Stokes scatter, $\omega > \omega_R$, Figure 2.18(a). If $\omega < \omega_R$, then the process is designated anti-Stokes Raman scattering, Figure 2.18(b). Figure 2.18(c) depicts a typical Raman spectrum. The spectrum is expressed in wavenumbers (cm^{-1}) = [1/λ (cm)] − [1/λ_R (cm)], with λ and λ_R being respectively the wavelengths of incident and scattered light [249].

The Raman scattering was measured using a Renishaw inVia Qontor Spectrometer at IFIMUP, University of Porto, with the technical support of Rui Vilarinho. The excitation laser with 633 nm polarized line of He-Ne, in the spectral range from 200 to 1400 cm^{-1}, an exposure time of 60 s and power of 1.1mW were the used conditions. A microscope coupled to the Raman set-up allows a detailed analysis of samples surfaces, in order to choose the areas of sample to analyse.

The obtained Raman spectra were analyzed using the commercial Igor Pro program.

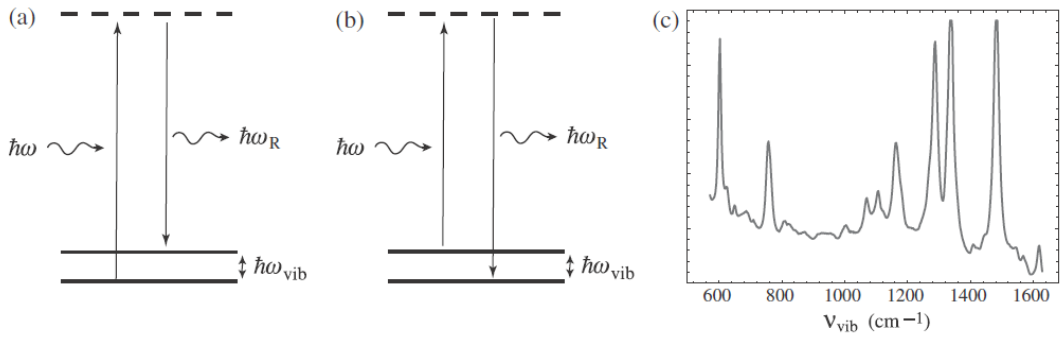

Figure 2.18. (a) Stokes Raman scattering ($\omega > \omega_R$). (b) Anti-Stokes Raman scattering ($\omega < \omega_R$). (c) Example of Raman-scattering spectrum representing the vibrational frequencies of a certain molecule (Reproduced from [249] with permission of Cambridge University Press through PLSclear).

2.3.3. Photoelectrochemical characterization

2.3.3.1. *j-V* curves

The photocurrent density is one of the most important parameters to evaluate the performance of a semiconductor material to be applied in PEC cells. The photocurrent is usually measured in a three-electrode configuration under 1 sun AM 1.5 G illumination (100 mW·cm^{-2}) because the photocurrent is proportional to the hydrogen or oxygen production rate [86]. The basic experimental setup for PEC photocurrent measurements consists in a three-electrode configuration PEC cell, a light source (a solar simulator or a xenon lamp with filters), and a potentiostat [86], Figure 2.19(a).

In this work, the photocurrent density-voltage (*j-V*) curves under dark and 1-sun simulated sunlight (100 mW·cm^{-2}, AM 1.5 G) were performed using a class B solar simulator with a 150 W Xe lamp (Oriel, Newport), under dark and 1-sun [Figure 2.19(b) and (c) respectively]. The *j-V* curves were recorded using a potentiostat attached to the PEC cell, a ZENNIUM (Zahner Elektrik, Germany) workstation together with Thales software for data acquisition, and a scan rate of 10 mV.s^{-1} for the potential range between 0.5 -1.8 V_{RHE}. The light beam was calibrated with a c-Si photodiode.

Measurements were performed using a “cappuccino” PEC cell [43,250], with an illuminated surface area of 0.528 cm^2. A three-electrode configuration was used: Ag/AgCl/saturated KCl (Metrohm, Switzerland) electrode as the reference electrode (RE), a platinum wire (Alfa Aesar, 99.9%) as the counter-electrode (CE) and the hematite

NWs photoelectrodes (grown on FTO substrate) as the working electrode (WE), as represented in Figure 2.19(a).

In the case of Fe_2O_3 photoelectrodes, the cappuccino cell was filled with a 1.0 M NaOH electrolyte solution, while in the case of WO_3, a 0.5 M $NaSO_4$ electrolyte solution was used.

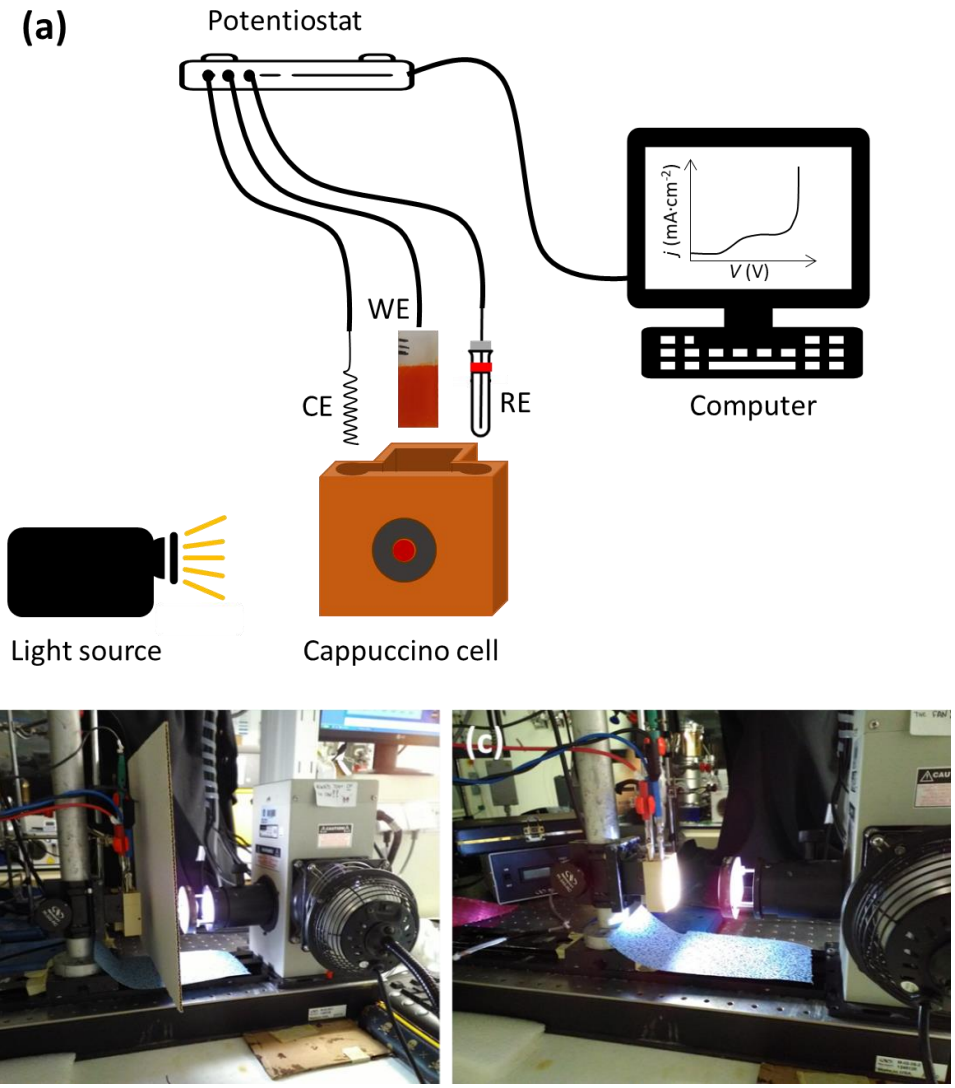

Figure 2.19. (a) Schematic representation of *j*-V measurement system (Adapted from [86]). Pictures of *j*-V measurements using a solar simulator Class B, under (b) dark and (c) 1-sun simulated light.

According to the Nernst equation, the measured potentials *vs.* Ag/AgCl are converted to the reversible hydrogen electrode (RHE):

$$E_{\mathrm{RHE}} = E_{\mathrm{Ag\,/\,AgCl}} + 0.059\ \mathrm{pH} + {E^0}_{\mathrm{Ag\,/AgCl}} \qquad (2.6)$$

where E_{RHE} is the converted potential *vs*. RHE, $E^0_{Ag/AgCl}$ = 0.1976 V at 25 °C, and $E_{Ag/AgCl}$ is the potential measured experimentally against the reference Ag/AgCl electrode.

2.3.3.2. Intrinsic Solar to Chemical Conversion Efficiency

The intrinsic solar to chemical (ISTC) conversion efficiency was determined based on the model proposed by Rothschild *et al.*, from the photocurrent density *vs.* potential curves measured under dark and illumination, in a three-electrode configuration [43,251]. The ISTC can be defined as:

$$ISTC = \left[\eta_{el}\frac{J_{photo}(mA\cdot cm^{-2})\times V_{photo}(V)}{P_{light}\ (mW\cdot cm^{-2})}\right]_{AM1.5G} \cong \frac{1.23\ (V_{RHE})}{U_{dark}(V_{RHE})}\left[\frac{J_{photo}(mA\cdot cm^{-2})\times V_{photo}(V)}{100\ (mW\cdot cm^{-2})}\right]_{AM1.5G} \quad (2.7)$$

with η_{el} the electrolysis efficiency, J_{photo} the generated photocurrent, V_{photo} the correspondent photopotential and U_{dark} the potential necessary to be applied to the photoanode to reach the respective current in the dark [43,251].

In addition, the intrinsic photovoltaic power, P_{light}, for the photoanodes was determined by the equation:

$$P_{light}(\mathrm{mW\cdot cm^{-2}}) = J_{photo}(\mathrm{mA\cdot cm^{-2}}) \times V_{photo}(\mathrm{V}) \quad (2.8)$$

Also, the fill-factor (*FF*) at the maximum power point was determined by the equation:

$$FF = \frac{V_{PP}\times J_{PP}}{V_{OC}\times J_{SC}} \quad (2.9)$$

with V_{PP} and J_{PP} the values of photopotential and photocurrent at the maximum power point, respectively; the V_{OC} and J_{SC} represent the open circuit voltage and short circuit current, respectively.

2.3.4. Optical absorption

To investigate the optical properties of hematite and tungsten trioxide photoanodes, the light absorption efficiency, light reflection efficiency (reflectance), and light

transmission efficiency (transmittance) were determined, using UV-vis spectrophotometry, in the range of 200 to 700 nm.

The light absorption efficiency *A* can be obtained from the light reflectance efficiency (*R*) and light transmittance efficiency (*T*):

$$A = 100 - T - R \tag{2.10}$$

R gives the percentage of light reflected by a sample illuminated by a light source, and refers to intrinsic property of the material, while *T* is the percentage of incident light that is transmitted through a sample at a specified wavelength (λ).

In general, commercial UV-Vis spectrophotometers consist in a light source, a monochromator with appropriate optical lenses and filters, and a detector [86].

UV-vis spectra were obtained using an UV-vis-NIR spectrophotometer (Shimadzu Scientific Instruments Inc., model UV-3600, Kyoto), equipped with a 150 mm integrating sphere (IS) and using $BaSO_4$ as 100% reflectance standard (regarded as a reference surface with a reflectance of 100%). By placing the sample inside the UV-vis spectrophotometer, in front of the incident light window, the measurements will be conducted by the integrating spheres in the interior of the equipment. These integrating spheres will concentrate the light reflected from the sample on the detector [86].

R and *T* were measured for all samples and FTO substrate, and then both were subtracted to the incident radiation to calculate the absorbance, Eq. (2.10). The absorbance was corrected by subtracting the FTO glass absorbance (working as control) [43,250].

The UV-vis spectroscopic measurements were also used to assess the optical band gap properties of the semiconductor materials, obtained from the Tauc plots [252]:

$$(\alpha h\upsilon) = A(h\upsilon - E_g)^n \tag{2.11}$$

where $h\upsilon$ is the incident photon energy (in eV), α the absorption factor, E_g is the optical band gap energy (in eV) and *A* and *n* are constants dependent on the electronic transition; $n = 2$ for direct and $n = 1/2$ for indirect allowed transitions [37,47].

Chapter 3

Photoelectrochemical Water Splitting: Thermal Annealing Challenges on Hematite Nanowires

Chapter 3

Photoelectrochemical Water Splitting: Thermal Annealing Challenges on Hematite Nanowires

In this chapter it is described the synthesis of hematite nanowires (NWs) by hydrothermal method. It was investigated the impact of annealing conditions, especially the annealing temperature and time, on the morphological, structural, optical and photoelectrochemical features of the nanowires (NWs) photoelectrodes. Likewise, the Sn diffusion from FTO substrate with annealing temperature and its impact on the hematite properties was studied. The unexplored parameter annealing time is of particular interest, since it allows the use of lower annealing temperature (such as 600 ºC) with considerably cheaper FTO substrates, that may be of interest to industrial scale-up, in a perspective of the PEC cells devices applications.

This chapter is based on the work: P. Quitério, A. Apolinário, D. Navas, S. Magalhães, E. Alves, A. M. Mendes, C. T. Sousa and J. P. Araújo. J. Phys. Chem. C 2020, 124, 12897−12911, https://doi.org/10.1021/acs.jpcc.0c01259.

3.1. Overview

Among several types of nanostructured photoelectrodes, one-dimensional (1D) nanostructures, such as nanowires (NWs) with high-aspect-ratios, have been suggested as potential candidates as they provide a more direct pathway for charge transportation up to the charge collector and reduce the recombination losses [8,33,39,64,104,105]. Since 2001, when Vayssieres *et al.* [91] demonstrated that hematite NWs can be easily prepared by hydrothermal method, several publications have shown that this methodology is the most effective one to increase the hematite photocurrent.[8,33,39,64,105,111,115] High-aspect-ratio NWs, with around 5 nm of diameter, have been grown vertically on a fluorine-doped tin oxide (FTO) substrate from an aqueous chemical bath solution and under the right conditions of temperature and pressure. This 1D quantum confinement has given rise to a blue-shift on the band gap and a reduction of the electron-hole recombination [91,105].

Additionally, it was observed that the use of dopants can highly increase the donor density improving the electrical conductivity of hematite [33,44,56,57,113-115,253]. The doping of bare hematite can be performed by Sn diffusion from the FTO substrate to the photoanode via a higher temperature annealing process (generally 750-800 °C) [33,64,65,111,113,114]. A Sn diffusion in the order of 0.9-9.9% (atomic %) was observed. This led to a conductivity improvement and to a photocurrent increase from 0.035 up to 1.24 $mA \cdot cm^{-2}$ (at 1.23 V_{RHE}) when the annealing temperature varied from 550 to 800 °C [33]. Although a higher annealing temperature (~1000 °C) is required for the complete conversion of hematite [65,254] the use of activation temperatures higher than 800 °C is limited by FTO deformation [33,64,111,113].

Thermal annealing promotes the Sn diffusion which increases the electron donor density, but also eliminates internal and superficial defects improving the hematite crystalline structure and reduces the surface recombination [65,66,111,255]. Then, it was suggested that the improved photoconversion performance results from both the morphological anisotropy of the precursor β-FeOOH NWs and the annealing temperature [65,66,111]. However, it should be noticed that the larger particle size usually obtained with higher annealing temperatures, compared with the short hole diffusion length (2-4 nm), strongly limits the photoconversion efficiencies [33,47,64,65].

Some discrepancies were observed in terms of annealing steps; while some authors reported the use of one-step annealing [64,113,256,257], others used a first step at 500-550 °C to convert the β-FeOOH phase into hematite followed by a second shorter step at higher temperatures (between 750 and 800 °C) for the hematite activation [32,33,56,113,258,259]. The effect of performing a rapid cooling process should be also mentioned as beneficial for the charge separation efficiency, improving the photocurrent values [260].

On the other hand, annealing time is an underestimated parameter, rarely reported, generally limited by substrate deformation [64]. However, the use of low-cost substrates with extended annealing time should be relevant for industrial applications. The influence of prolonged annealing time in morphology, crystallinity, electronic structure and photoactivity of NWs was not systematically studied so far.

In this Chapter, it is described the preparation of hematite photoanodes by a hydrothermal method, followed by different annealing conditions to achieve hematite pure phase. A systematic and broad study to understand the role of the optimum preparation and annealing conditions for obtaining the highest photocurrent was undertaken. A wide variety of parameters were analyzed. Namely, a complete XRD analysis revealing the preferential crystallographic orientation and its influence in the photocurrent efficiency, the use of RBS technique (unusual in this kind of material) for

assessing the Sn diffusion and distribution profiles in-depth through hematite, a complete XAFS analysis to complement the structural information, determine the electronic and local structure of Fe atoms, and a new approach in porosity determination using optical absorption data, were some of the important achievements here presented concerning the hematite photoanodes. The increase of photocurrent with temperature and time, besides being related to Sn % diffusion along the photoelectrode, is also correlated with nanowires morphology, crystalline order enhancement and porosity. Tin doped hematite displays higher conductivity to photogenerated carriers and decreases the band gap.

3.2. Experimental details

3.2.1. Hydrothermal synthesis

FTO glass substrates were cleaned as described in the Experimental Section, as reported by Francisco *et al.* [261], and then placed (tilted with FTO facing down) in a 40 mL capacity teflon stainless steel autoclave with 20 mL solution of 0.15 M $FeCl_3.6H_2O$ and 1 M $NaNO_3$, adjusted at pH 1.5 with HCl 37% [33]. The autoclave was heated at 95 °C for 4 h to obtain the iron oxide NWs. After hydrothermal growth, a yellow film layer of iron oxyhydroxide NWs was formed on the top of FTO substrates [Figure 3.1(a)]. The coated FTO was then washed with deionized water to remove any residual salts. Then a thermal annealing was necessary to obtain the α-Fe_2O_3 phase [Figure 3.1(b)]. Since hematite crystallization starts above 390 ºC [91], we set our starting annealing temperature at 550 ºC [33]. It was further reported that the ideal annealing temperature for complete conversion into hematite occurs at ~1000 ºC [254]. Unfortunately, the glass bending (glass becomes more curved and with signs of fusion) of the FTO substrates at high temperature occurred for temperatures above 825 ºC, so this set the maximum annealing temperature used.

To investigate the effect of the annealing conditions on the photoanodes photo-performance, several annealing parameters were studied: heating ramp, one-step *vs*. two-step annealing approach, temperature and time [33,56,64,66,256].

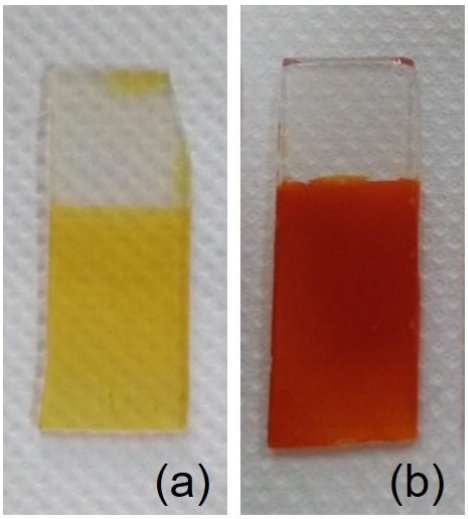

Figure 3.1. (a) Yellow film layer of iron oxyhydroxide (FeOOH) NWs formed on the top of FTO substrates after hydrothermal process; (b) conversion of FeOOH into hematite (orange film) after the annealing treatment.

For the two-step annealing approach, we performed a first annealing at 550 °C during 2 h, followed by a short annealing step (20 min) at higher temperatures (600-850 °C) [32,33,56,113,258,259]. Nonetheless, a study of the different possibilities of temperature and time for each stage has not been explored in detail. The preparation conditions are summarized in Table 3.1.

Table 3.1. Sets of samples prepared with different annealing conditions.

	One-step annealing			Two-step annealing			
Set	#1	#2	#3	#4		#5	
Temperature (°C)	600-850	800	600	550	800	550	600-825
Time (units)	20 (min)	5-25 (min)	3-72 (h)	2 (h)	20 (min)	2 (h)	20 (min)
Ramp (°C·min^{-1})	WR	WR	10	1-10; WR	8	10	8

WR – without ramp (*i.e.* sample placed directly in the furnace at the established temperature).

3.3. Results and Discussion

3.3.1. Photoelectrochemical performance

Photocurrent density-Voltage curves. The photoelectrochemical performance of the hematite photoanodes was assessed based on the photocurrent density-voltage (*j*-

V) curves. Figure 3.2 shows the *j-V* characteristic curves under dark and simulated sunlight for the several sets of α-Fe_2O_3 photoanodes described in the previous section (Table 3.1). The photocurrent was assessed under front-side illumination, which resulted in higher photocurrent than back-side illumination, as the majority carriers (electrons) have less transport limitations within hematite photoanodes than minority carriers (holes). The transport of generated electrons from hematite illuminated side through FTO direction is easier than the contrary trajectory that holes (with a short diffusion length of 2-4 nm) would have to travel, if photoanodes were back-side illuminated [16], Figure 3.3.

For the one-step annealing photoelectrodes (set #1), the photocurrent density (*j*) increases with temperature until it reaches 800 °C [Figure 3.2(a)]. Above this temperature, the FTO substrate deformation (glass bending) may explain the decrease of *j*, since a glass bending was visually observed. These results confirm that 800 °C is the best annealing temperature [33]. Fixing the annealing temperature at 800 °C and varying the time between 5 and 25 min (set #2), the *j-V* curves shows that 20 min seems to be the ideal annealing time before causing the FTO substrate deformation and consequently the decrease of *j* [Figure 3.2(b)]. In the same way, when the annealing temperature is set at 600 °C and the annealing time is varied between 3 and 72 h (set #3), *j* increases with time up to 48 h [Figure 3.2(c)]; afterwards, a decrease of *j* is observed (t = 72 h), with some FTO glass bending.

Regarding the two-step annealing photoanodes prepared with different annealing ramps (set #4), and although no significant differences are observed, the 10 °C·min^{-1} ramp shows a slight better *j* performance [Figure 3.2(d)]. According to these results, it was carried out a first annealing step at 550 °C, followed by a second annealing step ranging the applied temperatures between 600 and 850 °C (set #5). In this set, *j* increases with temperature up to 800 ºC [Figure 3.2(e)], as already observed for set #1 [Figure 3.2(a)]. In this case, the 825 ºC sample resulted in similar *j* values and was considered for characterization. Above this temperature, a decrease in *j* is also observed due to the same reason of FTO deformation mentioned above. For that, the samples with annealing at 850 ºC and 72 h were not considered to further characterization in this work.

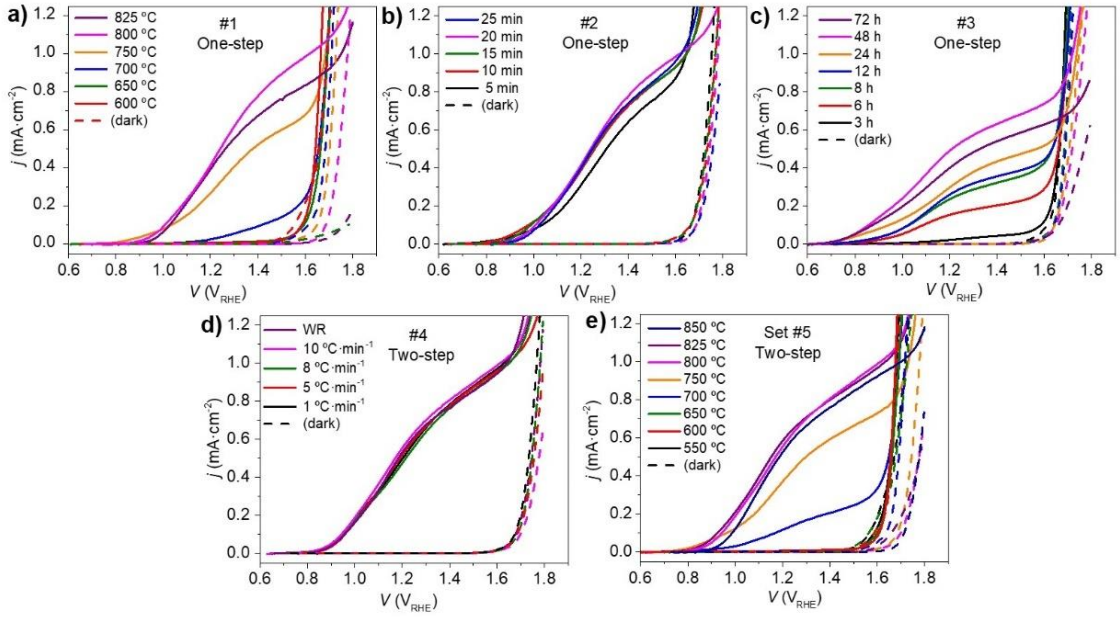

Figure 3.2. *j-V* characteristic curves for α-Fe_2O_3 samples with different annealing steps: (a) set #1 – samples prepared with different temperatures (600-825 °C) for 20 min; (b) set #2: samples prepared with different time (5-25 min) at 800 ºC; (c) set #3 – samples prepared with different time (3-72 h) at 600 °C; (d) set #4: samples prepared with two-step annealing, 550 ºC for 2 h followed by 20 min at 800 ºC, with different heating ramps in the first step: 1-10 ºC, without ramp (WR); (e) set #5 – samples prepared with two-step annealing, 550 °C for 2 h followed by 20 min at 600-825 °C.

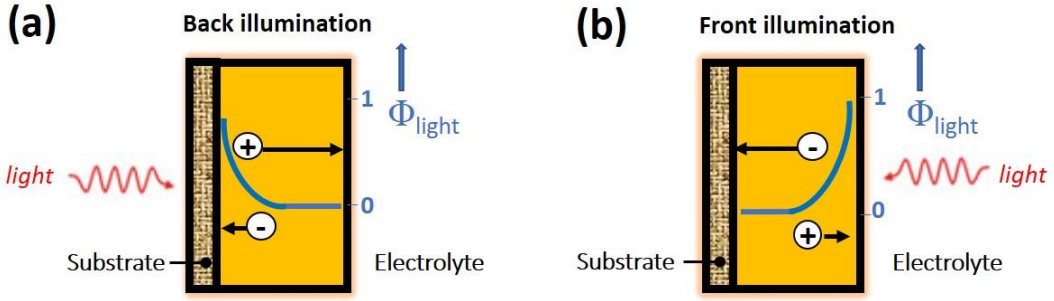

Figure 3.3. Scheme illustrating the difference between (a) back and (b) front-side illumination on a thin film photoanode (adapted from [16]).

Figure 3.4(a) shows the evolution of *j* (at 1.45 V_{RHE}) as a function of temperature for both one and two-step annealing processes (sets #1 and #5, respectively). Although they exhibit similar behaviours, slight higher *j* performance values are obtained for >650 °C when the two-step annealing process was used. Regarding the onset potential, V_{onset} in Figure 3.4(b), we observe a decrease as the annealing temperature increases. It was suggested that lower V_{onset} corresponds to the reduction of the surface trap states by

annealing temperature (attributed to the passivation of surface states just beneath the conduction band) and, consequently, recombination processes. It also has been attributed to the use of dopants/catalysts surface modification [33,64,66,85]. According to this idea, a favourable cathodic shift to lower potentials is observed for photoelectrodes with two-step annealing (set #5). In particular, it should be noticed that *j* is significantly low ~0.01 mA·cm^{-2} when the sample was annealed at 550 °C for 2 h and improves to 0.85 mA·cm^{-2} with the second annealing step at 800 °C, in accordance with the typical *j* values of bare hematite [56,64,114,259,262]. This behaviour goes with a minimum value of V_{onset} = 0.68 V_{RHE}.

By increasing the annealing time at 600 °C (set #3), Figure 3.4(a) shows that *j* gradually increases up to 48 h and reaches a maximum value of 0.66 mA·cm^{-2}. This value is 66 times higher than the one measured for the sample with two-step annealing (set #5) using the same temperature (550 °C for 2 h + 600 °C for 20 min). Moreover, this *j* is similar to the value achieved by the sample treated at 750 °C [Figure 3.4(a)] and with a lower onset potential: $V_{onset\ 48h}$ = 0.62 V_{RHE} *vs*. $V_{onset\ 750°C}$ = 0.70 V_{RHE} [see Figure 3.4(b)]. Therefore, the application of 600 °C for 48 h may allow to work with substantially cheaper FTO substrates, important to scale-up hematite photoanodes. Further annealing time revealed a *j* decrease, 0.57 mA·cm^{-2} at 72 h [Figure 3.4(a)]. On the other hand, the onset potential decreases with annealing time from 0.89 to 0.62 V_{RHE} for 3 to 48 h, respectively [Figure 3.4(b)].

In summary, sets #3 (time dependence) and #5 (temperature dependence) showed the most relevant results confirming that *j* depends mainly on both the annealing temperature and time. Thus, for now on, we will focus our attention on these two sets of samples (#5 and #3) in order to try to unveil the role of annealing temperature and time in the hematite photoanodes performance.

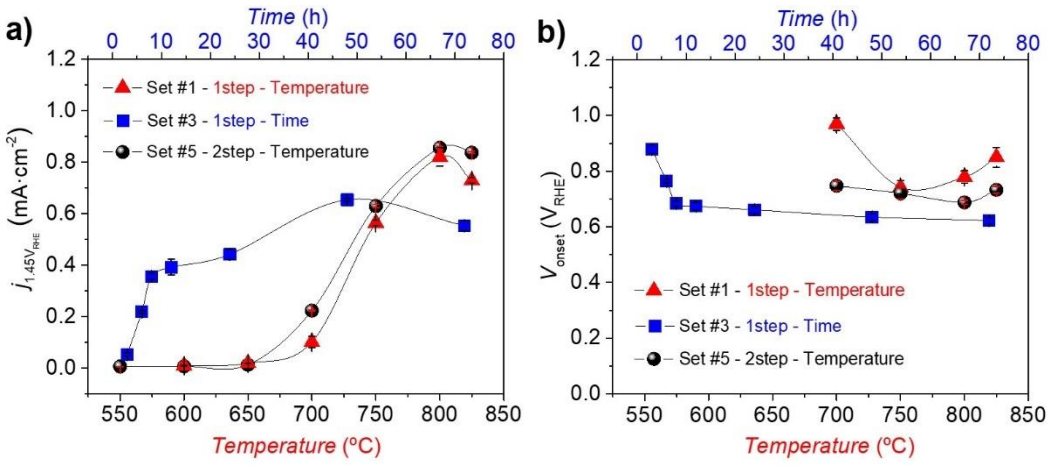

Figure 3.4. (a) *j* at 1.45 V_{RHE} and (b) V_{onset} for hematite photoanodes from sets #1, #3 and #5.

Intrinsic solar to chemical conversion efficiency. The intrinsic solar to chemical (ISTC) conversion efficiency was determined for the photoanodes with best *j-V* performance of each annealing schemes, temperature and time (800 ºC and 48 h), in order to evaluate the efficiency of these photoanodes in the conversion of photonic into chemical energy used to oxidize the water [43]. First, the photocurrent (J_{photo}) and photopotential (V_{photo}) were extracted from the *j-V* curves, determined by the difference between the light and dark currents and potentials, respectively (as illustrated by the black arrows in Figure 3.5(a). After calculating J_{photo} and V_{photo} from *j-V* curves, J_{photo} was plotted as a function of the V_{photo}. This yields the photocurrent density measured under short-circuit conditions (J_{sc}) and the open-circuit photopotential (V_{oc}), Figure 3.5(b). The intrinsic photovoltaic power of the photoelectrodes [represented in Figure 3.5(c) as P_{light}] is given by the product of J_{photo} by V_{photo}, Eq. (2.8); by plotting it *vs.* V_{photo}, the maximum power point (MPP) can be obtained and the respective voltage (V_{PP}) and current (J_{PP}).

For the 800 ºC photoanode, it was obtained a maximum power of 0.35 mW·cm^{-2} at a potential U_{light} of 1.3 V_{RHE} , i.e. the potential applied to the photoelectrode under light [represented in the secondary *y* axis, Figure 3.5(c)]. This corresponds to a maximum power conversion efficiency of 0.35% for 800 ºC, which means that this sample generated an electric power of 0.35 mW·cm^{-2} from the solar-simulated light power of 100 mW·cm^{-2}. A maximum power of 0.25% (at U_{light} = 1.2 V_{RHE}) was obtained for the 48 h photoanode. From the Eq. (2.9) the fill-factor (*FF*) was determined. *FF* of 46.6% and 45% at the maximum power point were obtained for 800 ºC and 48 h photoanodes, respectively, in accordance with the values usually reported for hematite [43,251]. *FF* for both samples is quite similar which may indicate that the 48 h photoanode is not being particularly more affected by factors such as charge recombination or low charge extraction [263,264].

Figure 3.5(d) shows the plot of ISTC conversion efficiency [calculated from Eq. (2.7)] for both photoanodes as a function of J_{photo}. For the 800 ºC and 48 h, ISTC maximum efficiencies of 0.24 % (at J_{photo} of 0.71 mA·cm^{-2} and U_{light} of 1.3 V_{RHE}) and 0.18% (at J_{photo} of 0.52 mA·cm^{-2} and U_{light} of 1.2 V_{RHE}) were obtained, respectively. In order to obtain the same photocurrent values in the dark, it would be necessary potentials of 1.8 and 1.72 $V_{RHE,}$ respectively for the 800 ºC and 48 h, taken from *j-V* dark curves in Figure 3.5(a). This means that the solar-simulated light power (100 mW·cm^{-2}) saves 0.49 V from the external power source, i.e., a power of 0.49 V × 0.71 mA·cm^{-2} = 0.35 mW·cm^{-2} in the case of 800 ºC photoelectrode, and 0.48 V in the case of 48 h sample, as well. However, the electric power saved is reduced by the conversion efficiency of the electrolysis reaction, η_{el}. From Eq. (2.7), $\eta_{el} \cong 1.23(V_{RHE})/U_{dark}(V_{RHE})$, which gives η_{el}(800ºC) = 68.33% and η_{el}(48h) = 71.51%. Then, the light induced contribution to the chemical

power produced by the 800 ºC photoanode is 0.24 mW·cm^{-2} (68.33% × 0.35 mW·cm^{-2}), while for 48 h it gives a value of 0.18 mW·cm^{-2} (71.51% × 0.25 mW·cm^{-2}), which corresponds to the ISTC efficiencies of 0.24% and 0.18% respectively. Thus, the ISTC of the photoelectrodes is given by the product of the electrolysis efficiency with the internal power, which maximum point determines the optimum operating conditions for the PEC cell [43,251]. These calculations yield the potential that should be applied to the photoanode in order to assure the conversion of solar to chemical power at its maximum internal conversion efficiency. The obtained values are in deep accordance with the literature for hematite photoelectrodes [43,251].

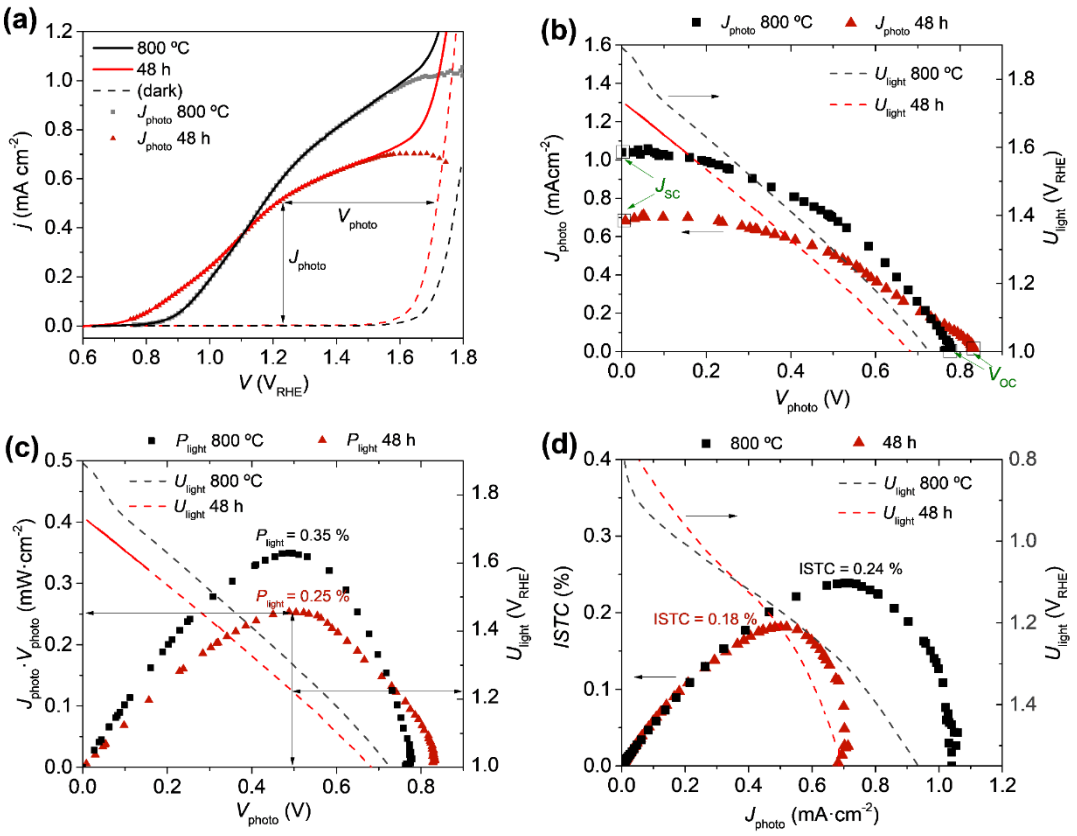

Figure 3.5. (a) *j*-*V* curves for the 800 ºC and 48 h photoanodes, obtained in the dark (dashed lines) and simulated solar illumination (solid lines) and the respective photocurrent, J_{photo}; (b) photocurrent (J_{photo}) as a function of the photopotential (V_{photo}); (c) intrinsic photovoltaic power (P_{light}) as a function of V_{photo}; (d) ISTC efficiencies as a function of J_{photo}. In the secondary *y* axis on the right, it is plotted the potential (U_{light}) applied to the photoanode under light.

3.3.2. Morphological characterization

From the SEM images [Figures 3.6(a)-(i)], morphological changes were observed with annealing temperature and time. The measured diameter (*D*) and thickness (*L*) are illustrated in Figures 3.6(b) and (c), respectively. The iron oxide NWs are entirely formed at the first stage of hydrothermal growth process, shown in Figure 3.6(a). At this stage, the NWs show a needle form, with square shape tips.

However, after the annealing treatment at 550 °C, the nanostructures became slightly porous, where the NWs show a more rounded shape, smoother, and without any clear changes in *D*, Figure 3.6(d). After the application of the second annealing step (from 600 up to 825 °C), the NWs shape becomes rounder and *D* increases [Figures 3.6(e) and (f) for 700 and 800 °C samples, respectively]. As the annealing temperature was increased, the fusion between neighbouring NWs [33,64] seems to take place, increasing *D* almost linearly from 42 to 97 nm for 550-800 °C, Figure 3.7(a).

Regarding the annealing time, a similar behaviour was observed: *D* increases with time and their shape becomes rounder, especially above the 8 h. Again, the fusion between NWs, induced by the timely continuous annealing at fixed temperature of 600 ºC [Figures 3.6(g), (h) and (i) for 6, 24 and 48 h, respectively], can be suggested. A small *D* increase with annealing time is observed up to 12 h (from 61 to 82 nm); afterward, *D* tends to keep a constant value for longer annealing time, Figure 3.7(a).

Likewise, with the increase of annealing temperature and time, it was noticed a euhedral shape, where the crystal contours and faces became more defined [suggesting more crystalline structures; Figures 3.6(e), (f), (h) and (i)] [33,64]. The transformation became more evident with the 800 °C and 48 h annealing conditions.

The NWs thickness (*L*) was determined from the SEM cross-sectional images, Figure 3.7(b). According to the literature [37,154], it is expected that a reduced thickness makes the electrons´ pathway easier (due to the shorter distance) to reach the charge collector, with a less probability of electron-hole recombination. In this work, it was observed that *L* slightly decreases with the annealing temperature (from 330 ± 50 to 285 ± 37 nm for 550 and 800 °C, respectively). On the other hand, *L* did not vary significantly with annealing time (from 262 ± 52 to 281 ± 38 nm, for 3 and 48 h, respectively). Although more details can be seen in Figure 3.7(b), this aspect will be further discussed in Section 3.4.

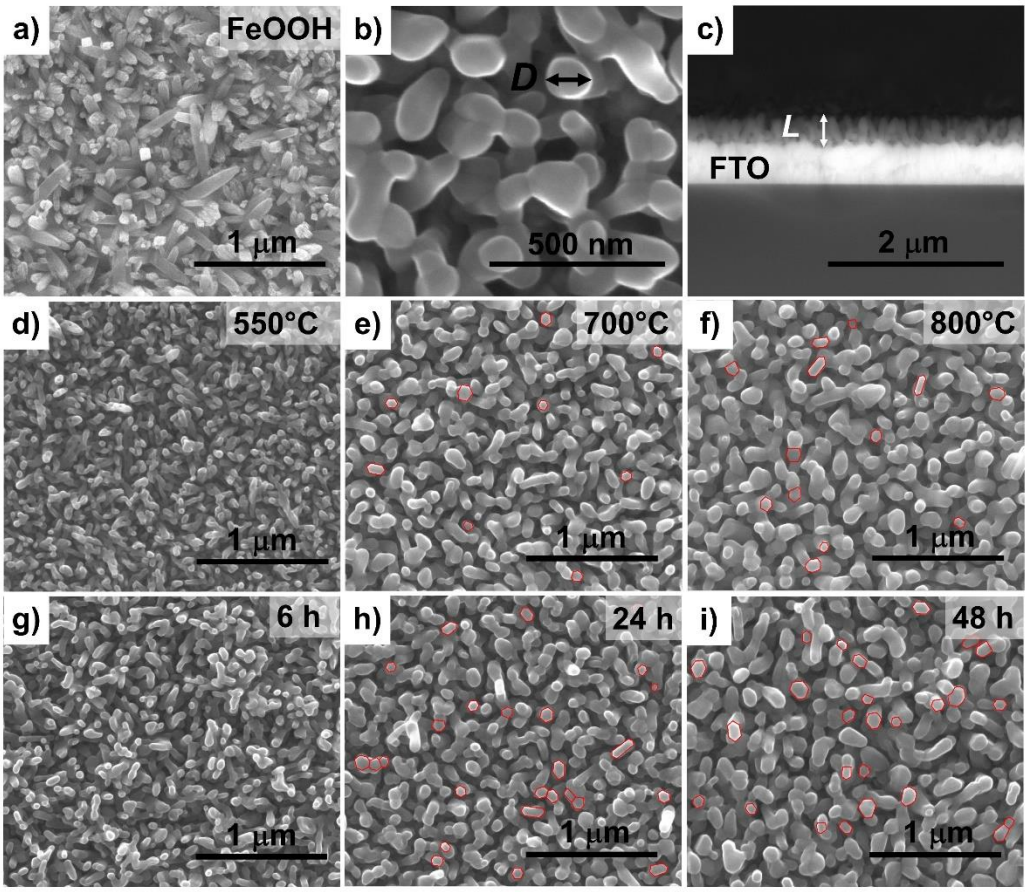

Figure 3.6. SEM images of (a) FeOOH NWs after the hydrothermal synthesis; (b) illustrative measurement of α-Fe_2O_3 NWs diameter (*D*) and (c) cross-section image with illustrative measurement of NWs thickness (*L*); α-Fe_2O_3 NWs with different annealing temperatures of (d) 550 °C, (e) 700 °C and (e) 800 °C, and different annealing times of (g) 6 h, (h) 24 h and (i) 48 h. In Figures 3 (e), (f), (h) and (i) it is shown the demarked contours (in red) of euhedral structures.

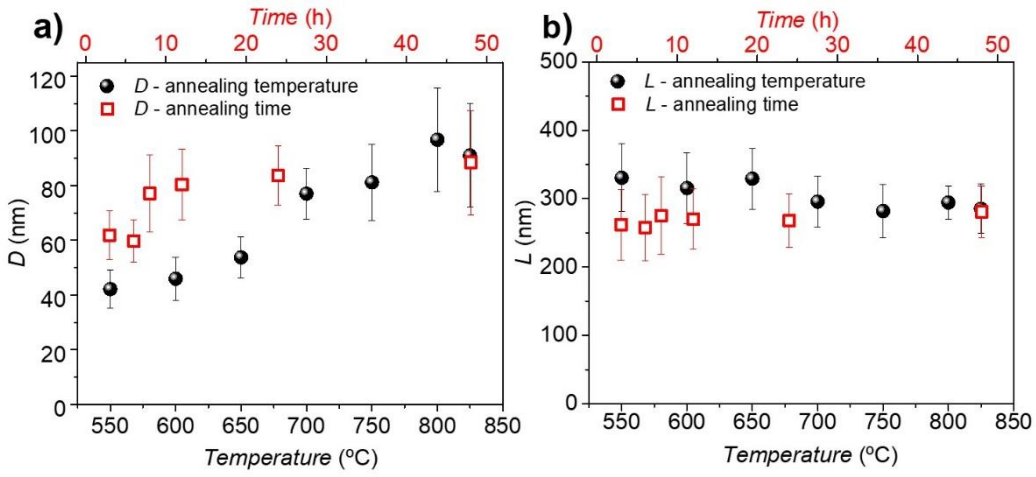

Figure 3.7. (a) Diameter (*D*) and (b) thickness (*L*) of α-Fe_2O_3 NWs as function of annealing temperature (550-800 °C) and time (3-48 h).

3.3.3. Structural characterization

X-ray diffraction analysis. From the XRD spectra (Figure 3.8), the crystalline phase of the iron oxide NWs was determined. The use of parallel beam (PB) with grazing incidence omega (ω) angles allows to remove almost totally the FTO signal, usually the more intense one in the literature [33,56,57,64,114,115]. After hydrothermal growth, the NWs present a peak with (211) orientation corresponding to the β-FeOOH phase (JCPDS 34-1266) [57]. For both sets of samples and after the annealing treatment, the thermodynamically stable hematite phase (JCPDS 33-0664), described as corundum crystalline structure with hexagonal closed-packed unit cell, was obtained [Figures 3.8(a) and (b)], with the preferential orientation at diffraction peak (110) [33,42,65,265]. Also, other peaks indexed to α-Fe_2O_3 structure, such as (012), (104), (113), (024), (214) or (300) were identified. For temperatures above 800 ºC (825 ºC), a peak (200) of SnO_2 from the FTO substrate increases [marked as * in Figure 3.8(a)]. This can be attributed to two main reasons: (i) the fact that the FTO at this range of temperature presents more signs of deformation and higher roughness, and it is technically more difficult to isolate the peak; (ii) we are using grazing angle diffraction (superficial incidence in sample), and probably detecting more the FTO substrate or the interface FTO substrate/hematite (with higher Sn concentration diffused from FTO).

XRD spectra were fitted using Pseudo-Voigt peak function, Figure 3.9. The peak (104) has been usually related with the existence of oxygen vacancies acting as electron trapping sites and recombination centers. Moreover, the low mobility of electrons and holes within the (104) plane explains its low conductivity [49]. The intensity of this peak decreases with the increase of annealing temperature and time [insets of Figures 3.9(a) and (b), respectively], ultimately improving the anisotropic conductivity. The increase of the anisotropic conductivity is also corroborated with the presence of the (110) preferential orientation for both sets of samples. The (110) reflection is indicative of growth along the [110] direction on the substrate, referred by several authors to have four orders magnitude higher anisotropic conductivity than the direction perpendicular to it [33,49,51,74,75]. However, a higher (104) contribution obtained for hematite NWs annealed with different time [Figure 3.9(b)] may be related to the lower *j* obtained in general for this set of samples [Figure 3.2(c)].

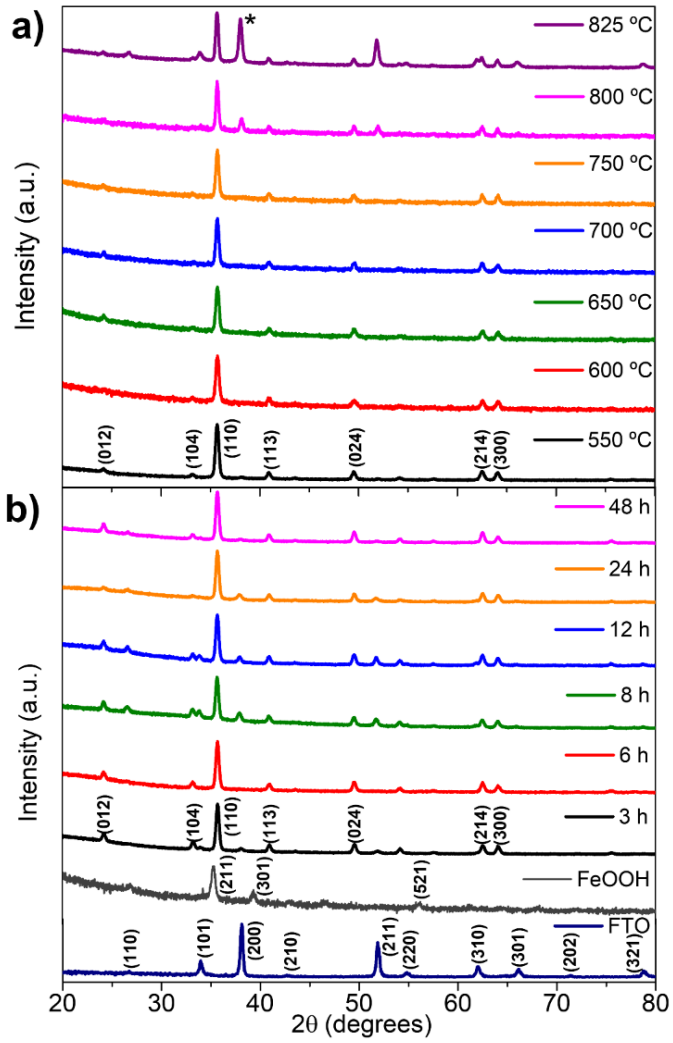

Figure 3.8. XRD spectra of α-Fe_2O_3 samples annealed with different (a) temperature (550-800 °C) and (b) time (3-48 h). The * symbol indicates FTO peak.

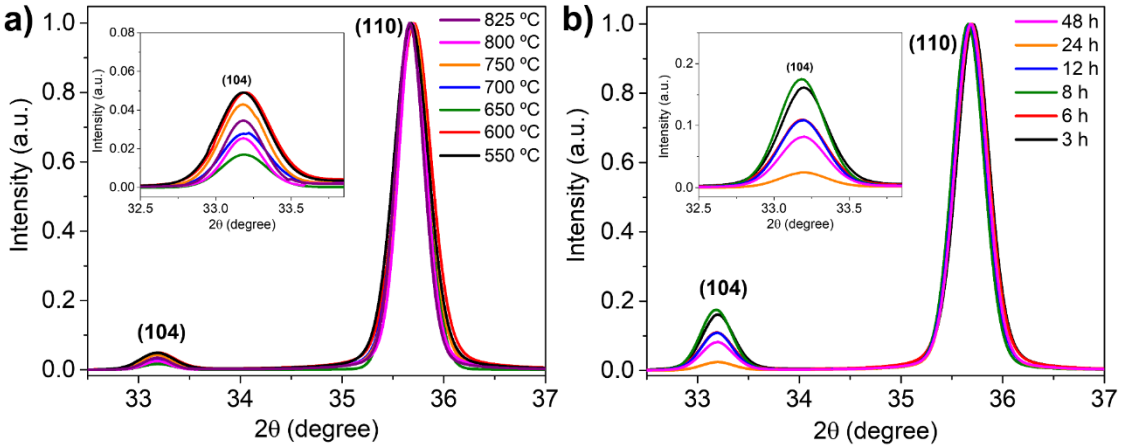

Figure 3.9. XRD refinement spectra of preferential orientation (110) of α-Fe_2O_3 samples annealed with different (a) temperatures and (b) time. Insets shows higher magnification of peak (104) refinements.

For both sets of samples also a different broadening of the preferential (110) peak is observed (Figure 3.9). A small narrowing of the peak is observed as the annealing temperature and time increase, being more evident in the set of different temperatures. The meaning of the XRD peak broadening is indicative of grain size refinement, but it is also related to other structural disorders, such as dislocations, microstrain or local strain heterogeneity [37,232,257].

From peak broadening analysis, crystallite size (D_{XRD}) and microstrain (ε) were estimated, using the Williamson-Hall method [235]:

$$w\cos\theta = \frac{k\lambda}{D_{XRD}} + 4\varepsilon\sin\theta \tag{3.1}$$

with w the full width at half-maximum (FWHM) of Bragg peaks, θ the diffraction angle, k the Scherrer constant (0.94) and λ the incident X-ray wavelength (1.540593 Å). From the $w{\cdot}\cos(\theta)$ *vs*. $4{\cdot}\sin(\theta)$ plots, D_{XRD} and ε were estimated from the intercept and slope, respectively (Figure 3.10).

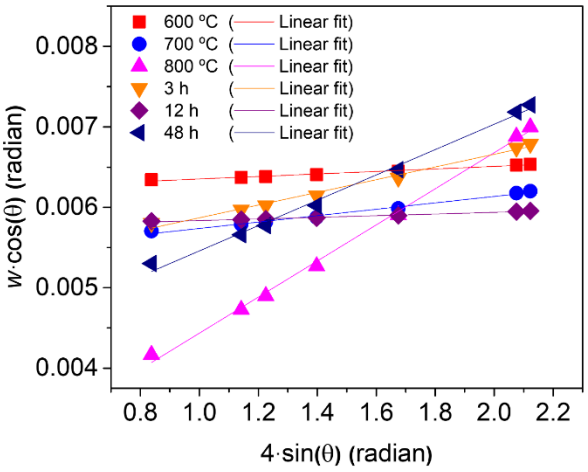

Figure 3.10. Linear fits using the Williamson-Hall relationship for representative samples from each annealing set (temperature and time).

Figure 3.11 shows the results of the D_{XRD} with annealing temperature and time and its relationship with j (at 1.45 mA·cm^{-2}) and D obtained from the SEM analysis. For samples with different temperature, D_{XRD} (and D) remains almost constant up to 700 °C and increases from 750 up to 800 °C, reaching a maximum value of 66 nm. Samples with higher annealing temperatures show good quality of nanostructures presenting larger crystallites and fewer lattice defects, conferred by short annealing at high temperatures [33,65,66]. This ultimately leads to good photoresponses since less

electron-hole recombination losses occur [37]. Although the 825 °C photoelectrode presents a comparable *j* to the 800 °C one, a lower D_{XRD} was obtained, probably affected by the FTO deformation at higher temperatures. Increasing annealing time up to 24 h, D_{XRD} presents approximately the same dimensions, Figure 3.11(b). On the other hand, at 48 h a slight D_{XRD} increase (to 37 nm) is observed in straight accordance with *j* and *D*.

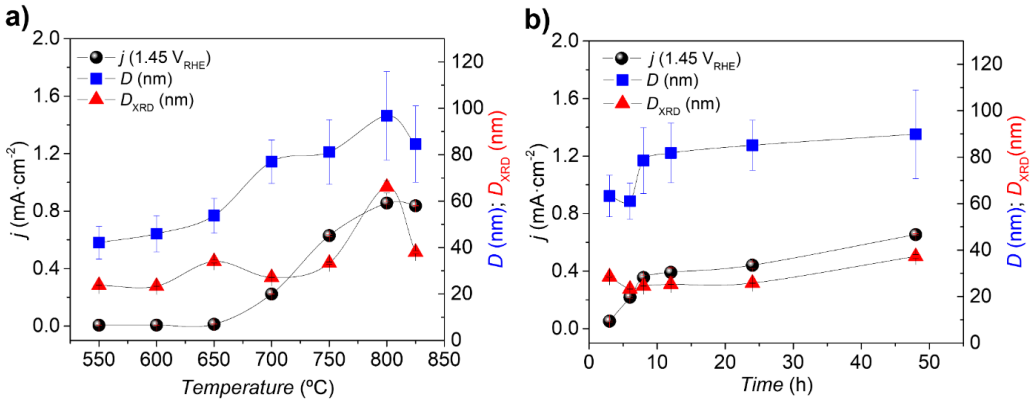

Figure 3.11. Results of photocurrent density (*j*), crystallite size (D_{XRD}) and NWs diameter (*D*) of α-Fe_2O_3 samples annealed with different (a) temperature and (b) time.

On the other hand, $\varepsilon < 0.2\%$ was obtained for almost all samples (Table 3.2). When ε takes such low values, it is usually considered not significant for physical properties and can be overlooked [37,266,267]. One exception is the 800 °C sample, with $\varepsilon = 0.22\%$. The ε parameter is correlated with the local strain non-homogeneity due to lattice dislocations/distortions and grain surface relaxation, that can be caused when dopants such as Sn are incorporated into hematite structure by Fe substitution [37,56,232]. Although not significant ($\varepsilon < 0.2\%$), ε also increases with increasing annealing temperature and time (Table 3.2). We believe that a surface relaxation, besides being caused by the increase of crystal size, is induced by the growing increment of Sn into hematite NWs, which could also justify the volume expansion of the unit cell, V_{cell} (see Table 3.2).

X-ray Absorption Fine Structure analysis. X-ray Absorption near the edge structure (XANES) analysis allows the determination of the electronic structure [259]. The XANES results for samples with different annealing temperature and time were compared with the iron oxide references α-Fe_2O_3, γ-Fe_2O_3 and Fe_3O_4 (Figure 3.12).

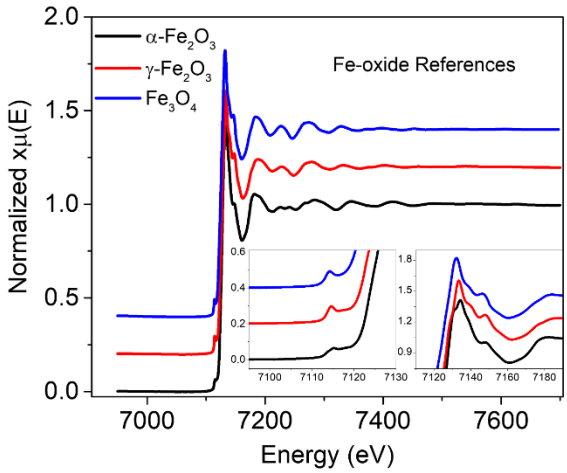

Figure 3.12. XANES spectra of Fe-oxide references: α-Fe_2O_3, γ-Fe_2O_3 and Fe_3O_4 (insets showing in detail the pre-edge and edge peaks).

It was identified the typical hematite structure for all samples (pre-edge and edge peak features and energy positions correspond to the one of hematite reference) as can be seen in Figures 3.13(a) and (b), respectively for annealing temperature and time. The position of pre-edge peak center (known as centroid) and its intensity are key factor for the Fe oxidation state determination. In the literature, the 7115 eV pre-edge peak is attributed to hematite and referred as the quadrupole transition of 1s → 3d [268]. Looking close to the pre-edge peaks in Figures 3.13(c) and (d), all the samples are aligned with the centroid position from the α-Fe_2O_3 reference [268].

Figure 3.14 shows the extended X-ray absorption fine structure (EXAFS) spectra, that allows the determination of the geometrical structure concerning the atoms around Fe [259]. The EXAFS were obtained by the k^3-weight functions of the Fourier transforms of Fe k-edge. All the hematite photoanodes showed two peaks in the Fourier transforms of EXAFS functions, as usually reported in literature [32,56,113,269].

While the first peak (0.6–2.0 Å) is attributed to the nearest Fe-O bond and commonly referred to the increase of ordering in the nanostructure [56,113,259,269], the second peak (2.1–3.9 Å) is related to the contribution from Fe-M (M= Fe or Sn, Ti or other dopant) and Fe-O bonds at a greater distance [56,113]. Furthermore, the intensity of this peak gives a perception of dopant environment around Fe atoms.

For both sets of samples with different annealing temperature and time, Figures 3.14(a) and (b), the peaks have higher intensity than the α-Fe_2O_3 powder reference, which indicates an enhanced bond ordering for the NWs grown on the FTO surface.[113] A slight increase in the first peak is noticed for the samples with 800 °C and 48 h annealing conditions (Figures 3.14 and 3.15). This indicates an enhancement of the structural order with the annealing temperature and time.

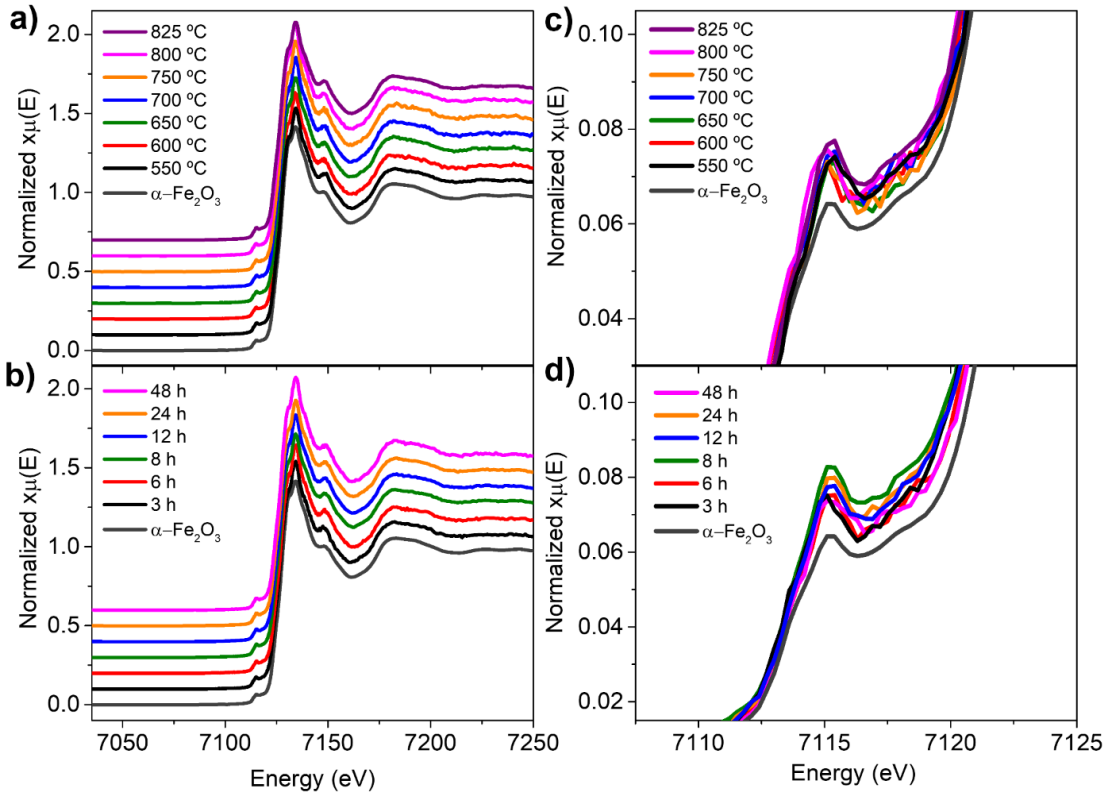

Figure 3.13. XANES spectra of hematite NWs with different annealing (a) temperature and (b) time; (c) detail of the pre-edge peaks for hematite NWs with different annealing (c) temperature and d) time. All spectra are compared with the α-Fe_2O_3 reference powder.

The second peak also increases with the annealing temperature, being more evident in the 800 ºC photoanode. This peak is ascribed to the backscattering of Sn atoms, that are incorporated into hematite lattice by diffusion from FTO substrate with annealing temperature. As higher is the Sn concentration, the stronger will be the atomic backscattering and thus more intense will be the second peak [56,113,269].

For samples with different annealing time, no significant differences were observed, however the slight increase in the second peak for the 48 h sample also indicates a Sn evolution through the hematite nanostructure, Figures 3.14(b) and 3.15(b).

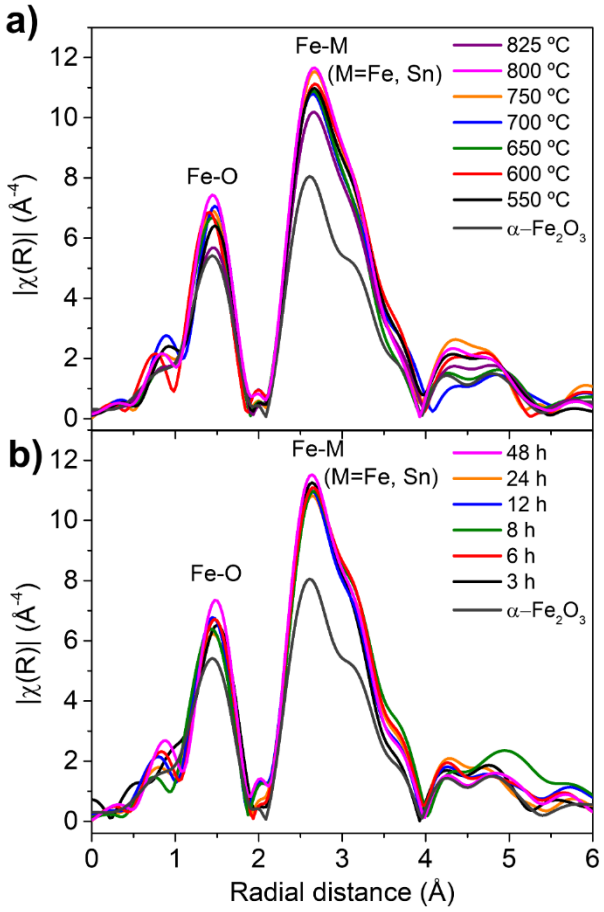

Figure 3.14. K^3-weigthed Fourier-transforms of Fe K-edge EXAFS functions for hematite NWs with different annealing (a) temperature and (b) time.

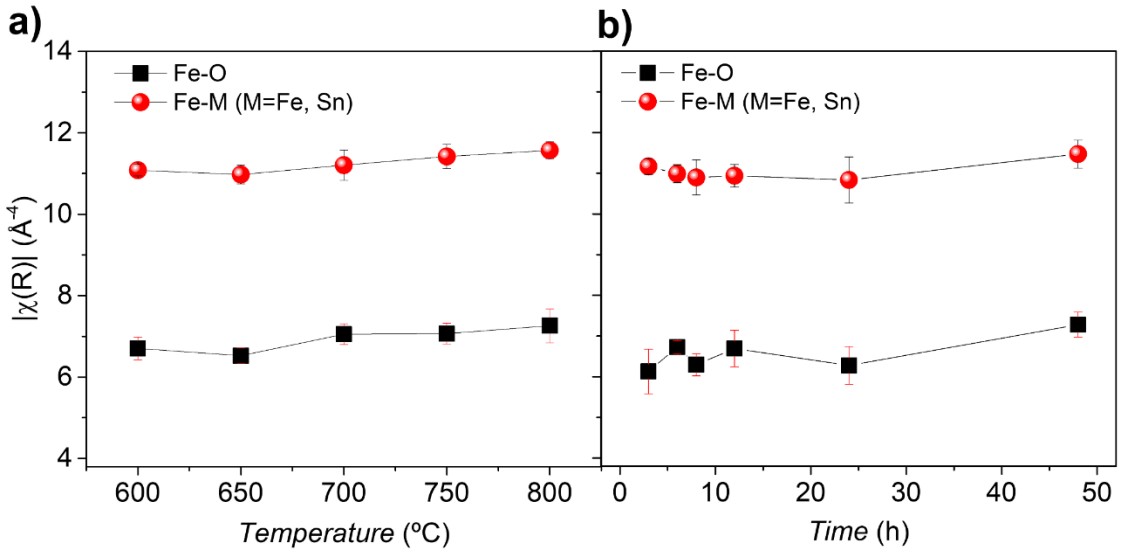

Figure 3.15. Maximum intensity of peaks Fe-O and Fe-M (from k^3-weighted Fourier transforms of EXAFS functions for Fe k-edge) for hematite NWs with different annealing (a) temperature and (b) time.

In the Fourier transformed data, the increase in the intensities of the first and the second peaks is directly correlated with decreasing the Debye–Waller factor (σ^2), which is related with the structural disorder [259]. By fitting the EXAFS data, using Artemis software [247], σ^2 was calculated (Table 3.2). σ^2 decreases as the annealing temperature increases, confirming the well ordering of the atomic structure and quality of the samples. This improvement of bond ordering is also in straight accordance with XRD results in which an increase of crystalline structure occurs for higher annealing temperature (Figure 3.11). It is more evident at 800 °C, in accordance with D_{XRD} analysis. Furthermore, σ^2 for all photoelectrodes is smaller than for the reference α-Fe_2O_3 confirming higher ordering of the NW structures nucleated upon FTO [114,259]. However, σ^2 presents in general higher values for the set of annealing time. This behaviour is probably caused by some FTO deformation with prolonged annealing time.

Table 3.2. Lattice parameters (a, b, c and V_{cell}) and microstrain (ε) obtained by structural refinement of XRD; Structural Debye Waller factor (σ^2) parameter obtained by EXAFS fits using Artemis software.

Sample	a=b (Å)	c (Å)	V_{cell} (Å^3)	ε (%)	σ^2 (Å^2)
600 ºC	5.0290	13.7532	50.20	0.01563 ± 8E-4	0.00782
700 ºC	5.0307	13.7567	50.25	0.0398 ± 0.002	0.00723
800 ºC	5.0313	13.7580	50.27	0.2244 ± 0.005	0.00656
3 h	5.0289	13.7526	50.20	0.07894 ± 0.004	0.00539
12 h	5.0327	13.7526	50.28	0.01025 ± 5E-4	0.00802
24 h	5.0312	13.7526	50.25	0.02648 ± 0.001	0.00825
48 h	5.0318	13.7526	50.27	0.1575 ± 0.006	0.00756
α-Fe_2O_3	-	-	-	-	0.01158

Rutherford Backscattering Spectrometry analysis. RBS is a very sensitive structural analysis technique that can be used to determine the distribution in depth of chemical elements [236-239]. In this work, it revealed to be crucial to evaluate the Sn diffusion induced by annealing temperature and its influence in our photoanodes photoresponse. While XPS (X-ray photoelectron spectroscopy) gives atomic percentage information with a resolution of 5-10 nm in depth, RBS is a powerful technique that allows the atomic determination along photoanodes total layers (in the order of the photoanodes total thickness and from the surface).

In order to determine the atomic Sn percentage along the photoelectrodes layers, the sample annealed at 800 °C with higher photocurrent efficiency (*j*) was analyzed using RBS and compared with samples with lower efficiencies (550 °C and 600 °C). Figures 3.16(a) and (b) shows respectively the RBS random spectra of the FTO substrate and the referred samples where the 2 MeV He^+ α particles are impinged at the sample with an incident angle (θ) of 5° with respect to the sample normal and are collected in a scattering angle θ_2 of -140°.

According to the random spectrum of the calibration sample (not shown), the Sn and Fe elements were identified at the surface for the studied samples. The Sn and Fe barriers are identified in Figure 3.16(b) as vertical arrows around channels 500 [E= 1710 keV] and 450 [E= 1573 keV], respectively.

In the simple cases, considering for example a non-rough Fe film with Sn at the surface, the chemical composition is straightforward as the ratio between the signals of the elements in the spectra and its scattering cross sections calculated for the backscattering angle and beam α particles energy (2000 keV). Not only the Sn % but other quantities, such as layer thickness, chemical composition, roughness and occupancy percentage of voids were derived via RBS simulation [237-239,242].

The total thickness of the Sn containing region depicted in Figure 3.16(b) was simulated using the NDF code [237,242] as having 580 nm, which agrees well with the FTO thickness taken from SEM images ($L_{FTO\ mean}$ ~ 525 ± 32 nm). On the other hand, the Fe signal suggests a total thickness of a region containing iron of around 200 nm. Moreover, measurements using different incident angles (20 ° and 30 ° not shown) indicate that both Fe and Sn are already present at the surface of the samples. The shape of the Sn and Fe signals between 1260 keV and 1520 keV suggests a roughness-diffusion mechanism according to the analysis of the NDF code [238,239]. On this mechanism, Sn atoms are moving towards the surface (deduced by the decrease of the Sn-yield in that energy range with increasing annealing temperature) and the Fe-yield is increasing smoothly suggesting a slightly increase of roughness as the annealing temperature increases. Furthermore, the shape of the Sn-signal changes from a sharp barrier-like spectra to a more tilted barrier if RBS random spectra of FTO [Figure 3.16(a)] is compared with the random spectra of annealed structures. Two hypothetic effects can produce such tilting: decreasing of detector resolution and roughness increasing. The first hypothesis is discarded due to measurement (10 keV) of the detector energy resolution.

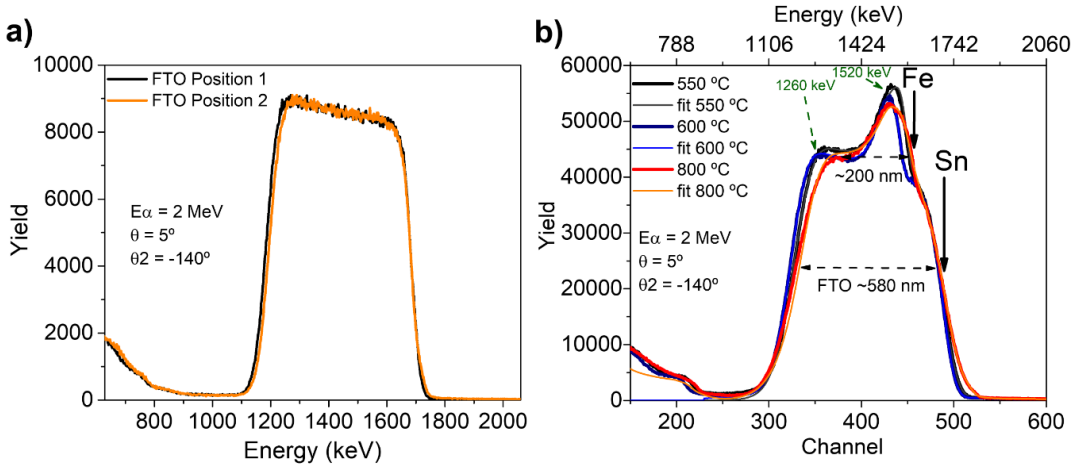

Figure 3.16. RBS spectra of (a) FTO substrate and (b) α-Fe_2O_3 NWs annealed at 550 °C, 600 °C and 800 °C, and respective fits.

Through the random spectra fitting, parameters such as Sn atomic % along the photoanodes thickness were determined for the samples annealed at 550 °C, 600 °C and 800 °C. It was found that the sample with 800 °C has an increase of Sn % along the NWs depth, reaching a maximum value of ~8% at the surface and distributed over a layer of ~162 nm. The larger amount of Sn is usually associated with the increase of photoactivity, due to the increase of donor density and thus the electrical conductivity [33,64,65,111,113,114,262]. Therefore, this kind of photoanodes shows improved electrical conductivity properties that ultimately lead to higher *j*. Similar Sn % results under the same conditions have been reported by XPS analysis [33]. On the other hand, the 550 °C photoanode presents only 0.6% of Sn at the surface and distributed alongside a layer with ~198 nm. This smaller Sn % justifies the reduced *j* obtained for the sample with 550 °C and is usually attributed to the low conductivity of bare hematite [8,33,39]. Figure 3.17(a) shows the Sn distribution along the NWs layers, i.e., Sn % × simulated thickness, where simulated thickness varies from 100-200 nm for 550-800 °C, and Sn % varies from 0.6-8%. In fact, the photoanode with 800 °C shows ~10 times more Sn than the one with 550 °C. The presence of higher Sn %, not only at the surface, but homogeneously distributed along the nanowires, allows the enhancement of the charge separation efficiency and transport along the photoelectrodes, leading to higher *j* [33,111,113,262]. Therefore, *j* is directly related with Sn doping through FTO diffusion.

Additionally, higher microstrain (ε) and volume expansion of the unit cell (V_{cell}) observed for the 800 °C photoelectrode, as referred above, can now be confirmed in good correlation with higher Sn diffusion at this temperature.

The simulation of the RBS spectra reveals also a decrease of the voids fraction as *D* increases with annealing temperature, Figure 3.17(b). In fact, as *D* increases, the empty space between NWs will decrease and thus the voids fraction naturally should decrease.

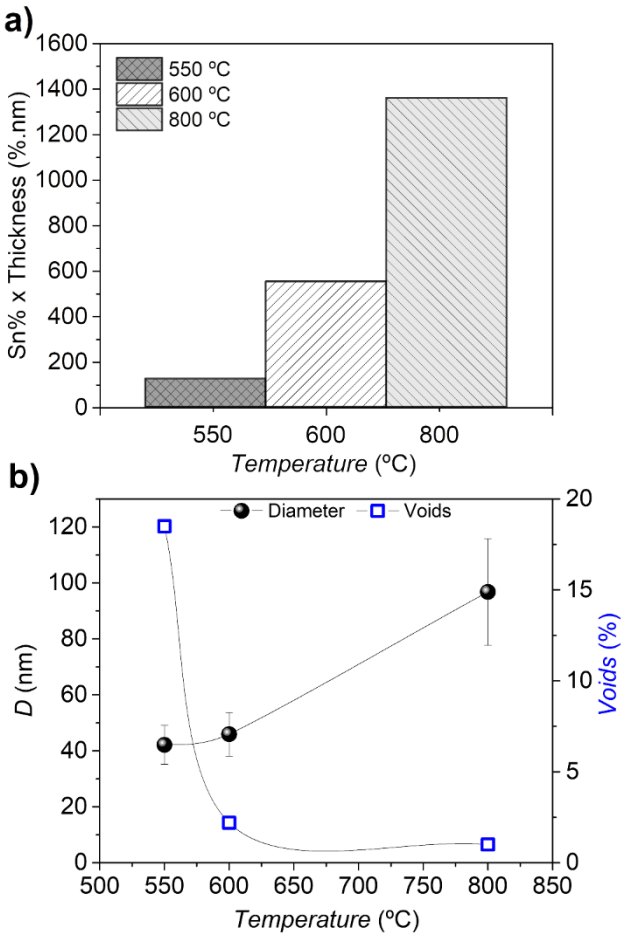

Figure 3.17. (a) Sn % × simulated thickness determined by RBS fits for samples with 550 °C, 600 °C and 800 °C; b) Voids % (from first layer ~100-200 nm) determined by RBS fits for samples with 550 °C, 600 °C and 800 °C, in comparison with NWs diameter (*D*).

3.3.4. Optical characterization

Figures 3.18(a) and (b) show respectively the absorption spectra for the photoelectrodes annealed with different temperature and time. The maximum absorption peak was observed at ~440 nm for samples annealed up to 700 °C and up to 8 h. Above this temperature and time, the maximum absorption shifts to higher wavelengths (red-shift) in the range of 531-540 nm (see also Table 3.3), which corresponds to samples with higher *j*, NWs diameter (*D*) and Sn incorporation (which enhances the hematite conductivity) [56,65,270].

Usually, hematite thin films display an intense absorption peak around 400 nm [43,113,250], whereas mesoporous nanostructures show two different absorptions peaks at 375 and 535 nm [271]. A transition in the absorption coefficient α = 535 nm has been previously attributed to spin forbidden ligand field (6A1 → 4E) transition and is related to changes in the nanostructures morphology [65,270]. The maximum absorption shift was also reported for mesoporous nanostructures and it is governed by the morphology (particle size and shape), annealing temperature or use of dopants. For example, a red-shift was observed with higher particle size and Sn incorporation [56,65]. As could be verified by EXAFS and RBS, the presence of Sn was confirmed in those samples with higher absorption, leading to increased photocurrent.

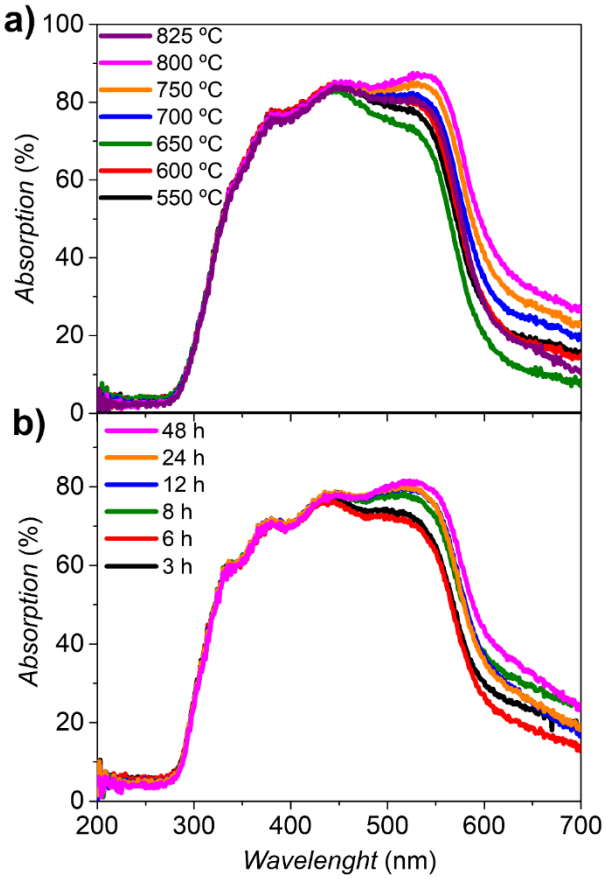

Figure 3.18. UV-vis absorption spectra of hematite NWs with different annealing (a) temperature and (b) time.

It is usually described that thicker samples absorb more visible light [37], but the analyzed samples do not show a significant difference concerning the thickness *L* (analyzed by SEM; Figure 3.19 and Table 3.3). Thus, the observed differences in the absorption should be due to NWs diameter (*D*) and/or porosity features. Considering the higher absorption peak at λ= 531 nm, near to the know absorption band at 18690 cm^{-1}

described by Marusak *et al.* [270], and assigned to ligand field transitions [which corresponds to an absorption coefficient (α) of (126.46 nm)$^{-1}$], the thickness ($L_{UV\text{-}vis}$) of the NWs was estimated:

$$-\alpha L_{UV\text{-}vis} = \ln(1\text{-}Absorbance) \quad (3.2)$$

and compared with the thickness L from SEM analysis (Figure 3.19).

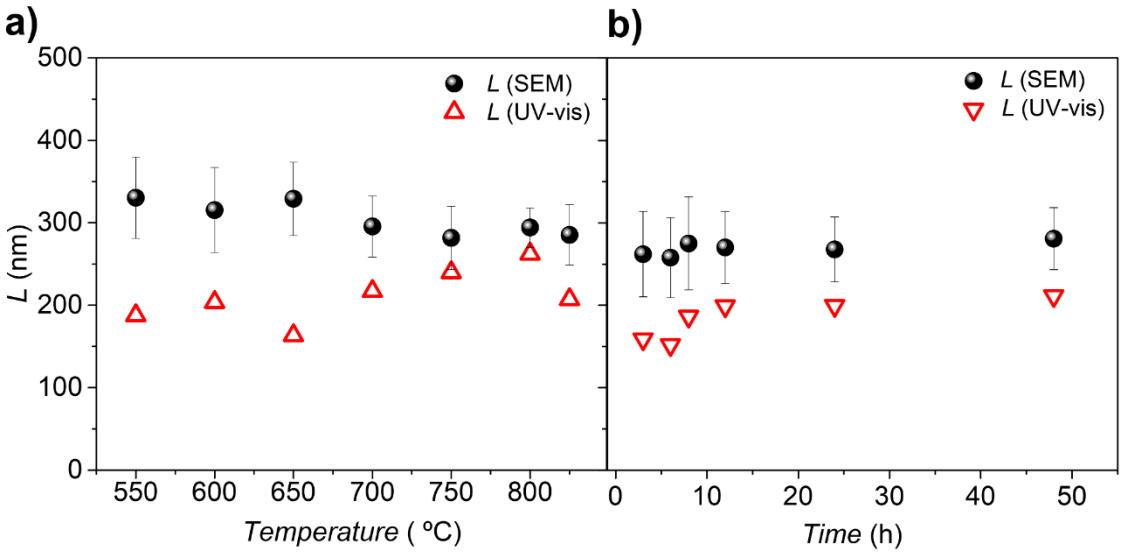

Figure 3.19. Comparison between the thickness determined by SEM cross-section images (L) and the thickness estimated by UV-vis absorption ($L_{UV\text{-}vis}$) for hematite NWs synthesized with different annealing (a) temperature and (b) time.

The porosity - P - of the photoelectrodes can be determined from L and $L_{UV\text{-}vis}$:

$$P = \frac{V_{bulk} - V_{oxide}}{V_{bulk}} \times 100\ \% = \frac{L - L_{UVvis}}{L} \times 100\ \% \quad (3.3)$$

where V_{bulk} is the volume of bulk material (NWs plus pores) and V_{oxide} is the volume of hematite NWs [272].

The porosity (P) of hematite NWs is shown in Figures 3.20(a) and (b). The results show an inverse porosity and j relation, as annealing temperature and time increase. P decreases from ~43 to 11% as the annealing temperature increases from 550 °C to 800 °C [Figure 3.20(a)]; on the other hand, the porosity decreases from ~40 to 25% as the annealing time increases from 3 h to 48 h [Figure 3.20(b)]. It should be emphasized the same decreasing trend obtained by RBS fits regarding the voids fraction, Figure 3.17(b), in strong correlation with the porosity results.

Moreover, the porosity average P_{mean} ~33% using all *P* values (temperature and time) obtained in Figure 3.20. On the other hand, if we analyze a SEM cross-section image of the NWs (Figure 3.21), by delimiting a rectangular area that represents the bulk area (A_{bulk} = 1088 μm^2), and delimit the area of the NWs (A_{oxide} = 732 μm^2), it is possible to estimate the porosity using Eq. (3.3); the porosity obtained using this approach is *P* ~32.7%, which corroborates with the effective porosity confirming the above results.

Usually in the literature, porous structures (higher *P*) indicate higher photoactive surface areas of the photoelectrodes [16]. Here, a porosity opposite trend with *j* occurs. *P* decreases with the increase of *j* for both groups of samples (figure 3.20). However, the photoresponse is not only determined by the morphology, other key factors influence the *j* behaviour in our samples such as the structure-crystallinity and Sn "unintentional" doping and conductivity:

i. Morphology: as annealing temperature and time increase, the nanowires diameter (*D*) increases, leading to a decrease of the empty space between NWs (and thus the porosity decreases);
ii. Structure-crystallinity: as annealing temperature and time increase, the crystallite size (D_{XRD}) also increase, the quality of the photoelectrodes at the level of crystalline order and lattice arrangement is improved;
iii. Sn "unintentional" doping and conductivity: as annealing temperature and time increase, the Sn diffusion from FTO into hematite leads to the increase of conductivity and the photocurrent increases.

Therefore, the photocurrent response of the hematite NWs photoanodes is the balance of these three factors. What we see here is that all factors i., ii., and iii. are more important than the impact of the surface area factor (porosity).

The band gap of the hematite photoelectrodes was obtained from the Tauc plots [252]:

$$(\alpha h\nu) = A(h\nu - E_g)^n \quad (3.4)$$

where $h\nu$ is the incident photon energy (in eV), E_g is the optical band gap energy (in eV) and *A* and *n* are constants dependent on the electronic transition; *n* = 2 for direct and *n* = 1/2 for indirect allowed transitions [37,47]. The determined band gap values, calculated for *n* = 1/2, agrees with the reported in the literature [8,39,65]. The band gap decreases with the increase of annealing temperature and time [Figures 3.20(c) and (d), and Table 3.4], as the *j* increase. In fact, with the increase of annealing temperature and time, we have higher Sn diffusion that leads to the enhancement of the photoelectrodes conductivity. The porosity and band gap evolution for both sets of samples (for higher annealing temperature and time) revealed a similar decreasing trend (Figure 3.20). As

referred above, this decrease was mainly attributed to particle size effects, crystalline order and changes in lattice parameters, usually induced by Sn doping [65,113], as observed in EXAFS studies and confirmed by RBS analysis.

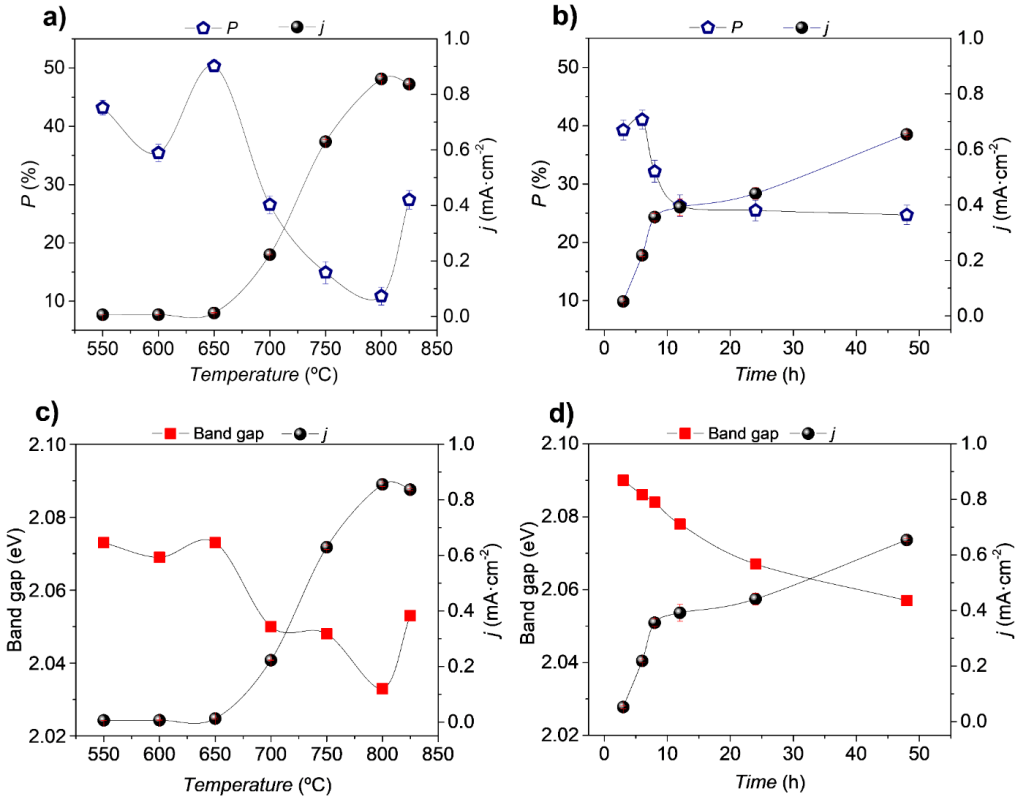

Figure 3.20. Porosity (*P*), calculated from SEM analysis of NWs thickness (*L*) and thickness from spectrophotometric analysis ($L_{UV\text{-}vis}$), for samples with different (a) temperature and (b) time, comparing with photocurrent density (*j*); optical band gap for hematite NWs with different annealing (c) temperature and (d) time.

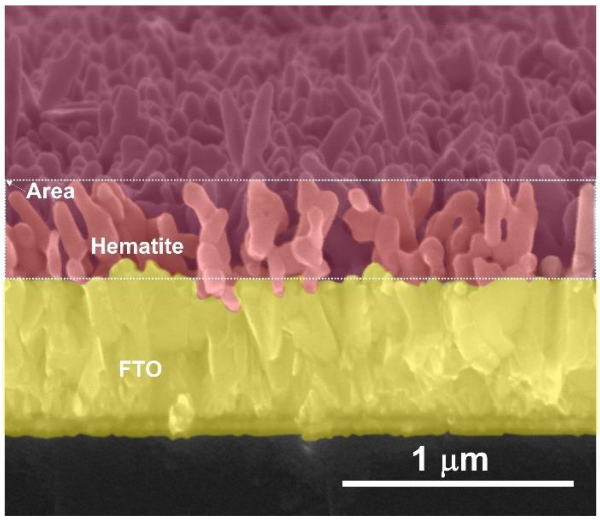

Figure 3.21. SEM cross-sectional image of hematite NWs with delimited bulk (dashed white line) and nanowires (reddish) areas.

Table 3.3. Absorption (at 440 and 531 nm), *L* (SEM) and $L_{UV\text{-}vis}$ for samples with different annealing temperature and time.

Sample	Absorption (%) (440 nm)	Absorption (%) (531 nm)	*L* (nm)	$L_{UV\text{-}vis}$ (nm)
550 ºC	84	77	330 ± 50	188
600 ºC	85	80	315 ± 52	204
650 ºC	84	73	329 ± 44	164
700 ºC	85	82	296 ± 37	217
750 ºC	85	85	282 ± 39	240
800 ºC	85	87	294 ± 24	262
825 ºC	84	81	285 ± 37	207
3 h	77	72	262 ± 52	159
6 h	76	70	258 ± 49	152
8 h	79	77	275 ± 56	187
12 h	79	80	270 ± 44	199
24 h	79	80	268 ± 39	200
48 h	78	81	281 ± 38	211

Table 3.4. Optical band gap for hematite NWs with different annealing temperature and time.

Temperature (ºC)	550	600	650	700	750	800
Band gap (eV)	2.073	2.069	2.073	2.050	2.048	2.033
Time (h)	3	6	8	12	24	48
Band gap (eV)	2.090	2.086	2.084	2.060	2.072	2.061

3.4. Conclusions

In this work, the impact of annealing temperature and time on the photo-performance of hematite nanostructured photoelectrodes was thoroughly investigated. Higher photocurrent densities typical of bare hematite were observed for photoelectrodes annealed with a two-step approach, at 550 °C for 2 h followed by 20 min at 800 °C (~0.9 $mA \cdot cm^{-2}$) and under one-step approach at 600 °C during 48 h (~0.7 $mA \cdot cm^{-2}$). Under the two-step annealing approach, the photocurrent increased with the increase of the temperature. This was ascribed to the improvement of structural crystalline order and the increase of the Sn amount diffused from FTO substrate layer within the hematite

crystalline lattice. The hematite nanowires showed a preferential crystal orientation along (110) plane for both annealing schemes (temperature and time) that confers improved conductivity ultimately leading to improved photocurrents. However, the photoelectrodes annealed with different time showed a more intense (104) crystalline reflection peak, indicating limited conductivity that results in lower photocurrents. XANES studies confirmed the presence of pure hematite crystallographic phase, while EXAFS confirmed the Sn doping, which was corroborated by RBS analysis. The sample with two-step annealing at 800 °C displayed the highest photocurrent, related to an improved donor density and electronic conductivity. Accordingly, the RBS analysis showed that the in-depth Sn % profile for this sample was ca. 10 times higher when compared with the sample annealed at 550 °C (with the lowest photocurrent). Additionally, the cross-sectional views allowed to estimate the thickness of the NWs porous like photoelectrodes. Combining with optical UV-vis absorption spectra, it was estimated the porosity of the hematite photoelectrodes active and effective layer. Furthermore, the photoelectrodes porosity and photocurrent are inversely related, for both annealing conditions (temperature and time). The differences observed in absorption spectra (red-shifted), caused by the increase of NWs diameter with higher annealing temperature and time, are clearly reflected in the porosity decrease. In addition, the porosity shows a decreasing performance similar to the one of the voids fraction obtained from the RBS simulation. The porosity also revealed a similar trend with the band gap, assigned to the Sn diffusion that affects the absorption. With this work, the underlying insights of the annealing conditions, temperature and time, and its impact in the performance of hematite NWs were unveiled, important for future improvement of hematite photoelectrodes.

Chapter 4

Doping and implantation strategies for hematite nanowires

Chapter 4

Doping and implantation strategies for hematite nanowires

This chapter describes the synthesis of doped hematite nanowires (NWs) by hydrothermal method. The effect of titanium doping and the influence of annealing conditions was investigated. The morphology and crystalline structure of the prepared samples were analyzed. The photoelectrochemical (PEC) performance and the stability of the photoanodes were evaluated. Improved photocurrent of 1.27 mA·cm^{-2} was obtained using both schemes, for Ti-dopant incorporation, but also with annealing temperature.

Another approach used in this work to improve the hematite´s conductive properties was the Sn ion implantation. The effect of Sn ion concentration (fluence) on hematite´s morphological, structural and optical properties, comparing with pristine hematite, was here under discussion.

4.1. Titanium doping by hydrothermal method

4.1.1. Overview

Hematite (α-Fe_2O_3) enables the absorption of about 40% of the solar spectrum energy [8,39,41] and its use for PEC water splitting predictions is reaching the theoretical solar-to-hydrogen conversion efficiency of 16.8%. However, the limiting performance of α-Fe_2O_3 is affected mainly due to its poor conductivity (~10^{-14} $\Omega^{-1}\cdot cm^{-1}$), low carriers mobility (~10^{-2} $cm^2\cdot V^{-1}\cdot s^{-1}$), and short hole diffusion length (2-4 nm), that leads to high electron-hole recombination and significant efficiency losses [29,45-47,90,133,273]. Among the several reported strategies to overcome the limiting challenges of successfully improve the semiconducting oxide photoresponse, dopant incorporation and material architecture control with nanostructuring techniques have been the most widely addressed.

The use of dopants in hematite leads to the increase of the charge density, provides more direct ways to electron transport, improves the electrical conductivity and reduce

the surface states playing an important role in PEC photoresponse [33,44,49,56,57,113-115,253,265]. Dopants such as Si, Ti or Sn, just to name a few, have been incorporated in hematite by different synthesis techniques. Among them, thin films physical and chemical deposition, spray pyrolysis, or hydrothermal techniques have been intensively explored in literature [8,39,54,55,60,65]. Sivula *et al.* introduced Si incorporation in mesoporous thin films of hematite (~500 nm), reaching a *j* of 2.3 $mA \cdot cm^{-2}$ [53,54,97]. For Si-doped lower thin films (~50 nm) obtained by spray pyrolysis, *j* of 0.35 $mA \cdot cm^{-2}$ could be obtained [55]. On the other hand, Sn dopant in hematite films with the same thickness (50 nm) obtained by PLD increased *j* to 1 $mA \cdot cm^{-2}$ [60].

One of the most common n-type cation dopants for hematite photoelectrodes is titanium (Ti) [32,37,57], and regarding its use, a state-of-the-art photocurrent of ~6 $mA \cdot cm^{-2}$ was already achieved, using NWs structures [115]. In particular, Ti-dopant by hydrothermal techniques has become one of the main sources of hematite photocurrent improvements [115,259,274,275].

In the present work, the use of Ti dopant combined with thermal annealing conditions were studied to understand their role in the morphology, crystalline structure, optical properties and PEC activity of α-Fe_2O_3 NTs prepared by a hydrothermal method. Our strategy is to use the acquired knowledge from the consistent study previously made (Chapter 3), to increase the crystallinity quality of the hydrothermal photoelectrodes by using improved thermal annealing conditions [33,66,67]. Also, the photocurrent stability and the internal solar-to-chemical (ISTC) conversion efficiency of prepared photoanodes were assessed. Uniform and high quality photoelectrodes were obtained reaching photocurrent density performances of 1.27 $mA \cdot cm^{-2}$.

4.1.2. Experimental details

The α-Fe_2O_3 NWs with and without Ti incorporation were prepared by hydrothermal method [91] (as described in Chapters 2 and 3). First, FTO (1.2 X 2.5 cm^2) substrates were previously cleaned as reported elsewhere [261] and placed in a Teflon stainless steel autoclave. Two schemes of samples were prepared by hydrothermal process (i) to obtain bare hematite NWs and (ii) Ti-doping hematite NWs. (i) Two FTO samples were immersed in autoclave with 20 mL solution of 0.15 M $FeCl_3.6H_2O$ and 1 M $NaNO_3$, adjusted at pH 1.5 with HCl 37% [33,276], and heated at 95 °C for 4 h (Chapter 3). (ii) In the case of Ti-doped samples, also two FTO samples were immersed in the same solution (i) plus 10 µL of Ti isopropoxide was added, and then heated at 95 ºC during 13 h [57].

The hydrothermal as-prepared samples from both systems are not in crystalline hematite phase ([67]; Chapter 3), so for this to occur it was necessary to perform an thermal annealing. Here, one or two-step annealing treatment approaches were used: the one-step annealing consists in annealing at 600 ºC for 3 h; the two-step annealing includes a first step at 550 ºC for 2 h and a second step fast annealing at 800 ºC for 20 min. As-prepared samples with and without Ti dopant were sintered for both one-step and two-step annealing. For Ti-doped samples, after the thermal annealing, the samples were again placed in autoclave with solution (i), and heated at 95 ºC for 20 min [57].

The morphological, structural and optical characterizations were performed using respectively SEM, XRD in BB and PB modes and RAMAN spectroscopy, and by UV-vis techniques. The PEC characterization was assessed by *j-V* curves, stability tests and ISTC determination (details are described in Chapter 2).

4.1.3. Results

Morphological characterization. After the autoclaving process the (undoped) as-prepared film layer of iron oxyhydroxides (β-FeOOH) NWs was formed on the top of FTO substrates [Figure 4.1(a); Section 3.3.2] [67]. The NWs are completely formed at this first stage due to the thermodynamically stable nucleation of Fe ions in solution, with controlled conditions of temperature and pressure [91].

After the one-step annealing at 600 ºC [Figure 4.1(b)], the NWs become more rounder, however they thicken, the diameter (*D*) notably increases, when subjected to a two-step annealing approach [Figure 4.1(c)]. The NWs *D* dimensions taken from the top SEM images [inset of Figure 4.1(c)] shows an increase from 63 (± 9) nm to 97 (± 19) nm, regarding the one-step to the two-step annealing approaches, respectively [Figure 4.2(a)]. This increase is usually ascribed to the fusion between neighbouring NWs [33,64,67].

As for the Ti-doped photoelectrodes, as-prepared films presented also the complete formation of the NWs, similar to non-doped β-FeOOH NWs [Figure 4.1(d)]. After the one-step annealing a more compact characteristic was attained comparing with the undoped samples [Figure 4.1(e)]. Indeed, the NWs are not so individualized with smaller NW dimensions and less porous structure comparing to the non-doped sample with the same annealing conditions. The same trend of the undoped samples in terms of the NWs diameter dimensions was observed for the two annealing schemes: *D* increases from 46 (± 15) nm to 79 (± 8) nm for the one-step and two-step annealing, respectively [Figure 4.2(a)].

Overall, the *D* sizes for the Ti-doped hematite NWs are smaller when compared with the bare hematite NWs.

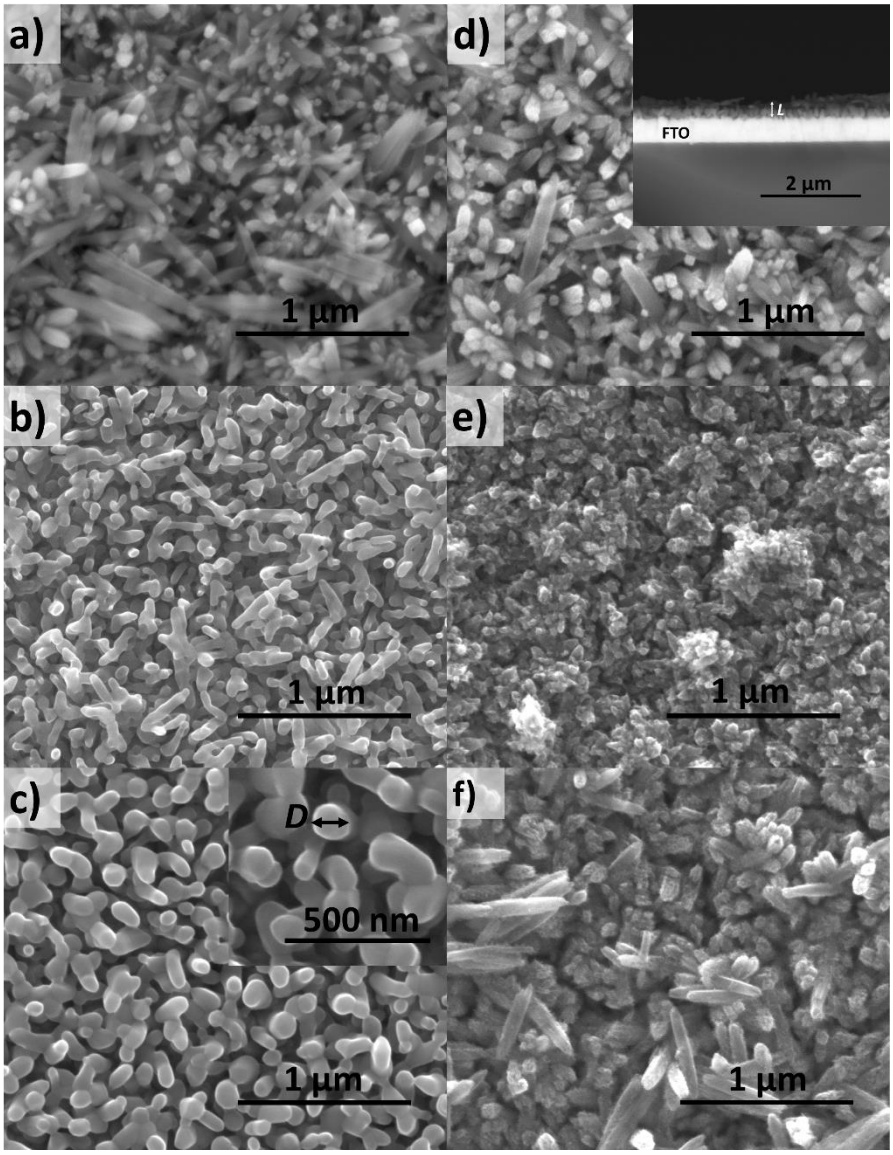

Figure 4.1. SEM images of (a) FeOOH NWs after hydrothermal synthesis, α-Fe_2O_3 NWs with (b) one-step and (c) two-step annealing (inset exemplifies the diameter, *D*, measurements). (d) Ti-doped FeOOH NWs after hydrothermal synthesis (inset shows a cross-section image illustrating the thickness *L* measurements), Ti doped α-Fe_2O_3 NWs with (e) one-step and (f) two-step annealing.

From the cross-sectional images [as represented in the inset of Figure 4.1(d)], the thickness *L* of the NWs was obtained [Figure 4.2(b)]. For undoped samples, *L* did not vary much, a mean value of ~280 nm was obtained for both annealing schemes. Comparatively, Ti-doped resulted in longer NWs, *L* ~395 nm for one-step and *L* ~333 nm

for two-step annealing; the slight *L* decrease can be induced by higher temperature annealing [262].

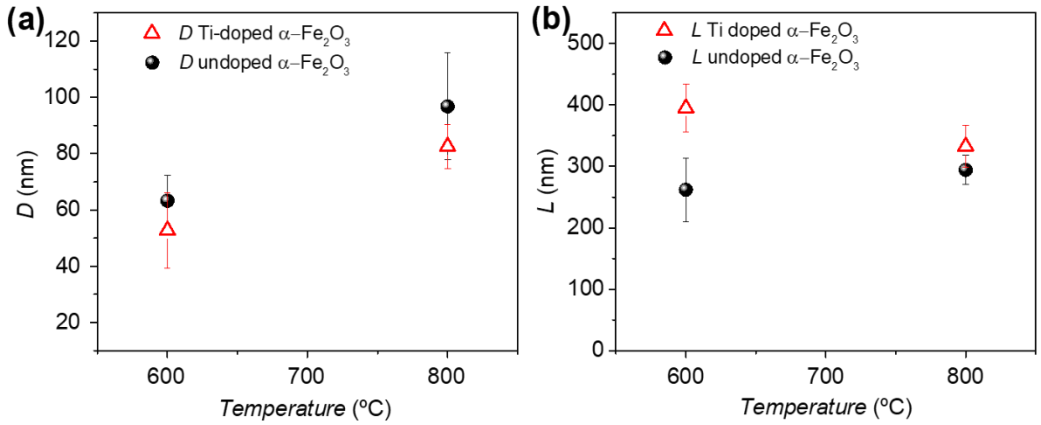

Figure 4.2 α-Fe_2O_3 NWs (a) diameter (*D*) and (b) thickness (*L*) as a function of annealing temperature, for undoped and Ti doped samples.

Structural analysis. Figures 4.3 and 4.4 shows the XRD diffractograms for both groups of photoanodes samples, bare hematite NWs and Ti-doped hematite NWs.

Here, we had the opportunity to use two distinct configuration modes of XRD, BB and PB, to determine the photoelectrodes crystalline structure. In BB focusing configuration, a deep incidence analysed area is considered. After autoclaving, the as prepared NWs present a peak with a (211) orientation corresponding to the β-FeOOH phase (JCPDS 34-1266). The crystalline phase of hematite (α-Fe_2O_3) was presented for both types of photoanodes, with or without Ti doping, regardless of the type of annealing approach applied. As the analysed NWs have a small thickness (~300 nm) the main peaks detected are relative to the FTO substrate, and only few peaks of hematite were obtained, in Figures 4.3(a) and (b), respectively for undoped and Ti-doped samples [33,56,57,64,114,115]. Even though, the diffractograms shows the thermodynamically stable hematite phase [91] with a main peak that grows in preferential orientation (110) (JCPDS 33-0664). Other hematite peaks, such as (104) or (300) are also present, although with low coherency resolution [Figures 4.3(a) and (b)]. Overall, the spectra for all the samples show no significant differences either for undoped or Ti-doped samples, i.e. no peaks indexed to the presence of Ti were observed [Figure 4.3(b)].

The spectra of PB with grazing incidence angles mode configuration were indexed to α-Fe_2O_3 crystallographic phase (JCPDS 33-0664), and several peaks such as (012), (104), (110), (113), (024), (214) or (300) are unveiled (Figure 4.4; as referred in Chapter 3 [67]).

For Ti doped samples, no significant changes in crystalline structure were noticed comparing to undoped ones, displaying the same hematite preferential orientation (110) [33,57]. The preferential orientation (110) is indicative of growth along the [110] direction vertical to substrate, that is referred to have higher anisotropic conductivity than the orthogonal direction [33,97] on the substrate. However, for Ti-doped hematite, other diffraction peaks such as (104) also increased, suggesting a less oriented growth of hematite in relation to the substrate, as reported in literature [32], especially with the 600 ºC annealing.

Furthermore, like the BB configuration, no additional peaks attributed to the presence of Ti element were revealed using PB configuration (Figure 4.4).

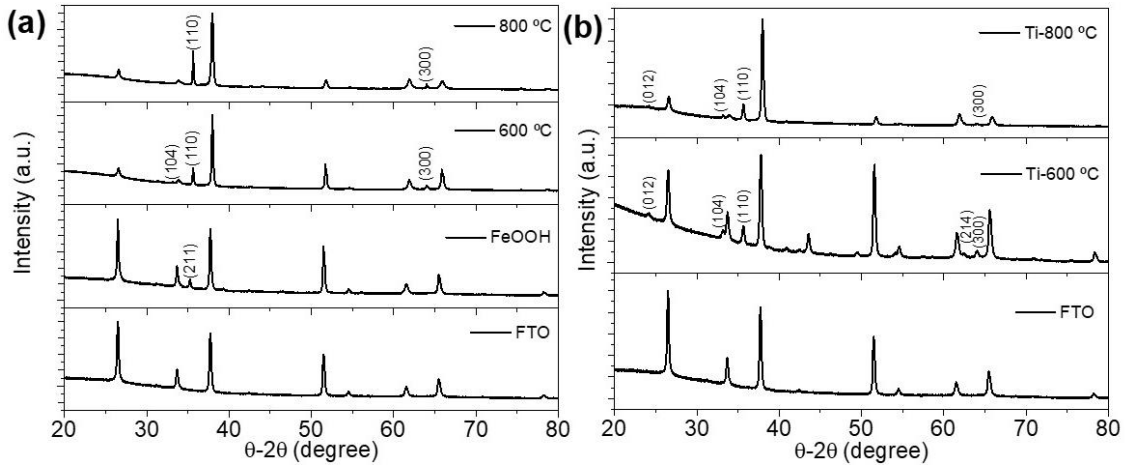

Figure 4.3. XRD diffractograms of non-doped and Ti-doped hematite nanowires, obtained using Bragg-Brentano measurements.

From the PB diffractograms we were able to determine the crystallite size (D_{XRD}) and microstrain (ε) using Williamson-Hall method [Eq. (2.2), Chapter 2] [235]. The results are presented in Table 4.1.

With a two-step annealing with temperature at 800 ºC, it is observed an increase of the crystallite size (D_{XRD}), from 28 to 66 nm [Chapter 3, section 3.3.3 [67]] comparing with one step-annealing (Table 4.1). This was ascribed to the hematite crystalline improvement promoted by temperature, showing good quality and less lattice defects [33,65,66]. However, with Ti-doping, smaller crystallites were obtained: 21 and 30 nm, for Ti-doped NWs at 600 ºC and at 800 ºC, respectively (Table 4.1). Deng *et al.* showed a similar tendency, when comparing Ti-doped hematite with pristine hematite [32]. Furthermore, Annamalai *et al.* [259] referred a higher Debye–Waller structural disordering in Ti-doped hematite comparing with bare hematite, through EXAFS data

analysis. It seems that Ti incorporations lead to disordered structures with smaller crystallites sizes (less improved lattice order arrangements).

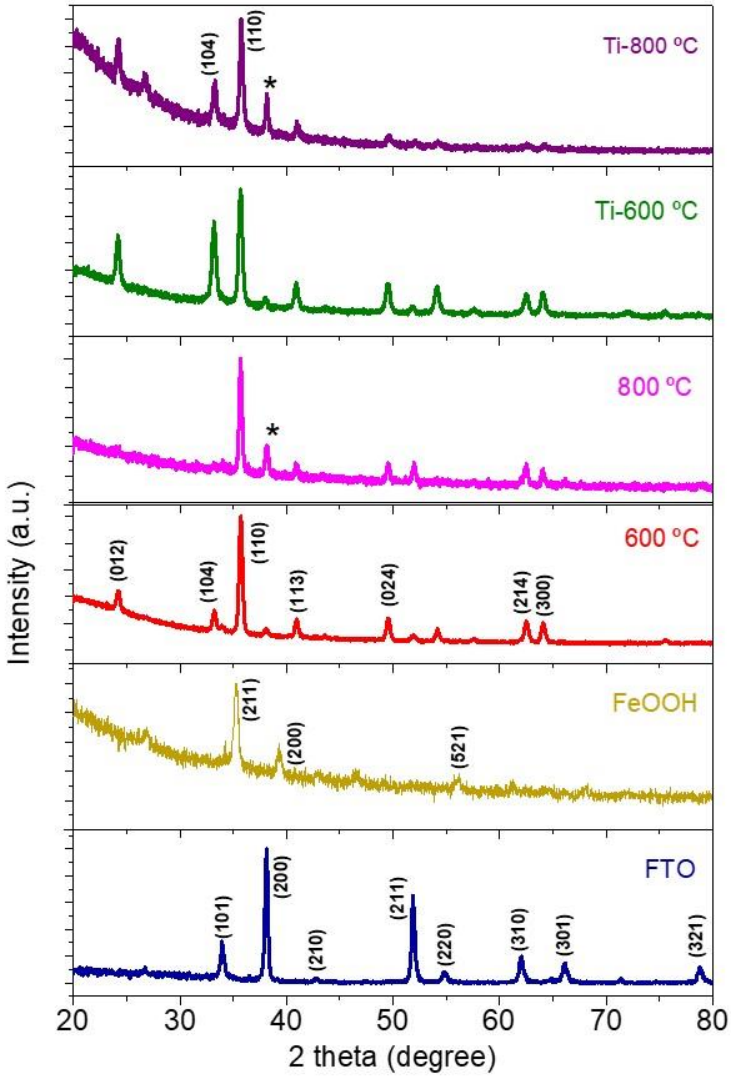

Figure 4.4. XRD diffractograms of as-prepared hydrothermal FeOOH nanowires (NWs), undoped and Ti-doped hematite NWs, obtained using grazing incidence angle measurements. The spectrum of F:SnO_2 (cassiterite) layer from FTO substrate is also shown.

ε parameter is correlated with structural lattice disordering, reflected by the local strain non-homogeneity due to lattice dislocations/distortions and grain surface relaxation. These features can arise from the Sn dopant incorporation in hematite structure by Fe substitution [37,56,232]. In fact, higher ε of 0.22% was obtained for 800 ºC sample due to the increase of Sn diffusion from FTO with temperature (Table 4.1). For Ti-doped samples, ε is not significant (in literature, ε < 0.2% can be considered negligible [37,266,267]). Although, a ε increase from 0.01 to 0.09% for Ti-600 ºC and Ti-800 ºC samples was found that can be related with the high temperature and Sn incorporation.

A surface relaxation, besides being caused by the increase of crystal size could also be induced by the growing increment of Sn into hematite NWs (Chapter 3).

Table 4.1. Crystallite size (D_{XRD}) and microstrain (ε) for hematite NWs with and without Ti-dopant.

Sample	**600 ºC**	**Ti-600ºC**	**800 ºC**	**Ti-800 ºC**
D_{XRD} (nm)	28 ± 0.3	21 ± 0.03	66 ± 0.005	30 ± 0.4
ε (%)	0.07894 ± 0.004	0.01 ± 5E-4	0.2244 ± 0.005	0.09 ± 0.004

In Figure 4.5, the Raman spectra shows the peaks correspondent to doubly degenerate E_g mode of hematite at 244, 293, 410 and at 612 cm^{-1} and to single degenerate A_{1g} mode at 225 and 497 cm^{-1} [277-279]. At 660 cm^{-1}, a peak starts to appear at Ti-doped (both one- and two-step annealing) and undoped (two-step annealing) samples; this peak was already assigned to surface disorder of hematite films, and could here be related with the introduction of Ti dopant [280].

A general peak broadening was found for samples with Ti doping, mainly due to the incorporation of dopants, causing some lattice distortion [277] (observed from the FWHM obtained through Igor software treatment). On the other hand, FWHM of the Raman peaks decreased for samples without Ti-dopant, suggesting the enhancement of α-Fe_2O_3 crystallinity [281], as corroborated by the XRD results obtained for D_{XRD} (Table 4.1).

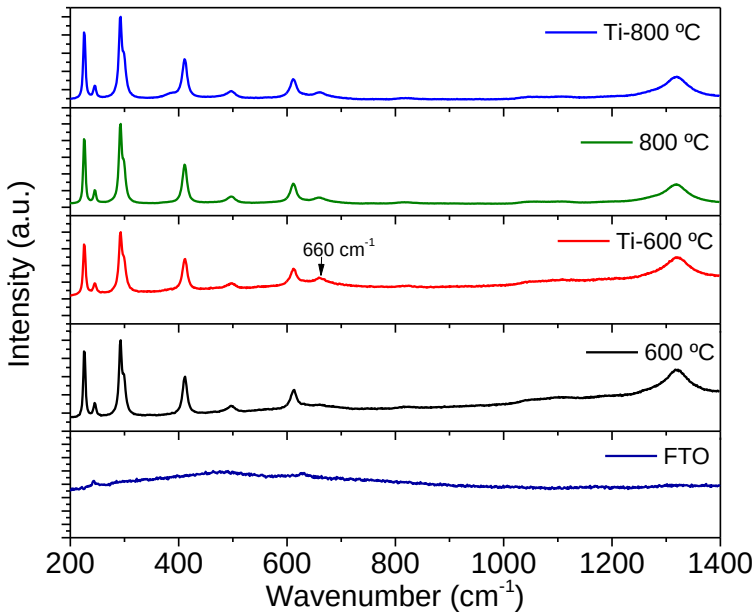

Figure 4.5. Raman spectra of undoped and Ti-doped hematite photoelectrodes.

Optical properties. In Figure 4.6(a), it is shown the absorption of the photoanodes annealed with one-step (600 ºC) and two-step (with additional annealing at 800 ºC), with and without Ti-dopant.

As happen already in the case of hematite NWs study of annealing temperature and time (Chapter 3), it is observed two different absorption peaks at 440 and 535 nm. The maximum absorption peak was observed at ~440 nm for samples annealed at 600 °C without dopant. With the addition of Ti, the absorption shifts to higher wavelength of 535 nm, ascribed to higher annealing temperature or the use of dopants [56,65]. Ti-doped and non-doped at 800 ºC present higher absorption. However, Ti-doped did not presented a significant red-shift (higher absorption was at 440 nm), probably affected by some glass bending due to high temperature affecting the absorption properties.

The optical band gaps for all the samples were determined using the Tauc formula [Eq. (2.11), presented in Chapter 2, section 2.3.4] [252]. The band gap was calculated for an indirect transition, through the plot of $(\alpha h\upsilon)^{1/2}$ *vs.* $h\upsilon$ [Figure 4.6(b)], and the results are displayed in Table 4.2. It was observed the decrease of the band gap with both the incorporation of Ti and with high temperature, from 2.090 to 2.045 eV. Higher Sn diffusion and Ti incorporation naturally leads to the enhancement of the photoelectrodes conductivity, as these substitutional tetravalent dopants (Sn^{4+} and Ti^{4+}) are expected to improve the electron-donor density, and thus the optical-absorption coefficient [33,65,114].

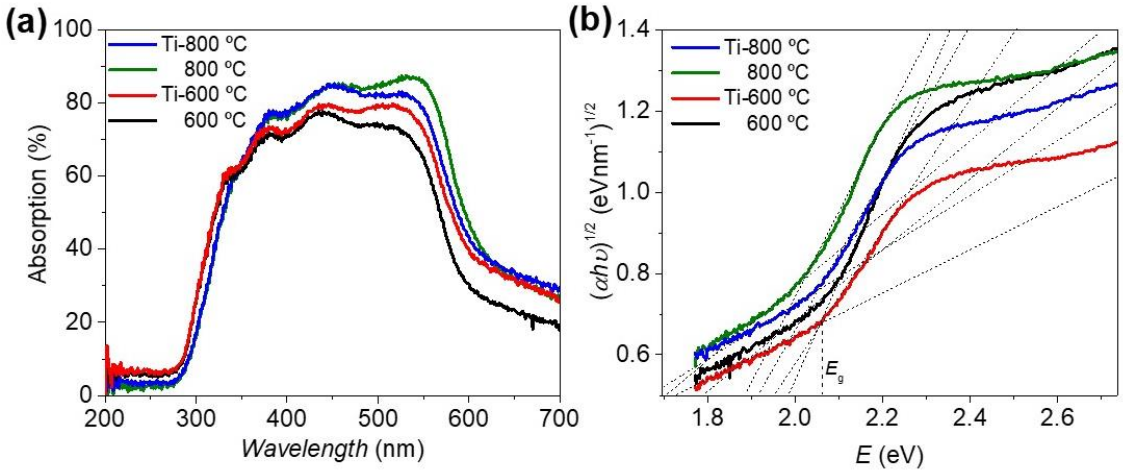

Figure 4.6. (a) UV-vis absorption spectra and (b) Tauc plots, $(\alpha hv)^{1/2}$ *vs. hv,* of undoped and Ti-doped hematite NWs photoelectrodes.

Table 4.2. Optical band gap for hematite NWs with and without Ti-dopant.

Sample	600 ºC	Ti-600ºC	800 ºC	Ti-800 ºC
Band gap (eV)	2.090	2.054	2.033	2.045

Photoelectrochemical performance. Figure 4.7 shows the photocurrent-density (*j-V*) curves for the synthetized α-Fe_2O_3 photoanodes. With one-step annealing, *j* is very low, ~0.02 mA·cm^{-2} (at 1.45 V_{RHE}), attributed to the low conductivity and short hole diffusion length of α-Fe_2O_3 [8,33,39]. The incorporation of Ti dopant allowed a *j* increase to 0.63 mA·cm^{-2} (1.45 V_{RHE}), ca. 30 times higher than undoped sample. With the two-step annealing, a *j* improvement (0.87 mA·cm^{-2} at 1.45 V_{RHE}) was observed, mainly attributed to the high temperature of 800 ºC that promoted the Sn diffusion from the FTO layer into the hematite structure, improving the conductivity and increasing the crystalline quality and structural order, as already explained in Chapter 3. By using both Ti dopant and two-step annealing, in which 800 ºC high temperature was used, the highest *j* of 1.27 mA·cm^{-2} (at 1.45 V_{RHE}) was obtained, which indicates a mutual effect of Sn diffusion (intrinsic Sn doping), Ti doping and the removal of surface defects induced by high temperature, increasing its conductivity [33,66,273].

The enhanced *j* can be attributed not only to the presence of added Ti, and Sn by diffusion, but also due to the different morphology, i.e., the improved surface area in Ti-doped hematite NWs with small diameters. Higher surface area due to the smaller NWs feature size [Figures 4.1(e) and (f)] increases the interface between the photoanode-electrolyte, enhancing the water splitting performance [16,32,33].

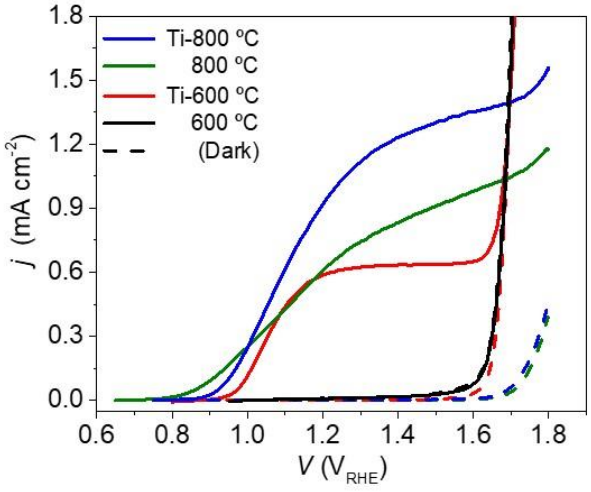

Figure 4.7. *j-V* characteristic curves for undoped and Ti doped α-Fe_2O_3 samples with one-step and two-step annealing.

The Ti dopant allowed a steeply photocurrent rise, *i.e.* indicative of lower recombination. However, an anodic shift of the onset potential (for higher potentials of 0.94 V_{RHE}) is observed in this case. For the undoped sample with two-step annealing, the Sn diffused from FTO with high temperature of 800 ºC promotes an earlier onset potential (~0.8 V_{RHE}) with a more gradual increase in the photocurrent.

A preliminary stability test was performed using a 600 ºC annealing Ti-doped α-Fe_2O_3 sample - Figure 4.8(a). *j* remained stable during a continuous measurement for 2 h applying a bias potential of 1.23 V_{RHE} under simulated 1-sun, showing a mean value of 0.570 ± 0.003 mA·cm^{-2}. The photocurrent over 0.8 – 1.8 V_{RHE} was also assessed before and after the stability test [Figure 4.8(b)]. It was verified a *j* stabilization, i.e., it does not decrease after the two hour of continuous measurement (the slight *j* increase after the stabilization test was probably due to the electrolyte heating). This results confirm the good stable properties of hematite, without signs of photocorrosion (when the photogenerated holes will oxidize the semiconductor, instead of water [16]).

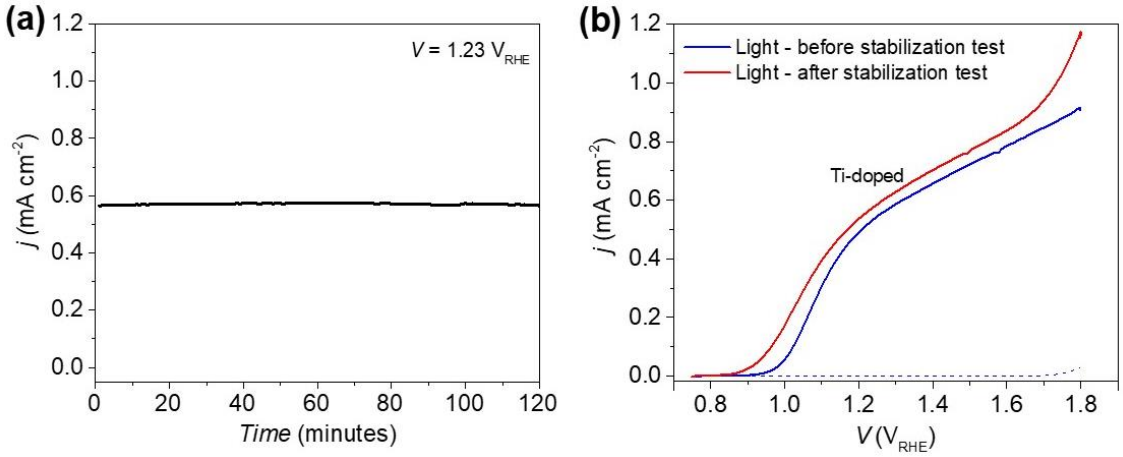

Figure 4.8. (a) Photocurrent stability test for Ti-doped α-Fe_2O_3 sample; and (b) respective *j-V* curves before and after the stability test.

To evaluate the efficiency of Ti-doped photoelectrodes in the conversion of photonic into chemical energy necessary for water splitting [43], the intrinsic solar to chemical (ISTC) conversion efficiency was determined. The photocurrent (J_{photo}) and photopotential (V_{photo}) were extracted from the *j-V* curves [Figure 4.9(a)], and J_{photo} was plotted as a function of the V_{photo} [Figure 4.9(b)], which yields the photocurrent density measured under short-circuit conditions (J_{sc}) and the open-circuit photopotential (V_{oc}).

The intrinsic photovoltaic power (P_{light}) of the photoelectrodes is given by the product of J_{photo} by V_{photo}, Eq. (2.8), and represented in Figure 4.9(c); by plotting it *vs.* V_{photo}, the

maximum power point (MPP) can be obtained and the respective voltage (V_{PP}) and current (J_{PP}). For Ti-600 ºC photoelectrode, it was obtained a maximum power of 0.28 mW·cm^{-2} (at a potential U_{light} of 1.17 V_{RHE}), while for Ti-800 ºC a power conversion efficiency of 0.67% (at U_{light} of 1.29 V_{RHE}) was achieved. The latter is significantly higher than correspondent sample at 800 ºC without Ti-dopant, with a P_{light} of 0.35% [represented in Figure 4.9(c); already shown in Chapter 3].

A significantly higher fill factor (*FF*) at MPP [Eq. (2.9)] was obtained for samples with Ti-dopant, $FF_{Ti\text{-}600ºC}$ = 70% and $FF_{Ti\text{-}800ºC}$ = 60%, comparatively with photoanodes without Ti, with a $FF_{800ºC}$ = 46.6%. Moreover, higher *FF* was obtained for the sample with Ti dopant at lower temperature (600 ºC), strengthening the effect of only Ti dopant, i.e. without the extra effect of the Sn dopant diffused from FTO into hematite with the higher temperature of 800 ºC. Higher *FF* could indicate photoanodes where lower recombination factor and higher charge extraction rates occur [263,264]. The *j-V* curves with Ti doping have a similar behaviour with the expected ideal hematite photoanode curve, with higher *FF*, in which a steep *j* increase is observed before reaching the *j* plateau (in Figure 1.10, Chapter 1).

Figure 4.9(d) shows the plot of ISTC conversion efficiency as a function of J_{photo}. ISTC maximum efficiencies of 0.21% (at J_{photo} of 0.56 mA·cm^{-2} and U_{light} of 1.17 V_{RHE}), 0.24% (at J_{photo} of 0.71 mA·cm^{-2} and U_{light} of 1.3 V_{RHE}) and 0.43% (at J_{photo} of 1.04 mA·cm^{-2} and U_{light} of 1.3 V_{RHE}) were obtained, respectively for Ti-600 ºC, 800 ºC and Ti-800 ºC photoanodes. In order to obtain the same photocurrent values in the dark, it would be necessary potentials of 1.7, 1.8 and 1.9 V_{RHE}, respectively for the Ti-600 ºC, 800 ºC and Ti-800 ºC photoelectrodes [taken from the *j-V* dark curves in Figure 4.9(a)]; for these photoelectrodes, the solar-simulated light power (100 mW·cm^{-2}) saves respectively 0.50, 0.49 and 0.64 V from the external power source, which yields a power of 0.28 mW·cm^{-2} (= 0.50 V x 0.56 mA·cm^{-2}), 0.35 mW·cm^{-2} (=0.49 V x 0.71 mA·cm^{-2}) and 0.67 mW·cm^{-2} (=0.64 V x 1.04 mA·cm^{-2}) [43,67,251]. These calculations give the potential that should be applied to the photoanodes in order to ensure the conversion of solar to chemical power at its maximum intrinsic conversion efficiency. The obtained values are in deep accordance with the literature for hematite photoelectrodes [43,251].

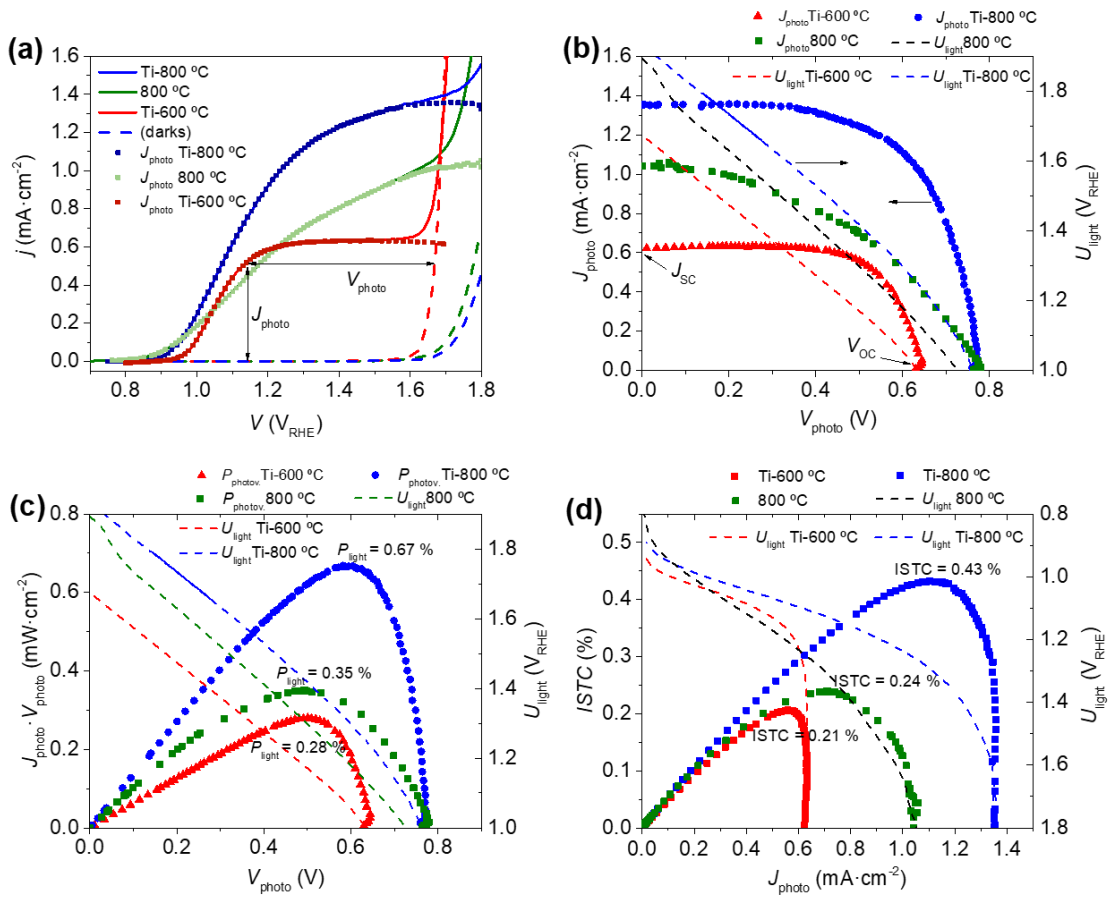

Figure 4.9. (a) *j-V* curves for the Ti-600 ºC, 800 ºC and Ti-800 ºC photoanodes, obtained in the dark (dashed lines) and simulated solar illumination (solid lines) and the respective photocurrent, J_{photo}; (b) photocurrent (J_{photo}) as a function of the photopotential (V_{photo}); (c) intrinsic photovoltaic power (P_{light}) as a function of V_{photo}; (d) ISTC efficiencies as a function of J_{photo}. In the secondary *y* axis on the right, it is plotted the potential (U_{light}) applied to the photoanode under light.

4.2. Sn implantation on hematite nanowires

4.2.1. Overview

Ion implantation is a powerful tool for *ex*-situ incorporation of ions into materials, with interest for many applications, from optoelectronics, to semiconductor industry [240,241,282]. In this process, the ions of one or more elements are introduced in the lattice of a solid material. The ions to be implanted are accelerated into the target material, causing changes in its properties, at the physical, chemical or electrical levels [241].

In Chapter 3 it was discussed the effect of Sn diffused from FTO into hematite through thermal annealing effect. This unintentional doping, although referred to improve hematite´s conductive properties, is not a controlled process [33,64,262]. Here, a

different approach was explored, the incorporation of positively charged Sn into the hematite lattice, in which the ions concentration (well known as fluence) can be controlled.

Few works have mentioned the use of this technique for water splitting, in which an increase of the photocurrent (from 0.2 to 1.2 $mA \cdot cm^{-2}$ at 0.6 V *vs.* SCE) and a maximum efficiency of 1.5% at 0.60 V *vs.* SCE was obtained for implanted Au/TiO_2 material [283].

In this work, the implantation of Sn into hematite NWs was performed, using two fluence regimes, 10^{15} and 10^{17} $atoms \cdot cm^{-2}$, in order to study the effects on the morphology, crystalline structure, optical properties and solar-to-current conversion of implanted hematite NWs.

4.2.2. Experimental details

Hematite NW samples were first prepared by hydrothermal method as already described in Chapters 2 and 3. FTO glass substrates were cleaned as described elsewhere [261], and then placed in a 40 mL capacity teflon stainless steel autoclave with 20 mL solution of 0.15 M $FeCl_3.6H_2O$ and 1 M $NaNO_3$, adjusted at pH 1.5 with HCl 37% [33]. The autoclave was heated at 95 °C for 4 h to obtain the iron oxide NWs. Then a thermal annealing was necessary to obtain the α-Fe_2O_3 phase: at 550 ºC for 2 h [33]. This thermal treatment was the minimum to obtain the hematite phase, maintaining nanowires with an optimum photoactive surface area [in figure 3.6(d)], with small diameters that could enable the holes transport to the photoelectrodes surface for water oxidation [262].

Within a collaboration between IFIMUP and IPFN - Instituto de Plasmas e Fusão Nuclear, CTN-IST, the α-Fe_2O_3 NWs were implanted with different fluences of Sn ions. To assess the composition and element distribution, Rutherford Backscattering Spectrometry (RBS) technique was also used. The ion implantation, RBS measurements and simulations were carried out by Dr. Sérgio Magalhães, at IPFN. This is an ongoing work and only preliminary results are here presented.

The implantation was carried out using two ion (Sn^+) fluences: lower and higher fluences of 10^{15} and 10^{17} $atoms \cdot cm^{-2}$, respectively, were settled in order to study the effect on hematite NWs properties. A Sn^+ maximum energy of 180 KeV and an angle of 0° (between the ion beam and the sample) were used. Previously to the ion implantation, SRIM (Simulation of Radiation of Ions in Matter [284]) software was used, an ion projected range of 46 nm was obtained (Figure 4.10).

After implantation, the samples were once again annealed, i.e. a second annealing with the same earlier conditions at 550 ºC for 2 h was performed to restructure the crystalline order and Sn atomic rearrangement in the hematite lattice.

A sample, the so-called control sample, consisting of hydrothermal hematite NWs without implantation and with first annealing at 550 ºC for 2 h, was prepared and subjected to the same characterization techniques as the implanted samples.

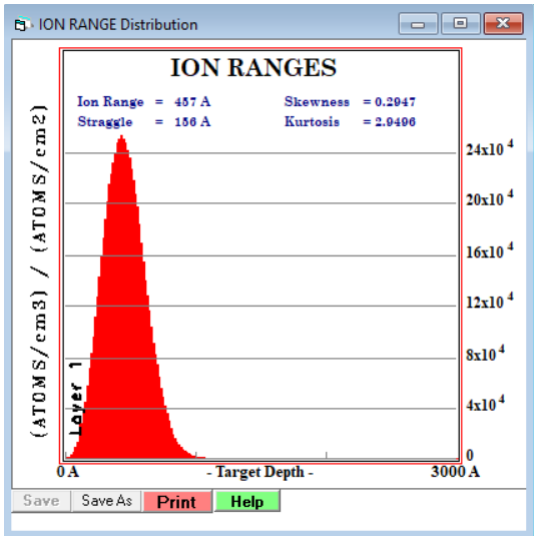

Figure 4.10. Image depicting the result of ion range determination, obtained by SRIM simulation software [284].

The morphological, structural, optical and photoelectrochemical characterization was performed using respectively SEM, XRD (PB mode), UV-vis spectrophotometry and *j-V* curves (Chapter 2).

4.2.3. Results and discussion

Morphological characterization. Figure 4.11 shows the SEM images of hematite NWs samples as-implanted with two fluences, lower (10^{15} ion·cm^{-2}) and higher (10^{17} ion·cm^{-2}) Sn concentration.

Ion implantation can cause damages in the lattice of the materials, creating defects or even changes in the morphology. However, some of these defects are recoverable performing thermal annealing at high temperatures [240]. Thus, the as-implanted samples were annealed again in order to rearrange the Sn atoms inside hematite lattice and to enhance the crystalline order.

The sample implanted with lower fluence (10^{15} ion·cm^{-2}) [Figure 4.11(a)] maintained the same morphology as the control sample 550 ºC [shown in Figure 3.6(d) in Chapter 3], although a slight coalescence of the nanowires was verified. The sample implanted with higher fluence (10^{17} ion·cm^{-2}) showed a significantly different morphology, with much higher porosity, and a larger diameter induced by higher ionic concentration [Figure 4.11(c)]. After the annealing post-implantation at 550 ºC, the morphology for both Sn implantation fluences was preserved [Figures 4.11(b) and (d), respectively for lower and higher fluences].

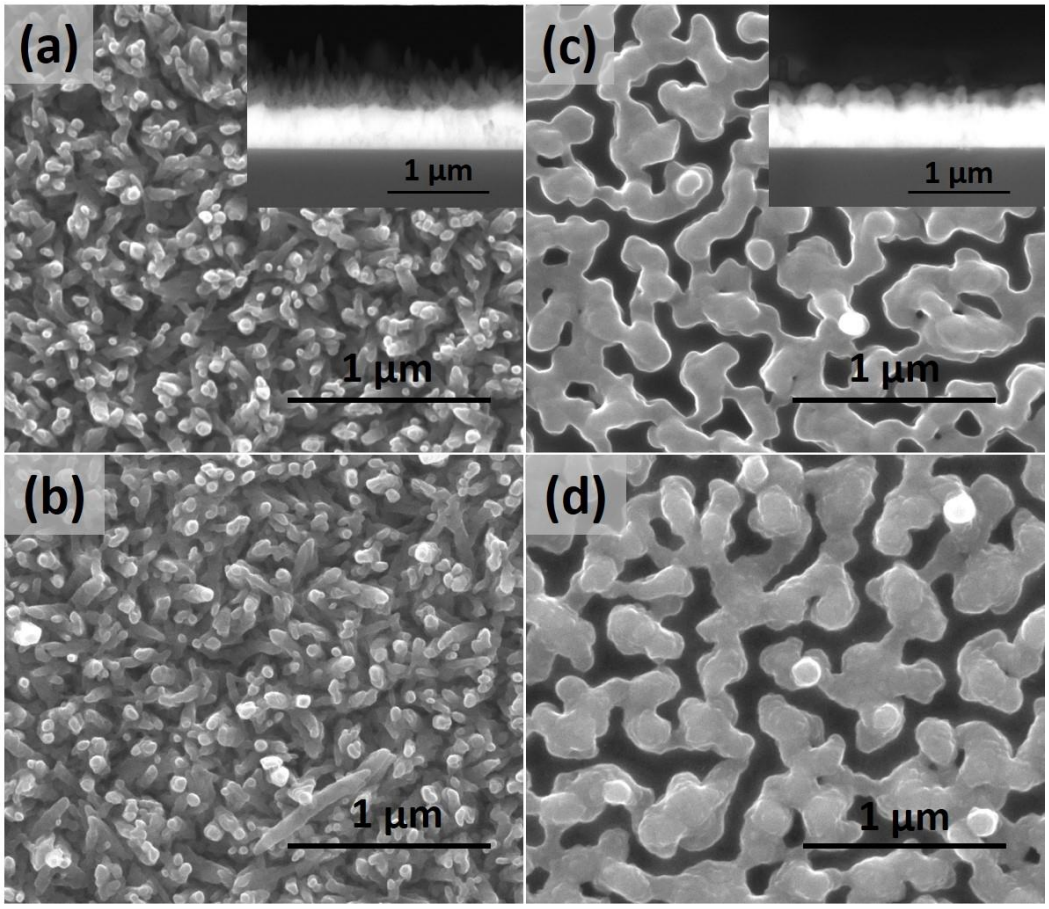

Figure 4.11. SEM top images of hematite NWs samples (a) as-implanted with a fluence 10^{15} ion·cm^{-2} and (b) after annealing at 550 ºC; (c) as-implanted with a fluence 10^{17} ion·cm^{-2} and (d) after annealing at 550 ºC.

Also, for the sample with higher Sn fluence, the NWs diameter (*D*) highly increased to ~135 nm (Table 4.3). This substantial increase of the NWs diameter can be a disadvantage for water splitting applications. Due to the typical low diffusion length (2-4 nm) of generated holes of hematite, higher NWs diameters may difficult the movement of minority carriers (holes) to the semiconductor surface for water oxidation, leading to higher electron-hole recombination and limited photocurrents [64,65,285]. On the other

hand, the thickness (*L*) of the samples with high fluence decreased from 330 to ~200 nm, comparing with the control sample at 550 ºC, whereas the low fluence samples practically maintained *L* and *D* (Table 4.3). The increase of *D* and decrease of *L* in samples implanted with higher fluence (Table 4.3) are associated to coalescence of NWs induced by the implantation process (probably due to the higher exposure time to beam and higher ionic concentration).

Table 4.3. Diameter (*D*) and thickness (*L*) for hematite NWs without and with Sn-implantation

Sample	550 ºC	10^{15}	10^{15} + 550 ºC	10^{17}	10^{17} + 550 ºC
***D* (nm)**	42 ± 7	44 ± 7	45 ± 7	133 ± 14	140 ± 17
***L* (nm)**	330 ± 50	317 ± 38	315 ± 33	196 ± 27	189 ± 32

Structural analysis. From the XRD spectra in Figure 4.12, the crystalline phase of the Sn-implanted iron oxide NWs was determined. Both low Sn fluence (10^{15} ions·cm^{-2}) samples (as-implanted and after the second annealing treatment) showed the hematite phase (JCPDS 33-0664) with the preferential orientation at diffraction peak (110), as the control sample (hematite NWs without implantation) [33,42,65,265]. Furthermore, the as-implanted sample presented broader peaks, comparing with the control sample and second annealing sample. Implantation technique can cause the lattice order to be diminished, due to the high energy of implantation and ionic concentration used [241,286]. However, with second annealing (at 550 ºC) after implantation, the crystallographic lattice order is re-established, and narrow diffraction peak spectrum was observed. For as-implanted sample with higher fluence (10^{17} ions·cm^{-2}), the hematite peaks are not perceptible, being more visible the peaks attributed to the SnO_2 crystallographic phase. However, with the second annealing, the hematite peaks in direction (110) and (214) are present; the intensity of (110) preferential orientation showed to be lower comparing with sample with lower Sn fluence and control sample. Also, additional peak at 2θ = 30 º could indicate the presence of (101) SnO phase (JCPDS 006-0395) [287].

In Chapter 3, the annealing conditions to obtain the hematite phase in the photoelectrodes were evaluated. The two-step annealing at 550 ºC for 2 h followed by short annealing at 800 ºC showed to be the best condition for improve the crystalline quality of the hematite NWs [276]. Thus, additional annealing with the optimized

conditions should also be considered with the Sn-implanted samples (this is an ongoing work).

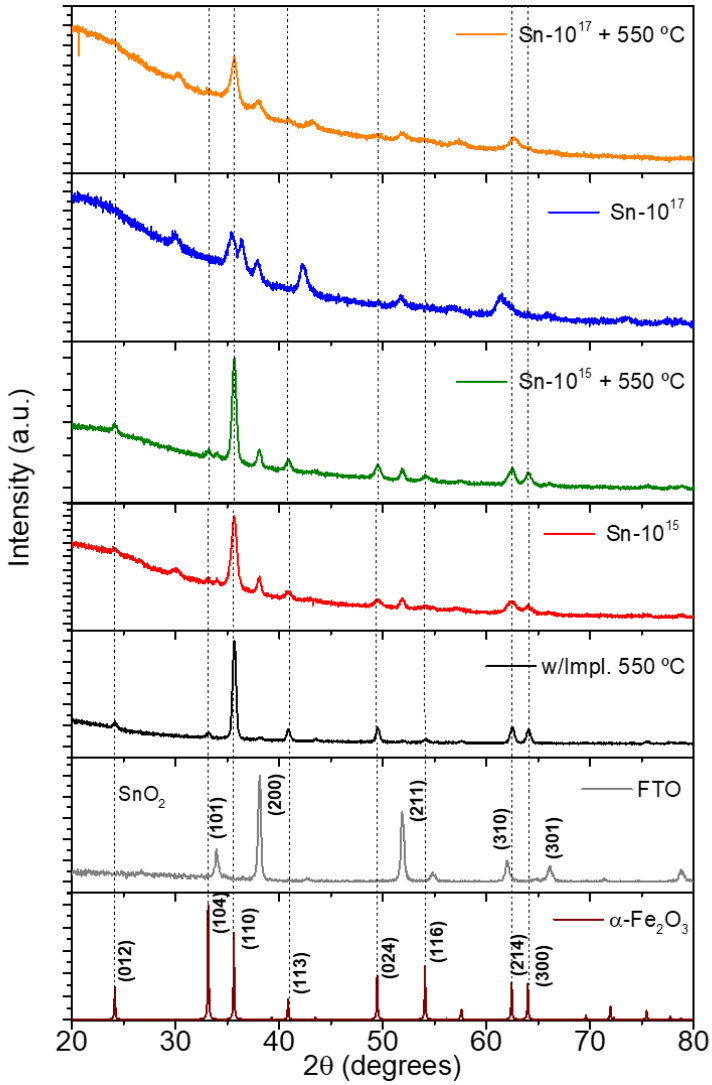

Figure 4.12. XRD spectra for hematite nanowires implanted with lower and higher Sn fluences: as-implanted and with the second annealing at 550 ºC. Reference hematite, FTO substrate and control sample (hematite NW annealed at 550 ºC for 2 h, without implantation) spectra are also represented.

As-implanted samples were analysed by Rutherford Backscattering Spectrometry (RBS) to evaluate the Sn in-depth profile and distribution along the hematite NWs. In Figure 4.13(a), (b) and (c) are shown the RBS spectra of control, as-implanted with lower fluence and higher fluence samples, respectively. As already described in Chapter 3, RBS allows the estimation of layer thickness, chemical composition, roughness and percentage of voids. The chemical elements present in a sample are found by comparison with channels of the known elements of a calibration sample. The energy of

the backscattered ions is measured in small energy intervals (or channels) [288]. The barriers correspond to the energy of backscattered ions from the target atoms. Accordingly, the elements at the surface for the studied NWs samples are identified with arrows, Sn and Fe, around channels ~500 and ~450, respectively [spectrum of control sample, Figure 4.13(a)]. Comparing with RBS spectra of FTO substrate, that present a sharp signal (Figure 3.16 in Chapter 3), at the NWs samples the Fe and Sn signals does not fall abruptly, the inclination of the Fe and Sn signal is indicative of samples with roughness. In Figure 4.13, it can be seen that the Sn signal only ends after the Fe signal ends (spectra read from right to left). This means that there is a region in-depth with both elements shared, Sn and Fe. The Fe signal also ends much sooner than the Sn signal, which means that there is Sn beyond the end of the Fe region.

For the as-implanted samples, the iron concentration profile also presents some changes comparatively with the control sample, i.e. a broader barrier was observed for as-implanted samples with lower and higher fluences [Figures 4.13(b) and (c), respectively]. Besides, the Fe and Sn barriers become more tilted in the higher fluence sample [Figure 4.13(c)] which is indicative of higher roughness in these NWs compared with control and low fluence. With higher fluence, it is also noticeable at around channel 500, a small "shoulder" on the Sn barrier which indicates the presence of Sn at the NWs surface [identified with a small arrow in Figure 4.13(c)].

For the as-implanted photoanodes, the total thickness of the Sn containing region (and Sn distribution) was simulated using the NDF code [237,242]. The fits also indicate the Sn distribution along the nanowires. For the sample with higher fluence (10^{17} ions·cm^{-2}), a considerably high amount of Sn atomic (~15-20%) along nanowires thickness ~170 nm (sum of *L* from layers 1 and 2, in Table 4.4) was determined. For the lower fluence (10^{15} ions·cm^{-2}), a significantly lower Sn atomic ~0.36% was estimated. The RBS for the implanted samples after the annealing at 550 ºC is still an ongoing work.

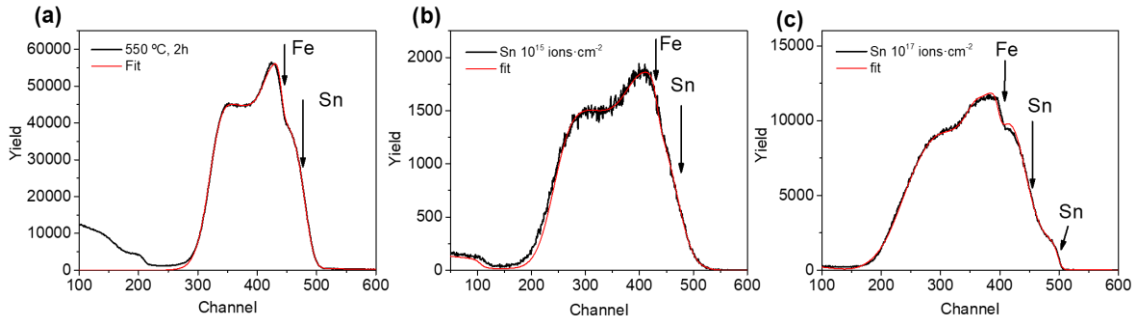

Figure 4.13. RBS spectra of α-Fe_2O_3 (a) control sample (first annealing at 550 °C; 2 h), (b) as-implanted with low fluence (10^{15} ions·cm^{-2}) and (c) as-implanted with high fluence (10^{17} ions·cm^{-2}).

Table 4.4. Parameters resulting from RBS data simulation of Sn as-implanted photoelectrode with 10^{17} ions·cm^{-2}.

Layer	*L* (nm)	Fe_2O_3 (%)	SnO_2 (%)	Volume Fraction (%)	Roughness (nm)
1	77.985	84.985	15.015	27.7	0.266
2	96.093	79.5065	20.4935	25.3	131
3	20.693	99.9995	0.0006	69.1	0.351
4	126.316	0	100	12.6	0.156

Photoelectrochemical performance. In Figure 4.14 are represented the *j-V* curves for as-implanted samples and with the second annealing at 550 ºC, under front and back-illumination.

Both as-implanted samples (low and high fluences) and sample with lower fluence with second annealing present low *j* values, like the control sample. For the sample with lower fluence, only a slight *j* increase comparing with control was observed in back-illumination. The Sn diffusion through the implantation could facilitate the charge carriers through the backside towards the FTO. Sample with higher fluence plus second annealing originated a *j* value of 0.16 mA·cm^{-2}, 16 times higher than the control sample (0.01 mA·cm^{-2}, Chapter 3). Although the morphology of the NWs was significantly changed with the implantation with higher Sn fluence (NWs with larger *D*), this Sn concentration conferred higher conductivity to the photoelectrodes, traduced in higher *j*. The larger amount of Sn is usually associated with the enhancement of photoactivity, due to the increase of donor density and thus the electrical conductivity [33,64,65,111,113,114,262].

The second annealing showed to improve the crystallinity of the sample, with the presence of hematite peaks observed by the XRD spectra (Figure 4.12), which could contribute also to the increase of *j* comparing with as-implanted sample. Nevertheless, it is crucial to study the effect of higher annealing temperature (800 ºC) in the photoelectrochemical properties of these photoelectrodes.

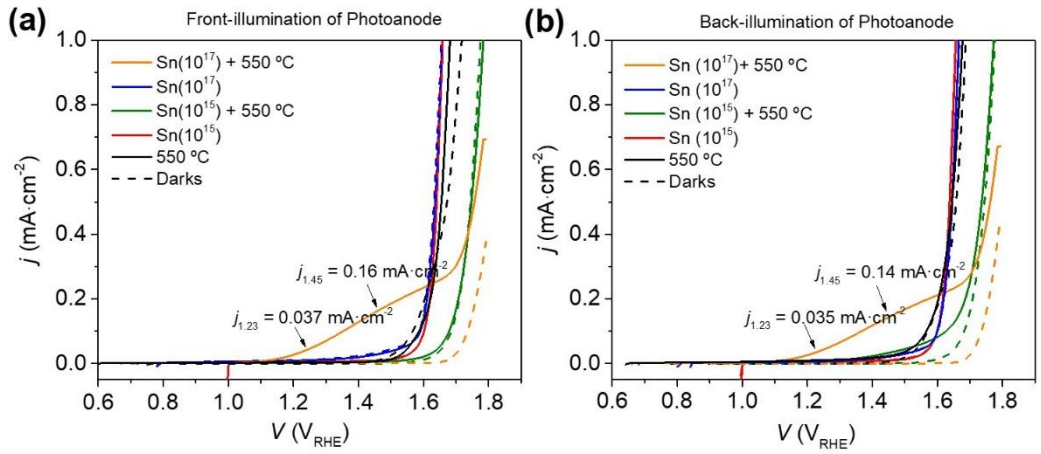

Figure 4.14. *j*-V curves for hematite nanowires as implanted and after the second annealing in (a) front-illumination and (b) back-illumination.

Optical properties. Figure 4.15 displays the absorption spectra of the photoelectrodes. The maximum absorption peak was observed at ~440 nm for control sample (already referred in Chapter 3) and for as-implanted sample with lower fluence [Figure 4.15(a)]. However, with higher fluence (both as-implanted and with the second annealing), also a red-shift to higher wavelength at 530 nm was observed, as referred above for NWs samples with Ti, also for samples annealed with higher temperature and time described in Chapter 3. As already discussed, this red-shift is related with the incorporation of Sn and changes in the morphology [56,65,270]. Moreover, above 600 nm, the absorption increases with the increase of Sn concentration and particle size; a similar behaviour with a subband increase at 600-750 nm was reported by Sivula *et al.* [65].

Likewise, the band gap [calculated from Eq. (2.11)] decreases due to the increase of implanted Sn, Table 4.5, since a lower band gap was observed for the sample with higher fluence in relation to the lower fluence and control samples. Thus, higher Sn diffusion by implantation leads to the enhancement of the photoelectrodes conductivity leading to an improvement of the photoelectrodes performance [8,39,65].

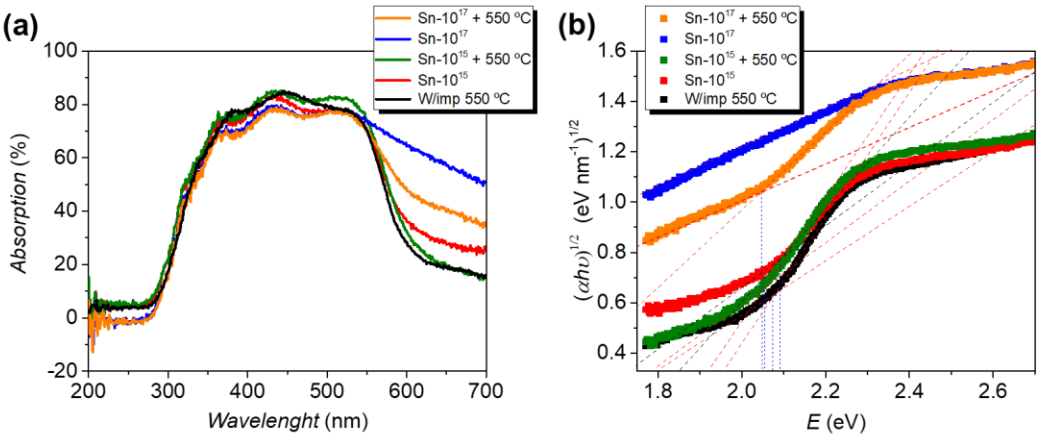

Figure 4.15. (a) Absorption spectra and (b) Tauc plots, for hematite nanowires as-implanted (with Sn 10^{15} and 10^{17} atoms·cm^{-2}) and after the second annealing, comparing with NWs without implantation.

Table 4.5. Optical band gap for hematite NWs without and with Sn-implantation.

Sample	550 ºC	10^{15}	10^{15} + 550 ºC	10^{17}	10^{17} + 550 ºC
Band gap (eV)	2.073	2.092	2.053	2.055	2.048

4.3. Conclusions

Hematite nanostructured photonodes were prepared using an easy and low-cost hydrothermal method for PEC water splitting applications. The nanowires are completely formed during the hydrothermal process; however, a thermal treatment is necessary to obtain the isolate α-Fe_2O_3 phase, confirmed by XRD analysis.

Doping strategies were implemented for water splitting applications' improvement. Ti doping at lower annealing temperatures (one-step annealing) highly increased the photocurrent density of α-Fe_2O_3 photoelectrodes, from 0.02 to 0.63 mA·cm^{-2} (1.45 V_{RHE}). High fill factor of 70% (steep increase of the current density curve) was obtained for Ti doped photoelectrodes annealed with a one-step annealing at 600 ºC. This could indicate photoanodes with lower electron-hole recombination and higher charge extraction rates. In the same way, using the two-step annealing (with a higher temperature of 800 ºC for 20 min) also improved the photocurrent, ascribed to the enhancement of crystalline ordering and diffusion of Sn from FTO layer to α-Fe_2O_3 lattice. Further increase of the photocurrent up to 1.27 mA·cm^{-2} was attained through the use of both higher annealing temperature and Ti doping, revealing that Sn and Ti doping have

a beneficial effect in the α-Fe_2O_3 photo-efficiency. These optimized α-Fe_2O_3 photoelectrodes showed a stable behaviour over 2 h, making them very promising for future studies and applications in photoelectrochemical cells.

On the other hand, the ion implantation is a technique not widely used in this kind of materials but allowed to improve the photocurrent of the hematite nanostructures. The morphology is strongly affected with the use of higher Sn fluence of 10^{17} ions·cm^{-2}, which could highly affect the transport of minority charge carriers in the photoelectrodes. More studies involving intermediate fluences and its effect in the morphology of nanowires should also be considered in future work. Further tests to improve the hematite crystalline phase are also necessary. Within this context, are still ongoing the use of the optimized annealing conditions already achieved for hematite nanowires (two step-annealing 550 ºC followed by a short annealing at 800 ºC). With the use of these annealing conditions, we intend to assess the Sn distribution and study its impact on the morphology, structural, optical and photoelectrochemical properties of the implanted hematite nanostructures. So far, Sn implantation seems an innovative and promising way for Sn incorporation into hematite, although more tests are needed to maintain the nanowires morphology, while optimizing the Sn content. Moreover, RBS demonstrated once more to be an important tool to determine the Sn distribution in depth along nanowires.

Chapter 5

The Insights of Hydrothermal and Anodic Growth of Iron Oxide Nanotubes

Chapter 5

The Insights of Hydrothermal and Anodic Growth of Iron Oxide Nanotubes

Highly ordered hematite (α-Fe_2O_3) nanotubes have been intensively studied as an ideal configuration for application in photoelectrochemical cells for water splitting, due to its high aspect-ratio and direct pathways for electrons transfer within the charge collector. In this work, hematite nanotubes were produced by two distinct methods: hydrothermal and electrochemical anodization. The hydrothermal conditions were optimized to obtain several morphologies: nanotubes, nanoneedles and nanospheres. Photocurrents ~0.06 mA·cm^{-2} were obtained for nanoneedles and nanospheres with only one-step annealing at 550 ºC.

The effect of anodization potential in the morphological features (such as length, pore diameter, interpore distance and porosity) of the nanotubes was also evaluated. The optimum anodization conditions for a faster and organized growth of NTs was found for bias voltage up to 60 V, in which long nanotubes with ~4.6 µm can grow in just 5 minutes. Higher photocurrent of ~0.5 mA·cm^{-2} was obtained for sample anodized at 20 V, also with one-step annealing at 550 ºC.

5.1. Nanotubes by hydrothermal method

5.1.1. Overview

One-dimensional (1D) iron oxide nanostructures are getting increasing attention due to their physical-chemical properties and potential applications in diverse areas such as biotechnology, gas sensors or solar energy harvesting [39,109,143,144]. Nanotubes (NTs) stand-out as ideal configuration for PEC applications, due to their high aspect-ratio and increased photoactive area in contact with the electrolyte [16].

Iron oxide NTs have been produced by hydrothermal method, where the shape of the formed structures depends on several hydrothermal parameters, e. g. temperature, time and the presence of chemical agent precursors such as $NH_4H_2PO_4$ or Na_2SO_4 added to

the hydrothermal solution [142-144,146,289]. For example, nanostructures such nanotubes, nanotires or nanospindles have been reported to grow through the presence of phosphate ions adsorbed to the crystallographic planes of hematite and by coordination with Fe^{3+} ion [289].

NTs formed by hydrothermal technique have been referred to NTs powder synthesis for hyperthermia applications mainly due to their magnetic properties [142,144,289,290]. Until now, few data are available about the PEC properties of this kind of nanostructures [146], making it very appealing as a research topic to explore.

In this work, the main objective was to prepare iron oxide NTs directly on FTO substrate, using the hydrothermal method. The effect of two different chemical precursor solutions in the morphology, structural properties and solar-to-current conversion efficiencies of resulting nanostructures was studied. Several experimental conditions were tested in order to optimize the synthesis conditions. Nanostructures as diverse as nanotubes, nanoneedles and nanospheres were obtained, while revealing promising PEC results.

5.1.2. Experimental details

Hydrothermal nanostructures directly grown on FTO

FTO glass substrates were cleaned as described already in the Chapter 2, and then placed in 40 mL capacity Teflon stainless steel autoclaves. Two chemical solutions were prepared, with and without sulphate ion precursor reagent [143,144,289]:

(i) 20 mL solution of 0.025 M $FeCl_3.6H_2O$ + 0.001 M K_2HPO_4.

(ii) 20 mL solution of 0.025 M $FeCl_3.6H_2O$ + 0.001 M K_2HPO_4 + 0.001 M $(NH_4)_2SO_4$.

The autoclaves were heated at 220 ºC for 48-72 h. After hydrothermal growth, the FTO with deposited nanostructures was thoroughly washed with deionized water. Then, a thermal annealing at 550 ºC for 2 h (10 °C·min^{-1}) in air was performed.

Hydrothermal nanotubes suspension coating on FTO

The NTs were formed by hydrothermal method using the chemical solutions (i) and (ii) described above, at 220 ºC for 72 h. After the hydrothermal process, the autoclaves were let to cool down to room temperature. The NTs formed in suspension were separated by centrifugation being the obtained precipitates abundantly washed with deionized water and ethanol, and finally dried in the heating chamber at 60 ºC.

The NTs were coated on FTO substrates using a polymer solution made with 2.5 mL ethanol, 5 mL ethylene glycol and 2.5 mg poly(vinylidene fluoride) (procedure adapted from [89]); the synthesized NTs (~5 mg) were dispersed on the polymer solution and

coated on the FTO surface, using a doctor-blade method. Then the FTO coated with the NTs was dried in air heating chamber (at 100 ºC) during 12 h, followed by a thermal annealing at 550 ºC for 2 hours (high temperature is also necessary to remove the organic solvents).

5.1.3. Results and discussion

Hydrothermal NTs synthesis directly grown on FTO was not reported so far in the literature for water splitting. We started its development at IFIMUP, during this thesis. In a first stage of this work, the synthesis process was optimized, involving several steps. Due to the high synthesis temperature (220 ºC) used, comparing with the one used in the synthesis of hematite NWs (90ºC) described in Chapter 3, here several difficulties were encountered.

First, we tested a synthesis time of 48 h, ascribed to the formation of the nanotubular shape [143]. While in the case of hematite NWs a complete covering of FTO surface was obtained within just 4 h, here we observed a poor deposition (not uniform) although a long hydrothermal time was used. Nevertheless, the synthesis with sulfate ion (SO_4^{2-}) revealed a much more uniform deposition [sample on the right in Figure 5.1 (a)].

Other difficulties related with the use of FTO substrates were found. For start, we used a more economical FTO substrate (FTO 22-7, Solaronix) since it was resistant to annealing temperatures up to 600 ºC. However, the high temperature necessary to form the NTs, 220 ºC (and consequently the high pressure inside the autoclave), led to deformation and even breaking of the FTO glass [samples on the left side in Figure 5.1 (a)]. Thus, a more resistant FTO (FTO 10-10, Solaronix) was necessary for this hydrothermal process.

The use of Kapton tape to define the electrical contact area in FTO for the photoelectrochemical measurements *(j-V* curves) in the cappuccino cell also revealed to be damaging during the autoclaving deposition procedure. Even with specifications to be used at high temperature, the Kapton disintegrated into the chemical solution, and no FTO deposition occurred after the 48 h. Therefore, another way to create the electrical contact was to first deposit material in all FTO surface and then remove the material in the area for electrical contact by immerging it in hydrochloric acid (HCl, 37%). This procedure allowed removing a small deposited area, leaving it for contact; however, the vapours of the acid also attacked the rest of the deposited area with the nanostructures. The most viable solution was to create an electrical contact area, before the hydrothermal process, by covering it using a non-reactive material, such as Teflon. Figure 5.1(b) shows the photoelectrodes resulting from hydrothermal method, in which

a FTO contact part was left clean (without deposition), by using Teflon small pieces to cover the referred area. Additional time up to 72 h also resulted in a better and uniform deposition, Figure 5.1(b).

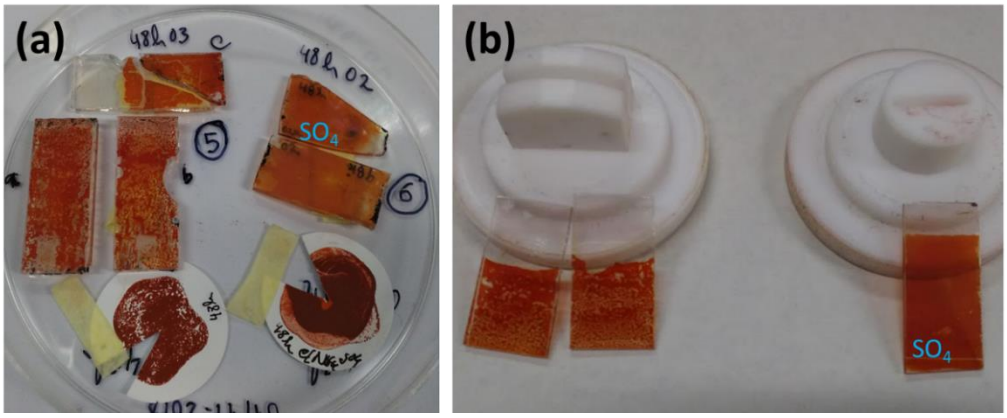

Figure 5.1. Iron oxide hydrothermal films deposited on FTO, with and with sulfate (SO_4) precursor reagent, (a) at 220 ºC for 48 h and (b) 220 ºC for 72 h. In each figure, the samples on the right correspond to samples with sulfate precursor.

Morphological characterization. From the SEM images we could observe the morphology of the resultant nanostructures. In fact, we could produce with success nanotubes in 48 h, as already reported [143,144]. However, they did not nucleate on the FTO substrate as was intended for PEC applications. Instead, the NTs nucleate on solution and some of them remained at the FTO surface (in Figure 5.2).

On the other hand, the fact that we used two chemical solutions, without and with sulfate ion, lead respectively to longer/thinner and shorter/thicker NTs [Figures 5.3(a) and (b) respectively].

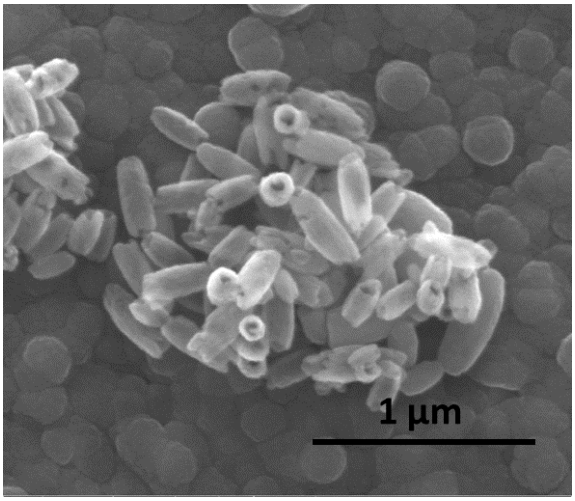

Figure 5.2. SEM image of iron oxide nanotubes obtained by hydrothermal method and laid on the top of FTO.

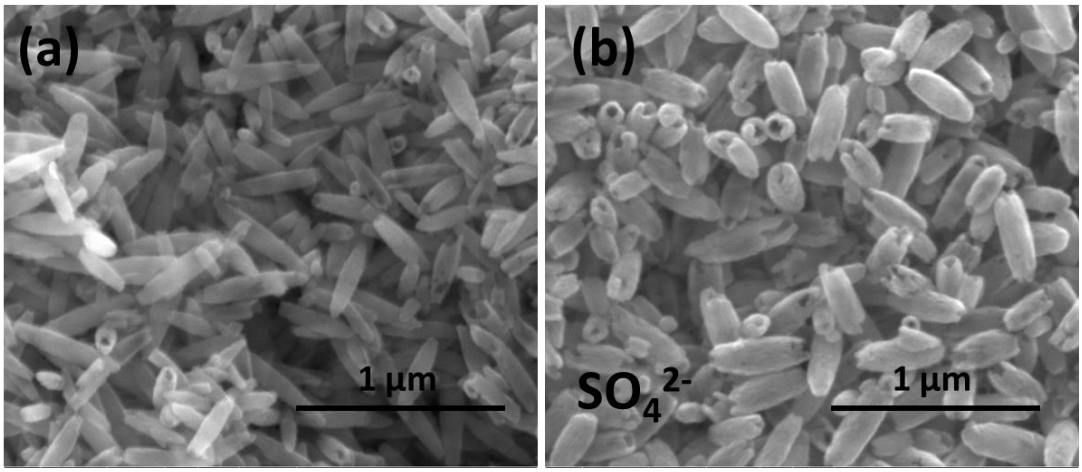

Figure 5.3. SEM images of iron oxide NTs obtained by hydrothermal method and dispersed on solution, (a) without and (b) with sulfate ion reagent.

The nanotubes are formed by a dissolution process mechanism promoted by the presence of phosphate ions [143]. Due to the strong acidic solutions (i) and (ii) used in this method, the presence of H^+ leads to the dissolution of Fe_2O_3 nanostructures being formed during the process, Eq. (5.1). In the presence of phosphate, a selective adsorption of phosphate ions to Fe^{3+} leads to formation of complex $[Fe(H_2PO_4)x]^{3-x}$ [Eq. (5.2)], which drives the Eq. (5.1) towards the right side, leading to the dissolution of the nanotubes during hydrothermal growth:

$$Fe_2O_3 + 6H^+ \rightarrow 2\ Fe^{3+} + 3H_2O \quad (5.1)$$

$$Fe^{3+} + xH_2PO^{4-} \rightarrow [Fe(H_2PO_4)x]^{3-x} \quad (5.2)$$

During hydrothermal process, the two extreme surfaces of the nanostructures formed in acidic solutions [with a needle shape, in the case of (i) solution] are attacked by the protons H^+, inducing the dissolution from surface to inner forming the tubes shown in Figure 5.3(a).

However, when both phosphate and sulfate ions are in solution, as both have a selective adsorption to the surface of Fe_2O_3 nanostructures, will confer some protection to the attack and dissolution by H^+ ions, avoiding higher dissolution and formation rates [143,144], and shorter structures are formed, Figure 5.3(b). While spindles like growing along [001] were referred to be formed in the presence of phosphate ions, ellipsoid nanoparticles were obtained with the addiction of sulfate ions, and absolute adsorption ability of phosphate is much stronger than sulfate [144].

In Figure 5.4 it is shown the FTO coated with the above obtained NTs powder dispersed in the polymer solution, with and without sulfate. For both samples was performed a one-step annealing at 550 ºC (2h) and two-step annealing 550 ºC (2h) followed by short annealing at 800 ºC (optimized conditions presented in Chapter 3). For both samples, with and without sulfate, a homogeneous coating was possible using this polymer and with a one-step annealing approach (although the sample without sulfate presented a scarcer cover). When we tested the two-step annealing approach, the detachment of the coated films of NTs occurred. Further tests are needed in order to optimize the adhesion of the NTs to the FTO surface.

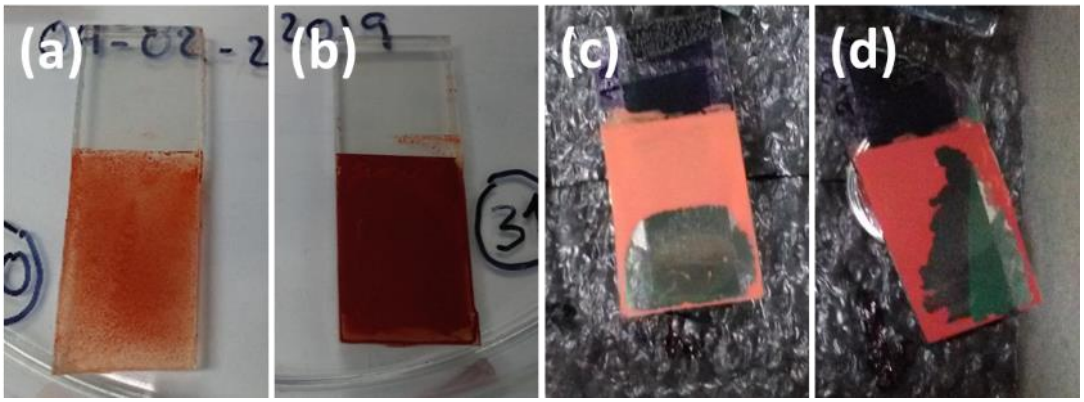

Figure 5.4. Nanotubes coated on the top of FTO substrate: annealed at 550 ºC (a) without sulfate and (b) with sulfate; annealed at 800 ºC (c) without sulfate and (d) with sulfate.

In Figure 5.5 we can observe respectively the morphology of the annealed samples, without and with sulfate and with one-step and two-step annealing. The morphology of the NTs was preserved after annealing, compared with samples without annealing (Figure 5.3). Also comparing samples without and with sulfate with one-step [Figure 5.5(a) and (b), respectively] and without and with sulfate with two-step annealing [Figure 5.5(c) and (d), respectively], no significant differences were observed. Even though, the shorter NTs (with sulfate) look more brittle, Figures 5.5(b) and (d), respectively for one-step and two-step anneling.

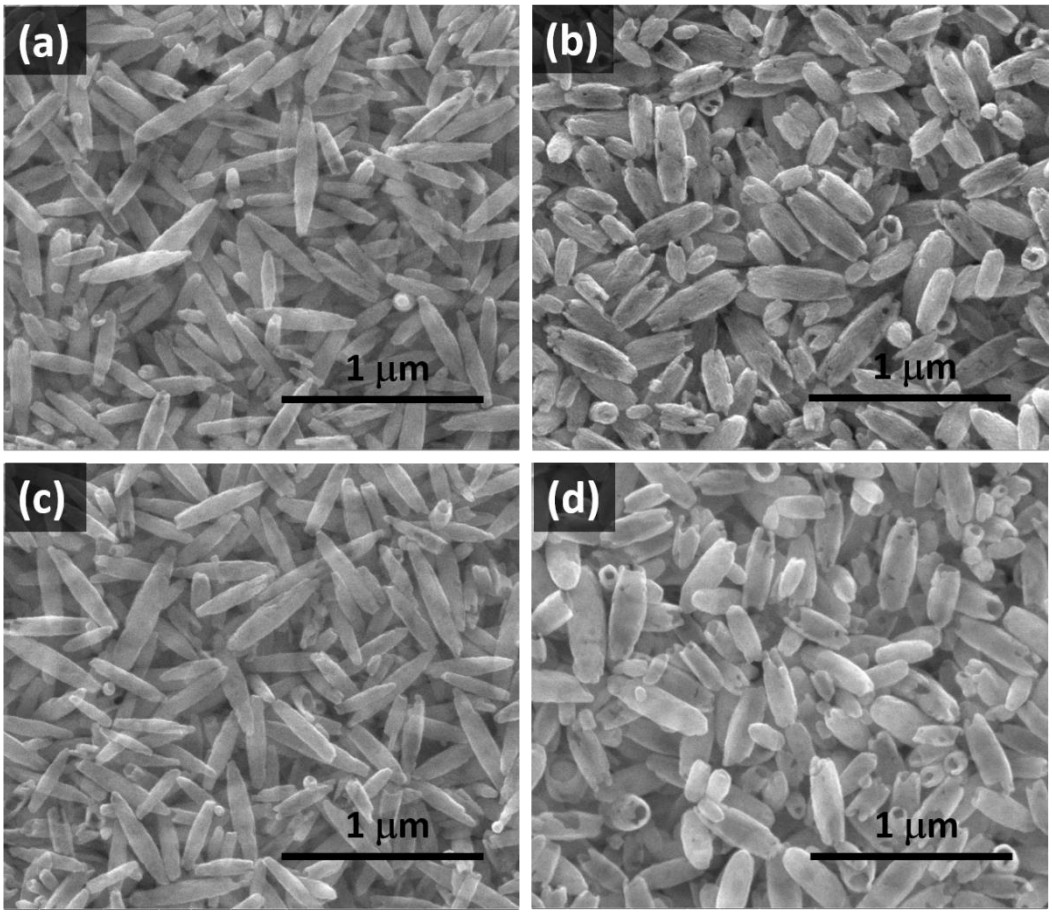

Figure 5.5. SEM images of nanotubes coated on the top of FTO substrate: annealed at 550 ºC (a) without sulfate and (b) with sulfate; (c) without sulfate, annealed at 800 ºC and (d) with sulfate, annealed at 800 ºC.

Using a precursor solution, without or with sulfate ion, we could obtain respectively more needle (spindle-like) or spherical (more round shape) nanostructures nucleated upon FTO during the hydrothermal process, as observed respectively in Figures 5.6(a) and (b) [in Figures 5.6(c) and (d) the respective cross-sectional views]. The mechanism of formation could be explained by the same principle of formation of NTs in solution, since analogous growth is observed (thinner and thicker structures respectively without and with sulfate ion).

In Table 5.1 are presented the diameters (*D*) and thickness (*L*) of the formed nanostructures (nanoneedles/spheres). While *L* is similar for both nanostructures, ~200 nm, *D* is higher for nanospheres (~113 nm) than for nanoneedles (~83 nm), due to low rate dissolution induced by presence of both phosphate and sulfate ions.

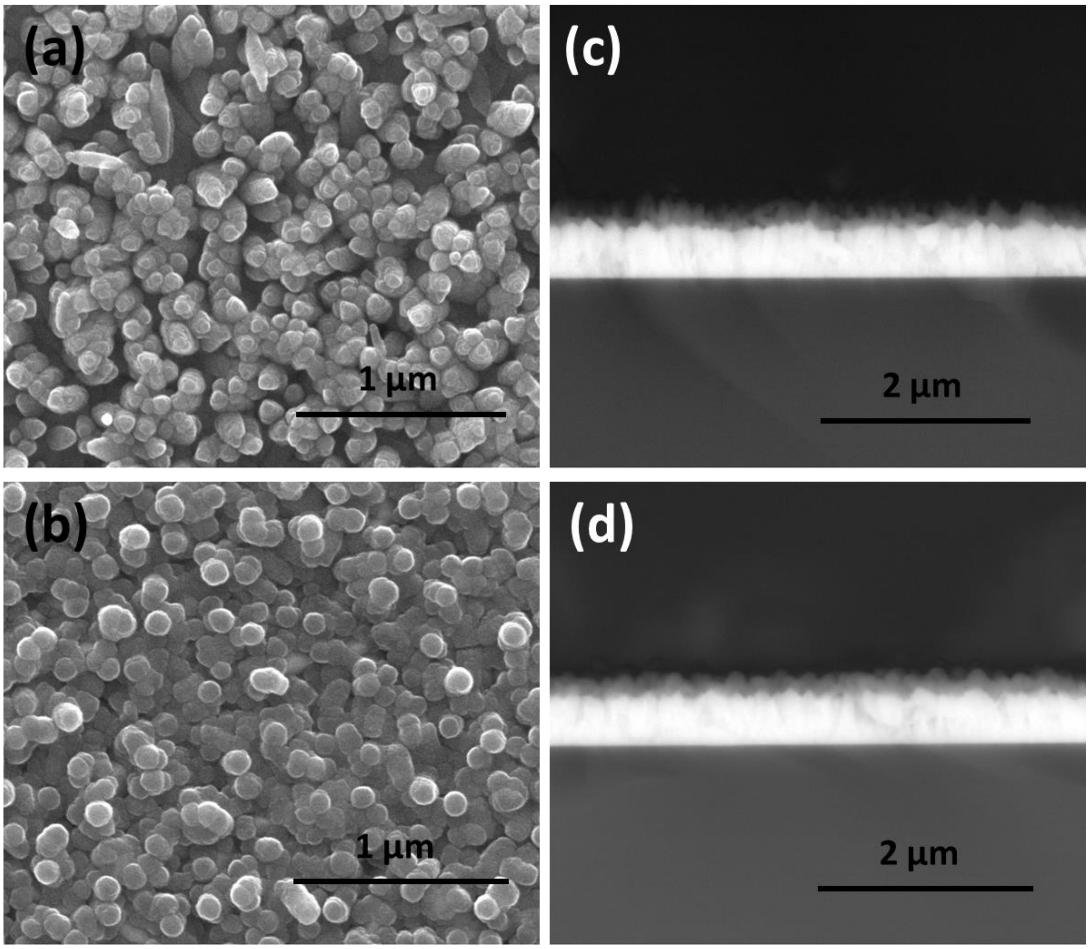

Figure 5.6. SEM images of iron oxide nanostructures obtained by hydrothermal method: (a) nanoneedles and (b) nanospheres, produced respectively without and with sulfate reagent; corresponding cross-sectional images of (c) nanoneedles and (d) nanospheres.

Table 5.1. Diameter (*D*) and thickness (*L*) of nanoneedles and nanospheres grown on FTO by hydrothermal method.

Sample	**Nanoneedles**	**Nanospheres**
Diameter (*D*) (nm)	83 ± 13	113 ± 6
Thickness (*L*) (nm)	198 ± 27	194 ± 17

Structural characterization. In Figure 5.7(a) are represented the XRD spectra (Bragg Brentano mode) for the NTs powder, i.e. the NTs formed in suspension. The typical hematite peaks are obtained at this early stage of hydrothermal process; no significant differences were observed for the NTs obtained with or without sulphate.

On the other hand, we measured the XRD for the samples nucleated directly on FTO (in Parallel Beam mode). For both samples, and after the annealing treatment at 550 ºC, the thermodynamically stable hematite phase (JCPDS 33-0664) was obtained [Figure 5.7(b]). While for nanoneedles, the preferential orientation at diffraction peak (104) was observed, for nanospheres both peak intensities in planes (104) and (110) showed to have practically the same intensity. Also, other peaks indexed to α-Fe_2O_3 structure, such as (012), (110), (113), (024), (214) or (300) were identified. However, other small peak contributions are also present and can be related with the presence of $Fe_4(PO_4)_3(OH)_3$ phase [144,145].

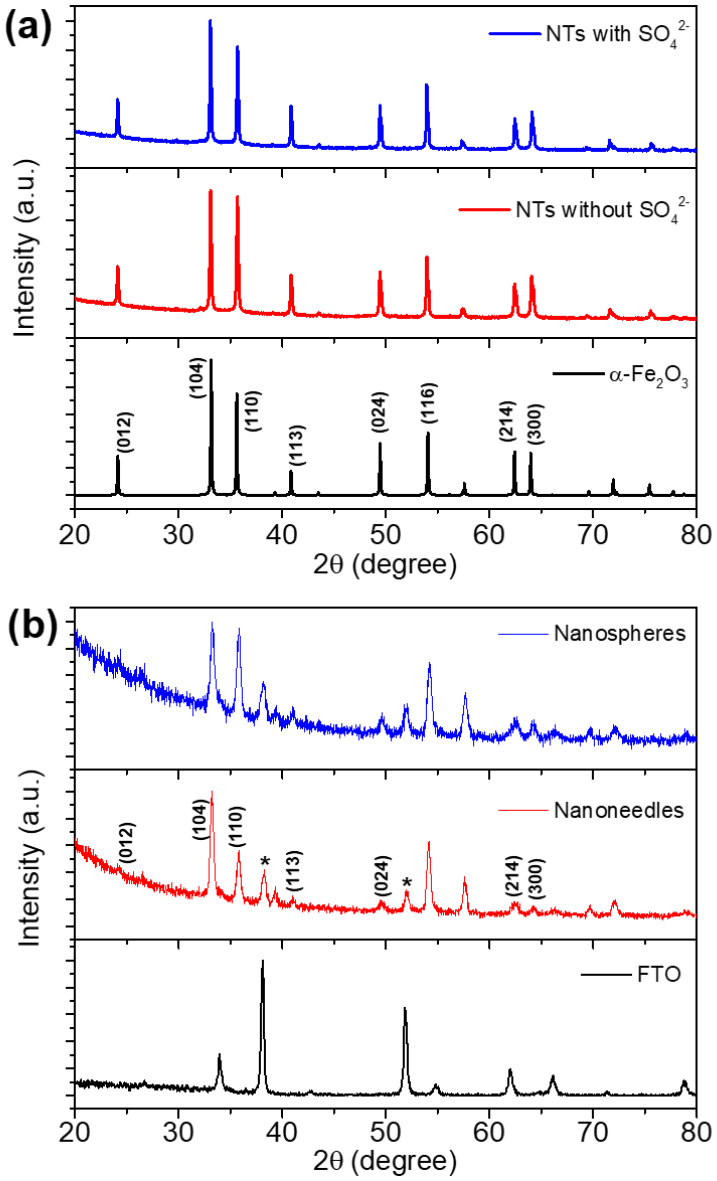

Figure 5.7. XRD spectra of iron oxide nanotubes (a) formed in suspension with and without SO_4; (b) nanoneedles and nanospheres annealed at 550 °C for 2 h. The * symbol indicates FTO peaks.

From the XRD spectra refinements in PB mode, the crystallite size (D_{XRD}) and microstrain (ε) were determined, using the Williamson-Hall relation, Eq. (2.2) in Chapter 2. Without sulfate (nanoneedles), higher values of D_{XRD} = 45 ± 4 nm and ε of 0.21% where obtained, comparing with samples with sulfate precursor (nanospheres), with D_{XRD} of 28 ± 0.4 nm and ε of 0.15%.

Photoelectrochemical performance. The photocurrent density-voltage (*j-V*) curves for both types of samples, with and without sulfate (with polymer or grown directly on FTO) were measured (Figure 5.8).

For the nanostructures nucleated on FTO, a photocurrent of ~ 0.06 mA·cm^{-2} (at 1.45 V_{RHE}) was obtained for sample without sulfate, slightly higher than with sulfate, ~ 0.057 mA·cm^{-2} [Figure 5.8(a)]. These *j* values are ~6 times higher than *j* of ~ 0.01 mA·cm^{-2} (at 1.45 V_{RHE}) obtained for the hydrothermal NWs annealed in the same conditions (Chapter 3), thus representing promising results. Optimization is still necessary to improve a homogeneous covering of FTO substrate, and the use of the optimized annealing conditions of two-step annealing at 550 ºC with additional short annealing at 800 ºC will be considered in future works.

For the NTs with polymer covered on FTO, only the sample with sulfate was measured (with better coverage), attaining a low *j* of <0.002 mA·cm^{-2} [Figure 5.8(b)]. Also, some detachment resulting from the contact with the electrolyte solution was observed during the *j-V* measurements. All other samples of NTs with polymer, due to the poor coverage on FTO, were not possible to measure.

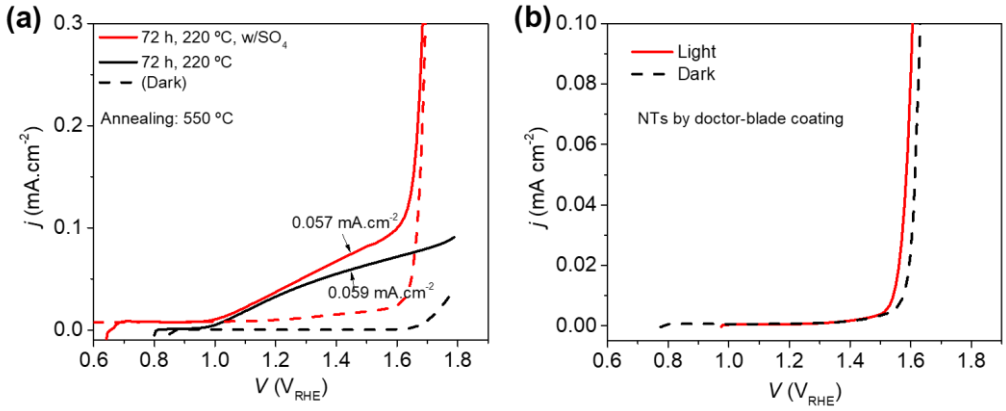

Figure 5.8. Photocurrent density-voltage curves, under dark and 1 sun, of (a) Fe_2O_3 nanoneedles and nanospheres, and (b) nanotubes with sulfate, all grown by hydrothermal method and annealed at 550°C in air. The nanotubes were obtained in hydrothermal dispersion and were coated on FTO with a doctor-blade.

5.2. Nanotubes by electrochemical anodization

5.2.1. Overview

Although the nanotubular configuration is a promising morphology to overcome the hematite limitations, the hydrothermal method showed some drawbacks, namely regarding the NTs adhesion to the substrate, time-consuming synthesis and limitations in NTs diameter and thickness, as explored in the previous section. An alternative widely reported in the literature consists in the electrochemical anodization of Fe foil to obtain nanoporous templates and NTs arrays of hematite [83,89,90,126,135,136,291].

Like the hydrothermal method, electrochemical anodization is considered a simple and inexpensive way of obtaining α-Fe_2O_3 NTs, in which precise shape of the nanostructures can be effectively controlled, depending on the experimental conditions e. g. electrolyte type and concentration, pH, time, stirring, applied potential, temperature, among others [83,89,90,135,136,291,292]. However, Fe anodization is affected by corrosion in aqueous solutions, which can be overcome with the use of organic electrolytes [136,293]. Also, the use of viscous ethylene glycol-based electrolytes proved to be a better choice concerning the growth of the NTs, without causing a fast etching effect as the HF-based ones [90,203].

As occurs with anodic TiO_2, the growth of the α-Fe_2O_3 NTs in F- based electrolytes is based on 3 simultaneous processes: the electric field-assisted oxidation of the metal to form the oxide (at the metal/oxide interface); the field-assisted dissolution of the formed oxide (at the oxide/electrolyte interface) and the NTs chemical dissolution due to the action of F^- and H^+ ions [89,90,203]. The chemical equations that describe the oxidation and dissolution reactions [89,132] are given respectively by Equations (1.8) and (1.9), already presented in Chapter 1.

The growth of the anodic oxide and the geometrical features of the NTs, such as length (L), barrier layer (δ_b), pore diameter (D_p), interpore distance (D_{int}) or wall thickness (W) depend on the anodization parameters like applied voltage, temperature, time, etc. [1,83,89,90,126,135,136,291]. The complete understanding of NTs features and growth mechanism is very important to produce optimized 1D NTs structures for specific applications, in particular to increment the PEC cells efficiencies.

Several works in literature reported the photoelectrochemical characterization of anodic nanostructures, in particular photocurrents have been obtained in the range of j=0.1-0.7 mA·cm^{-2} (in Table 1.1); j obtained for anodic NTs have shown to be dependent on anodization parameters (time, temperature, stirring), annealing conditions (ramp or atmospheres) [294-298]. Fast Fe anodization in just 3-15 min are often reported

[90,132,292,299,300] with NH_4F and ethyleneglycol based electrolytes. For instance, anodization at 50 V for 15 min followed by annealing at 500 ºC in air attained *j* ~0.078 mA.cm^{-2} [132]. On the other hand, anodization of 50 V for 5 min in 400 ºC oxygen atmosphere originated *j* ~0.352 mA·cm^{-2} at 0.6 VAg/AgCl [299]. Annealing conditions like temperature, time and atmospheres have been explored in order to improve the anodic nanotubes for enhanced photoperformances. While the annealing in air is not often reported, several groups refer the annealing atmosphere using oxygen, argon or hydrogen (Table 1.1). Recently a water splitting performance for a bi-layered nanostructure annealed in argon atmosphere at 500 °C was reported achieving a photocurrent density of 0.143 mA·cm^{-2} at 1.54 V (*vs.* RHE). By changing the annealing atmosphere with H_2 allowed to improve the photocurrent to 1.41 mA·cm^{-2} [89]. Likewise, the use of NTs conjugated with a dendritic layer lead to photocurrents of 1.8 mA·cm^{-2} at 0.5 $V_{Ag/AgCl}$ [83]. Also, the use of Fe-Ti alloys further increased the photocurrent to 2.0 mA·cm^{-2} at 0.65 $V_{Ag/AgCl}$ [134]. However, it lacks a direct correlation of the photocurrent water splitting performance with the NTs geometrical parameters [296,298,301].

An essential requirement for most of the nanodevices based on NTs oxides is to present a highly organized structure, i.e. NTs arranged in hexagonal closed packed-arrays - HCPA, since it enhances the charge carrier transportation and reduces the electron-hole recombination [213,302,303]. The ordering degree can be evaluated calculating the porosity (*P*) of the NT arrays. For an ideal HCPA arrangement, *P* can be estimated using the parameters D_p and D_{int} [304]:

$$P = \frac{2\pi}{\sqrt{3}}\left(\frac{D_p/2}{D_{int}}\right)^2 . \qquad (5.3)$$

Ideal porosity of 10% was reported earlier for alumina templates [304]. For Ti anodization, besides the typical dependence on applied potential, also a time dependence (in the case of longer anodization time) was demonstrated [1,305-307]. For HfO_2, the porosity was also determined, in which the walls of the nanotubes, or the electrolyte type, showed to be relevant factors to be considered [129,130]. So far, the organization and porosities determination of the nanoporous or NTs arrays for anodic iron oxide have been underestimated in the literature.

In this work we describe the synthesis of Fe_2O_3 NTs by electrochemical anodization of Fe foils. Anodization of Fe foils was conducted by short periods of 5 minutes and variable voltage (10-100 V) at controlled temperature of 45 ºC.The effect of anodization voltage on Fe_2O_3 NTs growth rate and geometrical features, namely *L*, D_{int}, D_p and *W* was reported. More organized NTs were obtained for applied voltages up to 60 V, while

higher voltages lead to more disorganization and stronger dissolution affecting the top of the NTs. A relation for the porosity with anodization charge curves and NTs thickness was assessed. Solar water splitting performances were determinate for all the samples with different anodization voltages after a thermal annealing (in air) and correlated with the anodic NTs geometrical parameters. Smaller NTs originated best performances, achieving 0.4 $mA \cdot cm^{-2}$ without any annealing atmosphere improvement.

5.2.2. Experimental details

The Fe_2O_3 NT arrays were obtained by electrochemical anodization of Fe foil pieces (99.99% high-purity from AlfaAesar, 0.25 mm). Prior to anodization, the Fe pieces were sonicated with acetone for 5 min. Anodization was carried out using a home-made setup, consisting in a two-electrode anodization cell with a platinum mesh as the cathode and the Fe foil sample (in contact with a copper cap) as the anode, both placed inside a container filled with an electrolyte solution. The electrolyte solution consisted in ethylene glycol with NH_4F (0.5 wt%) and H_2O (2 wt%), magnetically stirred at 45 ± 2 °C. Anodization of Fe foil was performed for 5 minutes, using different voltages (*V*) ranging from 10 to 100 V. A power supply Keithley 2004 Sourcemeter was used, and the current density transients were remotely controlled by a LabView application. After the anodization each sample was sequentially rinsed in high purity ethanol and hydrogen peroxide (method for NTs top cleaning) [308].

The morphology of the resulting nanotubes was characterized by *Scanning Electron Microscopy* (SEM) technique (described in Section 2.3.1.1.). The geometrical parameters (D_p, D_{int}, *W* and *L*) were determined using the *ImageJ* open source software [309]. For each sample, an average of 20 pore nanostructures were used, randomly chosen from the SEM images. For each parameter, the respective mean and standard deviation were calculated. From Eq. (5.3), the porosity (*P*) of the NTs was calculated, with respective error (using error propagation equation).

The structural analysis was performed using X-ray diffraction (XRD), in parallel-beam (PB) mode with grazing incidence (PBGI) angles (Section 2.3.2.1).

The photocurrent density−voltage (*j*−*V*) curves, under dark and 1-sun simulated sunlight, were performed as described in Section 2.3.3.1.

5.2.3. Morphological and Structural characterization

Figure 5.9. shows SEM images of the top of as-anodized iron oxide Fe_2O_3 NT arrays resultant from the anodization of Fe foil with variable anodization voltage (V_{anod}). Different V_{anod} originated self-ordered nanotubular structures, except for 10 V, in which a non-porous and inhomogeneous oxide layer was formed. The use of temperature during anodization plays an important role in the morphology of the formed anodic oxide [106,135,291,300], where high-aspect-ratio nanotubular shape takes place for temperatures ~45 °C for short anodization time [90]. Here, for V_{anod} from 20 up to 60 V, the NTs present a regular shape, well-defined walls and HCPA distribution [Figures 5.8(b)-(f)]. Also, an increase in the pore diameter with V_{anod} is noticed. Above 60 V a more irregular nanotube morphology is observed, with traces of surface dissolution [Figures 5.9(g)-(i)]. Moreover, for 100 V few NTs could be found, rather a highly damaged top surface due to the high rate dissolution ascribed to this range of anodization voltages [Figure 5.9(i)].

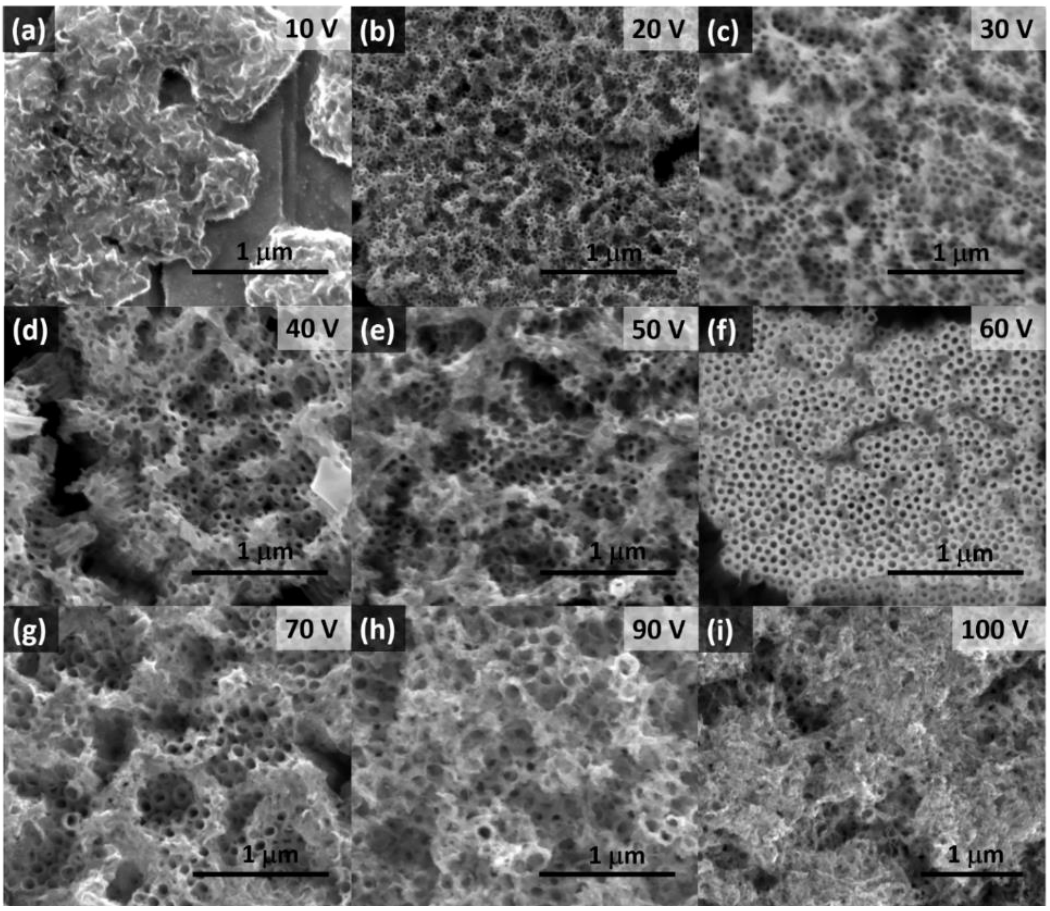

Figure 5.9. Top-view SEM images of the Fe_2O_3 nanotubes (NTs) anodized at (a) 10 V, (b) 20 V, (c) 30 V, (d) 40 V, (e) 50, (f) 60 V, (g) 70 V, (h) 90 V and (i) 100 V.

After the thermal annealing at 550 ºC for 2 h, several cracks between NTs arrays were detected (Figure 5.10). For all V_{anod}, we could observe the NTs arrays inside "islands" between the cracks. In the particular case of anodization at 20 V, few NTs were observed, besides a spongy-like structure between the NTs was found [Figure 5.10(a)].

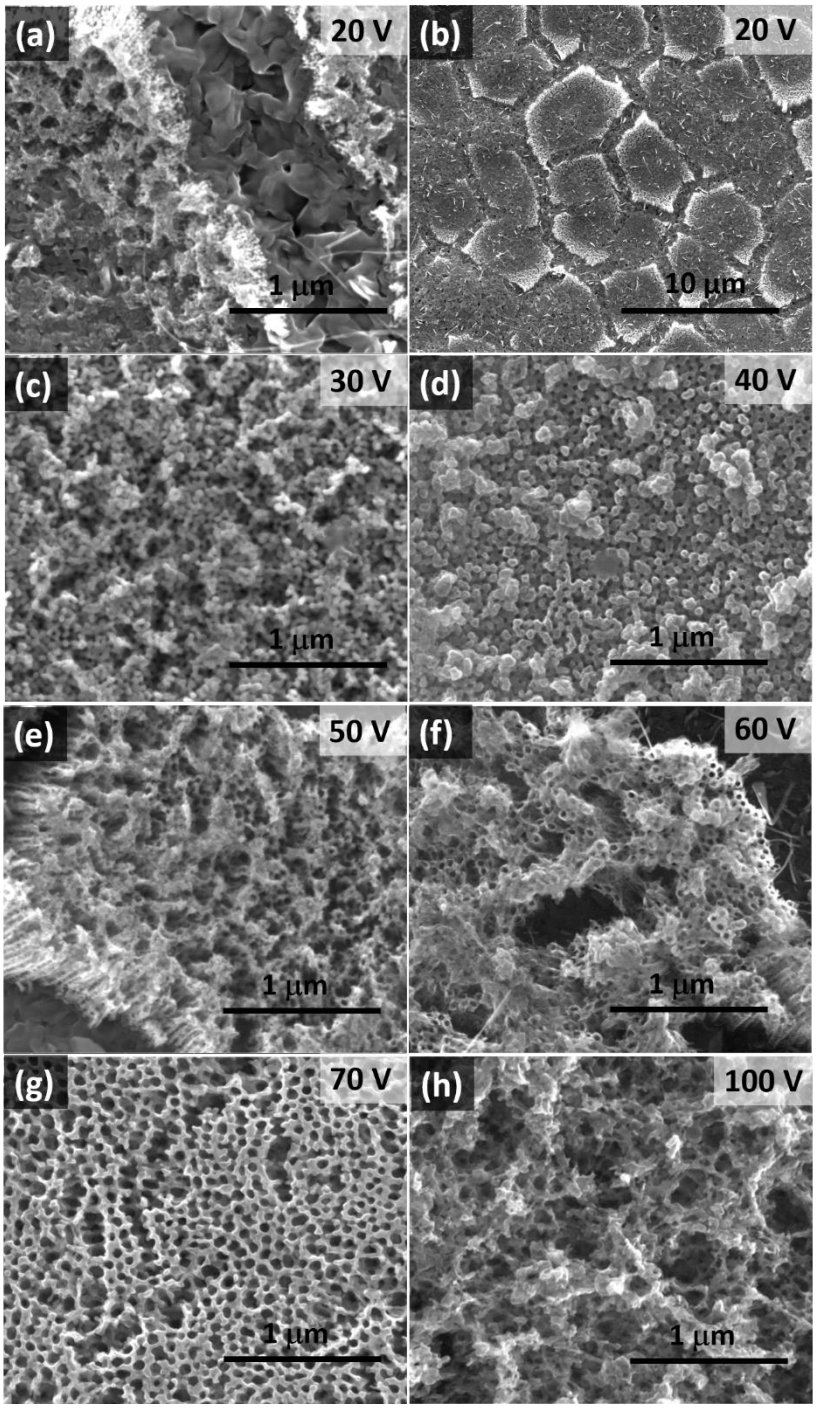

Figure 5.10. Top-view SEM images of the Fe_2O_3 nanotubes (NTs) anodized at (a) and (b) 20 V, (c) 30 V, (d) 40 V, (e) 50, (f) 60 V, (g) 70 V and (h)100 V, after annealing at 550 ºC for 2 h.

In Figure 5.11 are represented the geometrical parameters D_p, D_{int} and W of the as-anodized Fe_2O_3 NT arrays, taken from the SEM images (as illustrated in the inset of the figure). A linear increase of D_p, D_{int} or W with V was observed, as usually reported for Al, Fe or Ti anodization [1,126,135,212], up to 60 V. However, above 60 V, we observed higher standard deviation values (expressed in large error bars), indicative of more irregular nanotube features. In fact, a decrease of D_p and D_{int} is seen for the 100 V sample where we found a limited availability of pores to analyze, since the dissolution highly affects the NTs top morphology and organization [Figure 5.9(i)]. The D_p varies from 24 to 78 nm and D_{int} from 43 to 130 nm. Very thin nanotube W, from 10 to 18 nm, were obtained up to 70 V (above 70 V, no defined walls were observed).

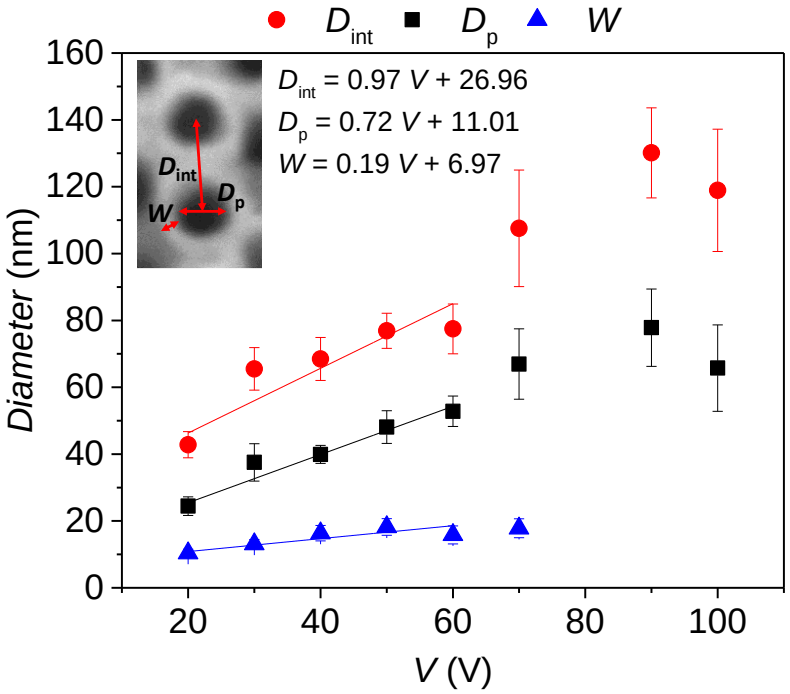

Figure 5.11. Interpore distance (D_{int}), pore diameter (D_p) and wall thickness (W) of Fe_2O_3 nanotubes as function of applied voltage (V_{anod}).

From the cross-section SEM images, vertically aligned and smooth-walled Fe_2O_3 NTs can be observed up to 70 V [Figures 5.12(a)-(d)]. From these images, it is also noticed that as V increases, the NTs length (L) increase as well, from 1.4 to 4.6 µm. However, above 70 V, more irregular shaped NTs are noticed, not so well-defined (not so straight) with a rougher morphological aspect [Figures 5.12(e) and (f)]. Also, the NTs tops are more dissolved, leading to a thickness decrease to 3.4 µm. This will be further discussed in detail in the next section 5.2.4.

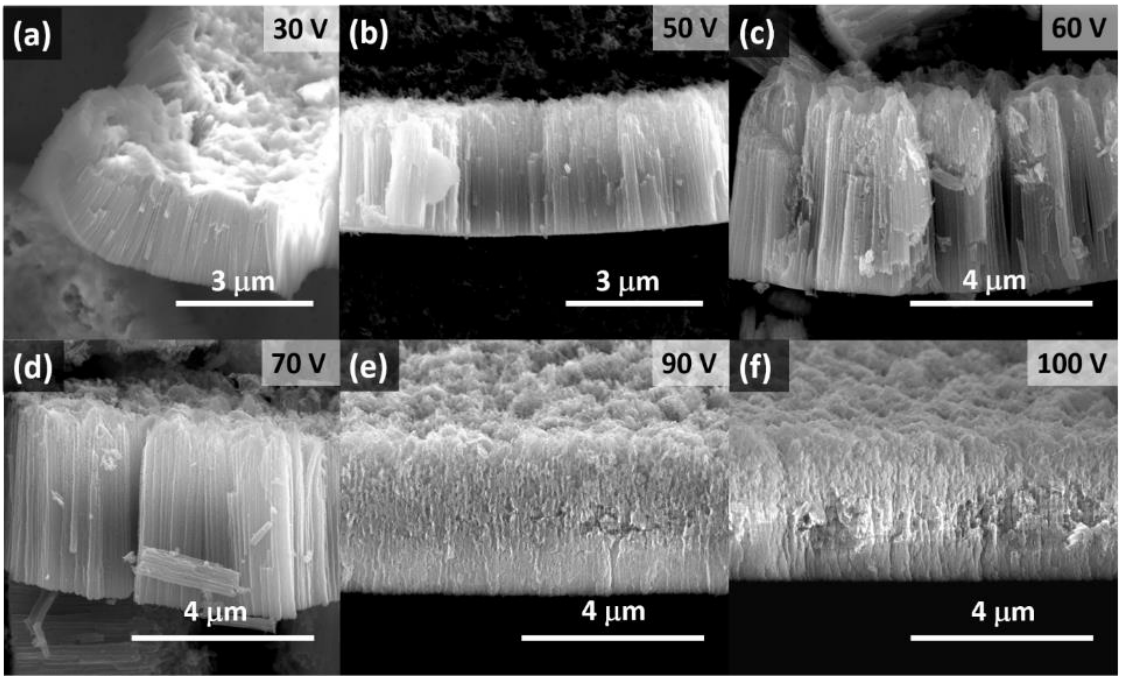

Figure 5.12. SEM cross-section images from Fe_2O_3 NTs anodized with (a) 30 V, (b) 50 V, (c) 60 V, (d) 70 V, (e) 90 V and (f) 100 V.

5.2.4. Anodization curves *vs.* growth rate regimes

In anodization process, the current density (j_{anod}) evolution through time [$j_{anod}(t)$] marks the growth progress of the oxide growth [126,201,310]. Figure 5.13(a) shows the typical anodization curves $j_{anod}(t)$ for Fe_2O_3 NTs arrays with variable V_{anod} from 10-100 V. As in the case of Al and Ti anodization [213,311-313], the formation of iron oxide NTs shows similar current density transients of anodization [four different stages shown in the inset of Figure 5.13(a)]: first, j_{anod} shows a quick drop caused by the initial oxide formation (stage I) until it reaches a minimum value (stage II) which indicates the maximum oxide thickness formed [Eq. (1.8)]; subsequently, j_{anod} increases due to pore nucleation (field-assisted oxide dissolution) which takes place in the presence of F^--based electrolytes (III), Eq. (1.9) . However, differently from the nanoporous alumina case where j_{anod} steady-state is achieved after the nucleation period, leading to a vertical growth of the nanotubes in a constant rate, in Fe anodization, j_{anod} slightly decreases as anodization proceeds (similar to TiO_2) [1,212,213,311,314]. The decrease in j_{anod} during anodization (stage IV) indicates that the oxidation rate is higher comparing with dissolution, which promotes a growth of the barrier layer thickness (δ_b) and consequently decreases the anodization rate. The j_{anod} is related to the V drop across the δ_b, according to the high-field conduction theory:

$$j_{anod} = \alpha e^{\beta \frac{V_{anod}}{\delta_b}} \quad (5.4)$$

where α and β are material-temperature dependent constants and the (V/δ_b) ratio is the effective electric-field (E) across the δ_b [126,310]. As V_{anod} increases, j_{anod} also increases and the time to achieve the nucleation period decreases, since higher V_{anod} promotes the ionic flow through the δ_b and a fast pore formation occurs [126,213]. In fact, we notice from Figure 5.13(a) that the nucleation period for 20 V is longer (~0.77 min) than for 100 V (only lasts for ~0.33 min).

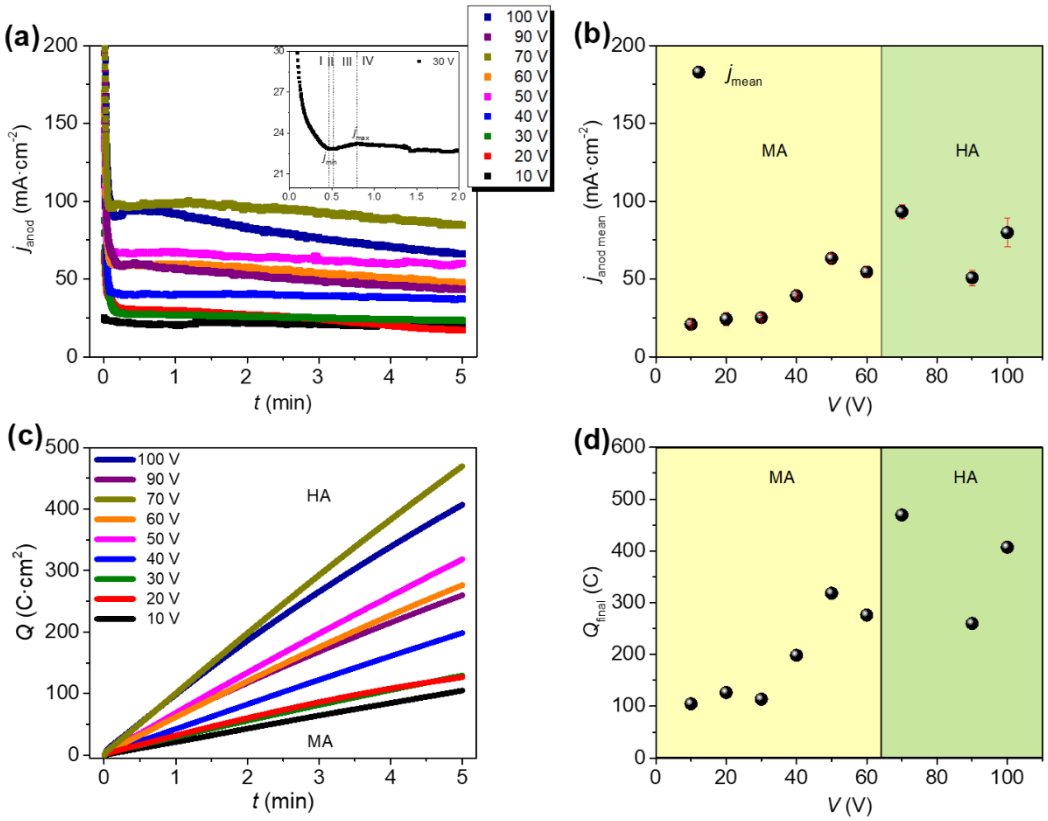

Figure 5.13. (a) Anodization curves monitored during the growth of Fe_2O_3 NTs arrays, with variable voltage in the range of 10-100 V; (b) current density mean values (correspondent to stage IV) as a function of the applied voltage (V); (c) charge curves [Q(t) integration of anodization curves] and (d) final charge values, Q, for each Fe_2O_3 NTs anodized with different voltage.

Figure 5.13(b) shows the mean values of j_{anod} as a function of V_{anod}. For each V_{anod}, the j_{anod} mean and standard deviation were determined during the stage IV corresponding to continuous NTs growth. From 10 to 60 V, j_{anod} mean increases almost linearly with V_{anod} [126,136]. In these conditions, the NTs grow within a self-ordering regime at low anodization rates, the so-called mild-anodization (MA) regime already

described for nanoporous alumina templates [314,315]. Above 60 V, the growth of NTs follows the hard-anodization (HA) regime. In HA, phenomena like oxide "burning" or "breakdown" occur induced by high voltages, leading to the decrease of NTs self-ordering [314,315]. The lack of tendency in the j_{anod} with the V_{anod} [Figure 5.13(b)], is a consequence of the decrease of structural order of resulting NTs observed in Figure 5.9(g)-(i). Due to the use of higher V_{anod} (higher j_{anod}), the HA regime is accompanied by a large heat release and gas evolution [314]. Moreover, HA regime is more sensitive to small temperature fluctuations in the order of 45 ± 2 °C, since the variation of j_{anod} mean is more noticed [higher error bars, Figure 5.13(b)]. In the presence of electric field (*E*), the ionic flux through the NTs is directly related with the diffusion coefficient (*D*) expressed by the Stokes-Einstein equation:

$$D = \frac{K_B T}{6\pi\eta r} \tag{5.5}$$

where k_B is the Boltzmann constant, *T* is the temperature, *η is* the dynamic viscosity and *r* is the radius of a particle [129,316,317]. This relation indicates a dependence of *D* on the temperature of the electrolyte. Although a controlled electrolyte bath temperature was applied, the slight deviation (45 ± 2 °C) is highly enhanced in HA systems due to the high current conditions (high electric field strength) due to the high local temperature in the electrolyte-oxide interface. Also, the ion migration [H^+ and F^- responsible for the oxidation and dissolution processes, Eq. (1.8) and Eq. (1.9) respectively], is significantly affected by high electric field strength characteristic of the HA regimes.

By integration of the anodization curves we obtain the amount of charge transferred during oxide formation, *Q*(*t*), in Figure 5.13(c) [213]. The same two regimes MA and HA [in Figure 5.13 (b)] can be observed by extracting the final *Q* [Figure 5.13(d)]. Nevertheless, 50 V sample presents higher *Q*(*t*) curve since a slight higher temperature bath solution was applied, when compared with the 60 V one.

For higher voltages (e.g. 100 V), the amount of *Q* transferred during anodization is significantly higher than for lower potentials (20 V), suggesting that higher NTs can be obtained with those conditions. In fact, the NTs template thickness (*L*) can be estimated using Faraday´s law:

$$L_Q = \frac{QM}{Fn\rho} \tag{5.6}$$

where *Q* is the charge flown during the anodization ($C.cm^{-2}$), *M* the molecular weight of the Fe_2O_3 oxide (159.69 g mol^{-1}), *F* is the Faraday constant (96500 C mol^{-1}), *n* the

number of electrons involved in the reaction (n = 6 e^-) and ρ the Fe_2O_3 density (5.24 g cm^{-3}) [201,318,319]. Accordingly, for instance one expects $L_Q \approx 4$ µm for 20 V, $L_Q \approx 9$ µm for 60 V and $L_Q \approx 13$ µm for 100 V (Figure 5.14). Comparatively, from the cross-sectional SEM images in Figure 5.12, the NTs effective thickness can be determined (L_{SEM}; Figure 5.14). L_{SEM} increases almost linearly with V_{anod} up to 60 V, reaching 4.6 µm in just 5 min. The high growth rate for short time is also boosted using heated electrolyte, as higher ionic flow is promoted by the increase of electrolyte temperature [90,291,320,321].

While D_p and D_{int} increases up to 90 V (Figure 5.11), L_{SEM} is affected by potentials above 60 V. As expected from the L_Q values estimated using Eq. (5.6), the increase in V_{anod} should lead to higher growth rate of the NTs, but a L_{SEM} decrease is observed for V above 60 V. The use HA conditions, allied with the electrolyte heating, not only increases the oxidation-dissolution rates at the bottom of the NTs, but also the chemical etching rate at the NTs tops (caused by the electromigration of F^- enhanced by high E and enhanced by electrolyte temperature [291]). This ultimately results in the decrease of NTs length, corroborated by the SEM images for V_{anod} above 60 V (with visible signs of dissolution, especially the 100 V sample) [126]. Also, the use of higher V_{anod} promoted more O_2 gas generation (electronic current contribution), observed experimentally during anodization, which additionally contributes to the increased dissolution [136,292,320]. Also, the two distinct NT growth regimes are observed in Figure 5.14: regime MA up to 60 V, where the NTs length increase almost linearly, and a second regime >60 V where the NTs evolution under the HA conditions shows a decrease. This fact also helps to explain the low anodization efficiencies (ratio between the nanotubes effective thickness measured from SEM images and the estimated thickness from Faraday´s law [318]) obtained for higher V. For example, for 100 V, 60 V and 20 V, efficiencies of 26%, 52 % and 34% were obtained, respectively. These low values can be attributed to the competition between oxidation/dissolution of NTs [318].

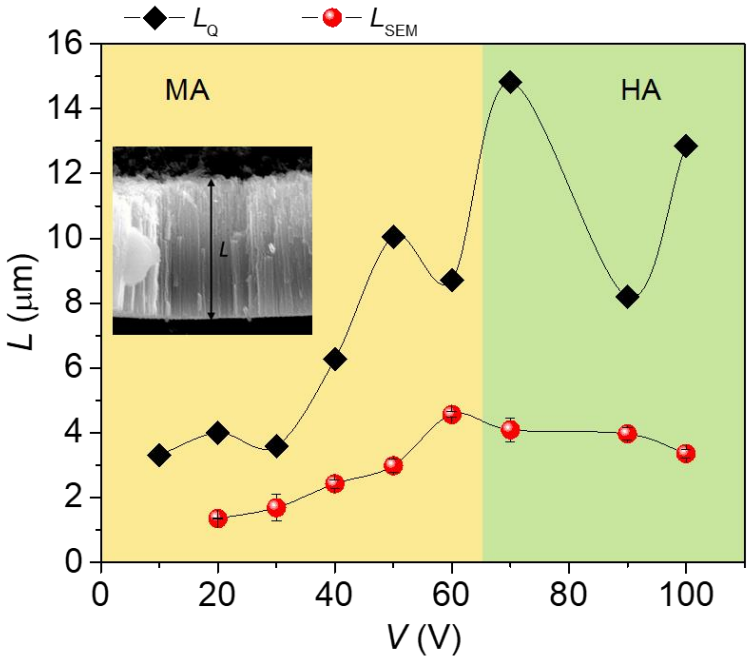

Figure 5.14. Fe_2O_3 NTs arrays thickness estimated from the charge (Q) curves, L_Q, and from SEM cross-sectional images, L_{SEM}, with variable anodization voltage.

5.2.5. Porosity

From Eq. (5.3), the porosity (P) of the Fe_2O_3 NTs was determined [Figure 5.15 (a)].

For Fe anodization, the overall porosities obtained are far from the 10% rule [304] optimized structures. Here, P takes a mean value around 35%. By increasing the applied V_{anod}, P also increases, i.e. P increases from 30% (20 V) up to 44% (60 V). Lower P is obtained for sample anodized at 20 V, corresponding to NTs with a more organized morphology and arranged in HCPA arrays structure [Figure 5.9(b)] closer to the 10% porosity rule. Further increasing the anodization voltage (70V-100V) the P decreases again, however here in the HA regime, the variation in porosity is manly attributed to the chemical dissolution of the NTs, as show in Figures 5.9(g)-(i).

A prediction of the film thickness from Q curves was already presented in Figure 5.14, L_Q, from Eq. (5.6). The charge transport during the formation of the anodic film is a reflection from both anodic current $j_{anod}(t)$ contributions: the ionic current (j_{ion}) and electronic current (j_e) [201,320]. Although L_Q and L_{SEM} present a similar increasing behaviour with V up to 60 V, L_{SEM} is significantly lower than L_Q, suggesting that the total anodic current is not reflected on the effective thickness observed from SEM images.

The thickness calculated by equation (5.6) has into account the whole thickness as non-porous anodized oxide. Schultze and Lohrengel, in their fundamental description

of the nature of passive films, considered a roughness factor *R* for the film thickness determination from the Faradays Law (regarding a crystalline film with a constant thickness) [201]. Then, equation (5.6) can be re-written as:

$$L_Q \times R = \frac{QM}{Fn\rho} \quad (5.7)$$

However, in the case of porous anodic films, the pores formation usually follows a HCPA distribution. For that, *R* factor can be replaced by the porosity (*P*). Figure 5.15(b) shows the relation of the L_Q corrected by the factor *P* comparing with the effective thickness of the NTs, L_{SEM}. By this way, a closest approach between the two thicknesses, expected and effective, was obtained. Both approaches show similar values (differences in the order of ~0.5 µm). Above 60 V, higher differences are observed, since HA also affects the current homogeneity and the NTs tops are strongly affected by chemical dissolution. Besides, it was stated that the field assisted dissolution, essentially chemical, is not reflected in the anodizing current [320,322-324].

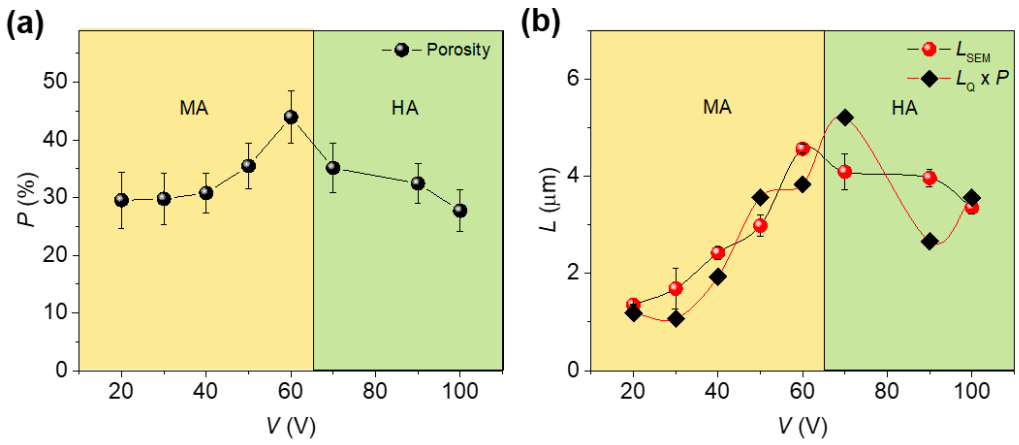

Figure 5.15. (a) Variation of the porosity (*P*) of Fe_2O_3 NTs arrays with potential (*V*). (b) Relation between nanotubes expected thickness taken from charge curves (L_Q) and porosity (*P*), in comparison with L_{SEM} effective thickness.

5.2.6. Structural characterization

The conversion of as-anodized NTs into hematite phase was further analyzed by XRD. The NTs arrays with different V_{anod} were annealed at 550 °C for 2 hours in air atmosphere. The crystalline phase of the annealed NTs was determined. The as-anodized NTs are amorphous, where no peaks can be observed, as can be seen by

the example of the PBGI pattern for the 60 V sample in Figure 5.16. After the annealing, the hematite crystalline phase (JCPDS 33-0664) was obtained, with prevalent peaks (110) and (104), as well as other hematite characteristic peaks in planes (012), (113), (024), (116) and (214). As already referred in Chapter 3, the prevalent peak (110) is assigned to the improved conductivity of hematite [49]. For 20 V sample, slight higher intensity of the (110) plane is observed, comparing with (104) one. This tendency seems to be inverted as *V* increases up to 60 V.

A minor magnetite (Fe_3O_4) phase contribution is also present, as previously reported [137,296,300]. In the future, we intend to study the magnetic properties of these samples, to confirm the presence of magnetite or other iron oxide phases contribution [308].

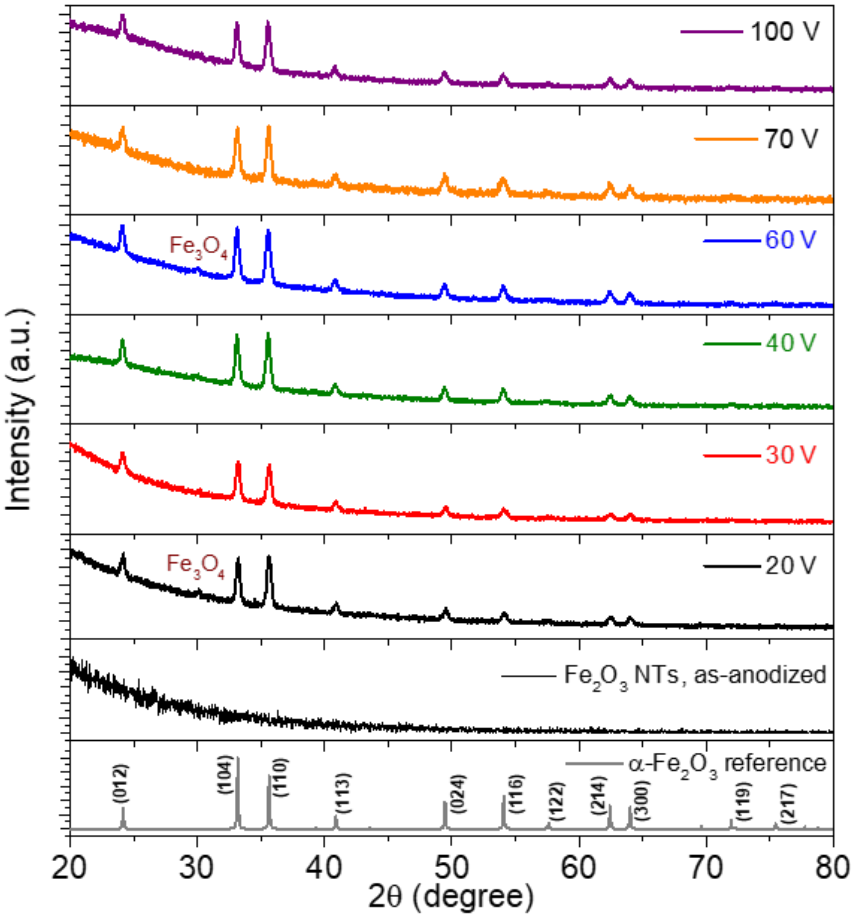

Figure 5.16. XRD patterns of Fe_2O_3 NTs arrays anodized at 20-100 V and after annealing at 550°C in air. The hematite reference and the as-anodized NTs at 60 V (without annealing), are shown for comparison.

5.2.7. Photoelectrochemical characterizations

The photocurrent density-voltage curves (*j*-*V*) are presented in Figure 5.17. In general, the photocurrent density (*j*) decreases by increasing the anodization voltage, V_{anod}. Higher *j* was obtained for the 20 V sample with *j* ~ 0.5 mA·cm^{-2} at 1.45 V_{RHE} (~0.31 mA·cm^{-2} at 1.23 V_{RHE}). On the other hand, lower *j* was obtained for 60 V sample with *j* ~ 0.2 mA·cm^{-2} at 1.45 V_{RHE} (~0.1 mA·cm^{-2} at 1.23 V_{RHE}). Furthermore, we can say that better photocurrents are obtained for smaller porosities (20 V sample), closer to the optimized self-organized nanoporous according to 10% rule [304], Figure 5.18(a). Therefore, increasing the porosity up to 44% (up to 60 V) lead to *j* decrease. However, by reaching greater anodization voltages (HA regime) we once again obtain smaller *P* from 35% to 28% (70V to 100 V), but low *j* performances are achieved (*j* = 0.26 to 0.19 mA·cm^{-2} at 1.45 V_{RHE}, respectively.) For HA regime the NTs are morphologically highly damaged at the top surface and along the tubes [Figures 5.9 (g)-(i)], in which the smooth walls become rough due to the high dissolution that occurs in high voltage regimes.

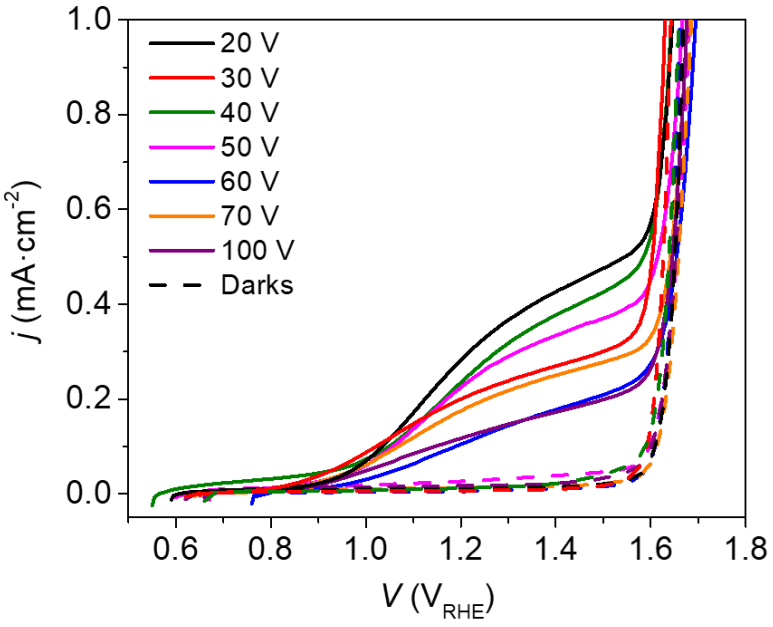

Figure 5.17. Photocurrent density curves, under dark and 1 sun, of Fe_2O_3 NTs arrays anodized at 20-100 V, followed by annealing at 550°C in air.

Furthermore, the same trend is observed with the NTs length, *L*; by increasing *L* up to 60 V, the photocurrents also decrease, Figure 5.18(b). This could be attributed to the fact that considerably longer NTs (~4.6 µm for 60 V) will be affected by longer pathways for charge transportation and higher e^--h^+ recombination rates.

The increasing of *D* and *W* features also lead to *j* decrease [Figure 5.18(c)]. In fact, larger *D* and thicker *W*, (24 to 78 nm; 10 to 18 nm respectively) were obtained when the anodization voltage is increased up to 70 V (above 70 V, no defined walls were observed). The thin *W* of NTs favor the diffusion of the photogenerated holes to the electrolyte-photoanode interface, avoiding e^--h^+ recombination and thus leading to an improvement of the photocurrent [89].

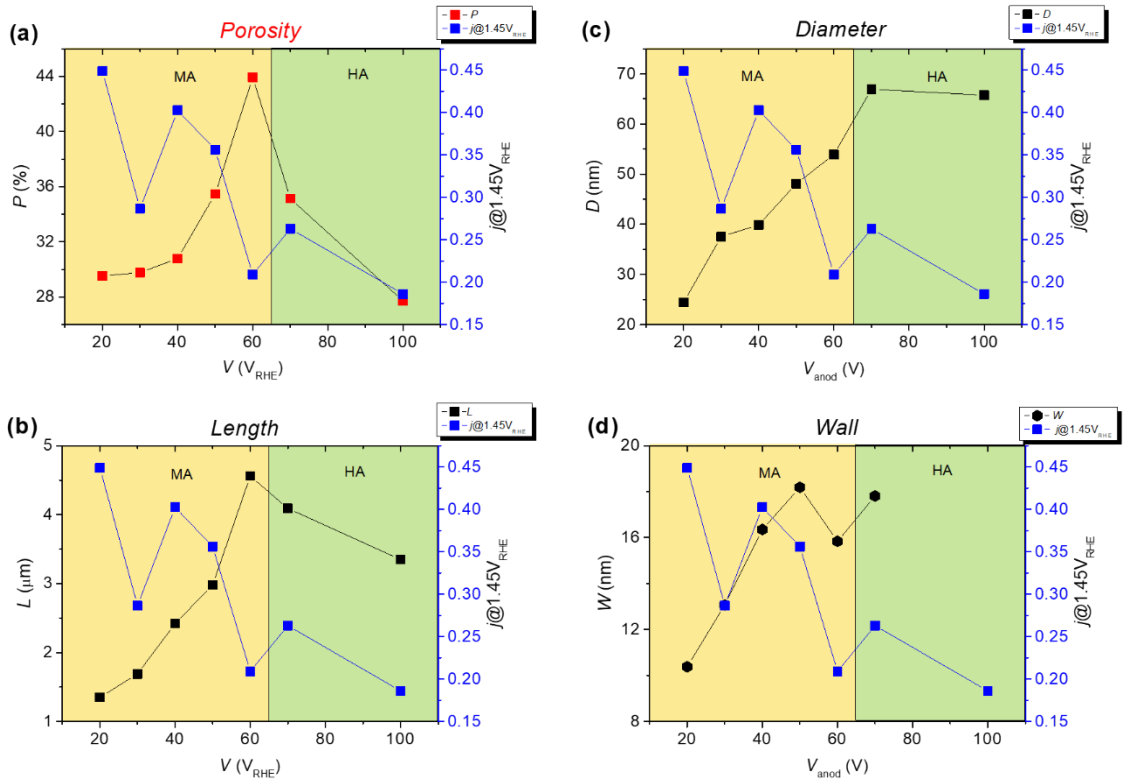

Figure 5.18. Relation between the photocurrent *j* (1.45 V_{RHE}) with (a) porosity *P*, (b) thickness *L*, (c) diameter *D* and (d) wall thickness *W* of the α-Fe_2O_3 nanotubes (NTs), anodized at 20-100 V.

Nevertheless, the overall photoanodes consisting on anodic NTs provided improved photocurrents compared with the ones obtained by the hydrothermal method: Fe_2O_3 NWs (*j* = 0.01 mA·cm^{-2} at 1.45 V_{RHE}) or hydrothermal nanoneedles/nanospheres (*j* = 0.06 mA·cm^{-2} at 1.45 V_{RHE}) under the same annealing conditions (Chapters 3 and 5.1., respectively).

To be noticed that, here no pre-treatment of the Fe foil was applied before anodization, or annealing with a specific atmosphere (attributed to the improvement of NTs organization or to isolate the hematite phase [89,137]), that could significantly improve the *j* results. This suggests that if we optimize our synthesis considering these parameters, we could obtain improved *j* > 0.5 mA·cm^{-2}. Also, the *j* obtained for 20 V sample is a high value compared with the typically reported in the literature

[132,291,294,298], considering the conditions used (fast anodization, no Fe foil pre-treatment, etc.).

The *j* values are also corroborated by the XRD results. Higher intensity of the (110) peak (Figure 5.16) was obtained for samples with higher *j*. The (110) contribution (associated to enhanced anisotropic conductivity of hematite), lead to higher *j* (as already observed for the case of hematite NWs on Chapter 3).

It is worth to stress, as discussed before, after the annealing it was observed several cracks between NTs arrays and a spongy-like structure then arises due to the Fe foil oxidation (Figure 5.10). These features could influence the photoresponse, in particular for the 20V sample since it is more evidenced for this sample [Figures 5.10(a) and (b)].This kind of porous structure was already reported to grow on the top of NTs, being related with the NTs thermal treatment, and referred to grow in thickness as the annealing temperature increased [132]. However, differently from the literature, here it seems to grow behind the NTs. It appears that the annealing treatment oxidized the Fe foil leading to a volume expansion of the Fe substrate that caused the cracks in the NTs template. Thus, the porous spongy-like structure is a result of the Fe foil oxidation during the annealing as shown in Figure 5.10, where we can observe some cracks forming islands of NTs surrounded by the sponge-like morphology.

The thermal oxidation highly affects the 20 V sample since in this case the NTs template is thinner. Nevertheless, the presence of the oxidized Fe spongy structure is a general tendency for all other samples with different V_{anod}, Figures 5.10(c)-(h).Thus, it must be taken in account that *j* is the contribution not only of the NTs morphology but also from the spongy-like structure [Figure 5.10(a)].

Although it was reported in literature that a bi-layered structure (NTs + spongy-like) enhanced the water splitting performance [132], further work is still necessary to understand the mechanism associated to the formation of this kind of structure, and evaluate the extent of its contribution on *j*. This and other parameters (such as annealing atmosphere, substrate pre-treatment, etc.) will be considered in future works for NTs synthesis optimization, and towards a deeper understanding of the NTs formation and growth, in order to improve the PEC cells efficiencies.

5.3. Conclusions

In this work, the production of Fe_2O_3 NTs was accomplished by two different methodologies: hydrothermal and electrochemical anodization.

The growth of hematite nanostructures by a simple hydrothermal method was investigated. Precursor phosphate and sulfate determine the shape resultant from hydrothermal process. Various experimental conditions were tested, including hydrothermal time and the presence of sulfate ion. The nucleation on FTO was not uniform and required more hydrothermal time of 72 h. SEM images showed the different morphologies obtained through this method. NTs are obtained in solution, while nano-needles/spheres grow on FTO respectively without and with sulfate ions. By X-ray diffraction, it was confirmed the presence of hematite crystalline phase. For both nanostructures, it was obtained higher photocurrent density values (~0.06 $mA \cdot cm^{-2}$) than the obtained by hematite nanowires with the same annealing conditions. The deposition by this method, either on FTO using a polymer solution or directly on FTO during hydrothermal process is not uniform and it is still ongoing the optimization of this method.

By anodization, the NTs were formed in just five minutes, with variable conditions of applied voltage. Similar to TiO_2, the anodization curves of Fe_2O_3 show a non-steady-state stage after the nucleation period, with oxidation rate prevailing over dissolution. The usual linear relation between pore diameter, interpore distance and wall thickness is verified up to 60 V. Above this voltage, a decrease in NTs organization is observed, referred to a growth regime of hard-anodization. In this regime, the use of high voltages (high electric field) with fluoride-based electrolytes, allied with temperature factor, favours the oxide breakdown and enhances the dissolution at the NT tops. Ultimately, the template thickness and NTs organization are highly affected for potentials above 60 V. A relation between the anodization charge curves and the porosity of the NTs is here established, in good correlation with the experimental data collected from SEM images. High aspect-ratio is obtained for the 20 V sample, with a porosity regime ~30%, while for 60 V, the porosity significantly increased to 44%. After annealing, the presence of hematite crystalline phase was confirmed in all samples, with higher intensity of both (110) and (104) planes, although for 20 V sample, slight higher intensity of the (110) plane is observed. The morphology of NTs was affected by the annealing step, where a sponge-like morphology, attributed to the Fe foil oxidation, was revealed between the NTs. Photocurrents in the order of 0.45 $mA \cdot cm^{-2}$ (at 1.45 V_{RHE}) were obtained for the 20 V sample, while for thicker 60 V sample, lower photocurrent of 0.2 $mA \cdot cm^{-2}$ (at 1.45 V_{RHE}) was obtained. The photocurrent was shown to decrease with the NTs template thickness due to the longer pathways for generated charge carriers to travel inside the photoelectrode, leading to higher recombination.

Chapter 6

Hydrothermal growth of WO_3 nanoplates multilayers

Chapter 6

Hydrothermal growth of WO_3 nanoplates multilayers

In this chapter it is described the synthesis of WO_3 nanoplates by hydrothermal method. It was investigated the impact of different hydrothermal conditions, especially the temperature, time, and layer-by-layer thickness increase approach. The morphological, structural, optical and photoelectrochemical features of the obtained photoelectrodes were studied. Ideal conditions were obtained with certain hydrothermal temperature and time in terms of photoresponse and then applied in the layer-by-layer hydrothermal growth approach. Photocurrents improvements over 70% where achieved with the studied conditions.

6.1. Overview

In recent years, α-Fe_2O_3 and WO_3 have gained a standing position among semiconductor oxide for photoelectrochemical water splitting applications due to several factors, such as low-cost, raw material availability with fairly easy synthesis and excellent chemical stability in aqueous media [16,21,40]. Hematite present a band gap in the range 2.1-2.2 eV and can absorb up to 40% of the solar spectrum energy [21,43]. However, it displays some limitations like the low electron mobility (0.01-0.1 $cm^2 \cdot V^{-1} \cdot s^{-1}$) and small charge carrier diffusion lengths (2-4 nm) [16]. On the other hand, WO_3 displays a broader band gap (2.6-2.8 eV), limiting the solar spectrum absorption, but presents standing advantages, such as higher electron mobility (6 $cm^2 \cdot V^{-1} \cdot s^{-1}$) and longer charge carrier diffusion lengths (~150 nm) making WO_3 a very appealing material for PEC applications [16]. To enhance these advantages, nanostructuring has emerged as one of the best tools.

The charge transport effectiveness can be improved (electron pathways and hole diffusion to the surface), as the photo-active surface area can be greatly increased, improving the absorption of visible light and narrowing the band gap

[21,40,158,159,325]. In fact, WO_3 has been the topic of intensive research for many technological applications, such as photocatalysis, photochromism and sensing [148].

Different synthesis methods to prepare WO_3 nanostructured photoelectrodes have been widely explored. Specifically, by physical route as the sputtering (reactive RF magnetron) and thermal evaporation methods; by electrochemical methods as the electrochemical anodization and electrodeposition; and the more intensely explored approach is by chemical routes, like sol-gel, hydrothermal, solvothermal, chemical vapor deposition, and spray-pyrolysis [37,162-166].

Hydrothermal methods stand out since they carry out several important advantages, such as being a low cost and scalable technique.

In this work, WO_3 nanoplates were prepared by hydrothermal method. First, it was tested the hydrothermal temperature (80-120 ºC). Then, WO_3 photoelectrodes were produced using several layers of nanoplates obtained by sequential steps of hydrothermal (12 h at 90 ºC) and annealing processes. The number of layers were tested up to a limitation of *j* performance was achieved. Using the same hydrothermal conditions (90 ºC and one layer), a continuous hydrothermal process using different hydrothermal time from 12 to 72 h was tested.

6.2. Experimental details

FTO glass substrates were cleaned as described in the Experimental Section, as reported by Francisco *et al.* [261], and then placed in a 40 mL capacity teflon stainless steel autoclave. A 20 mL solution of 0.01 M $Na_2WO_4.2H_2O$ + 0.0236 M $(NH_4)C_2O_4$ was prepared, consisting in the following steps. First, 0.066 g of $Na_2WO_4.2H_2O$ was dissolved in 8.6 mL of deionized water under constant stirring. Then, 2.8 mL of 3 M HCl was added drop by drop (a yellow precipitate was formed), followed by the addition of 0.067 g of $(NH_4)C_2O_4$. After few minutes, the solution became transparent and more deionized water was added up to a total volume of 20 mL. Finally the solution was continuously stirred for 30 min [162]. Several WO_3 photoelectrodes samples were prepared varying the hydrothermal parameters (hydrothermal temperature °C and time) that correspond to 3 distinctive groups of samples: 1st group of samples (Temperature), where we vary the hydrothermal temperature and fixed the number of layers (1 step of hydrothermal growth) during 12 h; 2nd group of samples, we vary the number of layers, i.e. we perform the hydrothermal step at 12 h at 90 °C followed by the annealing at 500 ºC for 2.5 h for several times, more precisely from 1 to 6 times; and a 3rd group (Time) where we vary

the hydrothermal time at a fixed temperature 90 ˚C and only performed 1 layer (1 step hydrothermal). The conditions are summarized in Table 6.1.

After hydrothermal growth, a yellow-green film layer was formed on the top of FTO substrates. Then a thermal annealing was performed at 500°C during 2.5 h (ramp: 5 ºC/min) in air atmosphere, after each hydrothermal step.

The morphological, structural and optical characterization was performed using respectively SEM, XRD in PB mode and by UV-vis techniques. The photoelectrochemical characterization was assessed by the photocurrent density-voltage curves. Details are described in Chapter 2.

Table 6.1. Groups of WO_3 samples prepared with different hydrothermal conditions

Hydrothermal parameters	Group of samples		
	1st	2nd	3rd
Temperature (°C)	80-140	90	90
Time (h)	12; (6)	12	12-72
Number of Layers	1	1-6	1

6.3. Results and discussion

6.3.1. Photoelectrochemical performance

Photocurrent density-Voltage curves. The photocurrent density-voltage (*j*-*V*) characteristic curves under dark and illumination conditions were obtained for the WO_3 photoelectrodes (Figure 6.1). The 1st group, samples prepared with different temperature, the 90 ºC display better performance [Figure 6.1(a) and (d)]. Furthermore, having this as the best temperature (with the best result), the photocurrent density (*j*) for the 2nd group of samples increased as the number of layers increases [Figure 6.1(b)]. On the other hand, for this group the optimum performance was observed for 5 layers with *j* under illumination of approximately 1 $mA \cdot cm^{-2}$ at 1.45 V_{RHE}. However, further thickness increase, number of layers to 6, led to *j* decrease (0.91 $mA \cdot cm^{-2}$). [Figure 6.1(b) and (d)]. Comparatively with reported values for bare WO_3 (~0.6 $mA \cdot cm^{-2}$ at 1.8 V_{RHE}) [175], here we obtained higher solar-to-current conversions.

For the 3rd group, we intend to represent the same timeline where the number of layers corresponds: 1 layer to 12 h, 2 layers to 24 h, 3 layers to 48 h, etc. The *j*(*V*) curves show that the hydrothermal time does not influence the photoresponse of the photoelectrodes,

giving approximately the same values (ranging from 0.56-0.59 mA·cm^{-2}) [Figure 6.1(c) and (d)].

In summary, the optimum experimental conditions to achieve the best *j* were obtained with hydrothermal temperatures of 90 °C during 12 h, and under these conditions a sample with one layer showed *j* = 0.56 mA·cm^{-2}, while the sample with 5 layers showed a *j* = 0.96 mA·cm^{-2}, i.e. corresponding to an increase in *j* of over 70% when compared with the sample with one layer.

Notice that similar values of photocurrent were obtained for samples with 140 °C during 6 h with 3 layers when compared with the sample with one layer at 90 °C during 12 h.

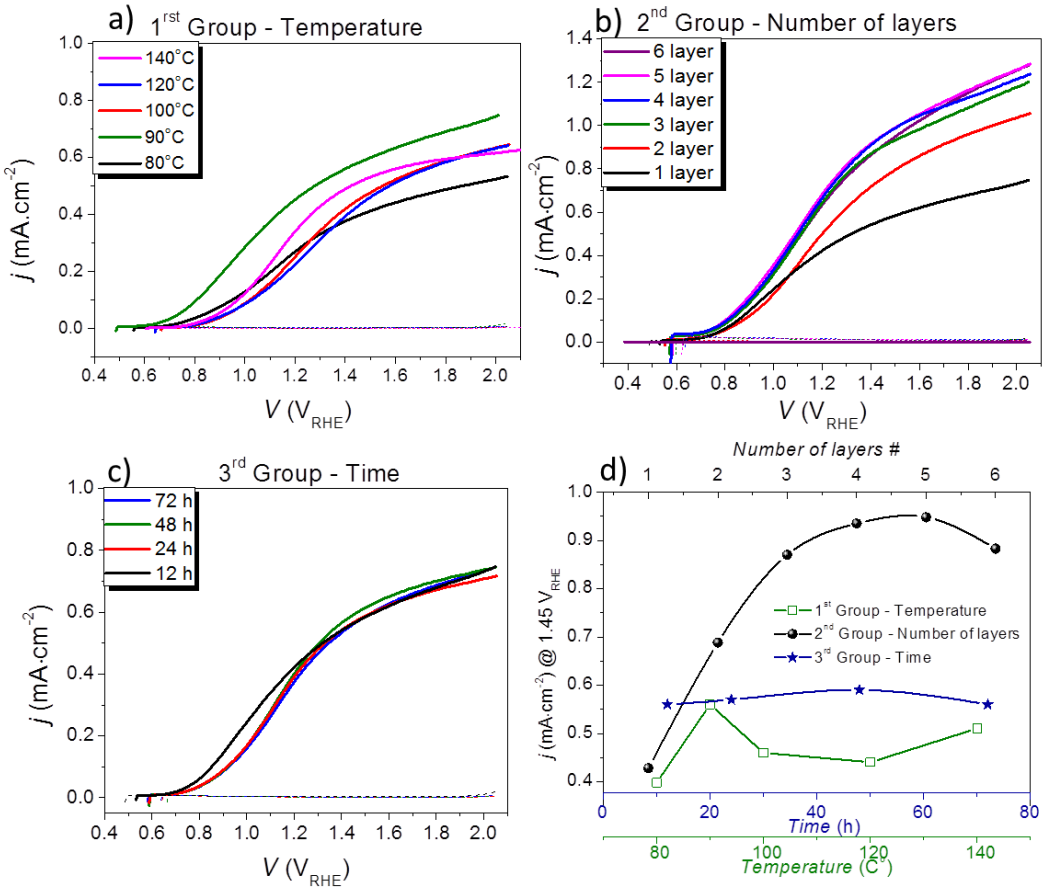

Figure 6.1. *j-V* characteristic curves for WO_3 samples: (a) 1st group (temperature) – samples prepared with different hydrothermal temperatures (80, 90, 100, 120 and 140 °C) for 12h and with 1 layer; (b) 2nd group (number of layers) – samples prepared with several layers (1 to 6 layers), i.e. sequential steps of hydrothermal growth, each step (1 layer) during 12 h at 90 °C; (c) 3rd group (time) – samples prepared with different hydrothermal time (12, 24, 48 and 72 h) at 90 °C with 1 layer; (d) temperature, number of layers and time hydrothermal parameters as a function of *j* at 1.45 V_{RHE} for the different groups of samples.

6.3.2. Morphological characterization

SEM images reveal that for all the samples, the WO_3 growth on the FTO substrates is a continuous porous film composed by nanoplates shallow parallelepiped geometry (Figures 6.2; 6.3; 6.5).

For the 1st group, we could observe in SEM images that after 90 ºC, by increasing the temperature the nanoplates dimensions also increase, i.e. the nanoplates mean edge is not very affected but the mean height (*t*) [illustrated in Figure 6.2(a)] is mostly affected. Thus, sample with 90 ºC showed nanoplates with thinner *t*, leading to films with high porosity degree [Figure 6.2(b)]. The improved *j* shown by this sample was assigned to the higher porosity presented by these photoelectrodes, made of connected nanoplates of WO_3 with thinner *t*. In fact, photoelectrodes with higher porosity presents an extended photo-active surface area, increasing the effective electrolyte-semiconductor interface area that promotes a more efficient charge collection, ultimately leading to increased photocurrents [5,16,21,170]. Additionally, optimized photocurrents could be due to the nanoplates particle size being close to the hole diffusion length of WO_3, estimated to be around 150 nm [150,178].

The thicker nanoplates films exhibit lower porosity as illustrated in Figure 6.2(e) leading to the decreased photocurrents presented in the previous section. Contrarily to reported in literature [162], were thicker width plates originated best results, here thinner width plates originated higher *j*. Additionally, in the 80 ˚C [Figure 6.2(a)] sample, this temperature was not enough to obtain a continuous film and the nanoplates were significantly larger when compared to all the other samples with different temperatures [Figures 6.2(b)-(e)].

As for the nanoplates thickness (*L*), we can see that after increasing the temperature, *L* also increases until 120 ˚C, although at 140 ˚C, *L* decreases [Figures 6.2(f)-(k), Figure 6.6]. We can correlate these results with the photocurrent results which show an inverse trend: thinner *L* leads to higher photocurrents (90 and 140 ˚C).

The 1st group allowed to identify the optimized temperature conditions to obtain higher *j* and relate it with the different morphological features of the nanoplates. The 90 ºC showed a better performance and was further used in 2nd and 3rd groups. The other samples (80, 100-140 ºC) were not considered for further characterization in this work.

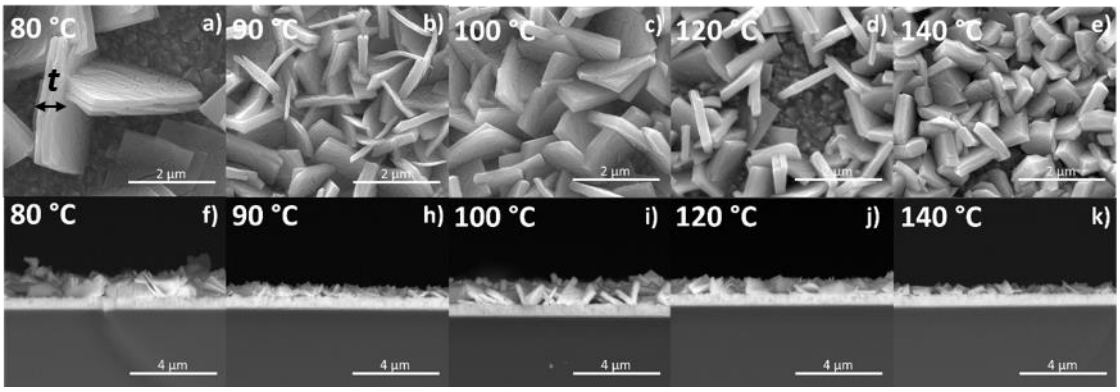

Figure 6.2. SEM images of the WO_3 samples 1st group (temperature) – samples prepared with different hydrothermal temperatures (80, 90, 100, 120 and 140 °C) for 12 h and 1 layer (a)-(e) top-views and (f)-(k) cross-sectional views.

For the 2nd group (number of layers), SEM top view images shows that the nanoplates dimensions, mainly *t*, starts to growth thinner (increasing the porosity) with the increasing number of deposited layers [Figure 6.3(a)-(f) insets]. However, surprisingly and more revealing differences are observed in the low magnification images [Figure 6.3(a)-(f)]. We can see that the homogeneity dispersion of the nanoplates is affected by waviness-like feature. This is more relevant after the 4 layers and increases until the 6th layer. This waviness dispersion gives a more porous characteristic to the photoelectrodes, which ultimately leads to the improved photoresponse (higher *j*). We believe that this growth characteristic is related to the fractal like characteristic of these structures' growth morphologies. Is worth to notice that a fractal like dendritic-tree was obtained in sample with layer number 5 [Figure 6.3(e)]. As for the cross-sectional view images, we can see that increasing the number of layers, *L* also increases (almost linearly) (Figure 6.4; Figure 6.6). As the photoelectrode thickness increases the performance also increases [Figure 6.1(b) and (d)]. Actually, the light absorbance and active area also increases and the percolation path to the FTO surface decreases. However, the thickest photoelectrode, layer number 6, *L*= 7 µm, shows a lower photocurrent which indicates that the photo-generated electrons recombine before reaching the collection point. This is probably due to the longer path that charge carriers have to travel coupled with the increase of size and number of nanoplate clusters, which can act as electron-hole recombination centers [21].

For the 3rd group (time ranging from 12 to 72 h), SEM top view images show that the nanoplates dimensions and *t* display approximately the same dimensions (porosity) with the increasing hydrothermal time [Figure 6.5(a)-(d)].

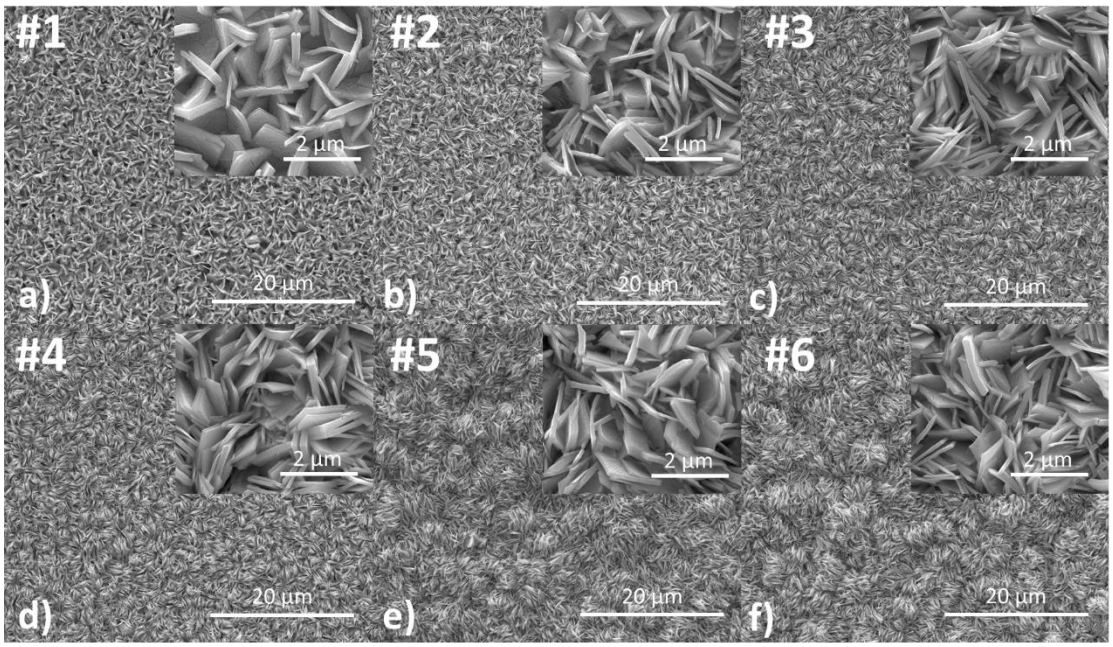

Figure 6.3. SEM images of the WO_3 samples 2nd group (number of layers) – samples prepared with several layers [1 to 6 layers, (a) to (f)], *i.e.* sequential steps of hydrothermal growth, each step (1 layer) during 12 h at 90 °C; top-view insets (higher magnification images).

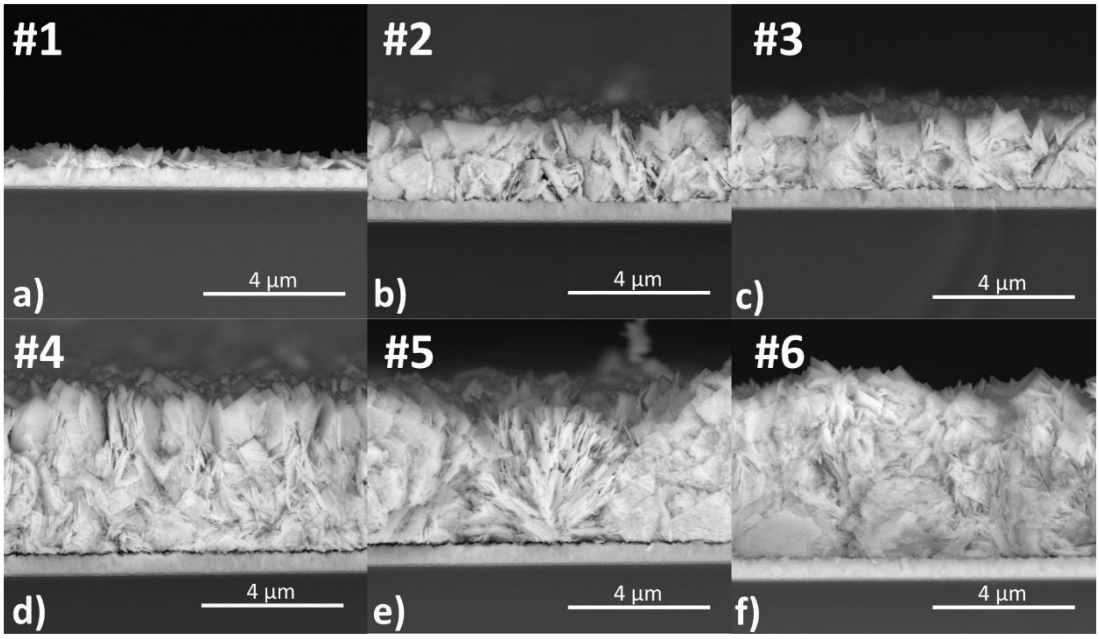

Figure 6.4. SEM images of the WO_3 samples 2nd group (number of layers) – samples prepared with several layers [1 - 6 layers, (a) to (f)], *i.e.* sequential steps of hydrothermal growth, each step (1 layer) during 12 h at 90 °C; cross-sectional views.

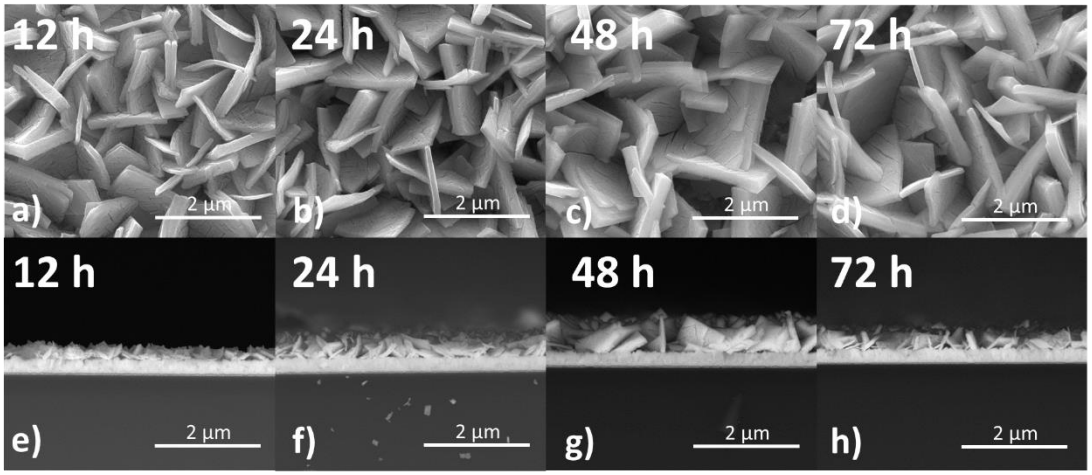

Figure 6.5. SEM images of the WO_3 samples 3rd group (time) – samples prepared with different hydrothermal time (12, 24, 48 and 72 h) at 90 °C with 1 layer; (a)-(d) top-views and (e)-(h) cross-sectional views.

On the other hand, slight increase of *L* is observed until the 48 h, from 0.52 to 1.5 (Figure 6.6). Increasing the hydrothermal time, *L* also increases but not so significantly when compared with the group of layer steps (2nd group) that have the same hydrothermal time as these samples (1 layer = 12 h; 2 layers = 24 h, etc). In fact, the photocurrent is almost constant for all these photoanodes. This is related to the rate-limiting growth behaviour of these structures that we believe that governs this growth process. It has been established by the literature that hydrothermal growth depends on parameters such concentration, volume, temperature and time. An accurate balance leads to several different morphological nanoshapes, depending on the type of material (TiO_2, ZnO, WO_3 or hematite) [8,148]. One thing that is common to this process is the rate-limiting growth behaviour. The hydrothermal is a rate-limiting process, where the thickness of the oxide films (the nanostructures, such nanowires, nanoplates, etc.) is limited in time.

To overcome these limitations, we present the approach of hydrothermal multi-layers, i.e. step-by-step layers deposition (2nd group), that offers the possibility to increase the photocurrent of these photoelectrodes. Although this strategy is time consuming, we believe that with the low temperature optimization and the fact that this is highly scalable method that leads to low-cost issues.

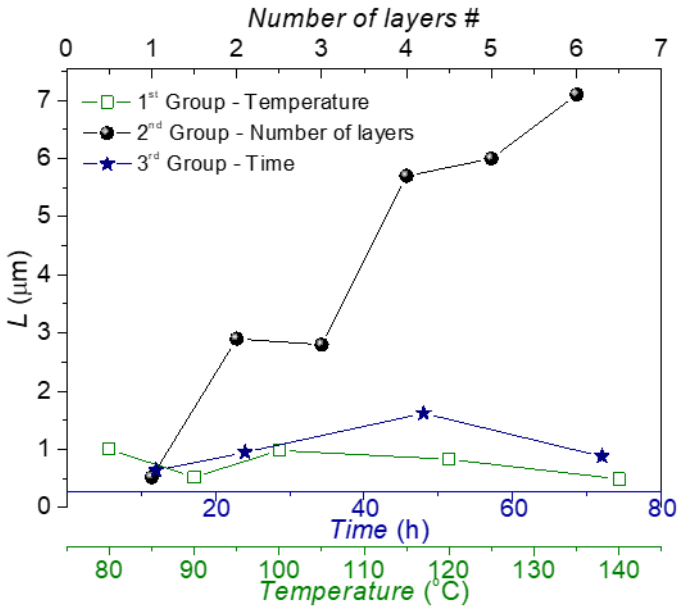

Figure 6.6. WO_3 photoelectrodes thickness (*L*) as a function of the hydrothermal parameters: temperature (1st Group), number of layers (2nd Group) and time (3rd Group); average *L* extracted from cross-section views of the SEM images.

6.3.3. Structural characterization

Figure 6.7 displays room temperature X-Ray Diffraction (XRD) patterns of WO_3 photoelectrodes in PB focusing method, for the 2nd group of samples (number of layers) and 3rd group of samples (time), respectively. After the thermal annealing for both groups, the XRD patterns reveal the polycrystalline character of the samples (Figure 6.7). The main diffraction peaks were indexed as the Bragg reflections of the WO_3 monoclinic phase (JCPDS 01-083-0950). Notice that it is clearly identified the characteristic WO_3 monoclinic triplet: the Bragg directions [002], [020] and [200] for the peaks at 23.08, 23.6 and 24.4°, respectively (insets of Fig. 6.7). The intense and sharp peaks feature reveals a complete conversion of the amorphous phase into a crystalline phase. The contribution of the F:SnO_2 layer (FTO) (cassiterite), underneath the WO_3 film was not detected in the samples spectra when compared with FTO spectrum, since the use of grazing incidence angles allows to remove the signal of the substrate.

With the increasing number of WO_3 layers (2nd group), the monoclinic triplet (Bragg directions [002], [020] and [200]) intensity decreases, changing the preferential growth direction in the Bragg directions [022], [-202] and [220] (being the latter the preferential direction with more intense peak). The crystallographic changes can be associated to

the different layer-by-layer surface nucleation growth, since the number of layers increases the surface morphology changes.

By changing the hydrothermal time (3rd group) no significant crystallographic changes were observed, as shown in the spectra for 12 or 72 h (Figure 6.7). The preferential growth direction remains the same (Bragg directions [002], [020] and [200]), characteristic WO_3 monoclinic triplet.

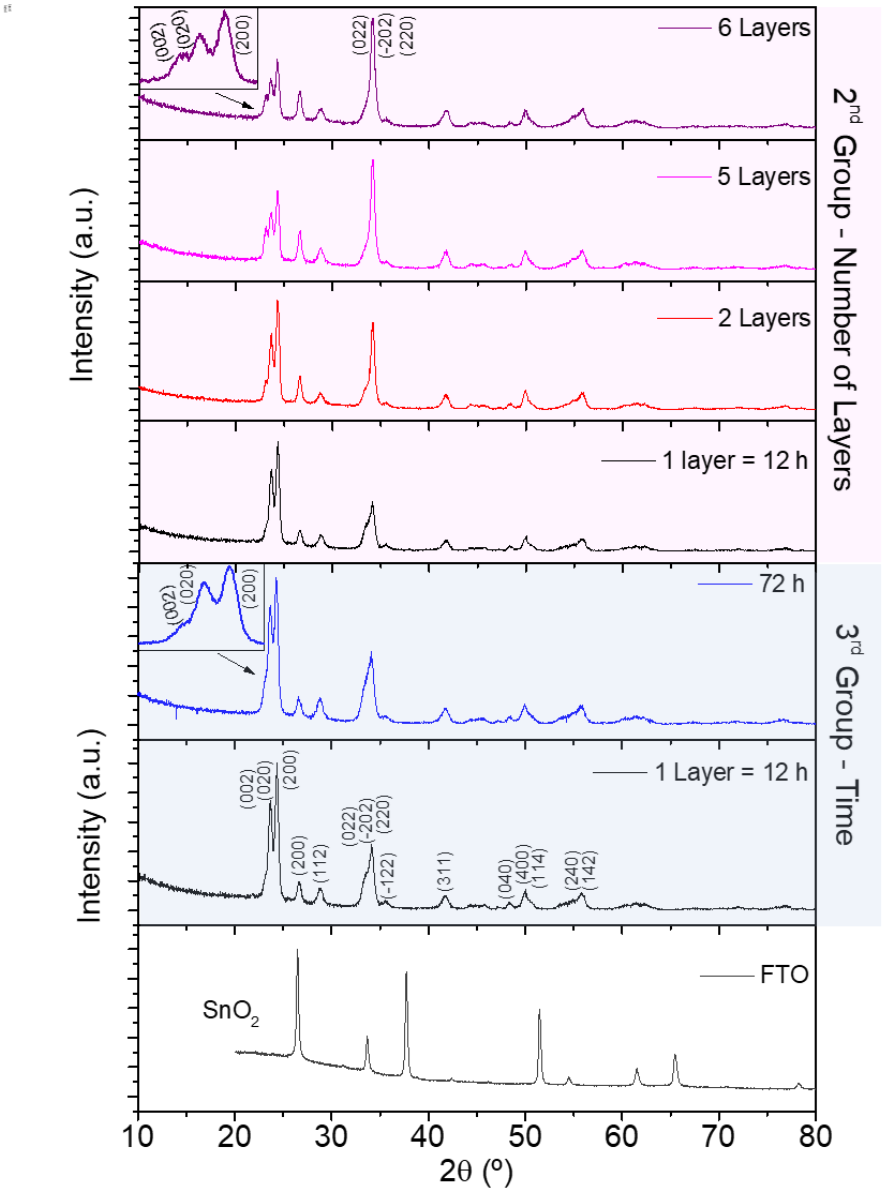

Figure 6.7. X-ray diffraction patterns spectra of WO_3 photoelectrodes in parallel-beam focusing method (from top to bottom): 2nd group (number of layers) – samples prepared with several layers (1 to 6 layers), *i.e.* sequential steps of hydrothermal growth, each step (1 layer) during 12 h at 90 °C; 3rd group (time) – samples prepared with different hydrothermal time (12 and 72 h) at 90 °C with 1 layer; The FTO glass substrate spectrum is presented. The diffraction peaks and the corresponding reflections for orthorhombic corresponds to monoclinic WO_3 phase (Reference JCPDS 01-083-0950).

6.3.4. Optical characterization

Figure 6.8 shows the UV-vis absorption spectra patterns of WO_3 photoelectrodes, for the 2nd group of samples (number of layers) and 3rd group of samples (time) [Figure 6.8(a) and (b), respectively]. The absorption spectra were obtained from the reflectance and transmittance data [by Eq. (2.10)]; the plotted absorption spectrum of the WO_3 photoelectrodes was obtained by removing the contribution of the transparent FTO substrates, as already described in Chapter 2 (section 2.3.4).

In general for the 2nd group samples, it is observed that thicker samples show enhanced light absorption spectra when compared to thinner ones. Furthermore, by enhancing the number of layers a small red-shift of the absorption edge is observed. However, both effects are only observed until 3 layers, for 4, 5 and 6 layers practically the same spectra are obtained. Thus, light absorption can be enhanced by increasing the thickness of the films, ultimately leading to improved photocurrents

As for the 3rd group of samples, equivalent spectra are observed from 12 to 72 h. This result is in line with *L* and photocurrents obtained for this group: increasing hydrothermal time, *L* increases (smoothly) and the photocurrent is practically the same.

The optical band gap for all the samples were determined using the *Tauc* formula, Eq. (2.11), for an allowed indirect transition (WO_3). The band gap values can be determinate by the plot of $(\alpha h\nu)^{1/2}$ *vs.* $h\nu$ [Figure 6.8(c) and (d)].

The obtained values of band gap energy (E_g) for the two groups of samples varies from 2.73 to 2.63 eV for the 2nd group samples and 2.73-2.72 eV for the 3rd group samples (with indirect transition, n = 1/2). Although E_g does not show significant differences by increasing the thickness of the photoelectrodes (2nd group) a decreasing tendency in E_g is observed for thicker samples. On the other hand, it is obvious enough that E_g does not get affected by varying the hydrothermal time (from 12 to 72 h) which is expected since for these samples there are no significant changes in morphology or crystallography. Also, the photocurrent of these photoelectrodes was approximately the same ranging from 0.56-0.59 $mA \cdot cm^{-2}$ [Figure 6.1(c) and (d)].

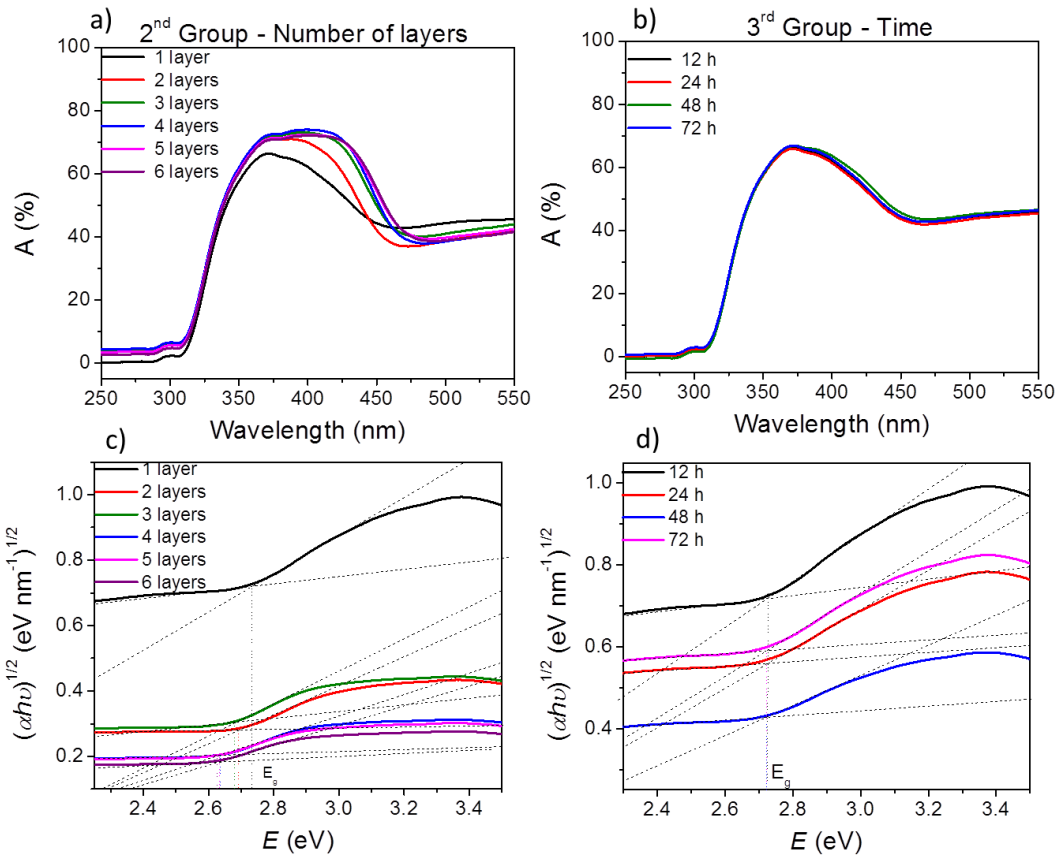

Figure 6.8. UV-vis absorption spectra and the *Tauc* plots (E_g is the band-gap) of the WO_3 photoanodes: (a) and (c) 2nd group (number of layers) – samples prepared with several layers (1 to 6 layers), *i.e.* sequential steps of hydrothermal growth, each step (1 layer) during 12 h at 90 °C; (b) and (d) 3rd group (time) – samples prepared with different hydrothermal time (12 and 72 h) at 90 °C with 1 layer.

6.4. Conclusions

Several WO_3 photoelectrodes were prepared with different hydrothermal parameters that correspond to 3 groups of samples: 1st group of samples (temperature), where we vary the hydrothermal temperature and fixed the number of layers (1 step of hydrothermal growth) during 12 h; 2nd group of samples, we vary the number of layers, i.e. we perform 12 h at 90 °C hydrothermal step several times, from 1 to 6 times; and a 3rd group (time) where we vary the hydrothermal time at a fixed temperature 90 °C and only performed 1 layer (1 step).

Optimum conditions were obtained with temperature of 90 ºC during 12 h with the higher photocurrents. The thinner nanoplates films exhibit higher porosity leading to the increase of photocurrents. Contrarily to reported in literature, where thicker height plates

originated best results, here thinner height plates originated higher photocurrent density. Low height plates constitute improved surface photoactive areas, benefitting the charge transport.

Increasing the hydrothermal time from 12 to 72 h, the same photocurrents were obtained. The growth rate limitation was observed, *i.e.,* increasing the hydrothermal time did not increase the nanoplates thickness.

Furthermore, increasing the number of layers (number of hydrothermal steps) with the conditions of 90 ºC during 12 h, we obtained photocurrents of almost 1 $mA \cdot cm^{-2}$. A *j* increase from 0.56 to 0.96 $mA \cdot cm^{-2}$ (at 1.45 V_{RHE}) respectively for 1 to 5 layers, was achieved, that corresponds to more than 70% improvement when compared with the sample with one layer. Comparatively with reported values for bare WO_3 (~0.6 $mA \cdot cm^{-2}$ at 1.8 V_{RHE}), here we obtained higher solar-to-current conversions.

In order to better understand the structural and photoelectrochemical charge transport properties of the resultant WO_3 photoanodes, other tests/techniques will be considered in future work, such as Raman spectroscopy, photocurrent stability measurements, or electrochemical impedance spectroscopy.

Chapter 7

The effect of electrolyte re-utilization in the growth rate and morphology of TiO_2 nanotubes

Chapter 7

The effect of electrolyte re-utilization in the growth rate and morphology of TiO_2 nanotubes

In an industrial context, the re-utilization of resources is very important to monetize processes, reducing the production costs without overlooking a proper performance of the devices. For specific applications such as dye-sensitized solar cells or photoelectrochemical devices, a high-aspect-ratio configuration of the produced TiO_2 nanotubes (NTs) is essential to achieve higher conversion efficiencies. In this work, we reported the effect of electrolyte re-utilization in the diameter, length and morphology of TiO_2 nanotubes (NTs) produced by electrochemical anodization. A detailed study of the bias voltage effect on the anodic NTs for fresh and re-used electrolytes was performed. Also, the possibility of obtaining NT arrays with ribs morphology just by re-using the electrolyte was unveiled. This chapter is based on the work: P. Quitério, D. Costa, A. Apolinário, C. T. Sousa, J. Azevedo, J. Ventura, L. Andrade, A Mendes, and J. P. Araújo. The effect of electrolyte re-utilization in the growth rate and morphology of TiO_2 nanotubes. Materials Letters 171 (2016) 224–227.

7.1. Overview

Titanium dioxide (TiO_2) is a semiconductor material that has been extensively studied due to its chemical stability, nontoxicity and high photocatalytic activity [203,326]. In particular, vertically oriented TiO_2 nanotubes (NTs) have unique physico-chemical properties, making them attractive for potential applications in many emerging fields, such the dye-sensitized solar cells (DSC) and the photoelectrochemical (PEC) cells [18,118,327].

Low-cost solar cells based on TiO_2 nanoparticles were first introduced by O'Regan and Grätzel in 1991 [193]. Their efficiency of up to 13% makes them an attractive alternative to conventional Si-based photovoltaics [328]. However, in the last years, the focus in the field of DSC has been redirected to 1-D TiO_2 nanostructures (e.g. NTs and

nanowires). Since they provide a more efficient charge transport, the NTs geometry ensures a faster electron transfer towards to the counter-electrode, minimizing the chance for charge trapping and e^--h^+ recombination [329,330].

Among the various synthesis methods, electrochemical anodization has been demonstrated to be an easy and low-cost approach to fabricate NT arrays. In the anodization process, there are three basic mechanisms responsible for the NT formation: (a) field-assisted oxidation and (b) field assisted-dissolution, both at the bottom of the tubes; and (c) chemical dissolution occurring mainly at the NTs top [209,213,331]. Differently from the nanoporous anodic oxide aluminium case [212,311,314], where the oxidation-dissolution rate is equally balanced, Ti anodization shows a non-steady-state stage where the oxidation rate is larger than the dissolution [213,332]. Since the NTs properties are closely related to the geometric surface areas, it is important to control NTs parameters such as length, pore size and wall thickness. Such tailoring can be easily achieved with this fabrication method by simply changing the anodizing parameters [316,333].

A common feature in Ti anodization is that the outer walls of the tubes show considerable thickness variations ribs, also known as bamboo morphology [333-335]. The growth of ribs around the nanotubes has been related with periodical pH burst at the pore bottom (in fluoride-based electrolytes) [210], or explained by the dehydration process of the hydroxide layer (double layer wall of NTs), or by the fluoride-rich layer in the outer wall of the NTs [306,335]. More recently, it was referred as a consequence of the chemical dissolution of the surface layer (at the NTs tops) [322,336]. This structure was also obtained using alternating voltage cycling instead of potentiostatic anodization, proving to be useful in the optimization of DSC structures [319,333,334,337].

The formation of gaps and ribs around the NTs has not been completely discussed so far, being recently investigated in detail [322,336]. These structures appear as consequence of the chemical dissolution of the surface layer (on top of the NTs), which allows the electrolyte entering among the NTs until it reaches the existing gaps at their base, forming the rib oxide at the electrolyte/Ti interface. The chemical dissolution at the surface top layer increases with higher amounts of NH_4F (for samples anodized at 60 V) [322].

The control of the NTs morphology is of crucial importance to adapt them to different applications. Usually all these Ti anodizations are performed in fresh electrolyte and the effect of electrolyte re-utilization in the TiO_2 NTs morphology is not completely understood. The re-use of the electrolyte (aging of electrolyte) was earlier reported to be critical in electrolytes with low water contents (≤1.0 wt%) [337-339]. It was referred that the increase in the water amounts (moisture absorption) during anodization process

would lead to an increase of NTs organization and growth rate. However, it is with fresh ethylene glycol electrolyte solutions with higher amounts of water (2 wt%) and 0.3 wt% NH_4F that the best NTs growth is achieved, since a faster growth rate is obtained [203]. Therefore, in order to make this nanostructured material a low coast choice, the question of electrolyte re-use can be key for their success in industrial applications.

In this work, we studied the effect of electrolyte (ethylene glycol with 2% water and 0.3 wt% NH_4F) re-utilization at different values of bias voltage (V_{anod}) on the anodization process and on the NTs morphology, particularly in the NT diameters and growth rate. A systematic comparative study is reported between the experimental measurements and the resulting anodization curves for each re-utilization. We also reported the possibility of achieving the ribs morphology just by re-using the electrolyte, with practical interest in DCS applications.

7.2. Experimental details

High purity Ti foils (99.99+%, 0.127 mm, Sigma-Aldrich) were used for the anodic growth of TiO_2 NTs. Prior to anodization, the Ti foils were ultrasonically cleaned sequentially with de-ionized water and ethanol, for 10 min each. Each anodization were performed using a home-made set-up, as reported on a previous work [126,213]. The electrolyte solution consisted in 98% ethylene glycol (EG), 2% DI water and 0.3 wt% NH_4F, at room temperature, with magnetic stirring. Different samples were prepared with bias voltages ranging from 20 to 60 V for fresh and re-used electrolytes. To be noticed that above the studied voltage range, we enter in the hard anodization (HA) regime [126,314], as in the case of Fe anodization presented in Chapter 5.

Particularly, three sets of experiments were carried out: for each potential we anodized a new Ti foil using (i) a fresh electrolyte (featuring first use electrolyte samples) (ii) the previously used electrolyte (second use electrolyte samples) and finally (iii) third use electrolyte samples. After each anodization, the samples were sequentially rinsed with ethanol. The morphology of the resulting TiO_2 NT templates was characterized by Scanning Electron Microscopy (SEM), as described in Chapter 2. The measurements of the TiO_2 NT template geometries, such as length or diameter, were performed using the *ImageJ* open source software [213].

7.3. Results and discussion

The behaviour of the NTs growth rate as a function of V_{anod} can be identified in the anodization curves. The 3 hour anodization curves for the set performed featuring different V_{anod} (ranging from 20 to 60 V) is represented in Figure 7.1(a). The curves show the typical anodization current transients for TiO_2 for all voltages [212,213]. After a steep decrease of the current density (j_{anod}), indicative of oxide formation and growth, such j_{anod}-decrease slows down due to the pore nucleation onset, reaching a minimum value of j_{anod} (j_{min}). Afterwards, a j_{anod} increase is seen associated with the continuous oxide dissolution (pore structure formation) until a local maximum (j_{max}) is reached. Finally, as the anodization proceeds, the NTs vertical growth is revealed by the progressive j_{anod}-decay during the remaining anodization time. This is due to the characteristic Ti non-steady state anodization that is characterized by a faster oxidation than dissolution at the NTs bottom [213].

It is clear from Figure 7.1(a) that the *j*-values increase with V_{anod}. The applied potential is directly correlated with the ionic flowing current, which is responsible for the field-enhanced oxidation and dissolution that affect the mechanisms involved in the first oxide formation, nucleation and pores growth. Thus, for lower V_{anod} the oxide formation and pore nucleation stages occur later, and consequently a longer time is needed to reach j_{min} and j_{max}. The increase of the electric field strength (higher V_{anod}) promotes a faster ionic diffusion that in turn lead to a faster oxide formation and nucleation period as visible in the j_{anod} (t) curves, with j_{min} and j_{max} being reached sooner as the potential increases. Within the studied range, 60 V is the most favorable regime for pore growth (j_{min} is reached sooner and nucleation is faster), while 20 V is the less favourable regime to self-organization, since it has a longer nucleation time. According to our previous work, the potentials tested above 60 V (70 and 80 V) resulted in more irregular anodization curves and NT shape morphologies, typical of HA conditions [126]. Figure 7.1(b) shows the mean current density (j_{mean}; average of *j*-values taken from j_{max} to the end of anodization) taken from the anodization curves as a function of V_{anod} for different electrolyte uses. The j_{mean} increases with V_{anod} due to the easier ionic diffusion and thus higher NT formation rate promoted by higher voltages. In addition, there is also an overall current decrease for re-used electrolyte [Figure 7.1(b)]. This is further confirmed in Figure 7.1(c) where we show the anodization curves for applied voltage of 60 V for 1st, 2nd and 3rd electrolyte use. Analyzing the $j(t)$ curves we can conclude that the electrolyte re-utilization leads to slower oxide formation, NT nucleation, j_{min} and j_{max}, and lower j_{mean}.

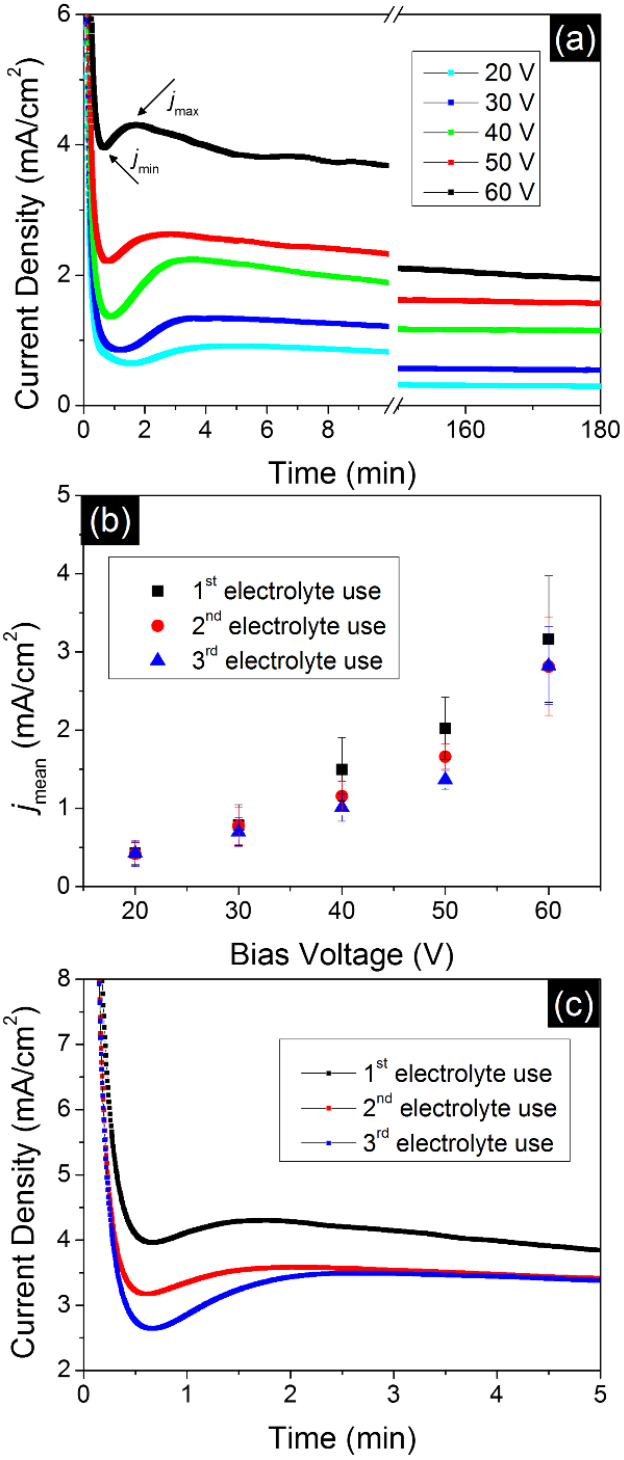

Figure. 7.1. (a) Anodization curves during the growth of TiO_2 NT arrays for different values of bias voltage. (b) Mean value of current density as a function of the applied voltage. (c) Anodization curves for 1st, 2nd and 3rd electrolyte use (for an applied voltage of 60 V).

The resulting NTs diameter and template thickness with variable V_{anod} are shown respectively in Figures 7.2(a) and (b), taken from the SEM images as illustrated in Figure 7.3. The outer tube diameter varies linearly from ~61 to 155 nm for bias voltages from 20 to 60 V [Figure 7.2(a)] with a slope of 2.5 $nm \cdot V^{-1}$. All electrolyte uses revealed similar outer tube diameters since they only depend on the applied voltage [209,316].

The resulting thickness of the NTs template (L) for each V_{anod} is shown in Figure 7.2(b) for 3 h anodization. It is noticed that L follows the same tendency of j_{mean}. A continuous increase of L with the applied voltage was observed due to the enhanced ionic transport. In Ti anodizations, the oxidation and dissolution processes occurring at the bottom of the NTs are given respectively by:

$$Ti + 2H_2O \rightarrow TiO_2 + 4H^+ + 4e^- \quad (7.1)$$

and

$$TiO_2 + 6F^- + 4H^+ \rightarrow TiF_6^{2-} + 2H_2O. \quad (7.2)$$

As the V_{anod} increases, both processes are enhanced due to an increased ionic flow at the NTs bottom. This fact, allied with the higher mobility of F^- anions through the electrolyte for higher bias voltages, leads to higher NT formation rates [203,316]. The presence of sufficient (but not excessive) F^- ions is very important to promote this mobility, enhancing the chemical dissolution of TiO_2 barrier layer (δ_b) which contributes to the growing of the NTs [340]. However, for 2nd and 3rd electrolyte use, an L decrease was observed for potentials above 40 V, with a higher dispersion of the L [Figure 7.2(b)]. We believe that this is a consequence of the electrolyte auto-acidification and also the decrease of the fluoride concentration. The electrolyte autocidification in re-used electrolyte increases the dissolution on top of the NTs, whereas the decrease of the fluoride concentration with successive anodizations, leads to a fluctuations in the NT arrays thickness [208,209].

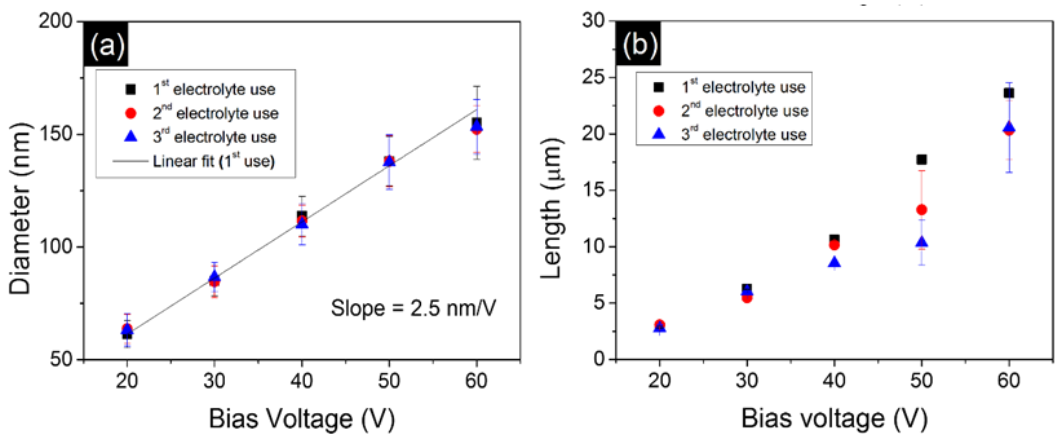

Figure. 7.2. (a) Diameter and (b) length of the TiO_2 NTs as a function of the applied voltage for fresh and re-used electrolytes (for 3 h of anodization).

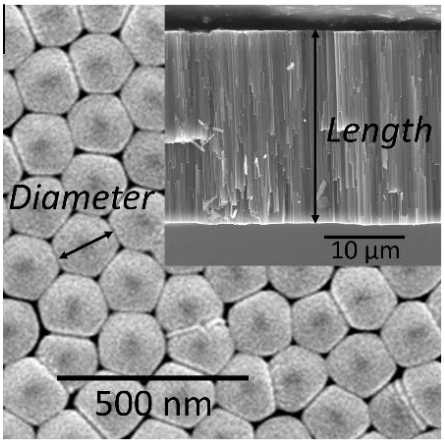

Figure. 7.3. SEM images of TiO_2 NTs bottom and cross-sectional view (inset), anodized for 3 hours at 60 V with fresh electrolyte (1st use), representing the measurements for diameter and length parameters.

Since the electrolyte re-utilization affects the anodization curves and the NTs *L* formation rate it may also affect the NTs morphology. In fact, we verified the formation of the bamboo type morphology (oxide ribs) for re-utilized electrolyte at the bias voltage of 60 V [306,335,341]. Here we show SEM images of the NTs for 1st, 2nd and 3rd electrolyte use [Figures 7.4(a), (b) and (c) respectively]. It is clear that for the 1st electrolyte use the walls are smooth. However, for the 2nd use some ribs on the surface of the NTs already appear, an effect that is much more pronounced for the 3rd utilization of the electrolyte. It was also observed that the ribs become more evident and thicker, and thus the average spacing between them goes from ~120 nm (2nd use) to ~100 nm

(3rd use). The formation of these structures can be explained by a mechanism that is related with the fluoride-rich layer in the outer wall of the NTs [335]. The electrolyte when in contact with e F-layer allows the dissolution between the NTs leading to the separation of interconnected pores into NTs. This gap between NTs accompanies the tubes growth allowing electrolyte and ionic diffusing between them. When the oxide residual layer at the bottom of the NTs gap is sufficiently thin, it allows the electromigration of O^{2-} near the Ti metal interface forming a thin oxide film (at the outer walls of the NTs), the so-called rib.

More recently, the ribs formation has been related with the NH_4F amount in the electrolyte. Lower NH_4F concentration the ribs cannot be formed, but higher 0.4 wt% NH_4F concentrations, the ribs are observed. These higher amounts of NH_4F enhances the electronic current with a strong O_2 release, affecting the NTs tops by chemical dissolution and allowing the electrolyte reaching the NTs gaps [322,336]. However, not only the amount of NH_4F is determinant for the ribs formation. Electrolytes with higher amounts of H_2O concentration (5-25%) showed NTs with increased number of ribs [335].

In this work, the formation of rib structures is related with the increase of H^+ concentrations (resulting from the oxidation process) that leads to local auto-acidification of the electrolyte (pH decreases) during anodization, due to its re-utilization. With a decreased pH, the dissolution rate in the gap between NTs increases and the formation of the rib arises.

The rib structures can also be obtained by anodization with acidic HF electrolytes [341] or by periodically varying the anodization potential [333]. However, achieving this morphology just by re-utilizing the electrolyte is a simple process while maintaining the high etch rate of the viscous organic electrolytes. The importance of this structures relies on the increase of the NTs surface area and thus the efficiencies of the DSCs [333] or PEC cells.

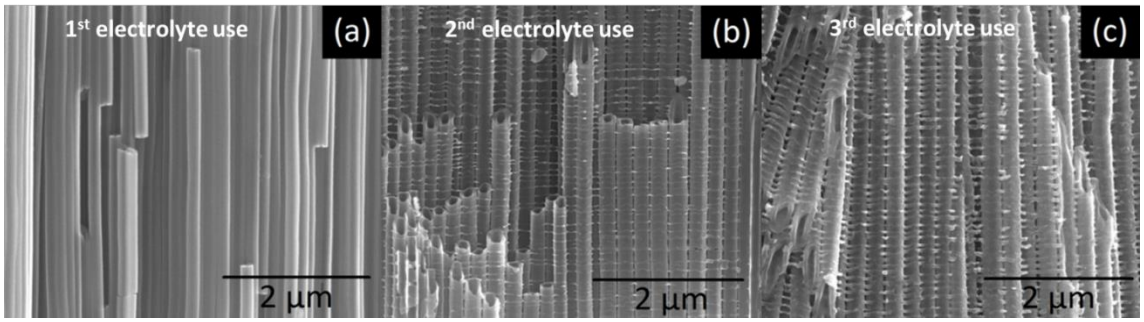

Figure. 7.4. Cross-sectional view of TiO_2 NTs obtained by potentiostatic anodization at 60 V and (a) first electrolyte use, (b) second electrolyte use and (c) third electrolyte use.

7.4. Conclusions

The usual linear relation between tube diameter and bias voltage was verified for the first electrolyte use, as well as for the re-utilization. The proximity of the results found for the three sets of experiments indicates that the dependence of the outer diameter relies only on the anodization voltage, not being significantly affected by the electrolyte re-utilization.

It was verified that the electrolyte re-utilization does not affect the growth rate for voltages from 20 to 40 V, but results in a decrease of the growth rate from 50 V, due to chemical dissolution effects on the NT tops, caused by the electrolyte acidification through successive anodizations. This acidification is also confirmed in the increase of the nucleation period (lower formation rate of the oxide) as the electrolyte is re-used, due to the F^- ions progressive failure and H^+ accumulation. This electrolyte re-utilization also leads to the formation of ribs in the nanotube walls, caused by local pH decrease due to successive re-utilizations. This type of morphology is important to increase the exposed surface area of the NTs arrays, with high practical interest in applications such as the DCSs or PEC devices.

Chapter 8

Work in Progress

Chapter 8

Work in progress

In this chapter we developed new promising photoanodes based on Fe thin films, deposited by physical vapor deposition methods, such as electron beam evaporation and ion beam deposition. These films were then used anodized to obtain iron oxide nanotubes.

Also, we started the synthesis of hematite thin films by Pulsed Laser Deposition, achieving a promising photocurrent performance of 0.34 mA.cm^{-2} at 1.45 V_{RHE}.

8.1. Thin films deposition by e-beam evaporation and ion beam deposition

A first experimental set was performed in order to optimize the synthesis of iron oxide NTs, obtained from electrochemical anodization of iron (Fe) thin films.

First, Fe thin films with thickness of ~ 500 nm were deposited onto the cleaned substrates (FTO) using electron-beam (e-beam) evaporation deposition technique. Basically, the e-beam technique consists on the evaporation of an anode target material (in this case Fe) which is bombarded with an electron beam originated by a charged tungsten filament. First a current pass through the tungsten filament leading to joule heating and consequent electron emission (thermionic emission [217]). Then a high voltage is applied to accelerate the electrons towards the Fe target. The energy of this electron beam is transferred to the Fe target, leading to it evaporation and deposition onto the substrate.

We verified that the as-deposited Fe thin films produced by this method presented several holes, i.e. areas without Fe deposited and where the FTO is exposed, observed by optical microscopy and SEM [Figure 8.1(a)-(c)]. This fact is probably related with the high rate depositions conferred by e-beam evaporation and the poor adhesion of Fe to the substrate.

New Fe depositions were prepared. Previously to the Fe deposition, a thin layer of titanium was deposited, with thickness of 20 nm, in order to promote the adhesion of Fe to the substrate. Then, the Fe was deposited with a thickness of ~ 500 nm.

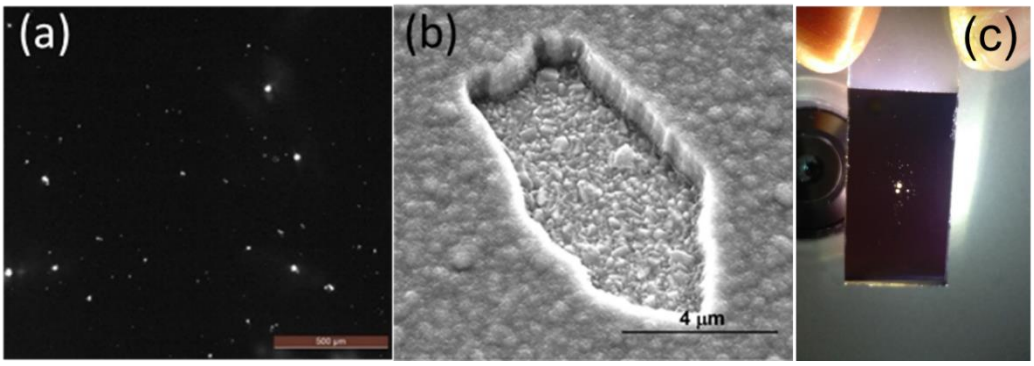

Figure 8.1. (a) Optical microscope image and (b) SEM image of as-deposited Fe thin film, revealing several holes and an inhomogeneous deposition. (c) FTO with Fe thin film deposited, showing against-light the holes in the film.

An anodization test was performed using a homemade device consisting in two-electrode anodization cell, with a platinum mesh used as the cathode and the Fe thin film (deposited on FTO) in contact with a copper cap used as the anode [90,342]. The electrolyte used was an ethylene glycol solution, containing NH_4F (0.5 wt%) and H_2O (2 wt%). The anodization occurred at room temperature (in order to obtain a low anodization rate, since the film only had 500 nm), with magnetic stirring, for 14 min at 20 V [Figure 8.2(a)]. In Figure 8.2(b) it is presented the SEM image of the sample after anodization, were we can observe several cracks, however a porous structure was formed inside the islands between the cracks [Fig. 8.2(c)]. During the anodization process, the poor adhesion of the film to the substrate (despite the Ti layer) originated the detachment of the film from the FTO substrates.

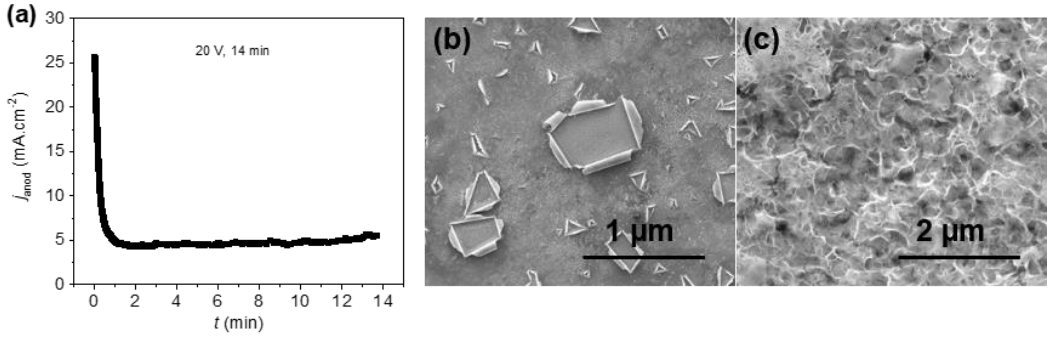

Figure 8.2. (a) Anodization curves of the Fe thin film anodized at 20 V for 14 min; SEM images of (b) the resulting anodized film, with signs of film detachment, and (c) irregular anodized areas without nanopores.

Other deposition techniques, such as ion beam deposition (IBD) were tested in order improve the Fe adhesion to the substrates. IBD allows to obtain high-quality and homogeneous thin film deposition, due the controlled low deposition rates of 0.54 $Å.s^{-1}$ [343]. In this case, the Ti deposition was not necessary, since a good Fe adhesion was obtained with IBD. Thin films, with thickness ~150 nm (confirmed with profilometer), were obtained. In the new deposited films, it was not detected the presence of holes, indicating a good quality of deposition (Figure 8.3). After the IBD deposition, a new layer ~500 nm thickness was deposited on the top of the Fe films by e-beam deposition, which resulted in Fe films with a total Fe thickness of ~650 nm.

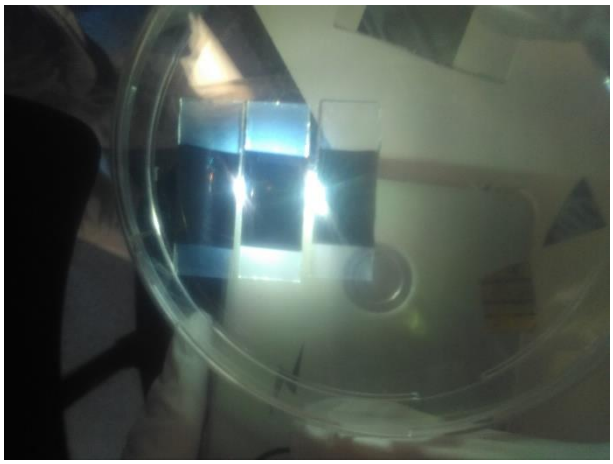

Figure 8.3. FTO with Fe thin film deposited by ion beam deposition, showing against-light a homogeneous deposition.

Then, several anodizations of the new thin films were performed. The electrolyte used was an ethylene glycol solution, containing NH_4F (0.5 wt%) and H_2O (2 wt%). The anodization tests occurred at a fixed potential of 50 V (in order to obtain ordered NTs, with pore diameters ~50 nm, as shown in Chapter 5, section 5.2.3,), with 3 different temperatures: room temperature, 35 ºC and 45 ºC. In these tests, we decided to immerse the Fe films deposited on FTO in the electrolyte solution, in order to create a higher anodized area for future PEC tests [figure 8.5(a)].

In Figure 8.4, we can observe the resulting anodization curves. The high anodization rate of Fe allied with the thinner Fe films lead to fast anodization times of 2 min and less. It is also noticed that the use of higher temperature also resulted in shorter anodization time, due to the increased oxidation-dissolution rates promoted by higher temperatures [90]. Additionally, the anodization curves become more irregular with the increase of temperature.

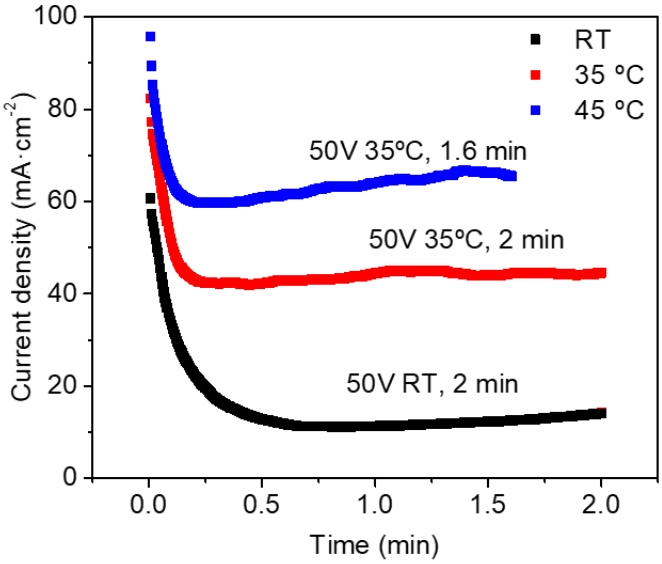

Figure 8.4. Anodization curves (current density evolution with time) of Fe films with different temperatures.

Figure 8.5(a) shows a resulting anodized Fe thin film sample; due to the high anodization rate, almost all of the Fe film was anodized, leaving the FTO exposed. However, by the SEM image in Figure 8.5(b), it is possible to observe the formation of NTs. This image corresponds to the sample anodized at 35 ºC. The anodization at room temperature (RT) resulted in a film layer without the formation of pores [Figure 8.6(a)], while the 45 ºC presented significant signs of dissolution [Figure 8.6(b)], without the formation of NTs, which could indicate higher dissolution rate promoted by higher temperature, differently from the anodization of Fe foil (Chapter 5).

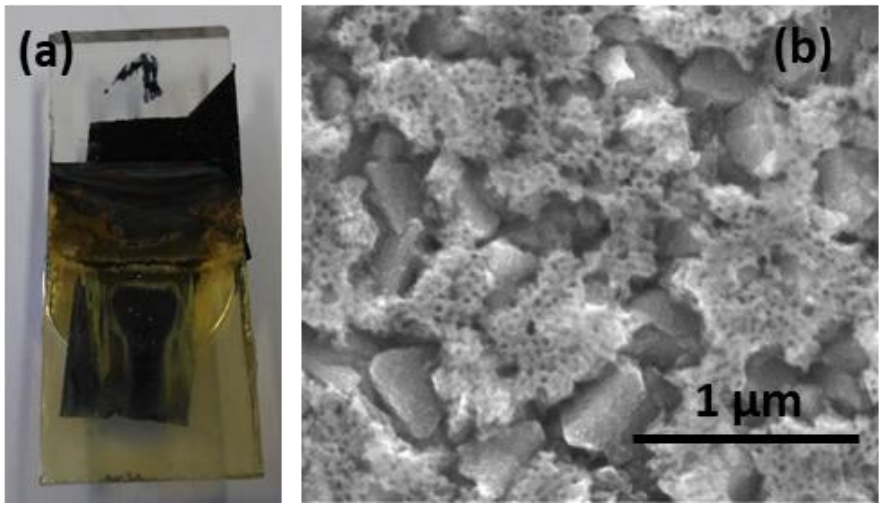

Figure 8.5. (a) Fe films after anodization at 35 ºC. (b) SEM images of Fe_2O_3 NTs.

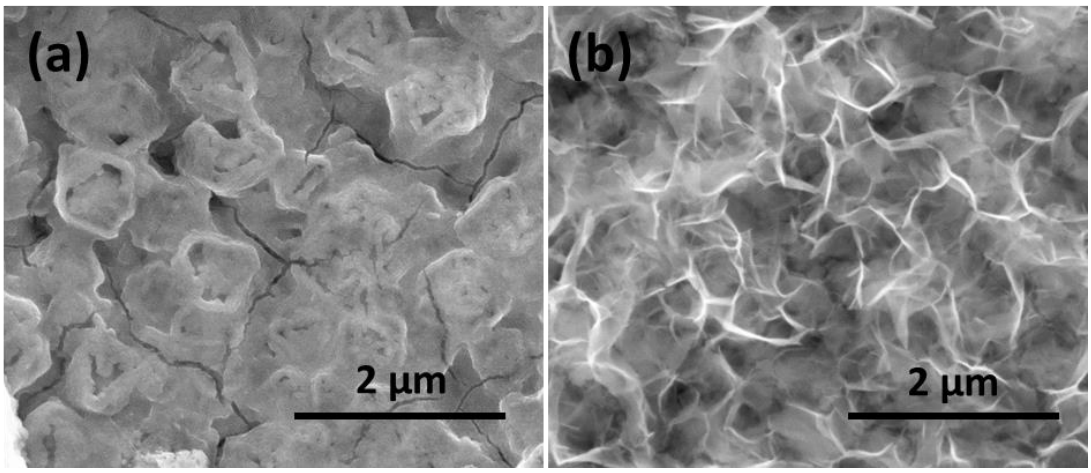

Figure 8.6. SEM images of Fe_2O_3 NTs anodized at (a) RT and (b) 45 ºC.

Future tests are necessary to optimize the anodization conditions, in order to obtain a more homogeneous area, without FTO exposed, that would lead to corrosion of the photoelectrodes [16,136,293]. After this optimization, the annealing conditions to form the hematite pure phase will be tested.

8.2. Pulsed laser deposition

Within a collaboration between IFIMUP and the Physics Department of Minho University, another approach to the deposition of Fe thin films through Pulsed Laser Deposition (PLD) technique started to be developed.

Depositions were performed on previously clean FTO substrates and with the deposition conditions described in Chapter 2, using Fe as target material for deposition. Two different laser energies were tested. Figure 8.7(a) and (b) show respectively the top and cross-sectional view of samples deposited with lower energy (250 mJ). A thin film thickness of 118 ± 25 nm was obtained. With higher energy (400 mJ), the morphology of the deposited samples did not significantly change, although a less roughness seems to be obtained with higher energy, Figure 8.7(c). Future tests using Atomic Force Microscopy should be performed to evaluate the topography of resulting films. Also, the PLD deposition method allows to obtain films with a resulting topography very close to the one of FTO substrate, Figure 8.7(b) and (d).

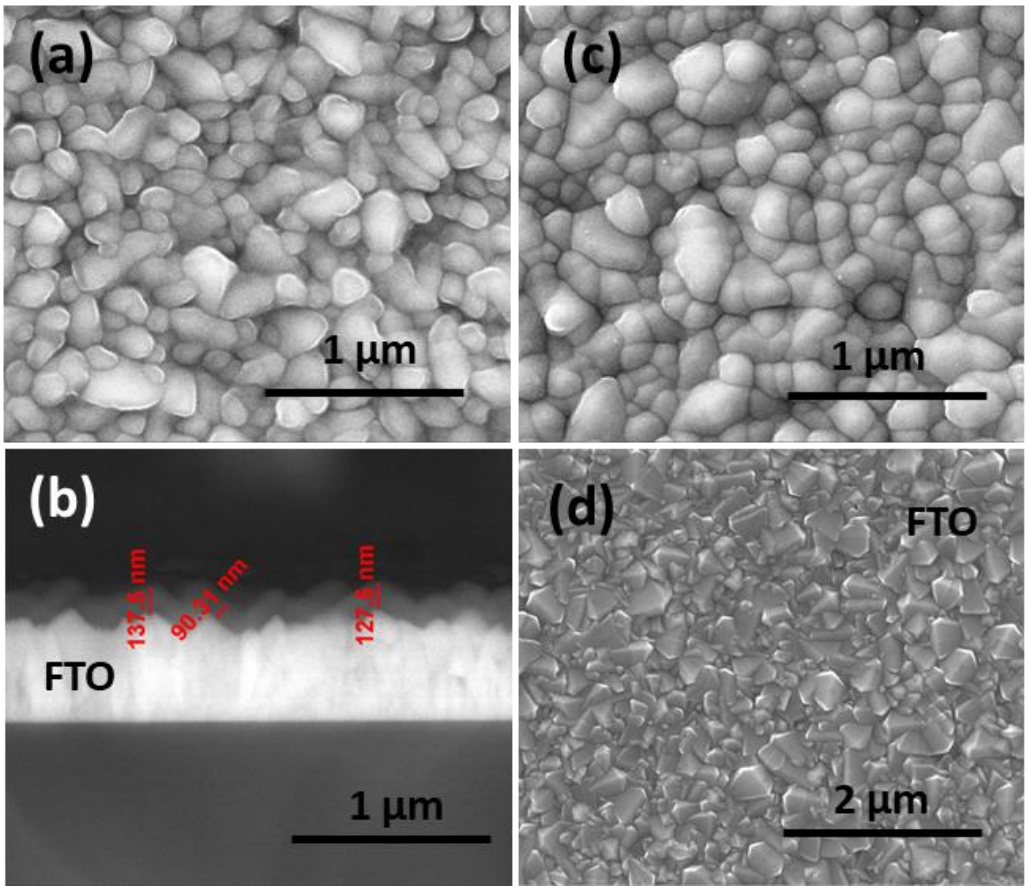

Figure 8.7. SEM images of thin films deposited by PLD deposition: (a) with energy of 250 mJ, top-view and (b) cross-sectional view; (c) with energy of 400 mJ, top-view. (d) Top view of FTO substrate.

Upon annealing at 550 ºC for 2 hours, followed by 800 ºC for 20 min (the optimum annealing conditions achieved with hematite NWs, Chapter 3, and ascribed to the Sn diffusion from FTO [276]), it can be seen that the deposition was not right homogeneous in the all 2 x 1 cm^2 deposition area, being more concentrated at the center of FTO (Figure 8.8). Further depositions are necessary in order to control the homogeneity of deposition conditions.

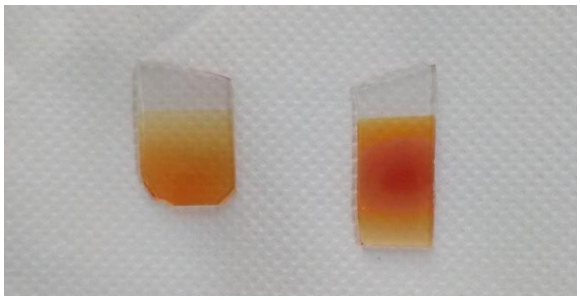

Figure 8.8. Fe thin films deposited by PLD after annealing at 550 ºC for 2 h, followed by 800 ºC for 20 min.

The photocurrent density was measured under dark and simulated sunlight, for both samples deposited with lower and higher laser energy, Figure 8.9. A promising value of 0.34 mA·cm^{-2} (at 1.45 V_{RHE}) was obtained with the sample deposited with high energy. This value is comparable with the one reported in literature with intentional Sn dopant [60].

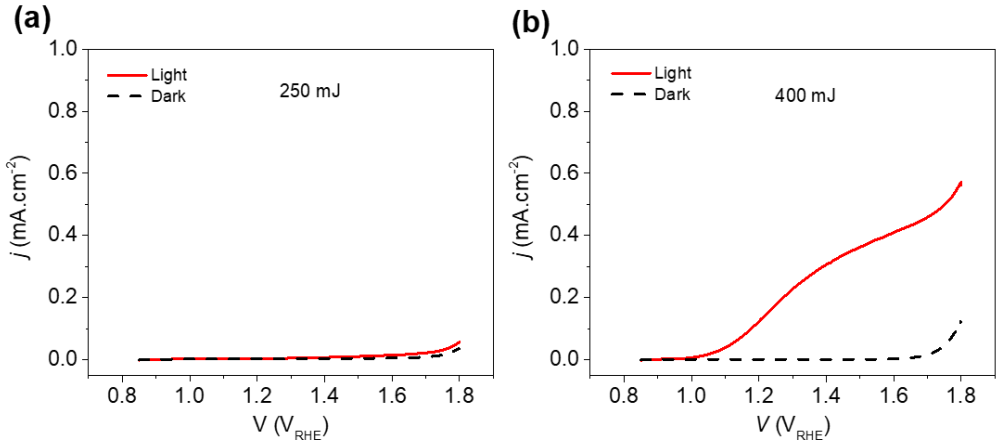

Figure 8.9. Current density-voltage curves of PLD film, measured in the dark and under 1 sun-simulated light.

8.3. Conclusions and future perspectives

To obtain thin films for anodization directly on FTO, we started using only the e-beam deposition, due to higher deposition rates that could be attained. However, inhomogeneous deposition lead to appearance of several holes in the films, i.e., areas without deposited film, with FTO exposed. Then, ion beam deposition (IBD), with controlled growth rates and uniform deposition was used. Prior to e-beam deposition, a thin layer ~150 nm was deposited by IBD onto FTO surface, resulting in good quality films without holes. Then, these films (with thicknesses ~500 nm) were used to form iron oxide NTs by anodization. The higher anodization rate and the low thickness of films lead to fast anodization of ~2 min or less. NTs formed on FTO were observed by SEM, however the fast anodization lead to several areas with exposed FTO.

In another study, the deposition of Fe films by pulsed laser deposition (PLD) originated promising results. Thin films with ~118 nm were obtained after ~1 hour deposition, with photocurrent density values in the order of 0.34 mA·cm^{-2} (at 1.45 VRHE). Taking into account these promising results, we aim to continue this work in the future, by optimizing the deposition and annealing conditions, and the intentional and controlled incorporation of dopants, such as Sn or Ti.

Chapter 9

Main Conclusions and Perspectives

Chapter 9

Main Conclusions and Perspectives

In this chapter, the main conclusions and achievements accomplished during this thesis are here addressed. In a first part, the main results obtained are presented. In a second part, an outlook of the ongoing work and future perspectives is described.

9.1. Main Conclusions

A systematic work of synthesis and optimization of several nanostructures for PEC cells applications was here established, followed by a complete physical-chemical and photoelectrochemical characterization. For that, it was fundamental the strong collaboration between both supervision research groups, IFIMUP and LEPABE.

The IFIMUP´s know-how in the preparation and characterization of advanced nanostructures, particularly alumina and titania nanoporous templates and nanotubes (obtained by electrochemical anodization and electrodeposition techniques), allied to LEPABE´s strong experience in DSC and PEC cells development and characterization, was crucial to achieve the objectives of this PhD.

Using two simple and low-cost fabrication methods, such as electrochemical anodization and hydrothermal synthesis, it was possible to develop several semiconductor materials, with distinct properties, that makes them suitable for PEC applications.

An intensive work was carried out on the development of different nanostructures by hydrothermal method, in which parameters such as chemical composition and concentration of the solution, temperature or solution pH were optimized to tune the photoanodes morphology. In this respect, nanostructures such as hematite nanowires (NWs) and nanotubes (NTs), and WO_3 nanoplates were successfully obtained. This work also helped to pave the way for the future development and optimization of these kind of materials, that can be also extensible to other photoelectrode materials.

Hematite is considered one of the most promising photoelectrodes for solar water splitting. Here, we explored the physical-chemical insights of hematite NWs produced by hydrothermal method. The impact of annealing temperature and time was thoroughly investigated, considering parameters such as heating ramp, one *vs.* two step annealing, temperature and time. The photocurrent density (*j,* at 1.45 V_{RHE}) increased with the increase of both temperature and time. The best solar-to-current conversions were observed for hematite photoelectrodes annealed with a two-step approach at 550 °C for 2 h followed by 20 min at 800 °C (~0.9 $mA \cdot cm^{-2}$), and under one-step approach at 600 °C during 48 h (~0.7 $mA \cdot cm^{-2}$). The optimized annealing time (600 ºC for 48 h) opens the possibility of using low cost substrates in the photoanodes fabrication. The intrinsic solar to chemical conversion efficiency was determined (ISTC). A maximum ISTC was obtained for the 800 ºC, with maximum efficiency of 0.25% (at J_{photo} of 0.71 mAcm-2 and U_{light} of 1.3 V_{RHE}). For 48 h, an ISTC of 0.18% (at J_{photo} of 0.52 mAcm-2 and U_{light} of 1.2 V_{RHE}) was obtained. X-ray diffraction (XRD) measurements, optimized to remove the FTO contribution (usually the more intense in literature), enabled a quantitative analysis: revealing the influence of the preferential crystallographic orientation in the photocurrent efficiency; two-step annealing scheme (800 ºC) resulted in the improvement of structural crystalline order, determined by Williamson-Hall analysis. The hematite NWs showed a preferential crystal orientation along (110) plane for both annealing schemes (temperature and time) that confers improved conductivity ultimately leading to improved *j*. However, the more intense (104) reflection peak in photoelectrodes group of annealing time could indicate limited conductivity that results in lower photocurrents. XANES studies confirmed the presence of pure hematite crystallographic phase, while EXAFS indicated the increase of bond ordering for both 800 ºC and 48 h photoelectrodes and confirmed the Sn doping diffused from FTO substrate layer within the hematite crystalline lattice, corroborating the RBS analysis. In RBS analysis, the shape of the Sn and Fe signals (between 1260 keV and 1520 keV) suggested a roughness-diffusion mechanism; it was showed that the in-depth Sn % profile for 800 ºC sample was ca. 10 times higher when compared with the sample annealed at 550 °C (with the lowest *j*). Combining the NWs thickness with optical UV-vis absorption data, it was estimated the porosity (*P*), based on the model described by Marusak. The results show an inverse porosity and *j* relation: *P* decreases from ~43 to 11% as the annealing temperature increases (550-800 ºC), and from ~40 to 25% as the annealing time increases (3-48 h). Usually in the literature, higher porosity indicates higher photoactive surface areas of the photoelectrodes. Here, *j* performance of the hematite NWs photoelectrodes is the balance three factor: morphology, crystallinity and conductivity due to Sn “unintentional” doping.

Besides annealing temperature, *j* performance was also significantly enhanced through Ti doping. Ti-doped hematite NWs were produced by hydrothermal method using small amounts of a titanium precursor reagent. It was investigated not only the effect of Ti-doping but also the influence of annealing temperature (at 600 ºC) and one step *vs.* two step annealing (550 ºC + 800 ºC). For both annealing schemes, hematite NWs with and without Ti-dopant were compared. Ti-hematite NWs presented a more compacted morphology, lower nanowire diameter and higher NWs thickness. The XRD analysis was assessed using two different configurations: Bragg-Brentano (BB) and grazing incidence angle XRD (GAXRD). While with BB, the main peaks are from the FTO, using GAXRD allows a more complete analysis and to refine the structural information in order to extract the crystallite size of the photoanodes. Ti-doped NWs showed also a preferential crystal orientation along (110) plane, but also more intense (104) reflection peaks (here, it does not seem to influence the conductivity, since higher *j* were obtained). Also, a lower crystallite size was obtained for Ti-doped samples compared with non-doped; it was ascribed to the low ordering conferred by Ti doping. However, a slight increase in the crystallite size for Ti-doped sample annealed at 800 ºC (comparing with Ti-doped at 600 ºC) is observed, as higher temperature was referred to improve the quality and crystalline order of hematite nanostructures (Chapter 3). The band gap decreased in the order: 800 ºC<Ti-800 ºC< Ti-600 ºC<600 ºC, promoted by the influence of Sn diffused from the FTO and Ti-intentional doping. The highest *j* values (~1.27 $mA \cdot cm^{-2}$ at 1.45 V_{RHE}) were obtained with Ti doping and two-step annealing, a significant increase comparatively with *j* ~0.85 $mA \cdot cm^{-2}$ for correspondent photoelectrodes without dopant (at 800 ºC). This *j* improvement is mainly attributed with both the influence of Sn (diffused from the FTO) and Ti dopant. Also, the Ti-doped photoanode revealed to be very stable under 2 h of continuous *j* measurements (at 1.23 V_{RHE}).

During this PhD, within a collaboration with IST-CTN, it was possible to use Sn ion implantation technique in hematite NWs prepared by hydrothermal method (and annealing at 550 ºC for 2 h). While lower fluence (10^{15} $ions.cm^{-2}$) did not seems to affect the morphology of NWs, implantation with higher fluence (10^{17} $ions.cm^{-2}$) significantly affected the morphology: the diameter of NWs increased from ~40 nm (without implantation) to ~135 nm, and a NWs thickness decrease from 330 nm to ~200 nm, also a gap between NWs was observed; the morphology was maintained after the annealing at 550 ºC. XRD analysis showed that crystalline properties were affected by Sn implantation, mainly with higher fluence. Although the typical peaks indexed to hematite crystalline structure with preferential orientation in (110) plane were obtained, broader peaks were observed after ion implantation. An increase in hematite absorption for

higher wavelengths (~600 nm) was observed, due to the presence of Sn. Also, a higher absorption at peak ~535 nm (attributed to the presence of Sn/morphological changes was observed for sample implanted with higher ionic fluence. The band gap decreased, in general, with Sn implantation followed by annealing. The *j* improved up to 0.16 $mAcm^{-2}$ (1.45 V_{RHE}) comparing with the very low *j* at 500 ºC (0.01 $mAcm^{-2}$ at 1.45 V_{RHE}). Further work is still required to test a second annealing with best conditions.

Hydrothermal method was also used to produce hematite NTs, however they did not grow on FTO, as in the case of hematite NWs. Instead, nanostructures with needle/spiral or spherical morphologies were grown. Comparatively with hematite NWs obtained at 550 ºC (*j* = 0.01 $mA \cdot cm^{-2}$), both nanoneedles and nanospheres yielded an improved and similar *j* ~0.1 $mA \cdot cm^{-2}$, with the same annealing conditions. Contrarily to the NWs, here the nanoneedles grow with a preferential crystallographic (104) orientation. Also, some small peaks indexed to the presence of Fe complexes with phosphate ions from hydrothermal solution were detected. Additionally, the NTs formed in solution were coated on FTO by doctor-blading, in order to perform *j-V* measurements. However, a poor adhesion to substrate lead to detachment and low *j* values. Nevertheless, these nanostructures constitute a promising work to be further considered and developed, testing other polymers.

Iron oxide NTs were also prepared by electrochemical anodization. Comparing with other typical anodization of Al or Ti, the high growth rates in Fe anodization allowed a fast growth of NTs in which long nanotubes with ~4.6 µm can grow in just 5 minutes. The usual linear relation between pore diameter, interpore distance, wall thickness and nanotubes length was verified with potentials from 20 up to 60 V. Besides, an improved of the NTs organization was seen in this potential range. Potentials above 60 V, ascribed to the regime of hard-anodization that affects the morphology, lead to the dissolution of NTs tops and to irregular shaped NTs. The optimum anodization regime for a faster and organized growth of NTs was found for bias voltage of 20 V, in which a porosity regime ~30% closer to the optimized self-organized nanoporous of 10% stated in literature. The crystallinity was assessed by GAXRD measurements: while as-anodized NTs are amorphous, after annealing (550ºC, 2h) the hematite crystalline phase was obtained. Although higher intensity of both (110) and (104) planes was verified for all samples, for 20 V sample a slight higher intensity of the (110) plane is observed, assigned to the improved conductivity of hematite. However, a minor magnetite (Fe_3O_4) phase contribution is still present. After the annealing the morphology of the nanotubes was maintained, however several cracks are observed, due to the Fe foil oxidation and expansion during annealing forming a spongy-like morphology. A photocurrent of ~0.5

mA cm^{-2} (1.45 V_{RHE}) was obtained for the 20 V sample, significantly higher than NWs produced by hydrothermal method with the same annealing conditions.

WO_3 nanoplates were prepared by hydrothermal method. Ideal conditions were obtained with temperature of 90 ºC during 12 h. Contrarily to reported in literature, were thicker height plates originated best results, here thinner height plates originated higher *j*. Low height plates constitute improved surface photoactive areas, benefitting the charge transport. Then, WO_3 photoelectrodes were produced using several layers of nanoplates obtained by sequential steps of hydrothermal (12 h at 90 ºC) and annealing processes. Higher thickness was reported to enhance the photoelectrodes efficiency. The number of layers were tested up to a limitation of *j* performance was achieved. A *j* improvement, from 0.56 to 0.96 mA·cm^{-2} (at 1.45 V_{RHE}) respectively for 1 to 5 layers, was achieved, a 6^{th} layer result in slight *j* decrease. Using the same hydrothermal conditions (90 ºC), a continuous hydrothermal using the time correspondent to 5 layers (60 h) was tested. However, growth rate limitation was observed, i.e., increasing the hydrothermal time did not increase the nanoplates thickness. Comparatively with reported values for bare WO_3 (~0.6 mA·cm^{-2} at 1.8 V_{RHE}), here we obtained higher solar-to-current conversions.

TiO_2 photoanodes have been widely investigated for dye-sensitized solar cells (DSC) and PEC devices, due to their photoelectronic properties. Taking previous works developed at IFIMUP on TiO_2 NTs as a reference, here we studied the parameter of electrolyte re-utilization and its effect on anodization curves [current density (*j*) *vs*. time (t)], and morphology of the nanotubes (diameters and growth-rate). Anodization were performed with 1^{st} (fresh electrolyte), 2^{nd} and 3^{rd} electrolyte utilization, and variable potential from 20-60 V. Current density values increase with the applied potential (*V*): *V* is directly correlated with the ionic flowing current, responsible for the field-enhanced oxidation and dissolution that affect the mechanisms involved in nanotubes formation and growth. A slight decrease of the anodization current density *j*(*t*) mean value was observed from 1^{st} to 3^{rd} electrolyte re-use, since electrolyte re-utilization leads to slower oxide formation and NTs nucleation. NTs diameter increases linearly with *V*, and all electrolyte uses revealed similar diameters, since it only depends on *V*. The resulting thickness of the NTs template (*L*) increase with *V* for all electrolyte uses; while a *L* linear increase with *V* for 1^{st} use is visible, for potentials above 40 V, a decrease in *L* for 2^{nd} and 3^{rd} electrolyte use in relation to 1^{st} use is observed, with a higher dispersion of the *L* values. This is a consequence of the electrolyte auto-acidification that increases the dissolution of the top of NTs. The decrease of the fluoride concentration with successive anodization leads to fluctuations in *L* values. The presence of ribs morphology was obtained with successive electrolyte re-use. The formation of rib structures is related with the increase of H^+ concentration with successive anodization using the same electrolyte

solution, that leads to local auto-acidification, promoting the dissolution of the fluoride-rich layer between NTs (in the outer wall of the NTs). These structures were reported by its practical interest in DCS and PEC applications.

Finally, we present a final chapter with the work in progress, where promising new photoanodes have been developed: thin films of iron deposited directly on the FTO using electron beam (e-beam) and ion beam deposition (IBD) techniques. First, we only used the e-beam deposition, due to higher deposition rates that could be attained. However, inhomogeneous deposition lead to appearance of several holes in the films, i.e., areas without deposited film, with FTO exposed. Then, a technique such IBD, with controlled growth rates and uniform deposition was used (prior to e-beam deposition, a thin layer ~150 nm was deposited by IBD onto FTO surface), resulting in good quality films without holes. Then, these films (with thicknesses ~500 nm) were used to form iron oxide NTs by anodization. The higher anodization rate and the low thickness of films lead to fast anodization of ~2 min or less. NTs formed on FTO were observed by SEM, however the fast anodization lead to several areas with exposed FTO. In another study, the deposition of Fe films by pulsed laser deposition (PLD) originated promising results. Thin films ~122 nm were obtained after ~1 hour deposition, with *j* values in the order of 0.34 $mA \cdot cm^{-2}$ (at 1.45 V_{RHE}). We aim to continue this work in the future, by optimizing the deposition and annealing conditions, and the incorporation of dopants, such as Sn or Ti.

9.2. Perspectives

From the promising results obtained throughout PhD work, it can now be proposed some of the most interesting future works that can be developed following this thesis.

- First, the use of Ti doping is being optimized, testing new approaches/reagents in order to optimize the hydrothermal growth of Ti-hematite NWs. Also, it will be essential in the future the determination of the Ti and Sn (diffused from FTO with higher annealing temperature) amount and their role on the improvement of the photoelectrodes conductivity; tests using X-ray photoelectron spectroscopy (XPS) and electrochemical impedance spectroscopy will be performed.
- The use of a co-catalyst coating in hematite photoelectrodes is also a future work. With the strong experience of LEAPBE´s group with this kind of process,

a co-catalyst incorporation may increase the photo-performance and improve the onset of these photoelectrodes.

- Incorporate metal plasmonic materials (Au or Ag) into the developed nanostructures, in order to increase the PEC´s efficiency, by promoting an effective light-harvesting and photo-excited charges separation, inducing favourable changes in the electromagnetic energy distribution.
- Within the well-established collaboration between IFIMUP and IST-CTN, several works involving the ion implantation and use of RBS are being planned. The Sn implantation of hematite NWs, using an intermediary ion fluence could be interesting to increase the Sn incorporation without affecting the morphology of the NWs, maintaining the high surface photoactive area of bare NWs. Also, the use of RBS technique to assess the evolution of hematite NWs produced with different thicknesses, comparing with other technique such as SEM, is also work under consideration.
- Improve the adhesion of hematite NTs (obtained by hydrothermal method) to the FTO substrate, testing new conditions, such as polymer concentration or solvent drying temperature, using spin-coating to promote a homogeneous covering. Other formulations using other polymers, could also allow a more effective adhesion to FTO.
- In relation of WO_3 nanoplates, the future incorporation of dopants and/or the use of heterojunctions with other semiconductor materials, such as α-Fe_2O_3 layers can highly improve the efficiency, by extending the absorption of visible light, enhance the separation of photogenerated charge carriers, or decrease the band gap.
- The fabrication of thin films by ion beam deposition, consisting on thin layers of iron, titanium or tungsten deposited directly on FTO substrate. The optimization of layers thickness, the incorporation of dopants (Sn) and studies of annealing conditions are factors to consider.
- After the optimization of thin films deposition, Laser Interference Lithography (LIL) technique, together with electrochemical anodization methods, can be used to attain highly ordered arrays of Fe_2O_3, TiO_2 or WO_3 NTs. LIL confers very regular hexagonal patterns of holes with well-defined interpore distances in which the nucleation occurs.
- The annealing conditions (temperature and time), as optimized in Chapter 3 (hematite nanowires), is an important parameter to consider in most of future

works. Annealing atmosphere (N_2, O_2 or Ar) parameter could be additionally considered.

- Include magnetic studies; determine the magnetic properties of iron oxide nanotubes obtained by hydrothermal method and by electrochemical anodization, and its impact in the photoelectrodes photoresponse.

Publications related to the PhD work

The developed work during this thesis resulted in scientific contributions directly related to the thesis, that includes publications, oral communications and poster presentations, in national and international conferences and workshops.

Also, during the development of this thesis, significant results were achieved during the 2 stays with accepted proposals for beamtime at an international synchrotron infrastructure, the Brazilian Synchrotron Light Laboratory (LNLS).

This thesis is based on the following works.

Publications (published, submitted and in preparation):

- Paula Quitério, José D.Costa, Arlete Apolinário, Célia T.Sousa, João Azevedo, João Ventura, Luísa Andrade, Adélio Mendes, João P. Araújo, The effect of electrolyte re-utilization in the growth rate and morphology of TiO_2 nanotubes. Materials Letters 171 (2016) 224–227, doi:10.1016/j.matlet.2016.02.085.
- Paula Quitério, Arlete Apolinário, Sérgio Magalhães, Eduardo Alves, Adélio Mendes, Célia Sousa and João P. Araújo. Photoelectrochemical Water Splitting: Thermal Annealing Challenges on Hematite Nanowires. Accepted for publication in The Journal of Physical Chemistry C. https://doi.org/10.1021/acs.jpcc.0c01259
- P. Quitério, A. Apolinário, A. Mendes, C. T. Sousa, and J. P. Araújo. Potential-dependent growth of self-ordered iron oxide nanotubes (in preparation to Materials, Special Issue "Nanostructured Anodic Oxides: Fabrication, Characterization and Application")
- P. Quitério, A. Apolinário, P. Dias, J. Azevedo, C. T. Sousa, A. Mendes and J. P. Araújo, Hematite nanowires photoelectrodes for photoelectrochemical hydrogen production: the effect of Ti dopant and annealing temperature, in preparation.
- P. Quitério, Sérgio Magalhães, A. Apolinário, E. Alves, A. Mendes, C. T. Sousa, and J. P. Araújo. Improvement of hematite nanowires photoactivity through Sn implantation, in preparation.
- P. Quitério, Sérgio Magalhães, A. Apolinário, E. Alves, A. Mendes, C. T. Sousa, and J. P. Araújo. Assessing hematite nanowires development by Rutherford Backscattering Spectrometry, in preparation.
- P. Quitério, A. Apolinário, A. Mendes, C. T. Sousa, and J. P. Araújo. Hydrothermal growth of WO_3 nanoplate multilayers, in preparation.

- P. Quitério, A. Apolinário, J. Azevedo, A. Mendes, C. T. Sousa and J. P. Araújo. A review on nanotubes for Photoelectrochemical Water Splitting, in preparation.
- P. Quitério, A. Apolinário, A. Mendes, C. T. Sousa and J. P. Araújo. Hematite nanotubes by hydrothermal growth, in preparation.

Oral communications:

- P. Quitério, A. Apolinário, S. Moraes, D. Navas, P. Dias, J. Azevedo, A. M. Mendes, C. T. Sousa and J. P. Araújo, X-ray Absorption Fine Structure (XAFS) Studies of Hematite Nanowires for PEC Cells, 8th Meeting of Portuguese Synchrotron Radiation Users - ENURS 2019, June 28, 2019, IFIMUP, FCUP, Porto.
- P. Quitério, A. Apolinário, P. Dias, J. Azevedo, A. M. Mendes, C. T. Sousa and J. P. Araújo, Hematite nanowires for PEC hydrogen production: the effect of Ti dopant and temperature, CMPNC 2019 - Condensed Matter Physics National Conference 2019, 8-10 May, 2019, Faculdade de Ciências, Universidade do Porto.
- Paula Quitério, Arlete Apolinário, Célia Sousa, Adélio Mendes and João Pedro Araújo, Fast anodic hematite nanotubes for photoelectrochemical cells, 13th International Workshop on Electrodeposited Nanostructures – EdnanoXIII, 30 August – 1 September 2018 in Bristol, UK.
- Paula Quiterio, Arlete Apolinario, Celia T. Sousa, Joao Azevedo, Paula Dias, Adelio Mendes, Joao P. Araujo. Synthesis and Characterization of High-Aspect-Ratio Hematite Nanostructures for Solar Water Splitting. ICHEFCT 2017: 19th International Conference on Hydrogen Energy and Fuel Cells Technology, Amsterdam, The Netherlands, December 04-05, 2017.

Poster communications:

- P. Quitério, A. Apolinário, C. T. Sousa, P. Dias, J. Azevedo, A. M. Mendes and J. P. Araújo, 1D Hematite photoanodes for photoelectrochemical hydrogen production, DCE19 – 3rd Doctoral Congress in Engineering, 27 – 28 June 2019, FEUP, Porto – Portugal.
- P. Quitério, A. Apolinário, C. T. Sousa, P. Dias, J. Azevedo, A. M. Mendes and J. P. Araújo, 1D Hematite photoanodes for photoelectrochemical water splitting, JEFFA19 - 4as Jornadas em Engenharia Física Física, Física Médica e Astronomia 2019, 16 May 2019, Departamento de Física e Astronomia (DFA) - Faculdade de Ciências da Universidade do Porto (FCUP), Porto, Portugal.

- P. Quitério, A. Apolinário, C. T. Sousa, P. Dias, J. Azevedo, A. M. Mendes and J. P. Araújo, Hematite photoanodes with high aspect-ratio for photoelectrochemical hydrogen production. ANEM2018, 12-14 December, The University of Western Australia, Crawley Campus, Perth, Australia.
- Paula Quitério, Arlete Apolinário, Bolaji Balogun, Miguel Luz, João Azevedo, Paula Dias, Célia Sousa, Adélio Mendes, João P. Araújo, Hematite nanostructures for photoelectrochemical hydrogen production, JEFFA – Jornadas de Engenharia Física, Física e Astronomia, 18 May 2018, Anfiteatro Prof. João Bessa Sousa (-120), DFA – Faculdade de Ciências da Universidade do Porto, Portugal. (http://www.je2fe.org/programa-2018).
- Paula Quitério, Bolaji Balogun, Miguel Luz, Arlete Apolinário, João Azevedo, Célia Sousa, Adélio Mendes, João P. Araújo, High aspect-ratio hematite nanostructures for photoelectrochemical water splitting, DCE 2017 - 2nd Doctoral Congress in Engineering, 8th - 9th June 2017 at FEUP, Porto, Portugal.
- Paula Quitério, Bolaji Balogun, Miguel Luz, Arlete Apolinário, João Azevedo, Célia Sousa, Adélio Mendes, João P. Araújo, High aspect-ratio hematite nanostructures for photoelectrochemical cells, JEFFA – Jornadas de Engenharia Física, Física e Astronomia, 24th Mars 2017, Anfiteatro Prof. João Bessa Sousa (-120), DFA – Faculdade de Ciências da Universidade do Porto, Portugal. (http://www.je2fe.org/copy_of_proceedings).
- P. Quitério, A. Apolinário, C. T. Sousa, J. D. Costa, J. Ventura, J. P. Araújo, Study of the TiO_2 nanotubes growth with the anodization charge curves, IN – Institute of Nanoscience and Nanotechnology Workshop, 7 July of 2016, Instituto Superior Técnico, Lisboa (https://sites.google.com/site/ingroupworkshop/2016-edition/program).

Nevertheless, several collaborations also took place, resulting in the following publications (published and submitted to publication), and oral communications:

- Guerreiro; Arlete Apolinario; Armandina Lopes; Aurelio Hierro-Rodriguez; Gerardo Aguilar; Jose Manuel Baptista; Nuno A. Silva; Orlando Frazão; Paula Virginia Quiterio; Pedro Jorge; Pedro Rodrigues; Suellen Silveira Moraes; Susana Silva; Tiago D. Ferreira; Jose Luis Santos; João Pedro Araujo, Functional metamaterials for optical sensing of hydrogen, Proceedings Volume 11207, Fourth International Conference on Applications of Optics and Photonics; 1120724 (2019), https://doi.org/10.1117/12.2527672
- Mourad Boutahir, Sidi Abdelmajid Ait Abdelkader, Bashiru B Balogun, J. Araújo, Joaquim Agostinho Moreira, Peter Eaton, Paula Quitério, Célia T. Sousa, Joana

C.R.E Oliveira, Abdelhai Rahmani, Hassane Chadli and Abdelali Rahmani, “Structure and Raman spetctroscopy analysis of graphene with vacancy defects: A combined experimental and theoretical study" (submitted to publication).

- Bashiru B. Balogun, Celia T. Sousa, Paula Quitério, Gleb N. Kakazei, João P. Araújo, Mondiu O. Durowoju, Sabastine C. Ezugwu and Paul U. Asogwa, Influence of annealing conditions on the pseudocapacitive performance of porous polyaniline thin films (submitted to publication).
- Arlete Apolinário, Célia T. Sousa, João Ventura, P. Quitério, P. Dias, João Azevedo, Luísa Andrade, Adélio M. Mendes and João P. Araújo, New trends on nanostructures for third generation solar cells, 4ª Jornadas em Engenharia Física, Física, Física Médica e Astronomia 2019, DFA, FCUP. Porto, Portugal.
- Célia Tavares de Sousa, M. Proença, A. Apolinário, J. Azevedo, P. Quitério, S. Moraes, J. Ventura, J.P. Araújo, Nanofabrication of advanced materials using self-organized templates, ISPDS-2, 2nd International Symposium on Physics Data Storage, October 31 to November 01-02, 2017, Meknes, Morocco.
- C.T. Sousa, A. Apolinário, P. Quitério, J. Azevedo, M. Proença, J. Ventura, D. Navas, J.P. Araújo, Bottom-up nanofabrication using self-organized porous templates, IN – Institute of Nanoscience and Nanotechnology Workshop, 7 July of 2016, Instituto Superior Técnico, Lisboa (https://sites.google.com/site/ingroupworkshop/2016-edition/program).

Bibliography

[1] P. Quiterio, A. Apolinario, C.T. Sousa, J.D. Costa, J. Ventura, J.P. Araujo, The cyclic nature of porosity in anodic TiO_2 nanotube arrays, J. Mater. Chem. A 3(7) (2015) 3692-3698. DOI: 10.1039/C4TA04607B.

[2] S. Shafiee, E. Topal, When will fossil fuel reserves be diminished?, Energy Policy 37(1) (2009) 181-189. DOI: https://doi.org/10.1016/j.enpol.2008.08.016.

[3] M. Höök, X. Tang, Depletion of fossil fuels and anthropogenic climate change—A review, Energy Policy 52 (2013) 797-809. DOI: https://doi.org/10.1016/j.enpol.2012.10.046.

[4] M.G. Walter, E.L. Warren, J.R. McKone, S.W. Boettcher, Q. Mi, E.A. Santori, N.S. Lewis, Solar Water Splitting Cells, Chemical Reviews 110(11) (2010) 6446-6473. DOI: 10.1021/cr1002326.

[5] M. Gratzel, Photoelectrochemical cells, Nature 414 (2001) 338-344. DOI: 10.1038/35104607.

[6] C.A. Grimes, O.K. Varghese, S. Ranjan, Light, Water, Hydrogen: The Solar Generation of Hydrogen by Water Photoelectrolysis, Springer US, Boston, MA, 2008.

[7] T. Lopes, P. Dias, L. Andrade, A. Mendes, An innovative photoelectrochemical lab device for solar water splitting, Sol. Energy Mater. Sol. Cells 128 (2014) 399-410. DOI: http://dx.doi.org/10.1016/j.solmat.2014.05.051.

[8] A.G. Tamirat, J. Rick, A.A. Dubale, W.-N. Su, B.-J. Hwang, Using hematite for photoelectrochemical water splitting: a review of current progress and challenges, Nanoscale Horiz. 1(4) (2016) 243-267. DOI: 10.1039/C5NH00098J.

[9] IRENA (2018), Renewable Power Generation Costs in 2017, International Renewable Energy Agency, Abu Dhabi.

[10] N.S. Lewis, Light work with water, Nature 414(6864) (2001) 589-590.

[11] M.K. Debe, Electrocatalyst approaches and challenges for automotive fuel cells, Nature 486(7401) (2012) 43-51. DOI: 10.1038/nature11115.

[12] Toyota FCV, Available at: https://www.toyota.pt/world-of-toyota/articles-news-events/2014/Toyota-disponibiliza-patentes-a-pilha-de-combustivel.json (Accessed March 12, 2020).

[13] Os carros elétricos com maior autonomia em 2020. Available at: https://www.portal-energia.com/veiculos-eletricos-10-carros-maior-autonomia-mercado-atual/ (Accessed May 28, 2020).

[14] Governo quer "fábrica gigante" de hidrogénio em Portugal, Available at: https://www.tsf.pt/portugal/economia/governo-quer-fabrica-gigante-de-hidrogenio-em-portugal-11528752.html (Accessed in January 03, 2020).

[15] European Union, 2012. Available at: https://ec.europa.eu/jrc/en/pvgis (Accessed August 12, 2018).

[16] R.v.d. Krol, M. Grätzel, Photoelectrochemical Hydrogen Production, Springer US2012.

[17] L. Tania, A. Luisa, M. Adelio, Photoelectrochemical cells for hydrogen production from solar energy, Solar Energy Sciences and Engineering Applications, CRC Press2013, pp. 293-341.

[18] A. Fujishima, K. Honda, Electrochemical Photolysis of Water at a Semiconductor Electrode, Nature 238(5358) (1972) 37-38.

[19] D.W.B. Alexander I. Kokorin, Chemical physics of nanostructured semiconductors, VSP2003.

[20] A. Duret, M. Grätzel, Visible Light-Induced Water Oxidation on Mesoscopic α-Fe_2O_3 Films Made by Ultrasonic Spray Pyrolysis, J. Phys. Chem. B 109(36) (2005) 17184-17191. DOI: 10.1021/jp044127c.

[21] R. van de Krol, Y. Liang, J. Schoonman, Solar hydrogen production with nanostructured metal oxides, J. Mater. Chem. 18(20) (2008) 2311-2320. DOI: 10.1039/B718969A.

[22] C.G. Morales-Guio, S.D. Tilley, H. Vrubel, M. Gratzel, X. Hu, Hydrogen evolution from a copper(I) oxide photocathode coated with an amorphous molybdenum sulphide catalyst, Nat Commun 5 (2014). DOI: 10.1038/ncomms4059.

[23] J. Luo, S.D. Tilley, L. Steier, M. Schreier, M.T. Mayer, H.J. Fan, M. Grätzel, Solution Transformation of Cu_2O into $CuInS_2$ for Solar Water Splitting, Nano Lett. 15(2) (2015) 1395-1402. DOI: 10.1021/nl504746b.

[24] S.D. Tilley, M. Schreier, J. Azevedo, M. Stefik, M. Graetzel, Ruthenium Oxide Hydrogen Evolution Catalysis on Composite Cuprous Oxide Water-Splitting Photocathodes, Adv. Funct. Mater. 24(3) (2014) 303-311. DOI: 10.1002/adfm.201301106.

[25] J. Azevedo, L. Steier, P. Dias, M. Stefik, C.T. Sousa, J.P. Araujo, A. Mendes, M. Graetzel, S.D. Tilley, On the stability enhancement of cuprous oxide water splitting photocathodes by low temperature steam annealing, Energy Environ. Sci. 7(12) (2014) 4044-4052. DOI: 10.1039/C4EE02160F.

[26] H. Luo, A.H. Mueller, T.M. McCleskey, A.K. Burrell, E. Bauer, Q.X. Jia, Structural and Photoelectrochemical Properties of BiVO4 Thin Films, J. Phys. Chem. C 112(15) (2008) 6099-6102. DOI: 10.1021/jp7113187.

[27] L.J. Minggu, W.R. Wan Daud, M.B. Kassim, An overview of photocells and photoreactors for photoelectrochemical water splitting, Int. J. Hydrogen Energy 35(11) (2010) 5233-5244. DOI: http://dx.doi.org/10.1016/j.ijhydene.2010.02.133.

[28] M. Grätzel, NanoPEC, http://www.fch-ju.eu/sites/default/files/FCH%20Programme%20review%202011-%20Project%20NanoPEC.pdf.

[29] O. Khaselev, J.A. Turner, A Monolithic Photovoltaic-Photoelectrochemical Device for Hydrogen Production via Water Splitting, Science 280(5362) (1998) 425-427. DOI: 10.1126/science.280.5362.425.

[30] G. Wang, Y. Ling, H. Wang, L. Xihong, Y. Li, Chemically modified nanostructures for photoelectrochemical water splitting, Journal of Photochemistry and Photobiology C: Photochemistry Reviews 19 (2014) 35-51. DOI: https://doi.org/10.1016/j.jphotochemrev.2013.10.006.

[31] T. Bak, J. Nowotny, M. Rekas, C.C. Sorrell, Photo-electrochemical hydrogen generation from water using solar energy. Materials-related aspects, Int. J. Hydrogen Energy 27(10) (2002) 991-1022. DOI: https://doi.org/10.1016/S0360-3199(02)00022-8.

[32] J. Deng, J. Zhong, A. Pu, D. Zhang, M. Li, X. Sun, S.-T. Lee, Ti-doped hematite nanostructures for solar water splitting with high efficiency, J. Appl. Phys. 112(8) (2012) 084312. DOI: 10.1063/1.4759278.

[33] Y. Ling, G. Wang, D.A. Wheeler, J.Z. Zhang, Y. Li, Sn-Doped Hematite Nanostructures for Photoelectrochemical Water Splitting, Nano Lett. 11(5) (2011) 2119-2125. DOI: 10.1021/nl200708y.

[34] A. Vilanova, P. Dias, J. Azevedo, M. Wullenkord, C. Spenke, T. Lopes, A. Mendes, Solar water splitting under natural concentrated sunlight using a 200 cm2 photoelectrochemical-photovoltaic device, J. Power Sources 454 (2020) 227890. DOI: https://doi.org/10.1016/j.jpowsour.2020.227890.

[35] K.R. Tolod, S. Hernández, N. Russo, Recent Advances in the BiVO4 Photocatalyst for Sun-Driven Water Oxidation: Top-Performing Photoanodes and Scale-Up Challenges, Catalysts 7(1) (2017) 13.

[36] J.R. McKone, N.S. Lewis, H.B. Gray, Will Solar-Driven Water-Splitting Devices See the Light of Day?, Chem. Mater. 26(1) (2014) 407-414. DOI: 10.1021/cm4021518.

[37] A. Apolinário, T. Lopes, C. Costa, J.P. Araújo, A.M. Mendes, Multilayered WO_3 Nanoplatelets for Efficient Photoelectrochemical Water Splitting: The Role of the Annealing Ramp, ACS Appl. Energy Mater. 2(2) (2019) 1040-1050. DOI: 10.1021/acsaem.8b01530.

[38] Y. Qiu, Z. Pan, H. Chen, D. Ye, G. Lin, Z. Fan, S. Yang, Current progress in developing metal oxide nanoarrays-based photoanodes for photoelectrochemical water splitting, Science Bulletin (2019). DOI: https://doi.org/10.1016/j.scib.2019.07.017.

[39] K. Sivula, F. Le Formal, M. Grätzel, Solar Water Splitting: Progress Using Hematite (α-Fe_2O_3) Photoelectrodes, ChemSusChem 4(4) (2011) 432-449. DOI: 10.1002/cssc.201000416.

[40] X. Liu, F. Wang, Q. Wang, Nanostructure-based WO_3 photoanodes for photoelectrochemical water splitting, Phys. Chem. Chem. Phys. 14(22) (2012) 7894-7911. DOI: 10.1039/C2CP40976C.

[41] A.B. Murphy, P.R.F. Barnes, L.K. Randeniya, I.C. Plumb, I.E. Grey, M.D. Horne, J.A. Glasscock, Efficiency of solar water splitting using semiconductor electrodes, Int. J. Hydrogen Energy 31(14) (2006) 1999-2017. DOI: http://dx.doi.org/10.1016/j.ijhydene.2006.01.014.

[42] R.M. Cornell, U. Schwertmann, The Iron Oxides: Structure, Properties, Reactions, Occurrences, And Uses, Wiley-VCH Verlag GmbH & Co. KGaA2004, pp. 9-38.

[43] P. Dias, A. Vilanova, T. Lopes, L. Andrade, A. Mendes, Extremely stable bare hematite photoanode for solar water splitting, Nano Energy 23 (2016) 70-79. DOI: http://dx.doi.org/10.1016/j.nanoen.2016.03.008.

[44] J. Xie, P. Yang, X. Liang, J. Xiong, Self-Improvement of Ti:Fe_2O_3 Photoanodes: Photoelectrocatalysis Improvement after Long-Term Stability Testing in Alkaline Electrolyte, ACS Appl. Energy Mater. 1(6) (2018) 2769-2775. DOI: 10.1021/acsaem.8b00445.

[45] F.J. Morin, Electrical Properties of αFe_2O_3 and αFe_2O_3 Containing Titanium, Phys. Rev. 83(5) (1951) 1005-1010. DOI: 10.1103/PhysRev.83.1005.

[46] F.J. Morin, Electrical Properties of α-Fe_2O_3, Phys. Rev. 93(6) (1954) 1195-1199.

[47] J.H. Kennedy, K.W. Frese, Photooxidation of Water at α - Fe_2O_3 Electrodes, J. Electrochem. Soc. 125(5) (1978) 709-714. DOI: 10.1149/1.2131532.

[48] R.F.G. Gardner, F. Sweett, D.W. Tanner, The electrical properties of alpha ferric oxideII.: Ferric oxide of high purity, J. Phys. Chem. Solids 24(10) (1963) 1183-1196. DOI: https://doi.org/10.1016/0022-3697(63)90235-X.

[49] S. Kment, P. Schmuki, Z. Hubicka, L. Machala, R. Kirchgeorg, N. Liu, L. Wang, K. Lee, J. Olejnicek, M. Cada, I. Gregora, R. Zboril, Photoanodes with Fully Controllable Texture: The Enhanced Water Splitting Efficiency of Thin Hematite Films Exhibiting Solely (110) Crystal Orientation, ACS Nano 9(7) (2015) 7113-7123. DOI: 10.1021/acsnano.5b01740.

[50] M. Barroso, S.R. Pendlebury, A.J. Cowan, J.R. Durrant, Charge carrier trapping, recombination and transfer in hematite (α--Fe_2O_3) water splitting photoanodes, Chemical Science 4(7) (2013) 2724-2734. DOI: 10.1039/C3SC50496D.

[51] M. Cornuz, M. Grätzel, K. Sivula, Preferential Orientation in Hematite Films for Solar Hydrogen Production via Water Splitting, Chem. Vap. Deposition 16(10-12) (2010) 291-295. DOI: 10.1002/cvde.201004292.

[52] J. Yan, F. Zhou, TiO_2 nanotubes: Structure optimization for solar cells, J. Mater. Chem. 21(26) (2011) 9406-9418. DOI: 10.1039/C1JM10274E.

[53] I. Cesar, A. Kay, J.A. Gonzalez Martinez, M. Grätzel, Translucent Thin Film Fe_2O_3 Photoanodes for Efficient Water Splitting by Sunlight: Nanostructure-Directing Effect of Si-Doping, Appl. Phys. Lett. 128(14) (2006) 4582-4583. DOI: 10.1021/ja060292p.

[54] I. Cesar, K. Sivula, A. Kay, R. Zboril, M. Grätzel, Influence of Feature Size, Film Thickness, and Silicon Doping on the Performance of Nanostructured Hematite Photoanodes for Solar Water Splitting, J. Phys. Chem. C 113(2) (2009) 772-782. DOI: 10.1021/jp809060p.

[55] P. Dias, T. Lopes, L. Andrade, A. Mendes, Temperature effect on water splitting using a Si-doped hematite photoanode, J. Power Sources 272 (2014) 567-580. DOI: http://dx.doi.org/10.1016/j.jpowsour.2014.08.108.

[56] A. Annamalai, H.H. Lee, S.H. Choi, S.Y. Lee, E. Gracia-Espino, A. Subramanian, J. Park, K.-j. Kong, J.S. Jang, Sn/Be Sequentially co-doped Hematite Photoanodes for Enhanced Photoelectrochemical Water Oxidation: Effect of Be2+ as co-dopant, Sci. Rep. 6 (2016) 23183. DOI: 10.1038/srep23183.

[57] T.-Y. Yang, H.-Y. Kang, K. Jin, S. Park, J.-H. Lee, U. Sim, H.-Y. Jeong, Y.-C. Joo, K.T. Nam, An iron oxide photoanode with hierarchical nanostructure for efficient water oxidation, J. Mater. Chem. A 2(7) (2014) 2297-2305. DOI: 10.1039/C3TA13830E.

[58] J. Liu, C. Liang, H. Zhang, Z. Tian, S. Zhang, General Strategy for Doping Impurities (Ge, Si, Mn, Sn, Ti) in Hematite Nanocrystals, J. Phys. Chem. C 116(8) (2012) 4986-4992. DOI: 10.1021/jp2105874.

[59] C.X. Kronawitter, I. Zegkinoglou, S.H. Shen, P. Liao, I.S. Cho, O. Zandi, Y.S. Liu, K. Lashgari, G. Westin, J.H. Guo, F.J. Himpsel, E.A. Carter, X.L. Zheng, T.W. Hamann, B.E. Koel, S.S. Mao, L. Vayssieres, Titanium incorporation into hematite photoelectrodes: theoretical considerations and experimental observations, Energy Environ. Sci. 7(10) (2014) 3100-3121. DOI: 10.1039/C4EE01066C.

[60] K.D. Malviya, H. Dotan, D. Shlenkevich, A. Tsyganok, H. Mor, A. Rothschild, Systematic comparison of different dopants in thin film hematite (α-Fe_2O_3) photoanodes for solar water splitting, J. Mater. Chem. A 4(8) (2016) 3091-3099. DOI: 10.1039/C5TA07095C.

[61] Gurudayal, S.Y. Chiam, M.H. Kumar, P.S. Bassi, H.L. Seng, J. Barber, L.H. Wong, Improving the Efficiency of Hematite Nanorods for Photoelectrochemical Water Splitting by Doping with Manganese, ACS Appl. Mater. Interfaces 6(8) (2014) 5852-5859. DOI: 10.1021/am500643y.

[62] Y. Liu, Y.-X. Yu, W.-D. Zhang, Photoelectrochemical properties of Ni-doped Fe_2O_3 thin films prepared by electrodeposition, Electrochim. Acta 59 (2012) 121-127. DOI: https://doi.org/10.1016/j.electacta.2011.10.051.

[63] A. Annamalai, P.S. Shinde, T.H. Jeon, H.H. Lee, H.G. Kim, W. Choi, J.S. Jang, Fabrication of superior α-Fe_2O_3 nanorod photoanodes through ex-situ Sn-doping for solar water splitting, Sol. Energy Mater. Sol. Cells 144 (2016) 247-255. DOI: https://doi.org/10.1016/j.solmat.2015.09.016.

[64] M. Rachel, R. Mahfujur, M.J.M. Don, W.C. A., Activation of Hematite Nanorod Arrays for Photoelectrochemical Water Splitting, ChemSusChem 4(4) (2011) 474-479. DOI: doi:10.1002/cssc.201100066.

[65] K. Sivula, R. Zboril, F. Le Formal, R. Robert, A. Weidenkaff, J. Tucek, J. Frydrych, M. Gratzel, Photoelectrochemical water splitting with mesoporous hematite prepared by a solution-based colloidal approach, J. Am. Chem. Soc. 132(21) (2010) 7436-44. DOI: 10.1021/ja101564f.

[66] O. Zandi, T.W. Hamann, Enhanced Water Splitting Efficiency Through Selective Surface State Removal, J. Phys. Chem. Lett. 5(9) (2014) 1522-1526. DOI: 10.1021/jz500535a.

[67] P. Quitério, A. Apolinário, D. Navas, S. Magalhães, E. Alves, A. Mendes, C.T. Sousa, J.P. Araújo, Photoelectrochemical Water Splitting: Thermal Annealing Challenges on Hematite Nanowires, J. Phys. Chem. C 124(24) (2020) 12897-12911. DOI: 10.1021/acs.jpcc.0c01259.

[68] S.C. Warren, E. Thimsen, Plasmonic solar water splitting, Energy Environ. Sci. 5(1) (2012) 5133-5146. DOI: 10.1039/C1EE02875H.

[69] A. Apolinario, Nanostructured Photoanodes for Solar Cells, PhD Thesis, University of Porto (2015).

[70] J. Li, S.K. Cushing, P. Zheng, F. Meng, D. Chu, N. Wu, Plasmon-induced photonic and energy-transfer enhancement of solar water splitting by a hematite nanorod array, Nat. Commun. 4(1) (2013) 2651. DOI: 10.1038/ncomms3651.

[71] E. Fabbri, A. Habereder, K. Waltar, R. Kötz, T.J. Schmidt, Developments and perspectives of oxide-based catalysts for the oxygen evolution reaction, Catalysis Science & Technology 4(11) (2014) 3800-3821. DOI: 10.1039/C4CY00669K.

[72] P. Dias, Innovative Photoelectrodes for Solar Water Splitting, PhD Thesis, University of Porto (2016).

[73] W. Li, X. Liu, H. Li, Hydrothermal synthesis of graphene/Fe^{3+}-doped TiO_2 nanowire composites with highly enhanced photocatalytic activity under visible light irradiation, J. Mater. Chem. A 3(29) (2015) 15214-15224. DOI: 10.1039/C5TA00763A.

[74] N. Iordanova, M. Dupuis, K.M. Rosso, Charge transport in metal oxides: A theoretical study of hematite α-Fe_2O_3, J. Chem. Phys. 122(14) (2005) 144305. DOI: 10.1063/1.1869492.

[75] T. Nakau, Electrical Conductivity of α-Fe_2O_3, J. Phys. Soc. Jpn. 15(4) (1960) 727-727. DOI: 10.1143/JPSJ.15.727.

[76] Ö. Özdemir, D.J. Dunlop, Hallmarks of maghemitization in low-temperature remanence cycling of partially oxidized magnetite nanoparticles, Journal of Geophysical Research: Solid Earth 115(B2) (2010) n/a-n/a. DOI: 10.1029/2009JB006756.

[77] Ö. Özdemir, D.J. Dunlop, T.S. Berquó, Morin transition in hematite: Size dependence and thermal hysteresis, Geochemistry, Geophysics, Geosystems 9(10) (2008). DOI: 10.1029/2008gc002110.

[78] A.I. Galuza, A.B. Beznosov, V.V. Eremenko, Optical absorption edge in α–Fe_2O_3: The exciton–magnon structure, Low Temperature Physics 24(10) (1998) 726-729. DOI: doi:http://dx.doi.org/10.1063/1.593675.

[79] P.S. Bassi, L. Xianglin, Y. Fang, J.S.C. Loo, J. Barber, L.H. Wong, Understanding charge transport in non-doped pristine and surface passivated hematite (Fe_2O_3) nanorods under front and backside illumination in the context of light induced water splitting, Phys. Chem. Chem. Phys. 18(44) (2016) 30370-30378. DOI: 10.1039/C6CP05379C.

[80] Y. Zhu, J. Xu, H. Jiang, D. Niu, X. Zhang, S. Hu, The effect of fluorine doping on the photocatalytic properties of hematite for water splitting, CrystEngComm 20(41) (2018) 6430-6437. DOI: 10.1039/C8CE01368C.

[81] M.P. Dare-Edwards, J.B. Goodenough, A. Hamnett, P.R. Trevellick, Electrochemistry and photoelectrochemistry of iron(III) oxide, Journal of the Chemical Society, Faraday Transactions 1: Physical Chemistry in Condensed Phases 79(9) (1983) 2027-2041. DOI: 10.1039/F19837902027.

[82] S.D. Tilley, M. Cornuz, K. Sivula, M. Grätzel, Light-Induced Water Splitting with Hematite: Improved Nanostructure and Iridium Oxide Catalysis, Angew. Chem. Int. Ed. 49(36) (2010) 6405-6408. DOI: 10.1002/anie.201003110.

[83] R.R. Rangaraju, A. Panday, K.S. Raja, M. Misra, Nanostructured anodic iron oxide film as photoanode for water oxidation, J. Phys. D: Appl. Phys. 42(13) (2009) 135303.

[84] A. Hagfeldt, U. Björkstén, M. Grätzel, Photocapacitance of Nanocrystalline Oxide Semiconductor Films: Band-Edge Movement in Mesoporous TiO_2 Electrodes during UV Illumination, The Journal of Physical Chemistry 100(20) (1996) 8045-8048. DOI: 10.1021/jp9518567.

[85] F. Le Formal, M. Grätzel, K. Sivula, Controlling Photoactivity in Ultrathin Hematite Films for Solar Water-Splitting, Adv. Funct. Mater. 20(7) (2010) 1099-1107. DOI: 10.1002/adfm.200902060.

[86] X. Shi, L. Cai, M. Ma, X. Zheng, J.H. Park, General Characterization Methods for Photoelectrochemical Cells for Solar Water Splitting, ChemSusChem 8(19) (2015) 3192-3203. DOI: 10.1002/cssc.201500075.

[87] Y. Qiu, S.-F. Leung, Q. Zhang, B. Hua, Q. Lin, Z. Wei, K.-H. Tsui, Y. Zhang, S. Yang, Z. Fan, Efficient Photoelectrochemical Water Splitting with Ultrathin films of Hematite on Three-Dimensional Nanophotonic Structures, Nano Lett. 14(4) (2014) 2123-2129. DOI: 10.1021/nl500359e.

[88] D.K. Zhong, M. Cornuz, K. Sivula, M. Grätzel, D.R. Gamelin, Photo-assisted electrodeposition of cobalt–phosphate (Co–Pi) catalyst on hematite photoanodes for solar water oxidation, Energy Environ. Sci. 4(5) (2011) 1759-1764. DOI: 10.1039/C1EE01034D.

[89] S.K. Mohapatra, S.E. John, S. Banerjee, M. Misra, Water Photooxidation by Smooth and Ultrathin α-Fe_2O_3 Nanotube Arrays, Chem. Mater. 21(14) (2009) 3048-3055. DOI: 10.1021/cm8030208.

[90] T.J. LaTempa, X. Feng, M. Paulose, C.A. Grimes, Temperature-Dependent Growth of Self-Assembled Hematite (α-Fe_2O_3) Nanotube Arrays: Rapid Electrochemical Synthesis and Photoelectrochemical Properties, J. Phys. Chem. C 113(36) (2009) 16293-16298. DOI: 10.1021/jp904560n.

[91] L. Vayssieres, N. Beermann, S.-E. Lindquist, A. Hagfeldt, Controlled Aqueous Chemical Growth of Oriented Three-Dimensional Crystalline Nanorod Arrays: Application to Iron(III) Oxides, Chemistry of Materials 13(2) (2001) 233-235. DOI: 10.1021/cm001202x.

[92] S.P. Schwaminger, R. Surya, S. Filser, A. Wimmer, F. Weigl, P. Fraga-García, S. Berensmeier, Formation of iron oxide nanoparticles for the photooxidation of water: Alteration of finite size effects from ferrihydrite to hematite, Sci. Rep. 7(1) (2017) 12609. DOI: 10.1038/s41598-017-12791-9.

[93] L. Fu, H. Yu, Y. Li, C. Zhang, X. Wang, Z. Shao, B. Yi, Ethylene glycol adjusted nanorod hematite film for active photoelectrochemical water splitting, Phys. Chem. Chem. Phys. 16(9) (2014) 4284-4290. DOI: 10.1039/C3CP54240H.

[94] C. Jorand Sartoretti, M. Ulmann, B.D. Alexander, J. Augustynski, A. Weidenkaff, Photoelectrochemical oxidation of water at transparent ferric oxide film electrodes, Chemical Physics Letters 376(1) (2003) 194-200. DOI: https://doi.org/10.1016/S0009-2614(03)00910-2.

[95] D.A. Wheeler, G. Wang, Y. Ling, Y. Li, J.Z. Zhang, Nanostructured hematite: synthesis, characterization, charge carrier dynamics, and photoelectrochemical properties, Energy Environ. Sci. 5(5) (2012) 6682-6702. DOI: 10.1039/C2EE00001F.

[96] J. Azevedo, M.P. Fernández-García, C. Magén, A. Mendes, J.P. Araújo, C.T. Sousa, Double-walled iron oxide nanotubes via selective chemical etching and Kirkendall process, Sci. Rep. 9(1) (2019) 11994. DOI: 10.1038/s41598-019-47704-5.

[97] A. Kay, I. Cesar, M. Grätzel, New Benchmark for Water Photooxidation by Nanostructured α-Fe_2O_3 Films, Appl. Phys. Lett. 128(49) (2006) 15714-15721. DOI: 10.1021/ja064380l.

[98] J.Y. Zheng, M.J. Kang, G. Song, S.I. Son, S.P. Suh, C.W. Kim, Y.S. Kang, Morphology evolution of dendritic Fe wire array by electrodeposition, and photoelectrochemical properties of α-Fe_2O_3 dendritic wire array, CrystEngComm 14(20) (2012) 6957-6961. DOI: 10.1039/C2CE26046H.

[99] S.C. Warren, K. Voïtchovsky, H. Dotan, C.M. Leroy, M. Cornuz, F. Stellacci, C. Hébert, A. Rothschild, M. Grätzel, Identifying champion nanostructures for solar water-splitting, Nat. Mater. 12(9) (2013) 842-849. DOI: 10.1038/nmat3684. http://www.nature.com/nmat/journal/v12/n9/abs/nmat3684.html#supplementary-information.

[100] J. Brillet, M. Cornuz, F.L. Formal, J.-H. Yum, M. Grätzel, K. Sivula, Examining architectures of photoanode–photovoltaic tandem cells for solar water splitting, J. Mater. Res. 25(01) (2010) 17-24. DOI: doi:10.1557/JMR.2010.0009.

[101] P. Liao, M.C. Toroker, E.A. Carter, Electron Transport in Pure and Doped Hematite, Nano Lett. 11(4) (2011) 1775-1781. DOI: 10.1021/nl200356n.

[102] T. Vincent, M. Gross, H. Dotan, A. Rothschild, Thermally oxidized iron oxide nanoarchitectures for hydrogen production by solar-induced water splitting, Int. J. Hydrogen Energy 37(9) (2012) 8102-8109. DOI: http://dx.doi.org/10.1016/j.ijhydene.2011.08.088.

[103] L. Li, Y. Yu, F. Meng, Y. Tan, R.J. Hamers, S. Jin, Facile Solution Synthesis of α-FeF3·3H2O Nanowires and Their Conversion to α-Fe_2O_3 Nanowires for Photoelectrochemical Application, Nano Lett. 12(2) (2012) 724-731. DOI: 10.1021/nl2036854.

[104] H. Sun, J. Deng, L. Qiu, X. Fang, H. Peng, Recent progress in solar cells based on one-dimensional nanomaterials, Energy Environ. Sci. 8(4) (2015) 1139-1159. DOI: 10.1039/C4EE03853C.

[105] L. Vayssieres, C. Sathe, S.M. Butorin, D.K. Shuh, J. Nordgren, J. Guo, One-Dimensional Quantum-Confinement Effect in α-Fe_2O_3 Ultrafine Nanorod Arrays, Advanced Materials 17(19) (2005) 2320-2323. DOI: 10.1002/adma.200500992.

[106] H.E. Prakasam, O.K. Varghese, M. Paulose, G.K. Mor, C.A. Grimes, Synthesis and photoelectrochemical properties of nanoporous iron (III) oxide by potentiostatic anodization, Nanotechnology 17(17) (2006) 4285.

[107] C.T. Sousa, D.C. Leitão, M.P. Proença, A. Apolinário, J.G. Correia, J. Ventura, J.P. Araújo, Tunning pore filling of anodic alumina templates by accurate control of the bottom barrier layer thickness, Nanotechnology 22(31) (2011) 315602.

[108] C.T. Sousa, A. Apolinario, D.C. Leitao, A.M. Pereira, J. Ventura, J.P. Araujo, Precise control of the filling stages in branched nanopores, J. Mater. Chem. 22(7) (2012) 3110-3116. DOI: 10.1039/C2JM14828E.

[109] S.J. Son, J. Reichel, B. He, M. Schuchman, S.B. Lee, Magnetic Nanotubes for Magnetic-Field-Assisted Bioseparation, Biointeraction, and Drug Delivery, Appl. Phys. Lett. 127(20) (2005) 7316-7317. DOI: 10.1021/ja0517365.

[110] J. Azevedo, C.T. Sousa, J. Ventura, A. Apolinario, A. Mendes, J.P. Araujo, Ultra-long Fe nanowires by pulsed electrodeposition with full filling of alumina templates, Materials Research Express 1(1) (2014) 015028.

[111] J.Y. Kim, G. Magesh, D.H. Youn, J.-W. Jang, J. Kubota, K. Domen, J.S. Lee, Single-crystalline, wormlike hematite photoanodes for efficient solar water splitting, Sci. Rep. 3 (2013). DOI: 10.1038/srep02681.

[112] K. Byrappa, N. Keerthiraj, S.M. Byrappa, 14 - Hydrothermal Growth of Crystals—Design and Processing, in: P. Rudolph (Ed.), Handbook of Crystal Growth (Second Edition), Elsevier, Boston, 2015, pp. 535-575.

[113] P.S. Shinde, S.H. Choi, Y. Kim, J. Ryu, J.S. Jang, Onset potential behavior in α-Fe_2O_3 photoanodes: the influence of surface and diffusion Sn doping on the surface states, Phys. Chem. Chem. Phys. 18(4) (2016) 2495-2509. DOI: 10.1039/C5CP06669G.

[114] A. Subramanian, E. Gracia-Espino, A. Annamalai, H.H. Lee, S.Y. Lee, S.H. Choi, J.S. Jang, Effect of tetravalent dopants on hematite nanostructure for enhanced photoelectrochemical water splitting, Appl. Surf. Sci. 427 (2018) 1203-1212. DOI: https://doi.org/10.1016/j.apsusc.2017.09.042.

[115] T.H. Jeon, G.-h. Moon, H. Park, W. Choi, Ultra-efficient and durable photoelectrochemical water oxidation using elaborately designed hematite nanorod arrays, Nano Energy 39 (2017) 211-218. DOI: https://doi.org/10.1016/j.nanoen.2017.06.049.

[116] J.-W. Jang, C. Du, Y. Ye, Y. Lin, X. Yao, J. Thorne, E. Liu, G. McMahon, J. Zhu, A. Javey, J. Guo, D. Wang, Enabling unassisted solar water splitting by iron oxide and silicon, Nat. Commun. 6 (2015) 7447. DOI: 10.1038/ncomms8447. http://www.nature.com/articles/ncomms8447#supplementary-information.

[117] G.K. Mor, O.K. Varghese, M. Paulose, K. Shankar, C.A. Grimes, A review on highly ordered, vertically oriented TiO_2 nanotube arrays: Fabrication, material properties, and solar energy applications, Sol. Energy Mater. Sol. Cells 90(14) (2006) 2011-2075. DOI: http://dx.doi.org/10.1016/j.solmat.2006.04.007.

[118] M. Paulose, K. Shankar, S. Yoriya, H.E. Prakasam, O.K. Varghese, G.K. Mor, T.A. Latempa, A. Fitzgerald, C.A. Grimes, Anodic Growth of Highly Ordered TiO_2 Nanotube Arrays to 134 μm in Length, J. Phys. Chem. B 110(33) (2006) 16179-16184. DOI: 10.1021/jp064020k.

[119] A. Mao, K. Shin, J.K. Kim, D.H. Wang, G.Y. Han, J.H. Park, Controlled Synthesis of Vertically Aligned Hematite on Conducting Substrate for Photoelectrochemical Cells: Nanorods versus Nanotubes, ACS Appl. Mater. Interfaces 3(6) (2011) 1852-1858. DOI: 10.1021/am200407t.

[120] J. Wu, L. Liu, S. Liu, P. Yu, Z. Zheng, M. Shafa, Z. Zhou, H. Li, H. Ji, Z.M. Wang, High Responsivity Photoconductors Based on Iron Pyrite Nanowires Using Sulfurization

of Anodized Iron Oxide Nanotubes, Nano Lett. 14(10) (2014) 6002-6009. DOI: 10.1021/nl503059t.

[121] M. Kumaresavanji, C.T. Sousa, A. Apolinario, A.M.L. Lopes, J.P. Araujo, Influence of sol–gel parameters in the fabrication of ferromagnetic $La_2/3Ca_{1/3}MnO_3$ nanotube arrays, Materials Science and Engineering: B 200 (2015) 117-123. DOI: https://doi.org/10.1016/j.mseb.2015.07.005.

[122] C. Eid, D. Luneau, V. Salles, R. Asmar, Y. Monteil, A. Khoury, A. Brioude, Magnetic Properties of Hematite Nanotubes Elaborated by Electrospinning Process, J. Phys. Chem. C 115(36) (2011) 17643-17646. DOI: 10.1021/jp203426j.

[123] H. Shan, C. Liu, L. Liu, L. Wang, S. Li, X. Zhang, X. Bo, X. Chi, Synthesis and acetone gas sensing properties of α-Fe_2O_3 nanotubes, Science China Chemistry 56(12) (2013) 1722-1726. DOI: 10.1007/s11426-013-4956-z.

[124] J. Bachmann, Jing, M. Knez, S. Barth, H. Shen, S. Mathur, U. Gösele, K. Nielsch, Ordered Iron Oxide Nanotube Arrays of Controlled Geometry and Tunable Magnetism by Atomic Layer Deposition, Appl. Phys. Lett. 129(31) (2007) 9554-9555. DOI: 10.1021/ja072465w.

[125] F. Keller, M.S. Hunter, D.L. Robinson, Structural Features of Oxide Coatings on Aluminum, J. Electrochem. Soc. 100(9) (1953) 411-419. DOI: 10.1149/1.2781142.

[126] A. Apolinário, P. Quitério, C.T. Sousa, J. Ventura, J.B. Sousa, L. Andrade, A.M. Mendes, J.P. Araújo, Modeling the Growth Kinetics of Anodic TiO_2 Nanotubes, J. Phys. Chem. Lett. 6(5) (2015) 845-851. DOI: 10.1021/jz502380b.

[127] P. Quitério, A. Apolinário, C.T. Sousa, J.D. Costa, J. Ventura, J.P. Araújo, The Morphological Characterization of Anodic TiO_2 Nanotube Arrays, Microsc. Microanal. 21(SupplementS5) (2015) 39-40. DOI: doi:10.1017/S1431927615014002.

[128] J.D. Costa, P. Quitério, A. Apolinário, C.T. Sousa, J. Azevedo, J. Ventura, L. Andrade, A. Mendes, J.P. Araújo, The effect of electrolyte re-utilization in the growth rate and morphology of TiO_2 nanotubes, Mater Lett 171 (2016) 224-227. DOI: https://doi.org/10.1016/j.matlet.2016.02.085.

[129] A. Apolinário, C.T. Sousa, G.N.P. Oliveira, A.M.L. Lopes, J. Ventura, L. Andrade, A. Mendes, J.P. Araújo, Tailoring the Anodic Hafnium Oxide Morphology Using Different Organic Solvent Electrolytes, Nanomaterials (Basel, Switzerland) 10(2) (2020). DOI: 10.3390/nano10020382.

[130] X. Qiu, J.Y. Howe, M.B. Cardoso, O. Polat, W.T. Heller, M. Parans Paranthaman, Size control of highly ordered HfO_2nanotube arrays and a possible growth mechanism, Nanotechnology 20(45) (2009) 455601. DOI: 10.1088/0957-4484/20/45/455601.

[131] W. Li, J. Li, X. Wang, S. Luo, J. Xiao, Q. Chen, Visible light photoelectrochemical responsiveness of self-organized nanoporous WO_3 films, Electrochim. Acta 56(1) (2010) 620-625. DOI: https://doi.org/10.1016/j.electacta.2010.06.025.

[132] B. Lucas-Granados, R. Sánchez-Tovar, R.M. Fernández-Domene, J. García-Antón, Study of the annealing conditions and photoelectrochemical characterization of a new iron oxide bi-layered nanostructure for water splitting, Sol. Energy Mater. Sol. Cells 153 (2016) 68-77. DOI: http://dx.doi.org/10.1016/j.solmat.2016.04.005.

[133] E.P. Haripriya, K.V. Oomman, P. Maggie, K.M. Gopal, A.G. Craig, Synthesis and photoelectrochemical properties of nanoporous iron (III) oxide by potentiostatic anodization, Nanotechnology 17(17) (2006) 4285.

[134] G.K. Mor, H.E. Prakasam, O.K. Varghese, K. Shankar, C.A. Grimes, Vertically Oriented Ti−Fe−O Nanotube Array Films: Toward a Useful Material Architecture for Solar Spectrum Water Photoelectrolysis, Nano Lett. 7(8) (2007) 2356-2364. DOI: 10.1021/nl0710046.

[135] S.P. Albu, A. Ghicov, P. Schmuki, High aspect ratio, self-ordered iron oxide nanopores formed by anodization of Fe in ethylene glycol/NH_4F electrolytes, Phys. Status Solidi RRL 3(2-3) (2009) 64-66. DOI: 10.1002/pssr.200802285.

[136] K. Shahzad, D. Kowalski, C. Zhu, Y. Aoki, H. Habazaki, Ex Situ Evidence for the Role of a Fluoride-Rich Layer Switching the Growth of Nanopores to Nanotubes: A Missing Piece of the Anodizing Puzzle, ChemElectroChem 5(4) (2018) 610-618. DOI: 10.1002/celc.201701103.

[137] R. Schrebler, L.A. Ballesteros, H. Gómez, P. Grez, R. Córdova, E. Muñoz, R. Schrebler, J.R. Ramos-Barrado, E.A. Dalchiele, Electrochemically Grown Self-Organized Hematite Nanotube Arrays for Photoelectrochemical Water Splitting, J. Electrochem. Soc. 161(14) (2014) H903-H908. DOI: 10.1149/2.0481414jes.

[138] C. Han, Y. Wang, T. Lu, S. Yang, L.Q. Wang, X.P. Song, Fabrication and magnetism of α-Fe_2O_3 nanotubes via a multistep ac electrodeposition, Chemical Physics Letters 633 (2015) 47-51. DOI: http://dx.doi.org/10.1016/j.cplett.2015.05.015.

[139] C.H. Kim, H.J. Chun, D.S. Kim, S.Y. Kim, J. Park, J.Y. Moon, G. Lee, J. Yoon, Y. Jo, M.-H. Jung, S.I. Jung, C.J. Lee, Magnetic anisotropy of vertically aligned α-Fe_2O_3 nanowire array, Appl. Phys. Lett. 89(22) (2006) 223103. DOI: doi:http://dx.doi.org/10.1063/1.2393165.

[140] Y. Zhao, C.W. Dunnill, Y. Zhu, D.H. Gregory, W. Kockenberger, Y. Li, W. Hu, I. Ahmad, D.G. McCartney, Low-Temperature Magnetic Properties of Hematite Nanorods, Chem. Mater. 19(4) (2007) 916-921. DOI: 10.1021/cm062375a.

[141] C. Díaz-Guerra, L. Pérez, J. Piqueras, M.F. Chioncel, Magnetic transitions in α-Fe_2O_3 nanowires, J. Appl. Phys. 106(10) (2009) 104302. DOI: doi:http://dx.doi.org/10.1063/1.3259394.

[142] C. Liu, J. Ma, Y. Liu, Formation mechanism and magnetic properties of three different hematite nanostructures synthesized by one-step hydrothermal procedure, Science China Chemistry 54(10) (2011) 1607. DOI: 10.1007/s11426-011-4392-x.

[143] C.-J. Jia, L.-D. Sun, Z.-G. Yan, L.-P. You, F. Luo, X.-D. Han, Y.-C. Pang, Z. Zhang, C.-H. Yan, Single-Crystalline Iron Oxide Nanotubes, Angew. Chem. Int. Ed. 44(28) (2005) 4328-4333. DOI: 10.1002/anie.200463038.

[144] C.-J. Jia, L.-D. Sun, Z.-G. Yan, Y.-C. Pang, L.-P. You, C.-H. Yan, Iron Oxide Tube-in-Tube Nanostructures, J. Phys. Chem. C 111(35) (2007) 13022-13027. DOI: 10.1021/jp073837q.

[145] S. Liu, Y.-H. Sun, P.-P. Dong, J.-M. Nan, Conversion of α-Fe_2O_3 from spindle nanorods to nanotubes, and their lithium-storage performance, Materials Science and Engineering: B 202 (2015) 15-24. DOI: https://doi.org/10.1016/j.mseb.2015.08.011.

[146] J. Chen, S. Macfarlane, C. Zhang, K. Yu, W. Zhou, Chemistry of Hydrolysis of $FeCl_3$ in the Presence of Phosphate to Form Hematite Nanotubes and Nanorings, Crystal Growth & Design 17(11) (2017) 5975-5983. DOI: 10.1021/acs.cgd.7b01083.

[147] S.K. Deb, Opportunities and challenges in science and technology of WO_3 for electrochromic and related applications, Sol. Energy Mater. Sol. Cells 92(2) (2008) 245-258. DOI: https://doi.org/10.1016/j.solmat.2007.01.026.

[148] H. Zheng, J.Z. Ou, M.S. Strano, R.B. Kaner, A. Mitchell, K. Kalantar-zadeh, Nanostructured Tungsten Oxide – Properties, Synthesis, and Applications, Adv. Funct. Mater. 21(12) (2011) 2175-2196. DOI: 10.1002/adfm.201002477.

[149] G. Hodes, D. Cahen, J. Manassen, Tungsten trioxide as a photoanode for a photoelectrochemical cell (PEC), Nature 260(5549) (1976) 312-313. DOI: 10.1038/260312a0.

[150] R. Solarska, R. Jurczakowski, J. Augustynski, A highly stable, efficient visible-light driven water photoelectrolysis system using a nanocrystalline WO_3 photoanode and a methane sulfonic acid electrolyte, Nanoscale 4(5) (2012) 1553-1556. DOI: 10.1039/C2NR11573E.

[151] M.D. Bhatt, J.S. Lee, Recent theoretical progress in the development of photoanode materials for solar water splitting photoelectrochemical cells, J. Mater. Chem. A 3(20) (2015) 10632-10659. DOI: 10.1039/C5TA00257E.

[152] J.M. Berak, M.J. Sienko, Effect of oxygen-deficiency on electrical transport properties of tungsten trioxide crystals, Journal of Solid State Chemistry 2(1) (1970) 109-133. DOI: https://doi.org/10.1016/0022-4596(70)90040-X.

[153] M.A. Butler, Photoelectrolysis and physical properties of the semiconducting electrode WO_2 J. Appl. Phys. 48(5) (1977) 1914-1920. DOI: 10.1063/1.323948.

[154] M. Gratzel, Photoelectrochemical cells, Nature 414(6861) (2001) 338-344. DOI: 10.1038/35104607.

[155] H.A. Wriedt, The O-W (oxygen-tungsten) system, Bulletin of Alloy Phase Diagrams 10(4) (1989) 368-384. DOI: 10.1007/BF02877593.

[156] M. Gillet, K. Aguir, C. Lemire, E. Gillet, K. Schierbaum, The structure and electrical conductivity of vacuum-annealed WO3 thin films, Thin Solid Films 467(1) (2004) 239-246. DOI: https://doi.org/10.1016/j.tsf.2004.04.018.

[157] L. Meda, G. Tozzola, A. Tacca, G. Marra, S. Caramori, V. Cristino, C. Alberto Bignozzi, Photo-electrochemical properties of nanostructured WO_3 prepared with different organic dispersing agents, Sol. Energy Mater. Sol. Cells 94(5) (2010) 788-796. DOI: https://doi.org/10.1016/j.solmat.2009.12.025.

[158] T. Zhu, M.N. Chong, E.S. Chan, Nanostructured Tungsten Trioxide Thin Films Synthesized for Photoelectrocatalytic Water Oxidation: A review, ChemSusChem 7(11) (2014) 2974-2997. DOI: 10.1002/cssc.201402089.

[159] S. Berger, H. Tsuchiya, A. Ghicov, P. Schmuki, High photocurrent conversion efficiency in self-organized porous WO_3, Appl. Phys. Lett. 88(20) (2006) 203119. DOI: 10.1063/1.2206696.

[160] J. Guo, Y. Li, S. Zhu, Z. Chen, Q. Liu, D. Zhang, W.-J. Moon, D.-M. Song, Synthesis of WO_3@Graphene composite for enhanced photocatalytic oxygen evolution from water, RSC Advances 2(4) (2012) 1356-1363. DOI: 10.1039/C1RA00621E.

[161] J. Su, X. Feng, J.D. Sloppy, L. Guo, C.A. Grimes, Vertically Aligned WO_3 Nanowire Arrays Grown Directly on Transparent Conducting Oxide Coated Glass: Synthesis and Photoelectrochemical Properties, Nano Lett. 11(1) (2011) 203-208. DOI: 10.1021/nl1034573.

[162] J. Yang, W. Li, J. Li, D. Sun, Q. Chen, Hydrothermal synthesis and photoelectrochemical properties of vertically aligned tungsten trioxide (hydrate) plate-like arrays fabricated directly on FTO substrates, J. Mater. Chem. 22(34) (2012) 17744-17752. DOI: 10.1039/C2JM33199C.

[163] T. Zhang, M. Paulose, R. Neupane, L.A. Schaffer, D.B. Rana, J. Su, L. Guo, O.K. Varghese, Nanoporous WO_3 films synthesized by tuning anodization conditions for photoelectrochemical water oxidation, Sol. Energy Mater. Sol. Cells 209 (2020) 110472. DOI: https://doi.org/10.1016/j.solmat.2020.110472.

[164] M. Rodríguez-Pérez, C. Chacón, E. Palacios-González, G. Rodríguez-Gattorno, G. Oskam, Photoelectrochemical water oxidation at electrophoretically deposited WO_3 films as a function of crystal structure and morphology, Electrochim. Acta 140 (2014) 320-331. DOI: https://doi.org/10.1016/j.electacta.2014.03.022.

[165] A. Kafizas, L. Francàs, C. Sotelo-Vazquez, M. Ling, Y. Li, E. Glover, L. McCafferty, C. Blackman, J. Darr, I. Parkin, Optimizing the Activity of Nanoneedle Structured WO_3 Photoanodes for Solar Water Splitting: Direct Synthesis via Chemical Vapor Deposition, J. Phys. Chem. C 121(11) (2017) 5983-5993. DOI: 10.1021/acs.jpcc.7b00533.

[166] B. Marsen, E.L. Miller, D. Paluselli, R.E. Rocheleau, Progress in sputtered tungsten trioxide for photoelectrode applications, Int. J. Hydrogen Energy 32(15) (2007) 3110-3115. DOI: https://doi.org/10.1016/j.ijhydene.2006.01.022.

[167] A. Tacca, L. Meda, G. Marra, A. Savoini, S. Caramori, V. Cristino, C.A. Bignozzi, V.G. Pedro, P.P. Boix, S. Gimenez, J. Bisquert, Photoanodes Based on Nanostructured WO_3 for Water Splitting, ChemPhysChem 13(12) (2012) 3025-3034. DOI: 10.1002/cphc.201200069.

[168] C. Ng, Y.H. Ng, A. Iwase, R. Amal, Influence of Annealing Temperature of WO_3 in Photoelectrochemical Conversion and Energy Storage for Water Splitting, ACS Appl. Mater. Interfaces 5(11) (2013) 5269-5275. DOI: 10.1021/am401112q.

[169] V. Cristino, S. Caramori, R. Argazzi, L. Meda, G.L. Marra, C.A. Bignozzi, Efficient Photoelectrochemical Water Splitting by Anodically Grown WO_3 Electrodes, Langmuir 27(11) (2011) 7276-7284. DOI: 10.1021/la200595x.

[170] S. Reinhard, F. Rechberger, M. Niederberger, Commercially Available WO_3 Nanopowders for Photoelectrochemical Water Splitting: Photocurrent versus Oxygen Evolution, ChemPlusChem 81(9) (2016) 935-940. DOI: 10.1002/cplu.201600241.

[171] Z. Ma, H. Hou, K. Song, Z. Fang, L. Wang, F. Gao, W. Yang, B. Tang, Y. Kuang, Engineering oxygen vacancies by one-step growth of distributed homojunctions to enhance charge separation for efficient photoelectrochemical water splitting, Chemical Engineering Journal 379 (2020) 122266. DOI: https://doi.org/10.1016/j.cej.2019.122266.

[172] M. Sarnowska, K. Bienkowski, P.J. Barczuk, R. Solarska, J. Augustynski, Highly Efficient and Stable Solar Water Splitting at (Na)WO_3 Photoanodes in Acidic Electrolyte Assisted by Non-Noble Metal Oxygen Evolution Catalyst, Advanced Energy Materials 6(14) (2016) 1600526. DOI: 10.1002/aenm.201600526.

[173] S.S. Kalanur, Y.-G. Noh, H. Seo, Engineering band edge properties of WO_3 with respect to photoelectrochemical water splitting potentials via a generalized doping protocol of first-row transition metal ions, Appl. Surf. Sci. 509 (2020) 145253. DOI: https://doi.org/10.1016/j.apsusc.2020.145253.

[174] S.S. Kalanur, Structural, Optical, Band Edge and Enhanced Photoelectrochemical Water Splitting Properties of Tin-Doped WO_3, Catalysts 9(5) (2019) 456. DOI: https://doi.org/10.3390/catal9050456.

[175] S. Bai, X. Yang, C. Liu, X. Xiang, R. Luo, J. He, A. Chen, An Integrating Photoanode of WO_3/Fe_2O_3 Heterojunction Decorated with NiFe-LDH to Improve PEC Water Splitting Efficiency, ACS Sustainable Chemistry & Engineering 6(10) (2018) 12906-12913. DOI: 10.1021/acssuschemeng.8b02267.

[176] Q. Wu, Q. Bu, S. Li, Y. Lin, X. Zou, D. Wang, T. Xie, Enhanced interface charge transfer via n-n WO_3/Ti–Fe_2O_3 heterojunction formation for water splitting, J. Alloys Compd. 803 (2019) 1105-1111. DOI: https://doi.org/10.1016/j.jallcom.2019.06.371.

[177] C.A. Bignozzi, S. Caramori, V. Cristino, R. Argazzi, L. Meda, A. Tacca, Nanostructured photoelectrodes based on WO_3: applications to photooxidation of aqueous electrolytes, Chemical Society Reviews 42(6) (2013) 2228-2246. DOI: 10.1039/C2CS35373C.

[178] S.J. Hong, H. Jun, P.H. Borse, J.S. Lee, Size effects of WO_3 nanocrystals for photooxidation of water in particulate suspension and photoelectrochemical film systems, Int. J. Hydrogen Energy 34(8) (2009) 3234-3242. DOI: https://doi.org/10.1016/j.ijhydene.2009.02.006.

[179] Y. Liu, Y. Li, W. Li, S. Han, C. Liu, Photoelectrochemical properties and photocatalytic activity of nitrogen-doped nanoporous WO_3 photoelectrodes under visible light, Appl. Surf. Sci. 258(12) (2012) 5038-5045. DOI: https://doi.org/10.1016/j.apsusc.2012.01.080.

[180] M. Park, J.H. Seo, H. Song, K.M. Nam, Enhanced Visible Light Activity of Single-Crystalline WO_3 Microplates for Photoelectrochemical Water Oxidation, J. Phys. Chem. C 120(17) (2016) 9192-9199. DOI: 10.1021/acs.jpcc.6b00389.

[181] S.K. Biswas, J.-O. Baeg, S.-J. Moon, K.-j. Kong, W.-W. So, Morphologically different WO_3 nanocrystals in photoelectrochemical water oxidation, Journal of Nanoparticle Research 14(1) (2012) 667. DOI: 10.1007/s11051-011-0667-6.

[182] S.S. Kalanur, Y.J. Hwang, S.Y. Chae, O.S. Joo, Facile growth of aligned WO_3 nanorods on FTO substrate for enhanced photoanodic water oxidation activity, J. Mater. Chem. A 1(10) (2013) 3479-3488. DOI: 10.1039/C3TA01175E.

[183] H.-L. Kuo, C.-Y. Kuo, C.-H. Liu, J.-H. Chao, C.-H. Lin, A highly active bi-crystalline photocatalyst consisting of TiO_2 (B) nanotube and anatase particle for producing H2 gas from neat ethanol, Catal Lett 113(1-2) (2007) 7-12. DOI: 10.1007/s10562-006-9009-1.

[184] Y. Liu, B. Zhou, J. Bai, J. Li, J. Zhang, Q. Zheng, X. Zhu, W. Cai, Efficient photochemical water splitting and organic pollutant degradation by highly ordered TiO_2 nanopore arrays, Appl. Catal. B 89(1–2) (2009) 142-148. DOI: http://dx.doi.org/10.1016/j.apcatb.2008.11.034.

[185] S.-H. Oh, R.R. Finõnes, C. Daraio, L.-H. Chen, S. Jin, Growth of nano-scale hydroxyapatite using chemically treated titanium oxide nanotubes, Biomaterials 26(24) (2005) 4938-4943. DOI: http://dx.doi.org/10.1016/j.biomaterials.2005.01.048.

[186] O.K. Varghese, D. Gong, M. Paulose, K.G. Ong, E.C. Dickey, C.A. Grimes, Extreme Changes in the Electrical Resistance of Titania Nanotubes with Hydrogen Exposure, Adv. Mater. 15(7-8) (2003) 624-627. DOI: 10.1002/adma.200304586.

[187] X. Lu, G. Wang, T. Zhai, M. Yu, J. Gan, Y. Tong, Y. Li, Hydrogenated TiO_2 Nanotube Arrays for Supercapacitors, Nano Lett. 12(3) (2012) 1690-1696. DOI: 10.1021/nl300173j.

[188] I. Paramasivam, H. Jha, N. Liu, P. Schmuki, A Review of Photocatalysis using Self-organized TiO_2 Nanotubes and Other Ordered Oxide Nanostructures, Small 8(20) (2012) 3073-3103. DOI: 10.1002/smll.201200564.

[189] S. Murgolo, I.S. Moreira, C. Piccirillo, P.M.L. Castro, G. Ventrella, C. Cocozza, G. Mascolo, Photocatalytic Degradation of Diclofenac by Hydroxyapatite–TiO_2 Composite Material: Identification of Transformation Products and Assessment of Toxicity, Materials 11(9) (2018) 1779.

[190] A.B. Tesler, M. Altomare, P. Schmuki, Morphology and Optical Properties of Highly Ordered TiO_2 Nanotubes Grown in NH_4F/o-H_3PO_4 Electrolytes in View of Light-Harvesting and Catalytic Applications, ACS Applied Nano Materials (2020). DOI: 10.1021/acsanm.0c01859.

[191] S. Shen, J. Chen, M. Wang, X. Sheng, X. Chen, X. Feng, S.S. Mao, Titanium dioxide nanostructures for photoelectrochemical applications, Progress in Materials Science 98 (2018) 299-385. DOI: https://doi.org/10.1016/j.pmatsci.2018.07.006.

[192] A. Kusior, A. Wnuk, A. Trenczek-Zajac, K. Zakrzewska, M. Radecka, TiO_2 nanostructures for photoelectrochemical cells (PECs), Int. J. Hydrogen Energy 40(14) (2015) 4936-4944. DOI: https://doi.org/10.1016/j.ijhydene.2015.01.103.

[193] B. O'Regan, M. Gratzel, A low-cost, high-efficiency solar cell based on dye-sensitized colloidal TiO_2 films, Nature 353(6346) (1991) 737-740.

[194] J. Gong, J. Liang, K. Sumathy, Review on dye-sensitized solar cells (DSSCs): Fundamental concepts and novel materials, Renewable and Sustainable Energy Reviews 16(8) (2012) 5848-5860. DOI: https://doi.org/10.1016/j.rser.2012.04.044.

[195] J. Ajayan, D. Nirmal, P. Mohankumar, M. Saravanan, M. Jagadesh, L. Arivazhagan, A review of photovoltaic performance of organic/inorganic solar cells for future renewable and sustainable energy technologies, Superlattices and Microstructures 143 (2020) 106549. DOI: https://doi.org/10.1016/j.spmi.2020.106549.

[196] Sony dye-sensitized solar cell prototypes, Available at: https://www.sony.net/SonyInfo/News/Press/201012/10-161E/ (Accessed March 28, 2020).

[197] D. Dambournet, I. Belharouak, K. Amine, Tailored Preparation Methods of TiO_2 Anatase, Rutile, Brookite: Mechanism of Formation and Electrochemical Properties, Chem. Mater. 22(3) (2010) 1173-1179. DOI: 10.1021/cm902613h.

[198] D. Regonini, C.R. Bowen, A. Jaroenworaluck, R. Stevens, A review of growth mechanism, structure and crystallinity of anodized TiO_2 nanotubes, Materials Science and Engineering: R: Reports 74(12) (2013) 377-406. DOI: https://doi.org/10.1016/j.mser.2013.10.001.

[199] P. Roy, S. Berger, P. Schmuki, TiO_2 Nanotubes: Synthesis and Applications, Angew. Chem. Int. Ed. 50(13) (2011) 2904-2939. DOI: 10.1002/anie.201001374.

[200] S.-D. Mo, W.Y. Ching, Electronic and optical properties of three phases of titanium dioxide: Rutile, anatase, and brookite, Physical Review B 51(19) (1995) 13023-13032. DOI: 10.1103/PhysRevB.51.13023.

[201] J.W. Schultze, M.M. Lohrengel, Stability, reactivity and breakdown of passive films. Problems of recent and future research, Electrochim. Acta 45(15–16) (2000) 2499-2513. DOI: http://dx.doi.org/10.1016/S0013-4686(00)00347-9.

[202] P. Schmuki, From Bacon to barriers: a review on the passivity of metals and alloys, Journal of Solid State Electrochemistry 6(3) (2002) 145-164. DOI: 10.1007/s100080100219.

[203] K. Shankar, G.K. Mor, H.E. Prakasam, S. Yoriya, M. Paulose, O.K. Varghese, C.A. Grimes, Highly-ordered TiO_2 nanotube arrays up to 220 μm in length: use in water photoelectrolysis and dye-sensitized solar cells, Nanotechnology 18(6) (2007) 065707.

[204] H. Tsuchiya, J.M. Macak, A. Ghicov, A.S. Räder, L. Taveira, P. Schmuki, Characterization of electronic properties of TiO2 nanotube films, Corrosion Science 49(1) (2007) 203-210. DOI: https://doi.org/10.1016/j.corsci.2006.05.009.

[205] V. Zwilling, M. Aucouturier, E. Darque-Ceretti, Anodic oxidation of titanium and TA6V alloy in chromic media. An electrochemical approach, Electrochim. Acta 45(6) (1999) 921-929. DOI: http://dx.doi.org/10.1016/S0013-4686(99)00283-2.

[206] R. Beranek, H. Hildebrand, P. Schmuki, Self-Organized Porous Titanium Oxide Prepared in H_2SO_4 / HF Electrolytes, Electrochemical and Solid-State Letters 6(3) (2003) B12-B14. DOI: 10.1149/1.1545192.

[207] G.K. Mor, O.K. Varghese, M. Paulose, N. Mukherjee, C.A. Grimes, Fabrication of tapered, conical-shaped titania nanotubes, J. Mater. Res. 18(11) (2003) 2588-2593. DOI: doi:10.1557/JMR.2003.0362.

[208] J.M. Macák, H. Tsuchiya, P. Schmuki, High-Aspect-Ratio TiO_2 Nanotubes by Anodization of Titanium, Angew. Chem. Int. Ed. 44(14) (2005) 2100-2102. DOI: 10.1002/anie.200462459.

[209] Q. Cai, M. Paulose, O.K. Varghese, C.A. Grimes, The Effect of Electrolyte Composition on the Fabrication of Self-Organized Titanium Oxide Nanotube Arrays by Anodic Oxidation, J. Mater. Res. 20(01) (2005) 230-236. DOI: doi:10.1557/JMR.2005.0020.

[210] J.M. Macak, H. Tsuchiya, L. Taveira, S. Aldabergerova, P. Schmuki, Smooth Anodic TiO_2 Nanotubes, Angew. Chem. Int. Ed. 44(45) (2005) 7463-7465. DOI: 10.1002/anie.200502781.

[211] M. Paulose, H.E. Prakasam, O.K. Varghese, L. Peng, K.C. Popat, G.K. Mor, T.A. Desai, C.A. Grimes, TiO_2 Nanotube Arrays of 1000 μm Length by Anodization of Titanium Foil: Phenol Red Diffusion, J. Phys. Chem. C 111(41) (2007) 14992-14997. DOI: 10.1021/jp075258r.

[212] C.T. Sousa, D.C. Leitao, M.P. Proenca, J. Ventura, A.M. Pereira, J.P. Araujo, Nanoporous alumina as templates for multifunctional applications, Appl. Phys. Rev. 1(3) (2014) 031102. DOI: doi:http://dx.doi.org/10.1063/1.4893546.

[213] A. Apolinario, C.T. Sousa, J. Ventura, J.D. Costa, D.C. Leitao, J.M. Moreira, J.B. Sousa, L. Andrade, A.M. Mendes, J.P. Araujo, The role of the Ti surface roughness in the self-ordering of TiO_2 nanotubes: a detailed study of the growth mechanism, J. Mater. Chem. A 2(24) (2014) 9067-9078. DOI: 10.1039/C4TA00871E.

[214] A. Apolinário, C.T. Sousa, J. Ventura, L. Andrade, A.M. Mendes, J.P. Araújo, Tailoring the Ti surface via electropolishing nanopatterning as a route to obtain highly ordered TiO_2 nanotubes, Nanotechnology 25(48) (2014) 485301. DOI: 10.1088/0957-4484/25/48/485301.

[215] F. Francisco, P. Dias, D. Ivanou, F. Santos, J. Azevedo, A. Mendes, Synthesis of Host-Guest Hematite Photoelectrodes for Solar Water Splitting, ChemNanoMat 5(7) (2019) 911-920. DOI: 10.1002/cnma.201900141.

[216] B.P. Kafle, Chapter 6 - Introduction to nanomaterials and application of UV–Visible spectroscopy for their characterization, in: B.P. Kafle (Ed.), Chemical Analysis and Material Characterization by Spectrophotometry, Elsevier2020, pp. 147-198.

[217] M. Ohring, Chapter 3 - Thin-Film Evaporation Processes, Materials Science of Thin Films (Second Edition), Academic Press, San Diego, 2002, pp. 95-144.

[218] H.H. Gatzen, V. Saile, J. Leuthold, Deposition Technologies, Micro and Nano Fabrication: Tools and Processes, Springer Berlin Heidelberg, Berlin, Heidelberg, 2015, pp. 65-203.

[219] C. Dias, Resistive Switching in MgO and Si/Ag Metal-Insulator-Metal structures. PhD Thesis, University of Porto (2019).

[220] What is Ion Beam Deposition? Available at: https://www.dentonvacuum.com/what-is-ion-beam-deposition/ (Accessed May 27, 2020).

[221] Pulsed Laser Deposition of Complex Materials: Progress Toward Applications, Pulsed Laser Deposition of Thin Films, pp. 1-31.

[222] W. Zhou, R. Apkarian, Z.L. Wang, D. Joy, Fundamentals of Scanning Electron Microscopy (SEM), in: W. Zhou, Z.L. Wang (Eds.), Scanning Microscopy for Nanotechnology: Techniques and Applications, Springer New York, New York, NY, 2007, pp. 1-40.

[223] J. Goldstein, Scanning electron microscopy and x-ray microanalysis, Kluwer Academic/Plenum Publishers, New York, 2003.

[224] A. Bogner, P.H. Jouneau, G. Thollet, D. Basset, C. Gauthier, A history of scanning electron microscopy developments: Towards “wet-STEM” imaging, Micron 38(4) (2007) 390-401. DOI: https://doi.org/10.1016/j.micron.2006.06.008.

[225] MATERIALS CHARACTERIZATION SERIES A2 - Brundle, C. Ricbard, in: C.A. Evans, S. Wilson (Eds.), Encyclopedia of Materials Characterization, Butterworth-Heinemann, Boston, 1992, p. ii.

[226] V. Kazmiruk, Scanning Electron Microscopy, InTech, Chapters 2012.

[227] SEM: Types of Electrons and the Information They Provide. Available at: https://www.thermofisher.com/blog/microscopy/sem-types-electrons-and-the-information-they-provide/ (Accessed February 12, 2020).

[228] C.A. Schneider, W.S. Rasband, K.W. Eliceiri, NIH Image to ImageJ: 25 years of image analysis, Nat. Methods 9(7) (2012) 671-675. DOI: 10.1038/nmeth.2089.

[229] Unidade de Imagem, Microestrutura e Microanálise - IMICROS. Available at: https://cemup.up.pt/webcemup/IMICROS/IMICROS_lab/IMICROS_lmev.htm (Accessed February 12, 2020).

[230] J. Bergström, 2 - Experimental Characterization Techniques, in: J. Bergström (Ed.), Mechanics of Solid Polymers, William Andrew Publishing2015, pp. 19-114.

[231] A. Khursheed, Scanning Electron Microscope Optics and Spectrometers, World Scientific2011.

[232] T. Ungár, Microstructural parameters from X-ray diffraction peak broadening, Scr. Mater. 51(8) (2004) 777-781. DOI: https://doi.org/10.1016/j.scriptamat.2004.05.007.

[233] W.H. Bragg, W.L. Bragg, The reflection of X-rays by crystals, Proceedings of the Royal Society of London. Series A, Containing Papers of a Mathematical and Physical Character 88(605) (1913) 428-438. DOI: doi:10.1098/rspa.1913.0040.

[234] N.I. Stresstech, X-ray diffraction, Available at: https://www.stresstech.com/en-fi/products/x-ray-diffraction-equipment/x-ray-diffraction/ (Accessed May 01, 2020).

[235] G.K. Williamson, W.H. Hall, X-ray line broadening from filed aluminium and wolfram, Acta Metall. 1(1) (1953) 22-31. DOI: https://doi.org/10.1016/0001-6160(53)90006-6.

[236] W.-K. Chu, J.W. Mayer, M.-A. Nicolet, Chapter 1 - Introduction, in: W.-K. Chu, J.W. Mayer, M.-A. Nicolet (Eds.), Backscattering Spectrometry, Academic Press1978, pp. 1-20.

[237] N.P. Barradas, C. Jeynes, R.P. Webb, Simulated annealing analysis of Rutherford backscattering data, Appl. Phys. Lett. 71(2) (1997) 291-293. DOI: 10.1063/1.119524.

[238] N.P. Barradas, Rutherford backscattering analysis of thin films and superlattices with roughness, J. Phys. D: Appl. Phys. 34(14) (2001) 2109-2116. DOI: 10.1088/0022-3727/34/14/305.

[239] N.P. Barradas, C. García Núñez, A. Redondo-Cubero, G. Shen, P. Kung, J.L. Pau, Analytical simulation of RBS spectra of nanowire samples, Nucl. Instrum. Methods Phys. Res. B 371 (2016) 116-120. DOI: https://doi.org/10.1016/j.nimb.2015.08.080.

[240] S. Magalhães, Caracterização e Modificação de Heteroestruturas de Nitretos do Grupo III, PhD Thesis, Aveiro University (2013).

[241] J. Cabaço, Effect of Ar implantation energy and angle on the reflection pattern of nitrides, Master Thesis, Porto University (2019).

[242] N.P. Barradas, C. Jeynes, M.A. Harry, RBS/simulated annealing analysis of iron-cobalt silicides, Nucl. Instrum. Methods Phys. Res. B 136-138 (1998) 1163-1167. DOI: https://doi.org/10.1016/S0168-583X(97)00809-4.

[243] M. Newville, Fundamentals of XAFS, Reviews in Mineralogy and Geochemistry 78(1) (2014) 33-74. DOI: 10.2138/rmg.2014.78.2.

[244] Newville, M. Fundamentals of XAFS, Technical report, 2004, Consortium for Advanced Radiation Sources, University of Chicago, IL.

[245] E.E. Alp, S.M. Mini, M. Ramanathan, X-ray absorption spectroscopy: EXAFS and XANES - A versatile tool to study the atomic and electronic structure of materials, United States, 1990, pp. 25-36.

[246] S.J.A. Figueroa, J.C. Mauricio, J. Murari, D.B. Beniz, J.R. Piton, H.H. Slepicka, M.F. de Sousa, A.M. Espíndola, A.P.S. Levinsky, Upgrades to the XAFS2 beamline control system and to the endstation at the LNLS, J. Phys. Conf. Ser. 712 (2016) 012022. DOI: 10.1088/1742-6596/712/1/012022.

[247] B. Ravel, M. Newville, ATHENA, ARTEMIS, HEPHAESTUS: data analysis for X-ray absorption spectroscopy using IFEFFIT, J. Synchrotron Radiat. 12(4) (2005) 537-541. DOI: doi:10.1107/S0909049505012719.

[248] 6.5. k-weights in plots and Fourier transforms. Available at: https://bruceravel.github.io/demeter/documents/Athena/ui/kweight.html (Accessed March 03, 2018).

[249] Surface plasmons, in: B. Hecht, L. Novotny (Eds.), Principles of Nano-Optics, Cambridge University Press, Cambridge, 2006, pp. 378-418.

[250] T. Lopes, L. Andrade, F. Le Formal, M. Gratzel, K. Sivula, A. Mendes, Hematite photoelectrodes for water splitting: evaluation of the role of film thickness by impedance spectroscopy, Phys. Chem. Chem. Phys. 16(31) (2014) 16515-16523. DOI: 10.1039/C3CP55473B.

[251] H. Dotan, N. Mathews, T. Hisatomi, M. Grätzel, A. Rothschild, On the Solar to Hydrogen Conversion Efficiency of Photoelectrodes for Water Splitting, J. Phys. Chem. Lett. 5(19) (2014) 3330-3334. DOI: 10.1021/jz501716g.

[252] J. Tauc, Optical properties and electronic structure of amorphous Ge and Si, Mater. Res. Bull. 3(1) (1968) 37-46. DOI: https://doi.org/10.1016/0025-5408(68)90023-8.

[253] A. Shavorskiy, X. Ye, O. Karslıoğlu, A.D. Poletayev, M. Hartl, I. Zegkinoglou, L. Trotochaud, S. Nemšák, C.M. Schneider, E.J. Crumlin, S. Axnanda, Z. Liu, P.N. Ross, W. Chueh, H. Bluhm, Direct Mapping of Band Positions in Doped and Undoped Hematite during Photoelectrochemical Water Splitting, J. Phys. Chem. Lett. 8(22) (2017) 5579-5586. DOI: 10.1021/acs.jpclett.7b02548.

[254] C. Vichery, I. Maurin, P. Bonville, J.-P. Boilot, T. Gacoin, Influence of Protected Annealing on the Magnetic Properties of γ-Fe_2O_3 Nanoparticles, J. Phys. Chem. C 116(30) (2012) 16311-16318. DOI: 10.1021/jp305069a.

[255] W. Si, F. Haydous, U. Babic, D. Pergolesi, T. Lippert, Suppressed Charge Recombination in Hematite Photoanode via Protonation and Annealing, ACS Appl. Energy Mater. 2(8) (2019) 5438-5445. DOI: 10.1021/acsaem.9b00420.

[256] J.Y. Kim, D.H. Youn, J.H. Kim, H.G. Kim, J.S. Lee, Nanostructure-Preserved Hematite Thin Film for Efficient Solar Water Splitting, ACS Appl. Mater. Interfaces 7(25) (2015) 14123-14129. DOI: 10.1021/acsami.5b03409.

[257] W.M. Carvalho-Jr, L. Mendonça-Ferreira, F.N. Costa, F.F. Ferreira, D.N.F. Muche, R.A. Tofanello, R.H.R. Castro, F.L. Souza, Annealing control of hydrothermally grown hematite nanorods: Implication of structural changes and Cl concentration on weak ferromagnetism, J. Alloys Compd. 799 (2019) 83-88. DOI: https://doi.org/10.1016/j.jallcom.2019.05.335.

[258] J. Wang, N.H. Perry, L. Guo, L. Vayssieres, H.L. Tuller, On the Theoretical and Experimental Control of Defect Chemistry and Electrical and Photoelectrochemical Properties of Hematite Nanostructures, ACS Appl. Mater. Interfaces 11(2) (2019) 2031-2041. DOI: 10.1021/acsami.8b16911.

[259] A. Annamalai, P.S. Shinde, A. Subramanian, J.Y. Kim, J.H. Kim, S.H. Choi, J.S. Lee, J.S. Jang, Bifunctional TiO_2 underlayer for α-Fe_2O_3 nanorod based photoelectrochemical cells: enhanced interface and Ti4+ doping, J. Mater. Chem. A 3(9) (2015) 5007-5013. DOI: 10.1039/C4TA06315E.

[260] J. Xiao, H. Huang, Q. Huang, L. Zhao, X. Li, X. Hou, H. Chen, Y. Li, Suppressing the electron–hole recombination rate in hematite photoanode with a rapid cooling treatment, J. Catal. 350 (2017) 48-55. DOI: https://doi.org/10.1016/j.jcat.2017.02.001.

[261] F. Francisco, P. Dias, D. Ivanou, F. Santos, J. Azevedo, A. Mendes, Synthesis of Host-Guest Hematite Photoelectrodes for Solar Water Splitting, ChemNanoMat 0(0). DOI: 10.1002/cnma.201900141.

[262] M. Li, Y. Yang, Y. Ling, W. Qiu, F. Wang, T. Liu, Y. Song, X. Liu, P. Fang, Y. Tong, Y. Li, Morphology and Doping Engineering of Sn-Doped Hematite Nanowire Photoanodes, Nano Lett. 17(4) (2017) 2490-2495. DOI: 10.1021/acs.nanolett.7b00184.

[263] D. Bartesaghi, I.d.C. Pérez, J. Kniepert, S. Roland, M. Turbiez, D. Neher, L.J.A. Koster, Competition between recombination and extraction of free charges determines the fill factor of organic solar cells, Nat. Commun. 6(1) (2015) 7083. DOI: 10.1038/ncomms8083.

[264] P. Dias, T. Lopes, L. Meda, L. Andrade, A. Mendes, Photoelectrochemical water splitting using WO_3 photoanodes: the substrate and temperature roles, Phys. Chem. Chem. Phys. 18(7) (2016) 5232-5243. DOI: 10.1039/C5CP06851G.

[265] A.J.E. Rettie, W.D. Chemelewski, D. Emin, C.B. Mullins, Unravelling Small-Polaron Transport in Metal Oxide Photoelectrodes, J. Phys. Chem. Lett. 7(3) (2016) 471-479. DOI: 10.1021/acs.jpclett.5b02143.

[266] G.N.P. Oliveira, P. Machado, A.L. Pires, A.M. Pereira, J.P. Araújo, A.M.L. Lopes, Magnetocaloric effect and refrigerant capacity in polycrystalline YCrO3, J. Phys. Chem. Solids 91 (2016) 182-188. DOI: https://doi.org/10.1016/j.jpcs.2015.12.012.

[267] M.P. Proenca, C.T. Sousa, A.M. Pereira, P.B. Tavares, J. Ventura, M. Vazquez, J.P. Araujo, Size and surface effects on the magnetic properties of NiO nanoparticles, Phys. Chem. Chem. Phys. 13(20) (2011) 9561-9567. DOI: 10.1039/C1CP00036E.

[268] M. Wilke, F.o. Farges, P.-E. Petit, G.E. Brown, Jr., F.o. Martin, Oxidation state and coordination of Fe in minerals: An Fe K-XANES spectroscopic study, Am. Mineral. 86(5-6) (2001) 714-730. DOI: 10.2138/am-2001-5-612.

[269] A. Annamalai, A. Subramanian, U. Kang, H. Park, S.H. Choi, J.S. Jang, Activation of Hematite Photoanodes for Solar Water Splitting: Effect of FTO Deformation, J. Phys. Chem. C 119(7) (2015) 3810-3817. DOI: 10.1021/jp512189c.

[270] L.A. Marusak, R. Messier, W.B. White, Optical absorption spectrum of hematite, α-Fe_2O_3 near IR to UV, J. Phys. Chem. Solids 41(9) (1980) 981-984. DOI: https://doi.org/10.1016/0022-3697(80)90105-5.

[271] K. Sivula, R. Zboril, F. Le Formal, R. Robert, A. Weidenkaff, J. Tucek, J. Frydrych, M. Grätzel, Photoelectrochemical Water Splitting with Mesoporous Hematite Prepared by a Solution-Based Colloidal Approach, Appl. Phys. Lett. 132(21) (2010) 7436-7444. DOI: 10.1021/ja101564f.

[272] V.P. Dimri, R.P. Srivastava, N. Vedanti, Chapter 5 - Reservoir Geophysics: Some Basic Concepts, in: V.P. Dimri, R.P. Srivastava, N. Vedanti (Eds.), Handbook of Geophysical Exploration: Seismic Exploration, Pergamon2012, pp. 89-118.

[273] P. Dias, L. Andrade, A. Mendes, Hematite-based photoelectrode for solar water splitting with very high photovoltage, Nano Energy 38 (2017) 218-231. DOI: https://doi.org/10.1016/j.nanoen.2017.05.051.

[274] A. Pu, J. Deng, M. Li, J. Gao, H. Zhang, Y. Hao, J. Zhong, X. Sun, Coupling Ti-doping and oxygen vacancies in hematite nanostructures for solar water oxidation with high efficiency, J. Mater. Chem. A 2(8) (2014) 2491-2497. DOI: 10.1039/C3TA14575A.

[275] J. Su, J. Zhou, S. Zong, Z. Zhou, C. Liu, B. Feng, The effect of thermal annealing on the interfacial properties and photoelectrochemical performance of Ti doped Fe_2O_3 nanowire arrays, RSC Advances 6(102) (2016) 99851-99858. DOI: 10.1039/C6RA19699C.

[276] P. Quiterio, A. Apolinário, D. Navas, S. Magalhaes, E. Alves, A.M. Mendes, C. Tavares de Sousa, J.P. Araújo, Photoelectrochemical Water Splitting: Thermal Annealing Challenges on Hematite Nanowires, J. Phys. Chem. C (2020). DOI: 10.1021/acs.jpcc.0c01259.

[277] N. Bhandary, A.P. Singh, P.P. Ingole, S. Basu, Enhanced photoelectrochemical performance of electrodeposited hematite films decorated with nanostructured NiMnOx, RSC Advances 6(42) (2016) 35239-35247. DOI: 10.1039/C6RA03984G.

[278] X. Zhang, Y. Niu, X. Meng, Y. Li, J. Zhao, Structural evolution and characteristics of the phase transformations between α-Fe_2O_3, Fe_3O_4 and γ-Fe_2O_3 nanoparticles under reducing and oxidizing atmospheres, CrystEngComm 15(40) (2013) 8166-8172. DOI: 10.1039/C3CE41269E.

[279] S.K. Sarma, R. Mohan, A. Shukla, Structural, opto-electronic and photoelectrochemical properties of tin doped hematite nanoparticles for water splitting,

Materials Science in Semiconductor Processing 108 (2020) 104873. DOI: https://doi.org/10.1016/j.mssp.2019.104873.

[280] D. Cao, W. Luo, M. Li, J. Feng, Z. Li, Z. Zou, A transparent Ti4+ doped hematite photoanode protectively grown by a facile hydrothermal method, CrystEngComm 15(13) (2013) 2386-2391. DOI: 10.1039/C3CE26811J.

[281] G. Wang, Y. Ling, D.A. Wheeler, K.E.N. George, K. Horsley, C. Heske, J.Z. Zhang, Y. Li, Facile Synthesis of Highly Photoactive α-Fe_2O_3-Based Films for Water Oxidation, Nano Lett. 11(8) (2011) 3503-3509. DOI: 10.1021/nl202316j.

[282] S. Magalhães, M. Fialho, M. Peres, K. Lorenz, E. Alves, Quantitative x-ray diffraction analysis of bimodal damage distributions in Tm implanted Al0.15Ga0.85N, J. Phys. D: Appl. Phys. 49(13) (2016) 135308. DOI: 10.1088/0022-3727/49/13/135308.

[283] A. Verma, A. Srivastav, D. Sharma, A. Banerjee, S. Sharma, V.R. Satsangi, R. Shrivastav, D.K. Avasthi, S. Dass, A study on the effect of low energy ion beam irradiation on Au/TiO_2 system for its application in photoelectrochemical splitting of water, Nucl. Instrum. Methods Phys. Res. B 379 (2016) 255-261. DOI: https://doi.org/10.1016/j.nimb.2016.04.006.

[284] J.F. Ziegler, M.D. Ziegler, J.P. Biersack, SRIM – The stopping and range of ions in matter (2010), Nucl. Instrum. Methods Phys. Res. B 268(11) (2010) 1818-1823. DOI: https://doi.org/10.1016/j.nimb.2010.02.091.

[285] K. Itoh, J.O.M. Bockris, Stacked thin-film photoelectrode using iron oxide, J. Appl. Phys. 56(3) (1984) 874-876. DOI: 10.1063/1.334028.

[286] D.R. Pereira, C. Díaz-Guerra, M. Peres, S. Magalhães, J.G. Correia, J.G. Marques, A.G. Silva, E. Alves, K. Lorenz, Engineering strain and conductivity of MoO3 by ion implantation, Acta Materialia 169 (2019) 15-27. DOI: https://doi.org/10.1016/j.actamat.2019.02.029.

[287] S.M. Ali, J. Muhammad, S.T. Hussain, S.A. Bakar, M. Ashraf, R. Naeem ur, Study of microstructural, optical and electrical properties of Mg dopped SnO thin films, Journal of Materials Science: Materials in Electronics 24(7) (2013) 2432-2437. DOI: 10.1007/s10854-013-1114-5.

[288] C. Marques, Modification Of Aluminium Oxides Through Ion Implantation Of Transition And Noble Metals, PhD Thesis, Universidade Nova de Lisboa (2009).

[289] C. Liu, J. Ma, H. Chen, Periodical structural conversion and its mechanism in hematite: from nanospindles, to nanotubes, to nanotires, RSC Advances 2(3) (2012) 1009-1013. DOI: 10.1039/C1RA00595B.

[290] B. Lv, Y. Xu, D. Wu, Y. Sun, Preparation and properties of magnetic iron oxide nanotubes, Particuology 6(5) (2008) 334-339. DOI: https://doi.org/10.1016/j.partic.2008.04.006.

[291] B. Lucas-Granados, R. Sánchez-Tovar, R.M. Fernández-Domene, J. García-Antón, Influence of electrolyte temperature on the synthesis of iron oxide nanostructures by electrochemical anodization for water splitting, Int. J. Hydrogen Energy 43(16) (2018) 7923-7937. DOI: https://doi.org/10.1016/j.ijhydene.2018.03.046.

[292] M. Martín-González, R. Martinez-Moro, M.H. Aguirre, E. Flores, O. Caballero-Calero, Unravelling nanoporous anodic iron oxide formation, Electrochim. Acta 330 (2020) 135241. DOI: https://doi.org/10.1016/j.electacta.2019.135241.

[293] N. Sato, 1989 Whitney Award Lecture: Toward a More Fundamental Understanding of Corrosion Processes, CORROSION 45(5) (1989) 354-368. DOI: 10.5006/1.3582030.

[294] B. Lucas-Granados, R. Sánchez-Tovar, R.M. Fernández-Domene, J. García-Antón, Iron oxide nanostructures for photoelectrochemical applications: Effect of applied potential during Fe anodization, Journal of Industrial and Engineering Chemistry 70 (2019) 234-242. DOI: https://doi.org/10.1016/j.jiec.2018.10.020.

[295] C.-Y. Lee, L. Wang, Y. Kado, M.S. Killian, P. Schmuki, Anodic Nanotubular/porous Hematite Photoanode for Solar Water Splitting: Substantial Effect of Iron Substrate Purity, ChemSusChem 7(3) (2014) 934-940. DOI: 10.1002/cssc.201300603.

[296] T. Mushove, T.M. Breault, L.T. Thompson, Synthesis and Characterization of Hematite Nanotube Arrays for Photocatalysis, Industrial & Engineering Chemistry Research 54(16) (2015) 4285-4292. DOI: 10.1021/ie504585q.

[297] M.-C. Huang, T. Wang, W.-S. Chang, C.-C. Wu, J.-C. Lin, C.-H. Lee, S.-H. Huang, Effect of anodizing temperature on surface morphology evolution of sputtered hematite films: A potential post-treatment method for further photoelectrochemical performance enhancement, Vacuum 129 (2016) 111-114. DOI: http://dx.doi.org/10.1016/j.vacuum.2016.04.021.

[298] B. Lucas-Granados, R. Sánchez-Tovar, R.M. Fernández-Domene, J.M. Estívalis-Martínez, J. García-Antón, How does anodization time affect morphological and photocatalytic properties of iron oxide nanostructures?, Journal of Materials Science & Technology 38 (2020) 159-169. DOI: https://doi.org/10.1016/j.jmst.2019.07.046.

[299] Z. Zhang, M.F. Hossain, T. Takahashi, Self-assembled hematite (α-Fe_2O_3) nanotube arrays for photoelectrocatalytic degradation of azo dye under simulated solar light irradiation, Appl. Catal. B 95(3) (2010) 423-429. DOI: https://doi.org/10.1016/j.apcatb.2010.01.022.

[300] K. Xie, M. Guo, H. Huang, Y. Liu, Fabrication of iron oxide nanotube arrays by electrochemical anodization, Corrosion Science 88 (2014) 66-75. DOI: https://doi.org/10.1016/j.corsci.2014.07.019.

[301] B. Lucas-Granados, R. Sánchez-Tovar, R.M. Fernández-Domene, J. García-Antón, Controlled hydrodynamic conditions on the formation of iron oxide nanostructures synthesized by electrochemical anodization: Effect of the electrode rotation speed, Appl. Surf. Sci. 392 (2017) 503-513. DOI: https://doi.org/10.1016/j.apsusc.2016.09.073.

[302] S.P. Albu, P. Schmuki, Highly defined and ordered top-openings in TiO_2 nanotube arrays, physica status solidi (RRL) – Rapid Research Letters 4(7) (2010) 151-153. DOI: 10.1002/pssr.201004159.

[303] K. Zhu, T.B. Vinzant, N.R. Neale, A.J. Frank, Removing Structural Disorder from Oriented TiO_2 Nanotube Arrays: Reducing the Dimensionality of Transport and Recombination in Dye-Sensitized Solar Cells, Nano Lett. 7(12) (2007) 3739-3746. DOI: 10.1021/nl072145a.

[304] K. Nielsch, J. Choi, K. Schwirn, R.B. Wehrspohn, U. Gösele, Self-ordering Regimes of Porous Alumina: The 10 Porosity Rule, Nano Lett. 2(7) (2002) 677-680. DOI: 10.1021/nl025537k.

[305] G.D. Sulka, J. Kapusta-Kołodziej, A. Brzózka, M. Jaskuła, Fabrication of nanoporous TiO_2 by electrochemical anodization, Electrochim. Acta 55(14) (2010) 4359-4367. DOI: https://doi.org/10.1016/j.electacta.2009.12.053.

[306] Z. Su, W. Zhou, Formation Mechanism of Porous Anodic Aluminium and Titanium Oxides, Adv. Mater. 20(19) (2008) 3663-3667. DOI: 10.1002/adma.200800845.

[307] Z. Su, W. Zhou, Formation, microstructures and crystallization of anodic titanium oxide tubular arrays, J. Mater. Chem. 19(16) (2009) 2301-2309. DOI: 10.1039/B820504C.

[308] Arlete Apolinario, Celia Sousa, André Pereira, Maria Fernandez-Garcia, Gonçalo Oliveira, Joao Ventura, João Azevedo, Paula Dias, Luisa Andrade, Adélio Mendes, and João Araújo. Unraveling the interplay between structural and magnetic properties of anodic iron oxide nanotubes for solar photoelectrochemical cells. Submitted to Physical Chemistry Chemical Physics (PCCP) 2020.

[309] W.S. Rasband, ImageJ, U. S. National Institutes of Health, Bethesda, Maryland, USA, http://imagej.nih.gov/ij/, 1997-2012. .

[310] N. Cabrera, N.F. Mott, Theory of the oxidation of metals, Reports on Progress in Physics 12(1) (1949) 163.

[311] V.P. Parkhutik, V.I. Shershulsky, Theoretical modelling of porous oxide growth on aluminium, J. Phys. D: Appl. Phys. 25(8) (1992) 1258.

[312] L.V. Taveira, J.M. Macák, H. Tsuchiya, L.F.P. Dick, P. Schmuki, Initiation and Growth of Self-Organized TiO_2 Nanotubes Anodically Formed in $NH4F/(NH4)2SO4$ Electrolytes, J. Electrochem. Soc. 152(10) (2005) B405-B410. DOI: 10.1149/1.2008980.

[313] X.-m. Zhong, D.-l. Yu, S.-y. Zhang, X. Chen, Y. Song, D.-d. Li, X.-f. Zhu, Fabrication and Formation Mechanism of Triple-Layered TiO_2 Nanotubes, J. Electrochem. Soc. 160(10) (2013) E125-E129. DOI: 10.1149/2.068310jes.

[314] W. Lee, R. Ji, U. Gosele, K. Nielsch, Fast fabrication of long-range ordered porous alumina membranes by hard anodization, Nat. Mater. 5(9) (2006) 741-747. DOI: http://www.nature.com/nmat/journal/v5/n9/suppinfo/nmat1717_S1.html.

[315] S. Ono, M. Saito, M. Ishiguro, H. Asoh, Controlling Factor of Self-Ordering of Anodic Porous Alumina, J. Electrochem. Soc. 151(8) (2004) B473. DOI: 10.1149/1.1767838.

[316] L. Sun, S. Zhang, X.W. Sun, X. He, Effect of electric field strength on the length of anodized titania nanotube arrays, J. Electroanal. Chem. 637(1–2) (2009) 6-12. DOI: http://dx.doi.org/10.1016/j.jelechem.2009.09.023.

[317] J.M. Macak, P. Schmuki, Anodic growth of self-organized anodic TiO_2 nanotubes in viscous electrolytes, Electrochim. Acta 52(3) (2006) 1258-1264. DOI: https://doi.org/10.1016/j.electacta.2006.07.021.

[318] G.F. Ortiz, I. Hanzu, P. Knauth, P. Lavela, J.L. Tirado, T. Djenizian, TiO_2 nanotubes manufactured by anodization of Ti thin films for on-chip Li-ion 2D microbatteries,

Electrochim. Acta 54(17) (2009) 4262-4268. DOI: http://dx.doi.org/10.1016/j.electacta.2009.02.085.

[319] D. Guan, P.J. Hymel, Y. Wang, Growth mechanism and morphology control of double-layer and bamboo-type TiO_2 nanotube arrays by anodic oxidation, Electrochim. Acta 83(0) (2012) 420-429. DOI: http://dx.doi.org/10.1016/j.electacta.2012.08.036.

[320] B. Chong, D. Yu, R. Jin, Y. Wang, D. Li, Y. Song, M. Gao, X. Zhu, Theoretical derivation of anodizing current and comparison between fitted curves and measured curves under different conditions, Nanotechnology 26(14) (2015) 145603. DOI: 10.1088/0957-4484/26/14/145603.

[321] F. Mohammadpour, F. Behzadi, M. Moradi, Fast anodically growth of long, small diameter TiO_2 nanotubes by electropolishing of Ti foils in an ethanol-containing solution, Mater Lett 150 (2015) 81-83. DOI: http://dx.doi.org/10.1016/j.matlet.2015.02.081.

[322] Y. Zhang, H. Fan, X. Ding, Q. Yan, L. Wang, W. Ma, Simulation of anodizing current-time curves and morphology evolution of TiO_2 nanotubes anodized in electrolytes with different NH4F concentrations, Electrochim. Acta 176 (2015) 1083-1091. DOI: http://dx.doi.org/10.1016/j.electacta.2015.07.110.

[323] J.W. Diggle, T.C. Downie, C.W. Goulding, Anodic oxide films on aluminum, Chemical Reviews 69(3) (1969) 365-405. DOI: 10.1021/cr60259a005.

[324] J. Oh, C.V. Thompson, The role of electric field in pore formation during aluminum anodization, Electrochim. Acta 56(11) (2011) 4044-4051. DOI: https://doi.org/10.1016/j.electacta.2011.02.002.

[325] J.K. Kim, K. Shin, S.M. Cho, T.-W. Lee, J.H. Park, Synthesis of transparent mesoporous tungsten trioxide films with enhanced photoelectrochemical response: application to unassisted solar water splitting, Energy Environ. Sci. 4(4) (2011) 1465-1470. DOI: 10.1039/C0EE00469C.

[326] S.K. Mohapatra, M. Misra, V.K. Mahajan, K.S. Raja, Design of a Highly Efficient Photoelectrolytic Cell for Hydrogen Generation by Water Splitting: Application of TiO_2-xCx Nanotubes as a Photoanode and Pt/TiO_2 Nanotubes as a Cathode, J. Phys. Chem. C 111(24) (2007) 8677-8685. DOI: 10.1021/jp071906v.

[327] J.M. Macák, H. Tsuchiya, A. Ghicov, P. Schmuki, Dye-sensitized anodic TiO_2 nanotubes, Electrochem. Commun. 7(11) (2005) 1133-1137. DOI: http://dx.doi.org/10.1016/j.elecom.2005.08.013.

[328] S. Mathew, A. Yella, P. Gao, R. Humphry-Baker, F.E. CurchodBasile, N. Ashari-Astani, I. Tavernelli, U. Rothlisberger, K. NazeeruddinMd, M. Grätzel, Dye-sensitized solar cells with 13% efficiency achieved through the molecular engineering of porphyrin sensitizers, Nat Chem 6(3) (2014) 242-247. DOI: 10.1038/nchem.1861. http://www.nature.com/nchem/journal/v6/n3/abs/nchem.1861.html#supplementary-information.

[329] M. Law, L.E. Greene, J.C. Johnson, R. Saykally, P. Yang, Nanowire dye-sensitized solar cells, Nat. Mater. 4(6) (2005) 455-459. DOI: http://www.nature.com/nmat/journal/v4/n6/suppinfo/nmat1387_S1.html.

[330] J. Jiu, S. Isoda, F. Wang, M. Adachi, Dye-Sensitized Solar Cells Based on a Single-Crystalline TiO_2 Nanorod Film, J. Phys. Chem. B 110(5) (2006) 2087-2092. DOI: 10.1021/jp055824n.

[331] J.M. Macak, H. Tsuchiya, A. Ghicov, K. Yasuda, R. Hahn, S. Bauer, P. Schmuki, TiO_2 nanotubes: Self-organized electrochemical formation, properties and applications, Curr. Opin. Solid State Mater. Sci. 11(1–2) (2007) 3-18. DOI: http://dx.doi.org/10.1016/j.cossms.2007.08.004.

[332] H.E. Prakasam, K. Shankar, M. Paulose, O.K. Varghese, C.A. Grimes, A New Benchmark for TiO_2 Nanotube Array Growth by Anodization, J. Phys. Chem. C 111(20) (2007) 7235-7241. DOI: 10.1021/jp070273h.

[333] D. Kim, A. Ghicov, S.P. Albu, P. Schmuki, Bamboo-Type TiO_2 Nanotubes: Improved Conversion Efficiency in Dye-Sensitized Solar Cells, Appl. Phys. Lett. 130(49) (2008) 16454-16455. DOI: 10.1021/ja805201v.

[334] X. Luan, D. Guan, Y. Wang, Facile Synthesis and Morphology Control of Bamboo-Type TiO_2 Nanotube Arrays for High-Efficiency Dye-Sensitized Solar Cells, J. Phys. Chem. C 116(27) (2012) 14257-14263. DOI: 10.1021/jp305280q.

[335] A. Valota, D.J. LeClere, P. Skeldon, M. Curioni, T. Hashimoto, S. Berger, J. Kunze, P. Schmuki, G.E. Thompson, Influence of water content on nanotubular anodic titania formed in fluoride/glycerol electrolytes, Electrochim. Acta 54(18) (2009) 4321-4327. DOI: http://dx.doi.org/10.1016/j.electacta.2009.02.098.

[336] B. Chong, D.-l. Yu, M.-q. Gao, H.-w. Fan, C.-y. Yang, W.-h. Ma, S.-y. Zhang, X.-f. Zhu, Formation Mechanism of Gaps and Ribs Around Anodic TiO_2 Nanotubes and Method to Avoid Formation of Ribs, J. Electrochem. Soc. 162(4) (2015) H244-H250. DOI: 10.1149/2.0721504jes.

[337] S.P. Albu, D. Kim, P. Schmuki, Growth of Aligned TiO_2 Bamboo-Type Nanotubes and Highly Ordered Nanolace, Angew. Chem. Int. Ed. 47(10) (2008) 1916-1919. DOI: 10.1002/anie.200704144.

[338] K.S. Raja, T. Gandhi, M. Misra, Effect of water content of ethylene glycol as electrolyte for synthesis of ordered titania nanotubes, Electrochem. Commun. 9(5) (2007) 1069-1076. DOI: http://dx.doi.org/10.1016/j.elecom.2006.12.024.

[339] S. Li, G. Zhang, D. Guo, L. Yu, W. Zhang, Anodization Fabrication of Highly Ordered TiO_2 Nanotubes, J. Phys. Chem. C 113(29) (2009) 12759-12765. DOI: 10.1021/jp903037f.

[340] Y. Xue, Y. Sun, G. Wang, K. Yan, J. Zhao, Effect of NH4F concentration and controlled-charge consumption on the photocatalytic hydrogen generation of TiO_2 nanotube arrays, Electrochim. Acta 155 (2015) 312-320. DOI: http://dx.doi.org/10.1016/j.electacta.2014.12.134.

[341] F. Zhang, S. Chen, Y. Yin, C. Lin, C. Xue, Anodic formation of ordered and bamboo-type TiO_2 anotubes arrays with different electrolytes, J. Alloys Compd. 490(1–2) (2010) 247-252. DOI: http://dx.doi.org/10.1016/j.jallcom.2009.09.169.

[342] A. Apolinario, C.T. Sousa, J. Ventura, J.D. Costa, D. Leitao, J.M. Moreira, J.B. Sousa, L. Andrade, A. Mendes, J.P. Araujo, The role of the Ti surface roughness on the self-ordering of TiO_2 nanotubes: a detailed study of the growth mechanism, Journal of Materials Chemistry A (2014). DOI: 10.1039/C4TA00871E.

[343] L. Peixoto, Magnetic nanostructures for biotechnological applications, Master Thesis, University of Porto (2018).